

# IMFUFA **tekst**

- I, OM OG MED MATEMATIK OG FYSIK

## **Isomorphs in Metals**

from equilibrium crystal dynamics to melting curve determination

Laura Friedeheim  
Phd thesis

**nr. 515 – 2021**

Roskilde University,  
Department of Science and Environment, IMFUFA  
P.O. Box 260, DK - 4000 Roskilde  
E-mail: imfufa@ruc.dk



## **Isomorphs in Metals**

from equilibrium crystal dynamics to melting curve determination

Laura Friedeheim

Phd thesis

IMFUFA tekst nr. 515/2021 — 156 sider — ISSN: 0106-6242

---

This thesis uses computer simulations as the main tool to explore the phase diagram of metals in the liquid and solid part of the phase diagram in the context of isomorph theory.

This work has two main goals. The first is to test the validity of isomorph theory and its predicted invariance along isomorphs throughout the solid and/or liquid part of the phase diagram of the candidate metals. The second key prediction from isomorph theory that this work focuses on pertains to the melting and freezing curve. Isomorphs that started from a point at coexistence are predicted to be closely related to the nearby freezing and melting curve and a method was devised that enables the prediction of the freezing and melting curve from data of the neighbouring isomorphs on the solid and the liquid side. The second goal of this thesis is therefore to combine predictions from isomorph theory with results from DFT to predict the freezing and melting curve over a significant range of the phase diagram from simulations at one state point only, making the most out of the costly DFT simulations.

The work is structured as follows: Some background information with focus on metals and isomorph theory will be given in the first chapter followed by a detailed review of isomorph theory and its predictions in the subsequent chapter. Chapter 3 provides an introduction to computer simulation in general. A review of the two methods employed in the simulations used for this work, density functional theory (DFT) and the effective medium theory (EMT) is given in chapter 4.

The results can be found in chapter 5 and 6 with each chapter corresponding to one of the two main focus points of this work. The first presents an investigation of the invariances predicted by isomorph theory in different candidate metals. The study includes (a) mono-atomic crystals (Ni, Cu, Pd, Ag, Pt, Au) and (b) liquid CuZr simulated using the EMT potential as well as (c) two metals (Mg, Al) simulated using DFT in the solid and liquid state. The second part of the results (Ch. 6) is dedicated to a method predicting the melting curve from nearby isomorphs that is applied to one EMT metal (Cu) and three DFT metals (Al, Mg, Na). The chapter also includes the review of and comparison to other state of the art methods to predict (points on) the freezing and melting curves.

This work establishes good isomorph invariance in all candidate metals with the exception of DFT-Mg investigated in the first part of the study. The second part demonstrates good agreement between the freezing and melting curves predicted by our method when compared to the literature. The agreement is best with other methods using DFT-based simulations while state points taken from experiments show more significant (though still small) deviations.

PhD Thesis by Laura Friedeheim

---

# *Isomorphs in Metals*

from equilibrium crystal dynamics to melting  
curve determination

---

Supervisor: Nicholas P. Bailey  
Co-supervisor: Jeppe C. Dyre

Glass & Time, Physics, IMFUFA  
Department of Science and Environment  
Roskilde University, Denmark

December 14, 2020





# Abstract

---

This thesis uses computer simulations as the main tool to explore the phase diagram of metals in the liquid and solid part of the phase diagram in the context of isomorph theory.

This work has two main goals. The first is to test the validity of isomorph theory and its predicted invariance along isomorphs throughout the solid and/or liquid part of the phase diagram of the candidate metals. The second key prediction from isomorph theory that this work focuses on pertains to the melting and freezing curve. Isomorphs that started from a point at coexistence are predicted to be closely related to the nearby freezing and melting curve and a method was devised that enables the prediction of the freezing and melting curve from data of the neighbouring isomorphs on the solid and the liquid side. The second goal of this thesis is therefore to combine predictions from isomorph theory with results from DFT to predict the freezing and melting curve over a significant range of the phase diagram from simulations at one state point only, making the most out of the costly DFT simulations.

The work is structured as follows: Some background information with focus on metals and isomorph theory will be given in the first chapter followed by a detailed review of isomorph theory and its predictions in the subsequent chapter. Chapter 3 provides an introduction to computer simulation in general. A review of the two methods employed in the simulations used for this work, density functional theory (DFT) and the effective medium theory (EMT) is given in chapter 4.

The results can be found in chapter 5 and 6 with each chapter corresponding to one of the two main focus points of this work. The first presents an investigation of the invariances predicted by isomorph theory in different candidate metals. The study includes (a) mono-atomic crystals (Ni, Cu, Pd, Ag, Pt, Au) and (b) liquid CuZr simulated using the EMT potential as well as (c) two metals (Mg, Al) simulated using DFT in the solid and liquid state. The second part of the results (Ch. 6) is dedicated to a method predicting the melting curve from nearby isomorphs that is applied to one EMT metal (Cu) and three DFT metals (Al, Mg, Na). The chapter also includes the review of and comparison to other state of the art methods to predict (points on) the freezing and melting curves. This work establishes good isomorph invariance in all

candidate metals with the exception of DFT-Mg investigated in the first part of the study. The second part demonstrates good agreement between the freezing and melting curves predicted by our method when compared to the literature. The agreement is best with other methods using DFT-based simulations while state points taken from experiments show more significant (though still small) deviations.



# Resumé

---

Denne afhandling bruger computersimuleringer som hovedværktøj til at undersøge fase-diagrammet for metaller i den flydende og faste del af fase-diagrammet med fokus på isomorfteori.

Arbejdet har to hovedmål. Det første er at teste gyldigheden af isomorfteori og dens forudsagte invarians langs isomorfer gennem den faste og/eller flydende del af fase-diagrammet for metallerne i studiet. Den anden vigtige forudsigtelse fra isomorfteori som arbejdet fokuserer på, vedrører smelte- og frysekurven. Isomorfe kurver der startede fra et tilstandspunkt ved sameksistens, forudsiges at følge tæt langs den nærliggende fryse- og smeltekurve. Ifølge isomorfteorien findes der en metode, der muliggør at forudsige smelte- og frysekurve ud fra de to nabo-isomorfer på den faste og den flydende side. Afhandlingens andet mål er derfor at kombinere forudsigtelser fra isomorfteori med resultater fra DFT. På den måde er det muligt at forudsige smelte- og frysekurverne med et signifikant rækkevidde gennem fase-diagrammet ud fra simuleringer ved kun et tilstandspunkt. Det er en vigtig fordel når man benytter dyre DFT-simuleringer.

Afhandlingen er struktureret som følger: Baggrund vedrørende metaller og isomorfteori præsenteres i første kapitel efterfulgt af en detaljeret gennemgang af isomorfteori og dens forudsigtelser i det efterfølgende kapitel 2. Kapitel 3 giver en generel introduktion til computersimulering. En detaljeret sammendrag af de to metoder der bliver anvendt i simuleringerne - density functional theory (DFT) og effektiv medium theory (EMT) - findes i kapitel 4.

Resultaterne findes i kapitel 5 og 6, hvor hvert kapitel svarer til et af de to hovedfokuspunkter i arbejdet. Første hovedfokuspunkt er at undersøge invarianterne som er forudsagt af isomorfteori i forskellige metaller. Undersøgelsen inkluderer (a) mono-atomiske krystaller (Ni, Cu, Pd, Ag, Pt, Au) og (b) flydende CuZr simuleret ved hjælp af EMT-potentialet samt (c) to metaller (Mg, Al) simuleret med DFT i fast og flydende tilstand. Den anden del af resultaterne (Ch. 6) omhandler en metode, der forudsiger fryse- og smeltekurven ud fra data langs nærliggende isomorfer. Metoden bruges her for et EMT-metal (Cu) og tre DFT-metaller (Al, Mg, Na). Kapitlet inkluderer også en gennemgang af og sammenligning med resultaterne fra andre avancerede metoder til at forudsige (tilstandspunkter på) fryse- og smeltekurverne.

Afhandlingen finder god isomorf invarians i alle undersøgte metaller, bortset fra Mg. Derudover demonstrerer arbejdet god overensstemmelse mellem smelte- og frysekurver forudsagt af vores metode sammenlignet med litteraturen. Overensstemmelsen er bedst med andre metoder som også brugte DFT-baserede simuleringer, mens tilstandspunkter taget fra eksperimenter viser mere signifikante, men stadigvæk små, afvigelser.



# Contents

---

|          |  |           |
|----------|--|-----------|
| <b>1</b> | <b>Introduction</b>  | <b>1</b>  |
| <b>2</b> | <b>R-simplicity and Hidden Scale Invariance</b>              | <b>7</b>  |
| 2.1      | A brief history about strong correlations . . . . .          | 8         |
| 2.2      | Generic definition of R-simplicity . . . . .                 | 10        |
| 2.3      | Fantastic isomorphs and where to find them . . . . .         | 13        |
| 2.4      | Some consequences and special cases . . . . .                | 17        |
| 2.4.1    | Perfect IPL isomorphs . . . . .                              | 17        |
| 2.4.2    | Isomorph relevance to the melting curve . . . . .            | 19        |
| 2.4.3    | Instantaneous equilibration . . . . .                        | 19        |
| <b>3</b> | <b>Molecular Dynamics</b>                                    | <b>21</b> |
| 3.1      | Pair potentials and beyond . . . . .                         | 21        |
| 3.2      | Ensembles . . . . .  | 23        |
| 3.3      | Observables . . . . .  | 24        |
| <b>4</b> | <b>Computational methods for Metals</b>                      | <b>29</b> |
| 4.1      | Electron gas and simple metals . . . . .                     | 30        |
| 4.2      | Density functional theory . . . . .                          | 32        |
| 4.2.1    | Hohenberg-Kohn-Sham . . . . .                                | 32        |
| 4.2.2    | Exchange-correlation functionals . . . . .                   | 35        |
| 4.2.3    | Simpler potentials derived from DFT considerations . . . . . | 43        |
| 4.3      | Effective medium theory . . . . .                            | 43        |
| <b>5</b> | <b>Hidden Scale Invariance in Metals</b>                     | <b>47</b> |
| 5.1      | Mono-atomic crystals (Ni, Cu, Pd, Ag, Pt, Au) . . . . .      | 47        |
| 5.1.1    | Invariance of structure and dynamics . . . . .               | 49        |
| 5.1.2    | EMT-cutoff bumps . . . . .                                   | 53        |
| 5.1.3    | Other isomorph related studies . . . . .                     | 55        |
| 5.2      | Liquid CuZr . . . . .  | 59        |
| 5.3      | DFT metals . . . . .   | 66        |

## CONTENTS

|   |            |
|---|------------|
| <b>6 Freezing and Melting in Metals</b>   | <b>81</b>  |
| 6.1 Method to predict freezing and melting curves . . . . .                         | 83         |
| 6.2 Melting curve of EMT-Cu . . . . .   | 85         |
| 6.3 Melting curves using DFT . . . . .  | 86         |
| 6.3.1 Aluminium . . . . .   | 87         |
| 6.3.2 Magnesium . . . . .   | 90         |
| 6.3.3 Sodium . . . . .  | 92         |
| 6.4 Re-entrant melting and R-simplicity . . . . .                                   | 94         |
| <b>7 Concluding Remarks</b>   | <b>97</b>  |
| <br>  |            |
| <b>Appendix</b>   | <b>101</b> |
| <br>  |            |
| <b>A Problems with Interface pinning and DFT</b>                                    | <b>101</b> |
| A.1 Interface Pinning Procedure . . . . .   | 102        |
| A.2 Free electrons in a non-cubic box . . . . .                                     | 103        |
| <br>  |            |
| <b>B Other details</b>  | <b>109</b> |
| B.1 Fixing pressure for melting pressure start point . . . . .                      | 109        |
| B.2 Polynomial fits to the DIC data . . . . .                                       | 111        |
| B.3 Pulay stress . . . . .  | 112        |
| B.4 Pressure anisotropy in the HCP DFT crystal . . . . .                            | 113        |
| <br>  |            |
| <b>C Reprints of articles</b>   | <b>117</b> |
| Hidden scale invariance at high pressures in gold and five other fcc metal crystals | 118        |
| <br>  |            |
| <b>D Reprints of posters</b>  | <b>131</b> |
| Isomorphs in metal crystals and glass-forming alloys . . . . .                      | 132        |
| Hidden scale invariance in liquid CuZr . . . . .                                    | 133        |
| <br>  |            |
| <b>Bibliography</b>   | <b>134</b> |





# 1

## Introduction

The phase diagram of a material can be viewed as a type of map, that provides information over the state of matter at a certain state point. The phase diagram of a typical one component system is shown in Figure 1.1. The two panels shows schematics of two possible ways to draw such a map, in the temperature pressure plane (right) and in the density temperature plane (left). In the temperature pressure plane, the lines indicate phase boundaries, thus separate the different phases: solid, liquid and vapor. In the density pressure plane, the line indicates the boundary between the pure phase and coexistence mixtures. This illustrates the interesting fact that e.g. a solid and a liquid state point at coexistence have the same temperature and pressure but different densities.

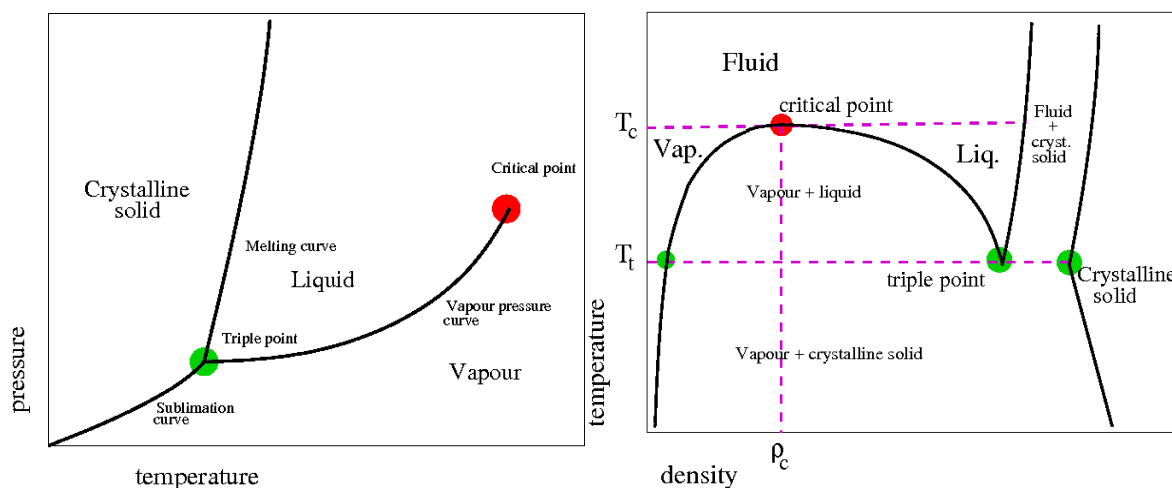


Figure 1.1: Schematics of the phase diagram in the temperature pressure plane (left) and in the density temperature plane (right). The lines mark the boundaries between phases. The red dot indicates the critical point, the point beyond which vapor and liquid become indistinguishable. The green dot is the triple point, the state point where all three phases can coexist in equilibrium. The figures are taken from the SklogWiki [1, 2]

The phase diagrams of real materials are generally well understood and mapped out from ambient conditions; around low pressures, temperatures and densities. However, the higher

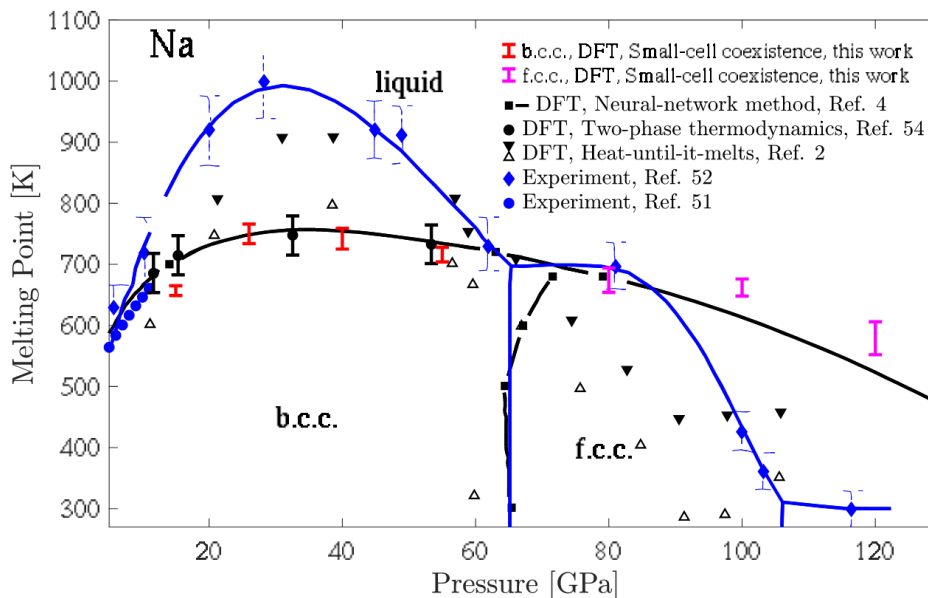


Figure 1.2: Melting data for Na determined by different methods, figure taken from Ref. [3]. The blue points are obtained from experiments, the black and red-ish points are from computer simulation using DFT.

temperature or pressure (or both), the harder it is to investigate such conditions in experimental setups. This means that upwards, outside from the upper part of both phase diagram schematics, the map gradually becomes ‘uncharted territory’. Where the metaphorical map ends, a given spot could be land or could be sea. And similarly, where the phase diagram is uncharted, a given state point could be solid or fluid.

Metals have a number of interesting features in the high pressure regime of their phase diagram. The solid phase for example undergoes several changes in crystal structure under increasing pressure. Also the temperature at which a metal melts when under high pressure deserves to be the main interest of research in itself. It is well known that some alkali metals exhibit a re-entrant melting behaviour. This means that the melting curve – the dependence of the melting temperature on the pressure – has a maximum temperature after which the melting temperature decreases again when pressure is further increased. One example of re-entrant melting is Sodium, whose phase diagram is shown in Figure 1.2. While the different methods do not agree on a maximum temperature the melting curve reaches, all methods find the maximum at around the same pressure.

Recent results from computer simulations [3] show that this is actually not the anomalous behaviour of alkali metals but rather a universal behaviour of the melting curve in most metals. The difference is just that the re-entrant melting point in non-alkali metals happens at such extreme pressures and temperatures that it is impossible to observe with current experimental techniques.

Simple materials in literature [4–6] are traditionally defined as systems consisting of classical particles whose interaction can be described by means of radially symmetric pair-potentials.

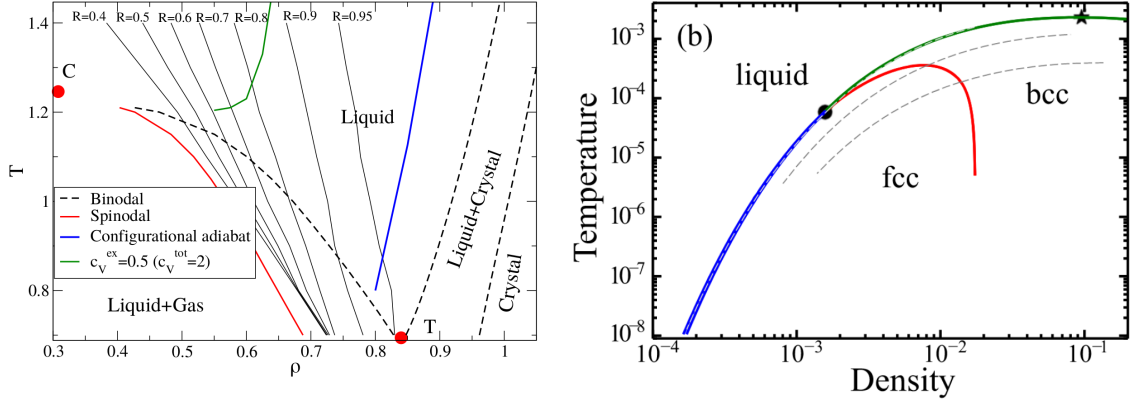


Figure 1.3: Phase diagrams studied in the context of isomorph theory. The left shows an isomorph (blue solid line) in the liquid regime of the LJ system. Figure taken from Ref. [7]. The right shows isomorphs (grey dashed lines) around the re-entrant point (star) in the EXP system. Figure taken from Ref. [8].

This means that the adjective *simple* refers to the mathematical description of the system rather than the system’s behaviour or thermodynamic phase diagram.

Simple is also used in the context of metals. Here the term simple metals refers to *sp*-bonded metals like Aluminium [9–11]. Such metals have a partially filled *sp* shell as the outermost shell, which results in the outer electrons interacting only weakly with the metal ions. This makes for a simple electronic band structure consisting of *sp* symmetry bands. These bands are very close to a free electron band and thus the simple metals are simple in the sense of Sommerfeld’s model of charge carriers in metals based on Fermi statistics [12].

This work deals with a novel kind of simplicity which is motivated by the success of isomorph theory [13–18] over the last decade in a variety of different (model) systems. Isomorph theory gives the word ‘simple’ a new interpretation with respect to the phase diagram of model system as well as real materials. The theory predicts the existence of curves – *isomorphs* – in the phase diagram along which structure and dynamics are invariant (when given in appropriately reduced units). *Isomorph* is a term from mathematics that derives from the Greek words *iso*, equal and *morphe*, shape or form. The presence of isomorphs in the phase diagram leads to the rather dramatic consequence that the phase diagram of such ‘simple materials’ is effectively one dimensional. This novel kind of simplicity – referred to as *R-simplicity* to avoid confusion – has been shown to exist in several systems. *R-simplicity* has been found in several groups of materials. Not limited to but included in this list are the following systems: Simple models of liquids [16, 17, 19], molecules [20, 21] and crystals [22] as well as in molecules and polymers in experiments [23–26]. As a general trend, it has been determined that most systems with non-directional interactions have this simple behaviour while directional bonding as well as competing length scales of interactions spoil it.

Figure 1.3 shows the phase diagrams of two different systems with isomorphs, the Lennard-Jones system on the left and the EXP system on the right. The Lennard-Jones system is the standard 6-12 system with the blue line tracing an isomorph in the liquid regime of the

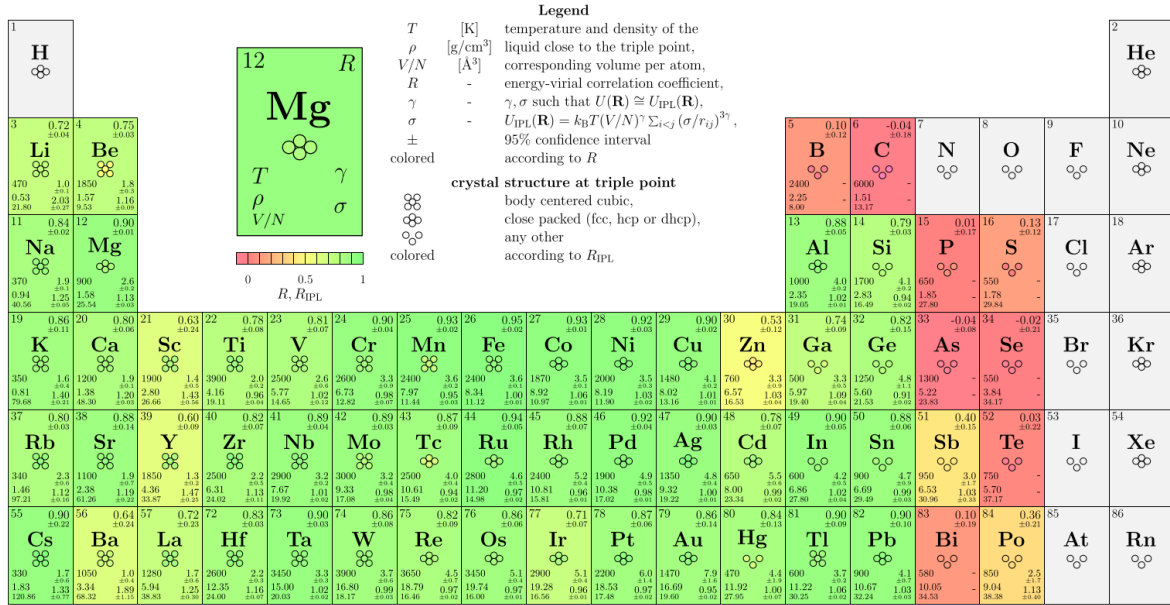


Figure 1.4: This figure, the 'periodic table of isomorph theory' has been taken from [29]. The elements are colored according to their  $R$  value, where green -  $R$  close to unity - means the material is R-simple.

phase diagram. The EXP system is governed by a purely repulsive potential of the form  $v(r) = \epsilon r^{-r/\sigma}$  with  $\sigma$  and  $\epsilon$  being a characteristic length and energy, respectively. The EXP phase diagram is pictured with three isomorphs (grey dashed lines) in the solid regime (the third coincides with the solid blue and green line marking the phase boundary). The EXP potential as been dubbed the “mother of all potentials” [27] since it can be shown that any system with a pair-potentials can be re-expressed by a sum of decaying exponential functions. Additionally, and this is especially interesting in the context of metals, the EXP potential can be regarded as a prototype model for metals whose interaction in the condensed phase is also dominated by repulsion. The fact that the EXP also exhibits re-entrant melting (with the temperature maximum marked in the figure by a star) is in agreement with Hong and van der Walle’s hypothesis of re-entrant melting being a universal feature of all metals.

The isomorphs shown in both systems in Figure 1.3 are similar in shape to the solid-liquid phase boundary. In fact it has been shown that isomorph theory can be used to calculate the melting pressure as a function of temperature from data along nearby isomorphs [28]. The reference also includes how to calculate the freezing and melting densities, resulting in a method to predict the freezing and melting curves in both the density-temperature and the temperature-density plane.

Isomorph theory relies on a scale invariant behaviour where a system’s potential-energy hypersurface follows a simple self-similar deformation when subjected to a change in density. This self similar scaling behaviour leaves the ordering of the potential energies of different, same-density configurations of particles unchanged under volumetric scaling to a different density. It is in most cases not obvious from the form of the interactions between the particles

that this scale invariance holds, hence why it has been dubbed *hidden* scale invariance.

A recent study using density functional theory [29] has shown that most metals do obey the scaling invariance at the one state point investigated, which was chosen to be close to the material's triple point. The 'isomorph periodic table' in Fig 1.4 shows results from this study. For every element, isomorph properties – the correlation coefficient  $R$  and the scaling exponent  $\gamma$  – have been calculated from simulations. An  $R$  value close to unity predicts that the material obeys hidden scale invariance at the given point in the phase diagram. The elements in Fig 1.4 are colored according to their  $R$  value, where green indicates an  $R$  value close to unity, while red means no correlations. The gray elements, where not included in this since they are not suited for DFT simulation. As most of the 'isomorph periodic table' is colored green or light green, this suggests that most metals can be expected to have isomorphs in parts of their phase diagram.

Metals cannot be accurately simulated using rigid pair-potentials only [30]. For example a Cauchy relation that is by construction obeyed by pair-potentials is not fulfilled by metals. Another example is the vacancy formation energy that is for real metals much lower than the energy cost predicted by a pair-potential. Instead, it is necessary to use more sophisticated models that include many-body contributions in some way. The weapon of choice for this work are the effective medium theory (EMT) and density functional theory (DFT). The EMT potential is a semi-empirical model that is derived from DFT using both, similar consideration to motivate expressions as well as directly fitting to results from DFT. This results in a model that includes many-body contributions at the computational cost similar to that of simple pair-potentials. Density functional theory is a highly accurate method widely used in computational physics and chemistry. While this method is computationally less expensive than other methods with similar accuracy, the costs remain fairly high.

One objective of this work is to extend the study of hidden scale invariance in realistic models of metals using both DFT and the EMT potential. The second objective of this work, after having established good isomorphs, is to apply the method to calculate the freezing and melting curves from nearby isomorphs.

Most isomorphs in this work are determined using the so-called direct isomorph check. This is a method that enables to find several state points along an isomorph including thermodynamic quantities at these state points from simulations at a single reference point. While there are other methods that are slightly more accurate, this is the only method that is computationally efficient enough to be used together with DFT simulations. The invariance of structure and dynamics along the isomorphs is confirmed through additional simulations at state points along the isomorph. The radial-distribution function, velocity auto-correlation function and other dynamic functions are calculated for these state points and compared to determine that structure and dynamics are indeed invariant. The same method to determine isomorph is also used in pursuing the second objective. This means that the freezing and melting curves are predicted from simulations at only one state point.

This work finds good isomorphs in a variety of candidate metals including both *sp*-simple and not simple metals. With regards to the second objective, this work shows good agreement

## *Chapter 1: Introduction*

between the calculated freezing and melting curve in one EMT and one DFT metal and the freezing and melting curves determined by other methods and experiments. Some features in connection with re-entrant melting are discussed at the end of this thesis, even though not all predictions from isomorph theory are expected to hold around the re-entrant point.

# 2

## *R-simplicity and Hidden Scale Invariance*

---

This chapter gives an overview over isomorph theory, its underlying (or *hidden*) scale invariance and what it means if a system is *R-simple*. Isomorph theory has been developed in a series of papers [13–17] and subsequently updated to the current, more generic formulation in [18]. We start with a brief recount of the history of the development of isomorph theory followed by the generic definition and a discussion of some consequences. And last but not least, the relation between the freezing and melting lines and their neighbouring isomorphs is highlighted. If a system is said to have isomorphs, it is equivalent to state that it obeys isomorph theory’s hidden scale invariance or that is R-simple.

The traditional definition of a *simple* liquid is a system of point-like particles with isotropic and usually strongly repulsive pair-interaction [6]. This means that the adjective ‘simple’ here refers to the mathematical simplicity of the Hamiltonian describing such a system, rather than the behaviour of the liquid in simulations or experiments or with respect to a certain feature. An alternative meaning for what makes a liquid (or solid for that matter) simple has been provided by isomorph theory. The simplicity of isomorph theory refers among other things to the phase diagram. Isomorph theory predicts the invariance of structure, dynamics and certain thermodynamics quantities along well defined curves, dubbed isomorphs, in the phase diagram. This effectively reduces the phase diagram by one dimension. It could be argued that this makes for a more useful

‘simple’ than the traditional, mathematically motivated definition. The schematic in Figure 2.1 illustrates the scaling behaviour of the potential energy landscape that underlies isomorph

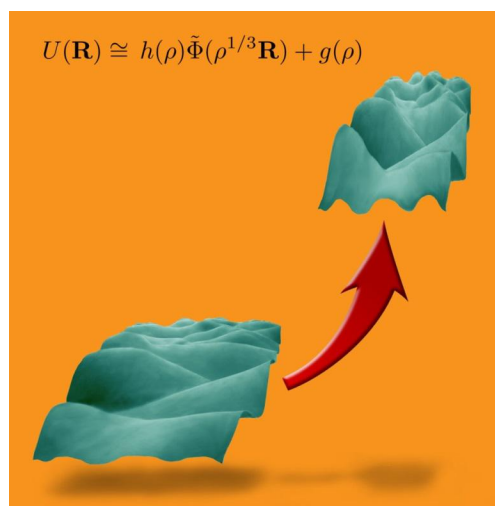


Figure 2.1: Illustration of the scaling behaviour of the potential energy hyper surface that underlies isomorph theory

theory. In most *R*-simple systems, this scaling behaviour is not obvious from the form of the potential which is why we speak of a hidden scale invariance.

## 2.1 A brief history about strong correlations

The story starts in 2008 with the discovery by the Roskilde group, that some model liquids have strong correlations between equilibrium fluctuations of the potential energy  $U$  and virial  $W$  when simulated in the NVT ensemble [13, 14]. The virial  $W$  is the configurational part of the pressure,  $PV = Nk_B T + W$ . An example of a time series of these fluctuations normalized by their respective average is shown in the first panel of Figure 2.2. The  $R$  value indicated in the panel is the Pearson correlation coefficient,

$$R = \frac{\langle \Delta W \Delta U \rangle}{\sqrt{\langle (\Delta W)^2 \rangle \langle (\Delta U)^2 \rangle}} \quad (2.1)$$

where the sharp brackets denote the canonical constant-volume (NVT) averages. It is convention that systems with  $R > 0.9$  are considered strongly correlated in the isomorph theory sense of the word. To avoid confusion with e.g. strongly correlated quantum systems, these systems are called *Roskilde* or more often *R-simple* systems.

If a system is *R-simple*, it has strong correlation between the fluctuations  $\Delta U$  and  $\Delta W$

$$\Delta W \cong \gamma \Delta U, \quad (2.2)$$

where the proportionality factor is called  $\gamma$ . The precise definition of  $\gamma$  is given in Eq. (2.4). The middle panel of Figure 2.2 shows a scatter plot of the same data as the time series in the left panel. The stronger the correlation, the more narrow the resulting elliptic shape in the scatter plot is. The dashed trend line in the middle panel gives the proportionality factor  $\gamma$ . The interpretation of  $\gamma$  as the slope in a  $U$  vs.  $W$  plot becomes clear from rewriting Eq. (2.2) as  $\gamma = \Delta W / \Delta U$ .

In contrast, the right panel in Fig. 2.2 shows a scatter plot for a system with no correlations, resulting in a round and shapeless scatter plot. No proportionality can be observed and calculating  $\gamma$  would not be meaningful for a system without strong correlations.

Whenever strong correlations are present (complying with the condition that  $R > 0.9$ ), then the system is said to have *isomorphs*. Isomorphs are curves in the phase diagram along which structure, dynamics and certain thermodynamical properties are invariant (to a good approximation) when given in appropriately reduced units. Reduced units [16] consist of the length unit  $l_0 = \rho^{-1/3}$ , the time unit  $t_0 = \rho^{-1/3} \sqrt{m/k_B T}$  and the energy unit  $e_0 = k_B T$ .

Isomorphs were introduced in Ref. [16] which showed that any isomorph invariant can be expressed as a function following  $h(\rho)/T = \text{const.}$  with  $\gamma \equiv d \ln h(\rho) / d \ln \rho$ , i.e. where  $\gamma$  varies only depending on density and is independent of temperature. This also motivates why  $\gamma$  is usually referred to as density scaling exponent or scaling exponent for short. The name

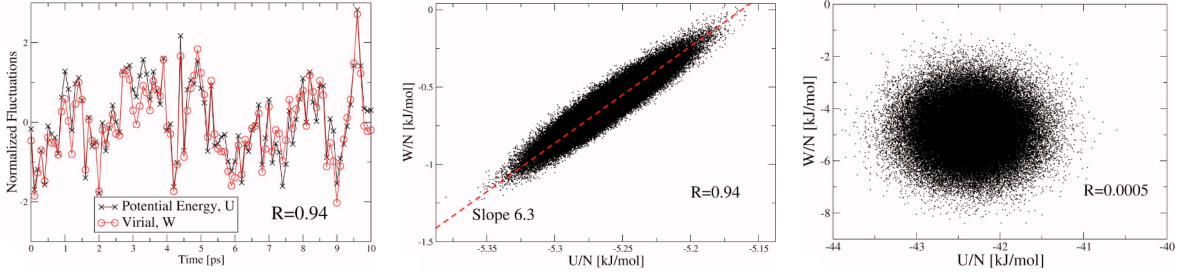


Figure 2.2: Figure taken from Ref. [13]. Correlation between (normalized) potential energy and virial as a time series (left) and scatter plot (middle) in a Lennard Jones System for a state point with strong correlations, ( $R = 0.94$ ). The slope,  $\gamma = 6.3$  is indicated in the scatter plot as a red dashed line (Note that an older definition for  $\gamma$  was used in the paper which differs from the one given in the text by a factor of  $R$ ). Shown for comparison (right) is a scatter plot for a state point in a system with no correlations; the TIP5P model for water, ( $R = 0.0005$ ).

was also motivated by the fact that the first experimental evidence for the theory comes from the so-called power-law density scaling relation [23–25].

The dependence or independence of  $\gamma$  has changed throughout the development of the theory. Initially  $\gamma$  was thought to be a constant, which fits most experimental data. It has since been shown that  $\gamma$  varies also with temperature not just density [18], which will be discussed in more detail in the next section. Following paper IV [16],  $\gamma$  is defined at any state point as

$$\gamma(\rho, T) = \left( \frac{\partial \ln T}{\partial \ln \rho} \right)_{S_{ex}} \quad (2.3)$$

Ref. [16] then goes on to show that  $\gamma$  can also be calculated directly in simulations from fluctuations, via

$$\gamma(\rho, T) = \frac{\langle \Delta W \Delta U \rangle}{\langle (\Delta U)^2 \rangle}. \quad (2.4)$$

As indicated by  $\gamma(\rho, T)$  both definitions hold also for the later version, where  $\gamma$  is no longer independent of temperature. Isomorphs in the phase diagram can be traced out in a step-wise fashion. One way to do this is by calculating  $\gamma$  from fluctuations of simulations at each state point via Eq. (2.4) followed by numerically integrating Eq. (2.3) by changing density in small increments.

Extensive simulations throughout the thermodynamic phase diagram of various different systems with various manifestations of strong correlations have been carried out and analysed [14–17, 19–22]. From these studies, some statements about the presence of strong correlations can be made:

1. No realistic system is strongly correlated throughout their entire phase diagram. The same goes for most model systems. One exception to this are systems interacting by an inverse power law.

2. Strong correlations are generally more present in the condensed part of the phase diagram. They tend to break down close to the triple point and are not present in the gas phase of any system. In particular when the virial becomes negative, the system becomes uncorrelated.
3. If a system is strongly correlated in the liquid part of the phase diagram, the strong correlations survive the phase transition and are also present in the solid part.

As hinted earlier, the original formulation as described above has since been updated and the new version will be discussed in the next section. The update does not render the majority of statements above wrong, but is of a more subtle nature. The original version is recovered as a first-order approximation from the newer, more accurate theory. This also explains the contradicting statements made about the temperature dependence of  $\gamma$ , in that  $\gamma$  depends much stronger on changes in density than in temperature which means that the temperature dependence can be neglected in the first order approximation.

## 2.2 Generic definition of *R*-simplicity

The new, generic definition of *R*-simple systems has been introduced in [18] in 2014. The original version can be recovered as a first order approximation of the reformulation. This better accommodates the approximate nature of the invariance of certain quantities along isomorphs. Following the reformulation, *R*-simple systems are now defined by the condition that

$$U(\mathbf{R}_a) < U(\mathbf{R}_b) \Rightarrow U(\lambda\mathbf{R}_a) < U(\lambda\mathbf{R}_b) \quad (2.5)$$

where  $\lambda$  is a scaling parameter and  $U(\mathbf{R})$  denotes the potential energy of the configuration with  $N$  particles and the configuration coordinates vector  $\mathbf{R} \equiv (\mathbf{r}_1 \dots \mathbf{r}_N)$ . The conditions can be expressed by the statement that the ordering of the potential energies of configurations at the same density,  $U(\mathbf{R}_a)$  and  $U(\mathbf{R}_b)$ , is preserved under a uniform scaling  $\lambda$  to a different density. Saying that *most* (not all) of the physical relevant configuration obey Eq. (2.5) is equivalent to a system having strong correlations with *R* close to unity. For  $R = 1$  all (relevant) configurations obey the ordering.

Using the reduced units that have been introduced in the previous section, the configuration vector  $\mathbf{R}$  can be expressed in its reduced form as  $\tilde{\mathbf{R}} \equiv \rho^{1/3}\mathbf{R}$ . If two configurations at two densities  $\rho_1$  and  $\rho_2$ , are isomorphic to each other, they have the same reduced configuration vector,  $\rho_1^{1/3}\mathbf{R}_1 = \rho_2^{1/3}\mathbf{R}_2$ . It has been shown that for systems that have isomorphs, the potential energy function  $U(\mathbf{R})$  can be represented by the *hidden-scale invariance identity* as follows [31, 32]:

$$U(\mathbf{R}) \cong h(\rho)\tilde{\Phi}(\rho^{1/3}\mathbf{R}) + g(\rho) \quad (2.6)$$

where the function  $\tilde{\Phi}(\rho^{1/3}\mathbf{R}) \equiv \tilde{\Phi}(\tilde{\mathbf{R}})$  is state point independent along an isomorph. This means that the hidden scale invariance identity can be regarded as a global, approximate scale invariance since the function  $\tilde{\Phi}$ , which governs structure and dynamics in reduced

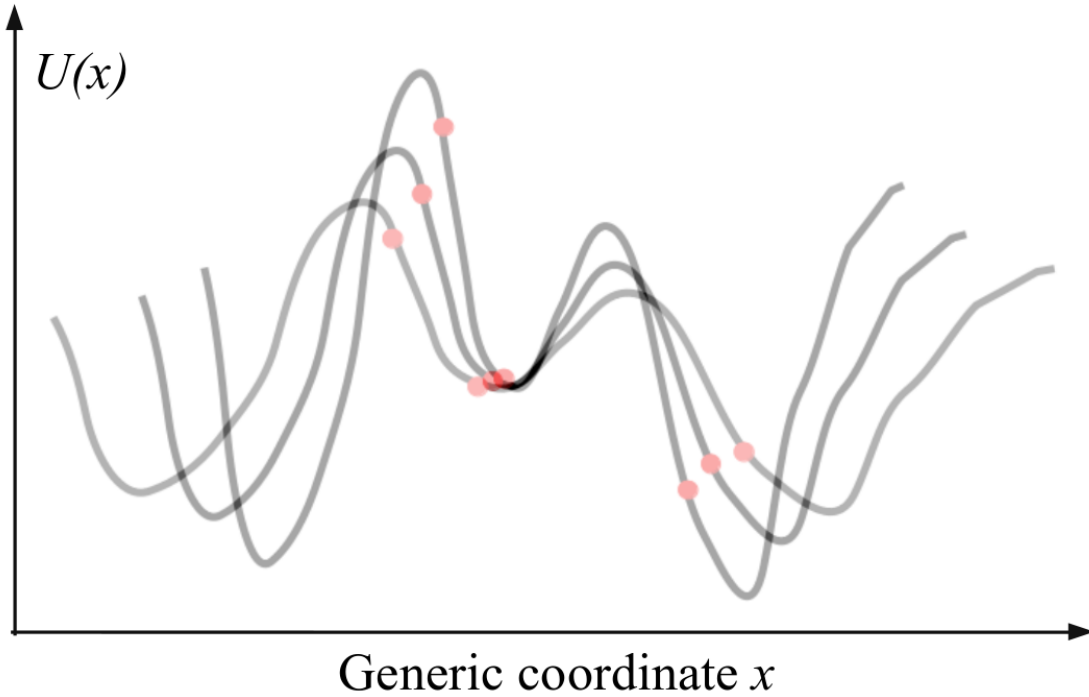


Figure 2.3: Schematic of the affine scaling of the potential energy hyper surface. In systems that obey Eq. (2.5), the ordering of potential energies of configurations at the same density is maintained. With the lines resembling the potential energies of different configurations at the same density, the red points on each line are related to their counterpart on the other lines by uniform volumetric scaling.

coordinates, remains unchanged under uniform scaling of  $\mathbf{R}$  [32]. In the generic version of 2014, this scaling identity has been updated to directly relate the potential-energy surfaces at two densities by eliminating  $\tilde{\Phi}(\tilde{\mathbf{R}})$  in Eq. (2.6). The resulting expression is

$$U(\mathbf{R}_2) \cong h(\rho_1, \rho_2)U(\mathbf{R}_1) + g(\rho_1, \rho_2) \quad (2.7)$$

where  $\rho_1$  takes the role of the reference density. The equation now describes the scaling of the potential-energy surface when density changes from  $\rho_1$  to  $\rho_2$ .

The scaling behaviour can be visualized in a few different ways. Figure 2.3 shows a cartoon version of Fig. 2.1, a simplified view of the scaling of a potential energy hyper surface that obeys Eq. (2.5). The line resembles the potential energies of different configurations at the same density and the different lines resemble different densities. Uniform scaling of all configurations to a different density transforms one line into another. The red dots on each line highlight particular configurations and that their ordering remains the same with respect to the other configurations on the same line.

Another way to illustrate the scaling using results from simulation is shown in Figure 2.4 taken from Ref. [18]. For this figure, 20 configurations were drawn from an equilibrium simulation. Each configuration was then scaled uniformly 20% up and down in density, the

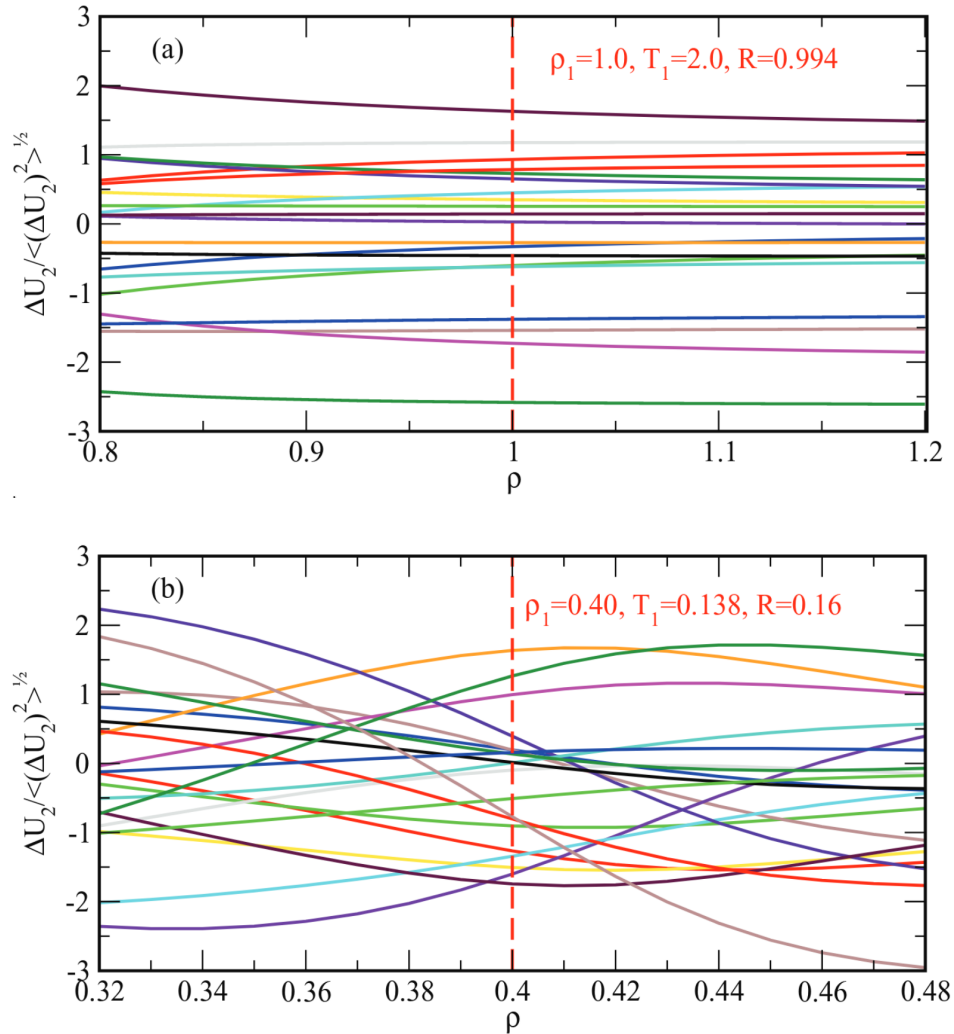


Figure 2.4: Figure taken from Ref. [18] to illustrate the new definition of a Roskilde-simple system. For each figure the potential energies of 20 configurations were taken from an equilibrium simulation at the density marked by the red dashed line. Every line was obtained from scaling each configuration 20% uniformly up and down in density and plotted as a function of density and then normalized. For an ideal Roskilde-simple system, the curves do not cross each other which is approximately true for the top panel, an LJ system that has strong virial potential-energy correlations ( $R = 0.99$ ). The bottom panel shows data for the Lennard-Jones Gaussian (LJG) system of a state point where  $R = 0.16$ .

potential energy calculated and subsequently normalized by subtracting the potential energy averaged over the 20 configurations determined at each density. For *R*-simple systems the lines obtained from this procedure should (approximately) not cross each other as can be seen in the left panel of Fig. 2.4. As a counter example, the right panel shows a substantial amount of crossing in a system that is not *R*-simple and thus does not obey the scaling.

The original version and this reformulation are closely related because of the original version being a first order approximation of its successor. This can be illustrated using the example

of the isochoric heat capacity  $C_V$ . According to the original formulation,  $C_V$  is expected to be invariant along isomorphs. This is often true to a good approximation but not exact. This description is improved by the reformulation, which now predicts the slight variation of  $C_V$  when following an isomorph through large parts of the phase diagram [18].

Another one of the finer differences pertains the role of the excess entropy  $S_{\text{ex}}$ . Excess entropy  $S_{\text{ex}}$  is the difference in entropy  $S$  of a system compared to the ideal-gas entropy  $S_{\text{id}}$  at the same density and temperature,  $S_{\text{ex}} = S - S_{\text{id}}$ . This means that  $S_{\text{ex}} = 0$  for an ideal gas and  $S_{\text{ex}} < 0$  for systems with interactions. In the original version of isomorph theory,  $S_{\text{ex}}$  has been identified as one of the quantities that is invariant along an isomorph. The reformulation now defines isomorphs as the configurational adiabats in the thermodynamic phase diagram, meaning that  $S_{\text{ex}}$  is by definition constant along isomorphs. This is also encapsulated in Eq. (2.3) by the fact that the derivative is defined along lines of constant  $S_{\text{ex}}$ .

A more crucial consequence involves the scaling exponent  $\gamma$  and its state point dependence as briefly mentioned in the previous section. Recall that the scaling exponent  $\gamma$  was named according to the initial interpretation of  $\gamma$  as being related to an effective inverse power law exponent. Assuming a constant  $\gamma$ , isomorphs of the form  $\rho^\gamma/T = \text{const.}$  is consistent with studies of isochrones, the experimentally accessible equivalent to isomorphs [23, 33–38]. However, it has been shown [13] that when determining  $\gamma$  from fluctuations (Eq. (2.2)) in simulations, there is some variation between state points. Additionally, in Ref. [20], it was shown that  $\gamma$  has to be only density and not temperature dependent if one assumes constant  $C_V$  along isomorphs. All of this is consistent with the new formulation which predicts a  $\gamma$  with both density and temperature dependence. In accordance with the view that the initial theory is a first-order expansion of the new formulation, the assumption of a constant  $C_V$  used in Ref. [20] is just that, a fairly good but still an assumption meaning that  $C_V$  actually varies slightly when following an isomorph over a long stretch in the phase diagram. This makes the findings of Ref. [20] consistent with the fully state point dependent  $\gamma$  of Ref. [18]. The same argument also conciliates the experimental findings with the new formulation, because the experimental window is small enough that only the approximately constant part of  $\gamma$  and other slowly varying quantities is observed.

One of the motivations of this work was to explore the variation of  $\gamma$  with state points in realistic models of metals. It has been found in [39] that  $\gamma$  does in fact vary significantly, both along an isomorph in a given metal and also between different metals using the EMT potential. This is further validated in Ref. [40] by observing the same in DFT metals as well.

## 2.3 *Fantastic isomorphs and where to find them*

If the computational resources permit, the straight forward way to trace out an isomorph is in a step-wise fashion. From a simulation at a given state point,  $\gamma$  can be calculated from fluctuations in simulation using Eq. (2.4). Assuming a constant  $\gamma$  for small changes in density, the next point on the isomorph can then be found numerically integrating Eq. (2.3). The size of the change in density that can be used as a step size varies somewhat depending on

the method used for the numerical integration. Using the Euler method, density should be increased by only about 1% while the Runge-Kutta method allows for bigger steps. The downside of the step-wise mapping is that, no matter the step size, it does require simulations after every step.

An alternative for computationally expensive simulations - like the ab-initio simulations in this work - is the direct isomorph check (DIC). The DIC has been introduced in paper IV of the series [16]. According to the original framework, Roskilde simplicity implies that isomorphic state points have approximately proportional configurational NVT Boltzmann factors

$$\exp\left(-\frac{U(\mathbf{R}_1)}{k_B T_1}\right) \cong C_{12} \exp\left(-\frac{U(\mathbf{R}_2)}{k_B T_2}\right), \quad (2.8)$$

where the constant  $C_{12}$  depends only on the state points  $(T_1, \rho_1)$  and  $(T_2, \rho_2)$ . Taking the logarithm and rewriting the expression, Eq. (2.8) becomes:

$$U(\mathbf{R}_2) \cong \frac{T_2}{T_1} U(\mathbf{R}_1) + k_B T_2 \ln(C_{12}). \quad (2.9)$$

(In the accompanying paper [39], the logarithm in the above equation was erroneously left out.) Recall that the reduced configuration vector is  $\tilde{\mathbf{R}} = \rho^{1/3} \mathbf{R}$  and that from the invariance of structure follows, that if two state points are isomorphic, their reduced coordinate vectors are the same:  $\rho_1^{1/3} \mathbf{R}_1 = \rho_2^{1/3} \mathbf{R}_2$ . Considering fluctuations about the respective mean values, Eq. (2.9) can then be expressed as:

$$\frac{T_2}{T_1} \Delta U(\mathbf{R}_1) \cong \Delta U(\mathbf{R}_2) = \Delta U\left(\left(\frac{\rho_2}{\rho_1}\right)^{1/3} \mathbf{R}_1\right). \quad (2.10)$$

From the above expression, the slope in Figure 2.5 can be explained. For the figure, a time series of configurations from an equilibrium simulation at state point  $\rho_1, T_1$  has been generated. Now we want to find the temperature  $T_2$  for a state point with a given density  $\rho_2$  that is isomorphic to the initial state point. To do so, every configuration has been uniformly scaled to density  $\rho_2$  and their potential energy has been calculated. Plotting the potential energies per configuration of the scaled vs. unscaled density against each other results in a scatter plot like the one shown in Fig. 2.5. The slope of the best fit line of such a scatter plot is according to Eq. (2.10) given by the quotient  $T_2/T_1$  of the initial temperature  $T_1$  and the temperature  $T_2$  for the target density  $\rho_2$ . Similarly, Eq. (2.7) implies Eq. (2.8) if  $T_2/T_1 = h(\rho_1)/h(\rho_2)$  which is thus the condition to identify isomorphic state points in the framework of the updated version [32].

The advantage of this method is that the same series of configurations can be scaled to several different densities. This means that only one simulation at one state point is required to map out an isomorph. In addition to that, from averaging over the scaled configurations at each density, reasonable estimates of thermal quantities like potential energy, pressure and virial can be obtained as well without actually running simulations at all the state points.

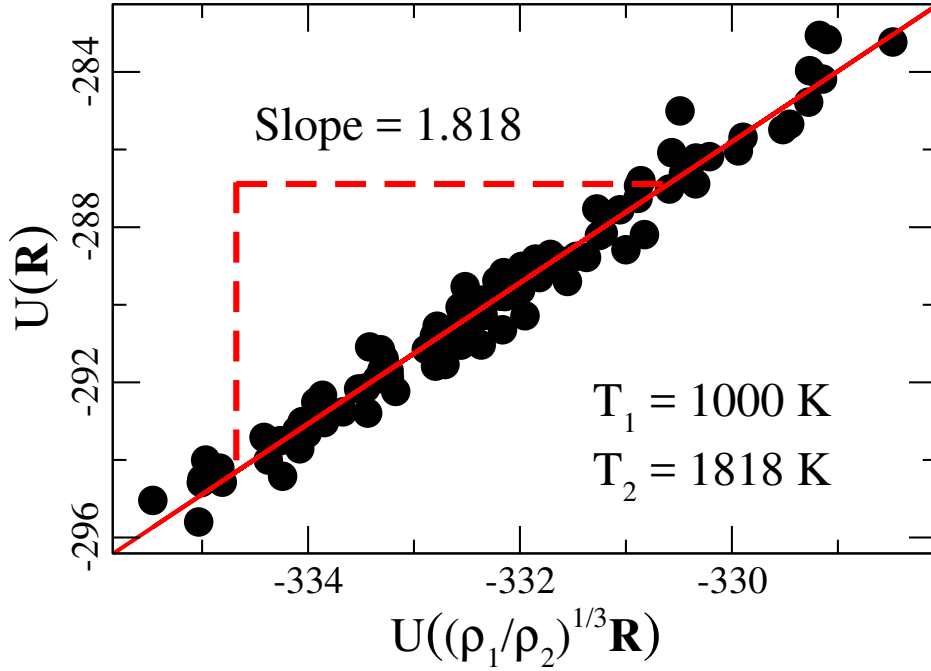


Figure 2.5: The unscaled potential energies are from configurations of a simulation at the initial state point, 256 articles liquid DFT-Mg at  $T_1 = 1000$  K,  $\rho_1 = 0.038 \text{ \AA}^{-3}$  (corresponds to  $P = 0.5$  kbar). The same configurations are then uniformly scaled to the second density, here  $\rho_2 = 1.3\rho_1$ . The direct isomorph check finds for the given density  $\rho_2$  the temperature  $T_2$  of a state point that is on the same isomorph as the initial state point  $(\rho_1, T_1)$ . Plotting the potential energies of scaled versus unscaled configurations results in a scatter plot where the slope of the best fit line is given by  $T_2/T_1$  (see Eq. (2.10)).

As a simple verification of the DIC is a direct comparison of the isomorphs found from the DIC with a step-wise generated isomorph which is shown in Figure 2.6. Comparing the red line (step-wise isomorph) with the black dots (DIC) gives an idea of how well both methods agree with each other. The initial point for both methods was the low density and temperature state point in the bottom left. From this point, density has been scaled in steps of 10% of the initial density with the highest point being at twice the initial density. Both methods are in near perfect agreement over the whole range of density.

Such a comparison is of course only possible for systems with potentials that allow for the tracing of a step-wise comparison isomorph which in this case is Au simulated with the effective medium potential (see Sec. 4.3). A suitable work-around for computationally too expensive systems in form of a simple consistency check has been introduced in [39]. Also the self consistency check is included in Figure 2.6. The inset shows a fit of the function  $\gamma(\rho) = a + b/\rho^n$  to the  $\gamma$  dependency on density found using the DIC. The fit parameters are given in the figure caption.

Recall that  $\gamma$  is defined in Eq. (2.3) as  $\gamma(\rho, T) = \left( \frac{\partial \ln(T)}{\partial \ln(\rho)} \right)$ . Equating the definition with the

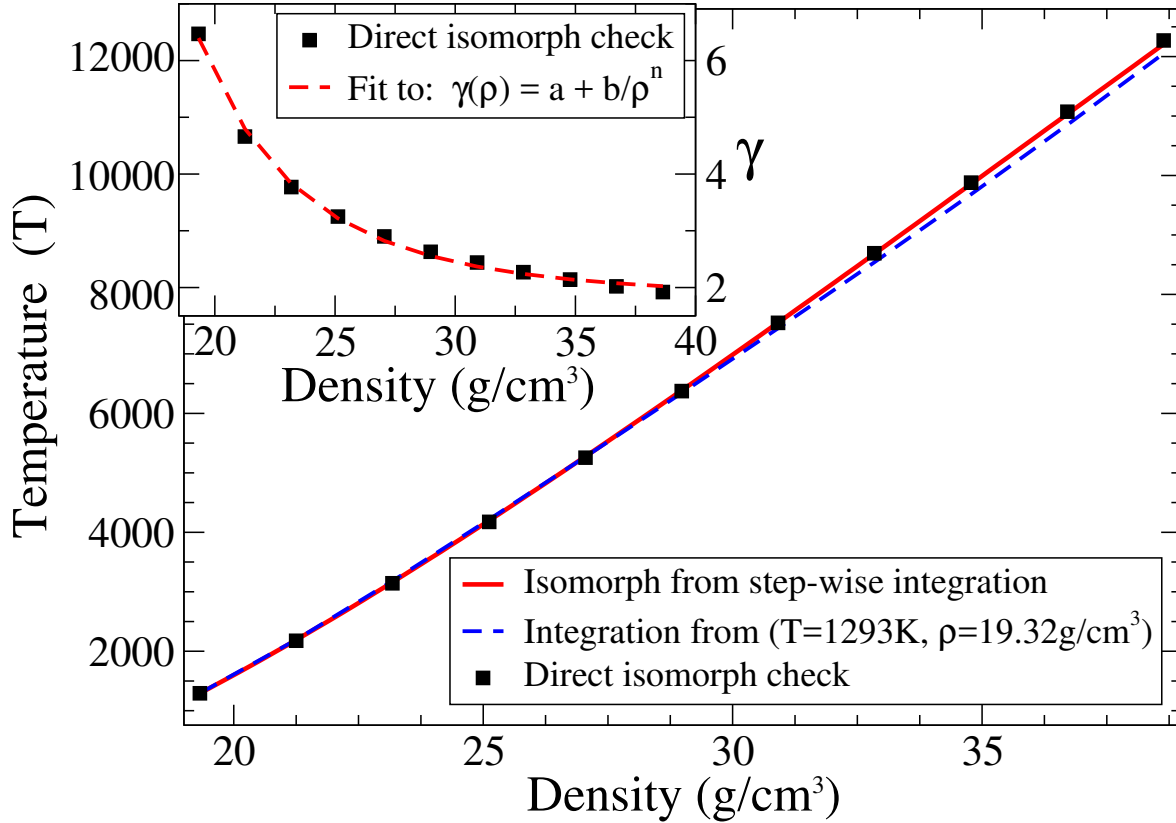


Figure 2.6: Comparison of the self consistent DIC check derived above with the DIC (black dots) and the step-wise generated Isomorph (red line). The inset shows the fit (dashed line) with parameters  $a = 1.82345$ ,  $b = 2.97769 \times 10^6$ ,  $n = 4.52073$  to the  $\gamma$  values obtained from the DIC (black squares). This means that all  $\gamma$  values used are from a simulation at the reference point and no simulations at the other state points were necessary. Using the fitted expression for  $\gamma$ , the blue dashed line in the main panel shows the state points obtained from integrating Eq. (2.3) resulting in the expression given in Eq. (2.12) from the initial point indicated. Good agreement between all three methods is observed, comparing this line to the analytic isomorph from step-wise integrating Eq. (2.3) and the DIC points. A version of this figure appeared in the appendix of [39]

fitted expression results in the integrate-able expression:

$$d \ln(T) = a d \ln \rho + b \frac{\ln \rho}{\rho^n} = a d \ln \rho + b d \ln \rho e^{-n \ln \rho} \quad (2.11)$$

Carrying out the integration and taking the exponential results in the following expression for the density dependence of temperature:

$$T = T_0 \left( \frac{\rho}{\rho_0} \right)^a \exp \left( \frac{-b}{n} (\rho^{-n} - \rho_0^{-n}) \right) \quad (2.12)$$

where  $\rho_0$  and  $T_0$  are the density and temperature of the reference point for the DIC. The fit

is shown as the red dashed line in the inset of Figure 2.6. The blue dashed line in the main panel is the obtained expression for  $T(\rho)$  using the bottom left state point as the reference point. It can be seen the blue dashed line deviates slightly from the exact, step-wise generated isomorph as well as the DIC isomorph at the state points furthest away from the reference point. This is not unexpected given the distance to the reference point and that the fit of  $\gamma(\rho)$  already shows slight deviations. Nonetheless also the fitted isomorph is reasonably close to the step-wise and the DIC isomorphs making this self consistency check a useful tool for ab-initio isomorphs where tracing a step-wise isomorph would be too computationally prohibitive.

## 2.4 Some consequences and special cases

Having a system with isomorphs in its phase diagram, a system that is R-simple has several interesting consequences. This section highlights some significant features of R-simple systems that are relevant to this work, but is by no means meant as an attempt at a complete list.

The first special case is the simplest system of the isomorph world. The only system with perfect correlation and therefore the only system where isomorph theory holds exactly. The other consequence regards the melting and freezing lines and their relation to nearby isomorphs. Some of these consequences are closely related to insights from perfect correlations, which is why the special case of perfect correlation needs to be discussed first.

A third particularly interesting feature is the existence of instantaneous equilibration after sudden changes - jumps - between isomorph state points.

### 2.4.1 Perfect IPL isomorphs

The significance of  $\gamma$  can be illustrated in a system that interacts using a simple inverse power law (IPL) meaning that the interactions scale with distance as  $\sim r^{-n}$ . IPL systems are the only systems with perfect isomorph correlation,  $R = 1$ . This also means that the proportionality expression (Eq. (2.2))  $\Delta W = \gamma \Delta U$  is exact.

The virial is defined as  $W(\mathbf{r}_1 \dots \mathbf{r}_n) \equiv -\frac{1}{3} \sum_i \mathbf{r}_i \nabla_{\mathbf{r}_i} U(\mathbf{r}_1 \dots \mathbf{r}_n)$ . Using an IPL potential energy function of the form  $U(\mathbf{r}_1 \dots \mathbf{r}_n) = a \sum_{i,j} (\mathbf{r}_i - \mathbf{r}_j)^{-n}$  where  $a$  is a constant, the expression for the virial becomes

$$W(\mathbf{r}_1 \dots \mathbf{r}_n) = -\frac{1}{3} \sum_i \mathbf{r}_i \frac{(-n)}{r_i} U(\mathbf{r}_1 \dots \mathbf{r}_n) \quad (2.13)$$

$$W(\mathbf{r}_1 \dots \mathbf{r}_n) = \underbrace{\frac{n}{3}}_{\equiv \gamma} U(\mathbf{r}_1 \dots \mathbf{r}_n) \quad (2.14)$$

from which  $\gamma$  can be identified as  $\gamma = n/3$  with  $n$  being the power law exponent. In this

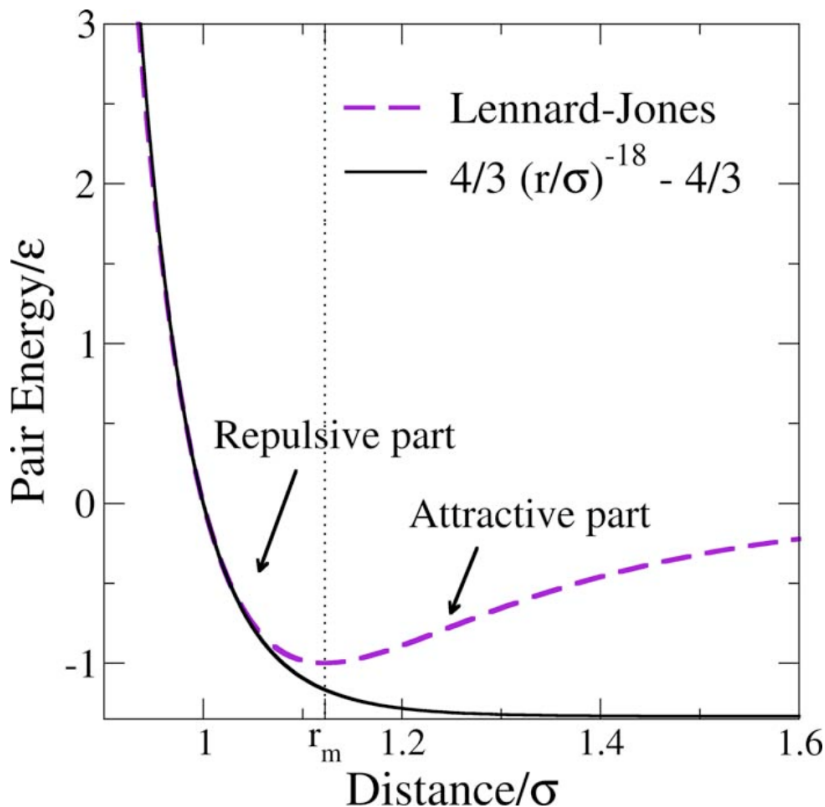


Figure 2.7: Figure taken from Ref. [13] to illustrate the ‘effective exponent’,  $n_{\text{eff}} = 18$  in comparison to the full Lennard-Jones potential. The dotted line indicates  $r_m$ , the distance at which the Lennard-Jones potential reaches its minimum ( $r_m = 2^{1/6}\sigma \approx 1.122\sigma$ ), which separates the attractive and repulsive part of the potential. While the attractive part deviates strongly, the repulsive part is matched by the inverse power law.

particular case, the scaling exponent  $\gamma$  is obviously state point independent and constant only depending on the power law exponent  $n$

It has been shown [13, 14], that the relation between  $\gamma$  and  $n$  can be generalized also to non-IPL systems. In this case  $n$  is replaced by an *effective inverse power law exponent*  $n_{\text{eff}}$  which is the exponent of the IPL that matches the potential for distances of the length-scale of typical interactions at the given state point. This can be demonstrated using the example from [13, 14], the Lennard-Jones (LJ) system. The expression for the potential reads:

$$v_{LJ} = 4\varepsilon \left[ \left( \frac{\sigma}{r} \right)^{12} - \left( \frac{\sigma}{r} \right)^6 \right] \quad (2.15)$$

where  $\varepsilon$  are the energy and  $\sigma$  the position of the minimum. While not obvious from the expression, the short-range repulsive part of the potential can be modeled by an IPL with the effective exponent  $n_{\text{eff}}$ . The value of  $n_{\text{eff}}$  depends on where the expressions IPL is matched to the full potential.

Figure 2.7 shows that an IPL with  $n_{\text{eff}} = 18$  matches the part of the LJ system at distances

smaller than  $r_m$ , the location of the minimum value of the LJ potential. For the corresponding  $\gamma$  this means that  $\gamma = n_{\text{eff}}/3 \cong 18/3 = 6$ . At even higher densities, the typical interaction length-scale is shorter and the  $r^{-12}$  term of the LJ potential dominates. This means that  $\gamma$  for very high density state points is expected to be  $\gamma = 12/3 = 4$  in the LJ system, which has been shown to be correct [13, 14]. A detailed discussion of this and similar, effective matching expressions is given in paper II [14].

### 2.4.2 Isomorph relevance to the melting curve

The temperature  $T_m$  at which a material melts (or freezes) is generally well known at ambient pressure. This temperature is however pressure dependent and the term melting curve refers to the curve given by the function  $T_m(P)$ . The high pressure part of this curve is often not well mapped out.

The relevance of the nearby isomorphs to the melting and freezing line can be illustrated with a simple argument. Isomorphs are defined as curves along which structure and dynamics are (approximately) invariant. The melting and freezing line mark the border between the solid and liquid phase in the phase diagram, thus areas of fundamentally different structure and dynamics. A reasonable expectation would therefore be, that the melting and freezing lines themselves are isomorphs (or very close to one), since they should not be able to cross each other. This is however only exactly true in the one special case of the previous section, the IPL system with its perfect correlation and exact isomorphs.

As a consequence of isomorph theory being an approximate theory in all other systems, an isomorph generated from a point at freezing or melting actually deviates slightly from the melting or freezing line away from the reference point. However, these neighbouring isomorphs alone can already give a good estimate of the general trend of the melting and freezing line. In addition to that, a method was recently devised in Ref. [28] to recover the melting pressure and freezing and melting densities in form of a first order expansion. Moreover nearby isomorphs can be considered as excellent zeroth-order approximations of the melting and freezing lines. Additionally, several phenomenological melting rules, including the Lindemann melting criterion, can be understood as consequences of the melting curve being close to an isomorph [16, 28]. The method requires only quantities easily available from the neighbouring isomorphs. This is mentioned here already for the sake of completeness, but the details of the method will be reviewed later on in section 6.1 where it is being used.

### 2.4.3 Instantaneous equilibration

Isomorph theory predicts the invariance of structure and dynamics when given in reduced units. A way to conceptualize the role of the reduced units is to imagine watching a film of the individual particle's movements [41]. Superficially, the movie will not be the same when looking at different state points. What the reduced units now encode is a prescription of how much faster or slower the movie needs to be played and to what extent the picture needs to

be magnified or compressed, so that a movie of one state point will be perfectly congruent to the movie filmed at another state point that is isomorphic to the first. The scaling is given by the reduced units which in turn only depend on the densities and temperatures at the state points as well as fixed factors (the particle mass and Boltzmann's constant) meaning there is no guess-work or fitting required only the knowledge that the two state points are isomorphic.

This means that having mapped out an isomorph beforehand, an equilibrium simulation at any state point on this isomorph can be stopped and scaled accordingly to any other isomorphic point. If the simulation is continued at the new state point, no equilibration is necessary, the system is already perfectly adjusted to the new density and temperature. Due to this feature, isomorphs can also be thought of as *worm holes* through the phase diagram.

Instantaneous equilibration has been validated in both experiments and simulation, though for technical reasons the experimental instantaneous change in state point is of course less abrupt than its counterpart in simulations. The first simulated jump is shown in paper 4 of the isomorph theory series [16]. Successful jumps in experiments are presented in Ref. [42].

# 3

## Molecular Dynamics

---

Molecular dynamics (MD) is a method to simulate the physical movement of atoms or molecules. For a given system of atoms and/or molecules their path throughout space as a function of time for every particle - the *trajectory*  $\mathbf{r}_i(t)$  - can be determined from numerically integrating Newton's equation of motion,  $\mathbf{F}_i = m_i \ddot{\mathbf{r}}_i$ , for each particle  $i$ . Different algorithms exist specifying how to carry out the numerical integration in detail. Prominent examples of these algorithms are the Verlet [43, 44], the Runge-Kutta [45, 46] or the predictor-corrector integration method [47].

The forces acting on each particle coming from all the surrounding atoms, typically to within a predefined cutoff distance, are described in terms of an interatomic potential  $U$ . The complete time evolution of the system is then determined in small time intervals  $\Delta t$ , via calculating all forces acting between the particles based on their current position  $\mathbf{r}_i(t_0)$  from  $\mathbf{F}_i = -\nabla_{\mathbf{r}_i(t_0)} U$  and subsequently updating all positions accordingly to the next time step,  $\mathbf{r}_i(t_0 + \Delta t)$ . The time step is usually of the order of femto-seconds.

In order to simulate (infinite) large systems efficiently, MD simulations that aim to emulate bulk materials often employ periodic-boundary conditions. This means that the original simulation cell is imagined to be copied and repeated over and over again in all directions. A one-dimensional schematic of this is shown in Figure 3.1. Particles leaving the cell on one side re-enter on the opposite site. This reduces the size of the simulation cell but is also a possible source of error. If the cell is too small, particles can 'feel' their own movement if there are not enough particles between their own mirror images. Additionally, if the cutoff distance is larger than half the box size, a particle can switch suddenly from being 'seen' on one side to being seen as coming from the other side which causes a discontinuity in the force.

### 3.1 Pair potentials and beyond

The computationally most expensive step when calculating the time evolution of a system in a classical MD simulation, is the calculation of the potential energy of each particle depending

on the particles position and the potential  $U$ . The actual cost depends on the ‘form’ of the potential  $U$ . Since the potential encodes the interaction of the particles with each other, the choice of potential needs to be the best compromise between computational costs on one side and an as accurate as possible description of the physics that one wants to study.

In simple pair potentials, the total force acting on a given atom is simply the sum of pairwise interactions, neglecting all three-body and higher contributions. Thus, these type of potentials are computationally much more efficient than more realistic potentials that do include many-body contributions or go even further to include things like quantum-mechanical effects. On the opposite site of pair-potentials with respect to the balance between accuracy vs. efficiency, are the ab-initio methods, such as DFT or the even more accurate coupled-cluster method. Note that in this work by ab-initio we usually mean DFT unless stated otherwise. On the middle ground between those extremes live fitted and empirical potentials. The number of particles that can reasonably be simulated hence depends on the potential used and can range from a few to a few thousand particles with DFT and similar methods while simpler potentials can handle much larger systems [48, 49].

The group of simple pair potentials includes various very popular potentials, like the Lennard-Jones type potentials. Arguably the simplest potential might be the hard-spheres model [6] meaning a billiard table like system where the only interaction is the abrupt, repulsive ‘bounce’ when two hard sphere like particles touch. Despite its simplicity, hard sphere systems have been proven to be an extremely successful system to study a variety of universal features of statistical physics in solids, liquids and gasses.

Unfortunately, this work studies metals which cannot be described by rigid pair potentials. For example, the elastic properties of metals are not described correctly by pair-potentials. Metals do not obey the Cauchy relation between elastic constants  $C_{12}=C_{44}$ , these are however obeyed by definition in systems simulated using a pair-potential. Contributions beyond the pair level need to be included to correctly reproduce the elastic properties of metals. Another well

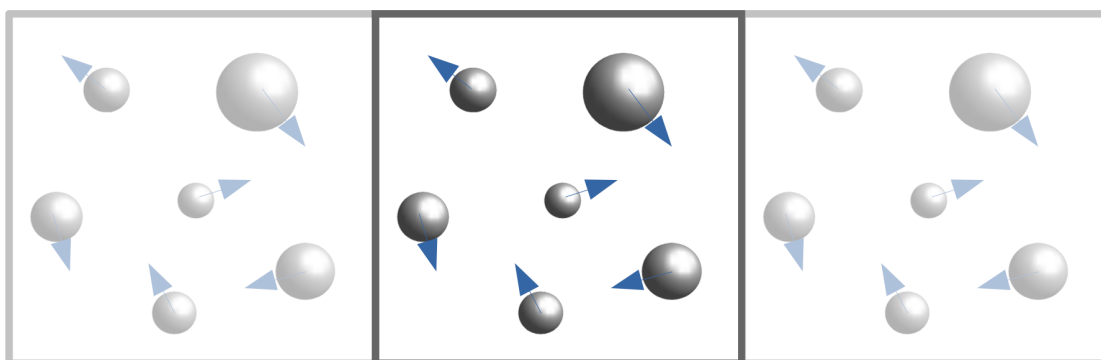


Figure 3.1: Schematic to illustrate periodic boundary conditions. The box in the middle – the simulation box – is repeated in all direction to emulate a much bigger system. The arrows indicate particle movements and demonstrate how a particle leaving the box on one side and re-entering on the opposite side can be thought of as two different particles in the periodic images of the simulation box.

known problem is that the vacancy formation energy is overestimated. In the pair potential prediction, the cost for removing one atom from its surrounding is the sum of the energies to break one bond each for all nearest neighbours. From experiments it is known that the energy should be significantly lower which is correctly reproduced by many-body models [30, 50]. Metallic behaviour is also heavily dominated by the rearrangement of electrons especially by the ones in the outer, incompletely filled shells of each atom.

Therefore, an accurate description of metals in simulations should take the electronic structure of every new arrangement of atoms into account. This is explicitly handled for example in density functional theory (DFT) where especially the version by Hohenberg, Kohn and Sham enjoys ever increasing popularity. Even though the theory itself is a few decades old, the ongoing improvements in computation hardware increased the accessible simulation sizes from only a handful atoms to around a few hundred. As density functional theory is one of the weapons of choice for this work, a detailed review is given in Chapter 4.

The other method used is the effective medium theory (EMT) potential [51], one of the middle ground potentials. The EMT potential is a semi-empirical potential that was constructed from DFT considerations. However, instead of calculating the electronic structure explicitly, the potential introduces the concept of an *effective medium* that handles the cohesiveness of the metal (and inspired the name of the potential). Also this potential is discussed in more detail in Chapter 4.

## 3.2 Ensembles

The concept of ensembles in statistical physics was introduced by Willard Gibbs in 1902 in his book “Elementary principles in statistical mechanics” [52] which formed the basis of modern statistical mechanics. The idea of ensembles formalizes that the same macroscopic conditions can be obtained from several equally possible microscopic states. This means that a closed system at, e.g., fixed temperature and pressure can be thought of as ‘static’ with respect to the macroscopic quantities – conserved number of particles, constant pressure and temperature. However, on the microscopic level, this corresponds to an infinite series, an *ensemble*, of particle configurations. There exist different ensembles that are defined by the choice of which macroscopic quantities are fixed to control the systems. Each ensemble has its own statistical characteristics and correspond to different (close to) real world scenarios that are illustrated in Figure 3.2. The ensembles from left to right are the micro canonical ( $NVU$ ), the canonical ( $NVT$ ), the grand canonical ( $\mu VT$ ) and the isobaric-isothermal ( $NPT$ ) or Gibbs ensemble. Instead of their name, ensembles are often referred to by simply naming the three fixed quantities given in brackets. These are the number of particles  $N$ , the volume  $V$ , the inner energy  $U$ , the chemical potential  $\mu$  and the pressure  $P$ .

Most of this work’s simulations are carried out using the canonical ( $NVT$ ) ensemble as the isomorph theory property of strong correlations between equilibrium virial and potential energy fluctuations is most salient in this ensemble. The part of the work exploring the melting line additionally uses the  $NPT$  ensemble. The ensemble dependency of isomorph

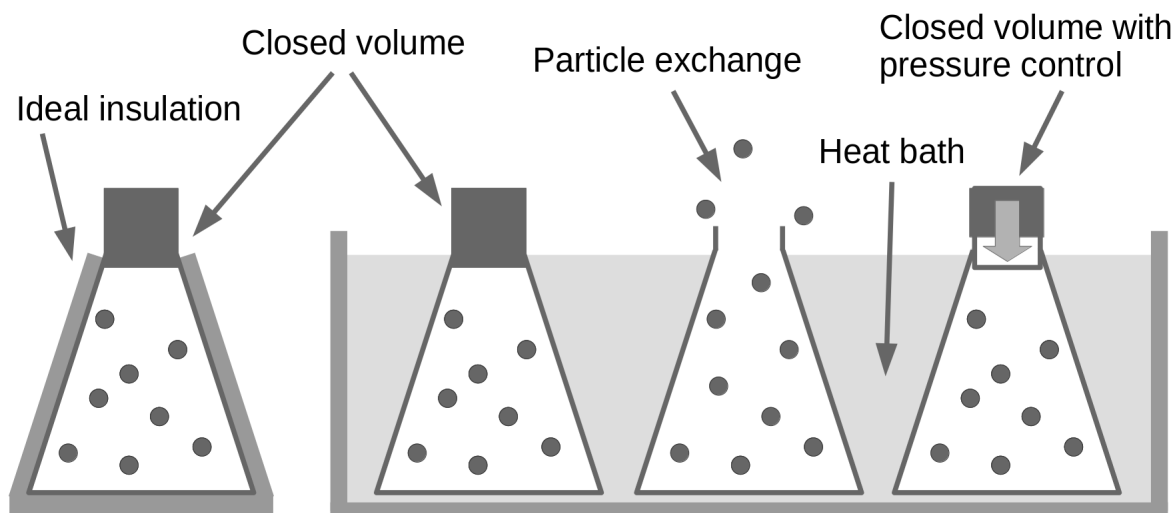


Figure 3.2: Schematic illustrating which real world situations correspond to the different ensembles. From left to right the ensembles are: the micro canonical, canonical, grand canonical and the Gibbs or isobaric-isothermal ensemble.

theory is explored briefly in Ref. [15]. The correlation coefficient associated with the presence of isomorphs in the phase diagram is defined in terms of fluctuations from constant-volume averages. This means that the correlation coefficient is ill defined in the  $NPT$  ensemble where volume is not fixed. In this case the natural alternative choice for quantities to correlate are the enthalpy  $H$  and volume  $V$ . However, a correlation coefficient defined in such a way can never be unity, even for systems that are perfectly correlated in the  $NVT$  ensemble.

### 3.3 Observables

Output from MD simulations is saved in the form of trajectories. From this a series of functions can be calculated that can be used to study the collective structure and dynamics of the system. One of these functions is the radial distribution function, RDF for short or alternatively also called  $g(r)$ . The RDF can be thought of as something akin to the probability of finding another particle at a certain distance  $r$  away from a given particle. For a system of  $N$  particles of the same type in a volume  $V$ , the function can be calculated as

$$g(r) = \frac{V}{N} \frac{dn_r}{4\pi r^2 dr} \quad (3.1)$$

where  $dn_r$  gives the number of particles that can be found within a shell of thickness  $dr$  at distance  $r$ . The right panel of Figure 3.3 illustrates how to calculate the RDF. The left panel shows typical RDFs for the states of matter: solid, liquid and gas. The sketch includes a normalization on both axis. The RDF is normalized so that a completely structureless system would have a RDF of 1. In the figure, the distance is normalized by the inverse cubed root of the density which corresponds to the distance being expressed in reduced units. A typical

RDF of a crystal has sharp peaks of characteristic shape depending on the crystal structure. In this case the RDF peaks are at the typical distances to the neighbouring shells surrounding every atom, i.e. at around  $\sqrt{n}\sigma$ , where  $\sigma = \rho^{-1/3}$  is the nearest neighbour distance and  $n = 1, 2, 3, \dots$  the number of neighbour shells [53]. An ideal crystal at zero temperature has infinitesimal small, sharp peaks. At higher temperatures, the peaks become softer and smeared out. This also changes the exact position of the peak slightly. For a typical liquid, the first peak is still quite pronounced, but the remaining ‘peaks’ look more like oscillations around the RDF = 1 line. As shown in Figure 3.3, a gas has nearly no structure beyond a small first peak after which it becomes a flat line.

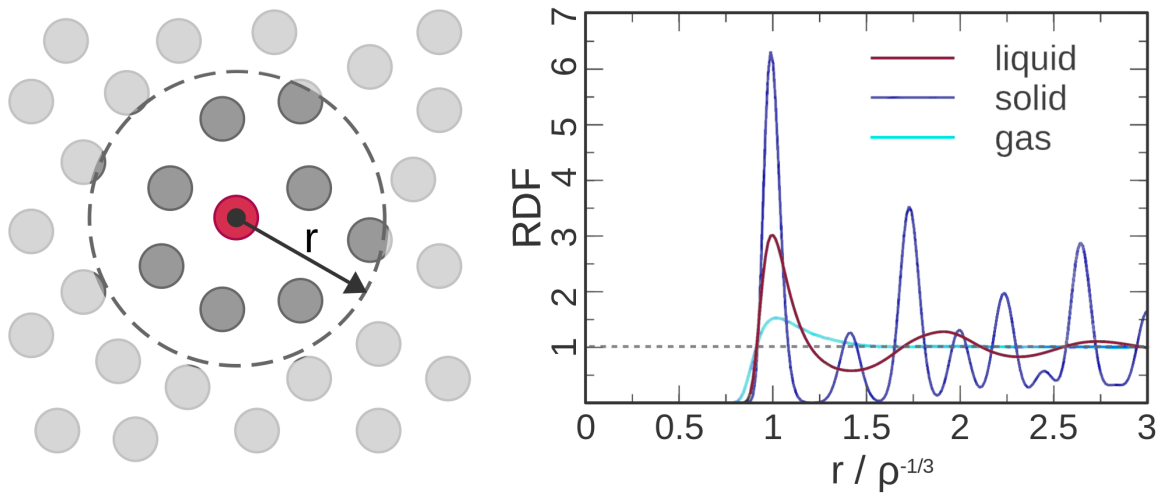


Figure 3.3: Illustration of a ‘shell’ that is used to calculate the RDF of the particle in the center (left). Typical RDFs for solid, liquid and gaseous state points are sketched on the right. The dashed line indicates where RDF = 1. Figures are adapted from figures in Ref. [54]

The RDF is the most basic and for our purposes sufficient function to describe structure. The RDF is limited to pair correlation only and more sophisticated techniques exist to describe structure beyond the pair level, the so-called higher-order measures of structure. These higher-order measures include among others the Voronoi decomposition, calculation of bond-angle distributions, common-neighbour analysis and the topological cluster classification [6, 55, 56]. Albeit not subject of this work, it needs to be mentioned that there exist limited evidence of incomplete isomorph invariance in higher-order structure detailed in Ref. [56].

While this work uses only the RDF to describe structure, dynamics require a few different functions that are sensitive to visualizing different parts of the dynamics. Among them are the velocity autocorrelation function (VAF) and the vibrational density of states (VDOS) can be used. The VAF gives the correlation of a particles velocity at  $t = t_0$  and the same particles velocity at a later time. It is defined as

$$VAF(t) = \frac{\sum_{i=1}^N \langle v_i(0) \cdot v_i(t) \rangle}{\sum_{i=1}^N \langle v_i(0) \cdot v_i(0) \rangle} \quad (3.2)$$

with the denominator providing the normalization. The normalization factor can also be

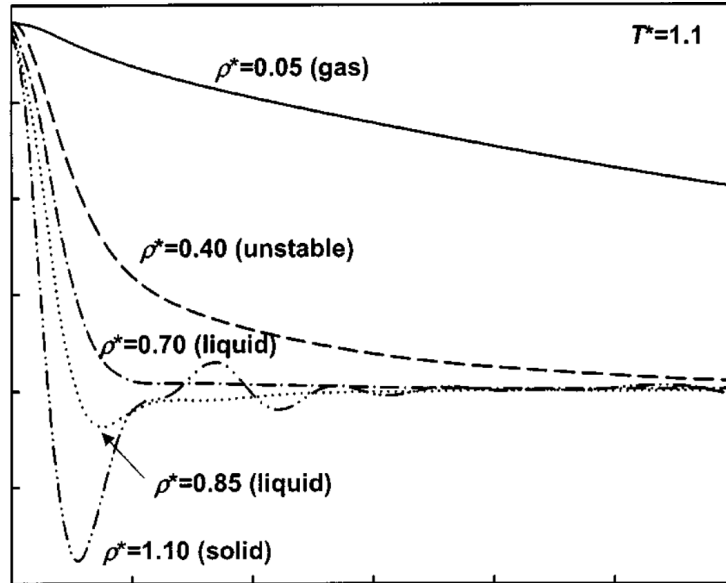


Figure 3.4: Velocity autocorrelation function of the LJ system at constant temperature and different densities. The different densities correspond to different phases and give an impression of the typical characteristics associated with the respective phases. Figure taken from Ref. [57].

expressed as  $\sum_{i=1}^N \langle v_i(0) \cdot v_i(0) \rangle = 3Nk_B T$ . The phonon or vibrational density of states  $\rho(\omega)$  is closely related to the VAF and can be calculated from the Fourier transformed of the VAF from:

$$\rho(\omega) = \frac{1}{3Nk_B T} \int_{-\infty}^{\infty} \sum_{i=1}^N \langle v_i(0) \cdot v_i(t) \rangle C(t) e^{i\omega t} dt, \quad (3.3)$$

where  $C(t) = e^{-(t/t_c)^2}$  with  $t_c$  fixed in reduced units. The Gaussian function  $C(t)$  is included to smoothly truncate the integrand since it otherwise decays too slowly compared to the data-sampling window.

Another observable to quantify dynamics is the mean-squared displacement (MSD). The MSD gives the average square of the distance travelled taken over all particles in the system. It is defined as follows:

$$MSD = \langle (\Delta \vec{r}(t))^2 \rangle = \frac{1}{N} \sum_i^N (\vec{r}_i(t) - \vec{r}_i(0))^2 \quad (3.4)$$

All states of matter have an initial ballistic part in their MSD. The ballistic regime is the initial part of the MSD where the particle essentially travels free before its movement is influenced by the surrounding neighbour particles. When expressed in reduced units, the slope of the MSD in this regime is always given by  $\langle (\Delta \vec{r}(t))^2 \rangle = 3\Delta t^2$ . This follows from a simple prove:

Recall from Chapter 2 that the isomorph reduced units for length and time (denoted by a

tilde) are  $\tilde{l} = l\rho^{1/3}$  and  $\tilde{t} = t\rho^{1/3}\sqrt{k_B T/m}$ , respectively. The length of the path travelled by a particle with velocity  $v_i$  in the time interval  $\Delta t$  is given by  $\Delta r_i = v_i \Delta t$ . The expectation value of the path length is  $\langle \Delta r_i^2 \rangle = \langle v_i^2 \rangle \Delta t$  and analogously, the expectation value of the path length in reduced units is given by

$$\langle \Delta \tilde{r}_i^2 \rangle = \rho^{2/3} \langle \Delta r_i^2 \rangle = \rho^{2/3} \langle v_i^2 \rangle \Delta t. \quad (3.5)$$

Using that velocity and temperature are related via  $\frac{1}{2}m \langle v^2 \rangle = \frac{3}{2}k_B T$ , the right hand side can be rewritten so that we can recognize the expression for the reduced time:

$$\langle \Delta \tilde{r}_i^2 \rangle = \frac{3k_B T}{m} \rho^{2/3} \Delta t = 3 \left( \left( \rho^{1/3} \sqrt{\frac{k_B T}{m}} \right) \Delta t \right)^2 = 3\Delta \tilde{t}^2. \quad (3.6)$$

In crystals, a typical MSD shows the 'cage' a given particle is confined to by its neighbours. Thus the crystal MSD is monotonically rising over a short initial time (the ballistic regime), until the particle has travelled too far against the repulsion of one of its neighbours and bounces back until it is repelled again from one of the neighbours on the opposite side. This results in a plateau in the crystal MSD as there is no absolute distance travelled by an atom rattling back and forth in its cage. However, in a liquid the atom is not kept in its cage and instead continuous to move on between its surrounding atoms that are themselves free to move. In a typical liquid MSD, this second part – the diffusive part – has a lower slope than in the ballistic part. This results in a kink in the liquid MSD where the dynamics change from the ballistic to the diffusive regime.

In the context of isomorph theory this means that the relevant part of the MSD is the plateau/diffusive regime, where a collapse of the data is a meaningful prediction of isomorph theory, e.g. the diffusion constant is one of the quantities that is predicted to be invariant. Less meaningful is the collapse of the ballistic regime since this is simply a trivial consequence of the correct use of reduced units.

One more possible function used in this work to visualize dynamics is the intermediate scattering function (ISF). The ISF is given by the Fourier transformed of the van Hove function  $G(\vec{r}, t)$  and is defined as follows:

$$F(\vec{k}, t) \equiv \int G(\vec{r}, t) \exp(-i\vec{k} \cdot \vec{r}) d\vec{r}. \quad (3.7)$$

The van Hove function [58] is also called the time-dependent pair-correlation function and in isotropic systems  $G(\vec{r}, t)$  is equivalent to a time-dependent RDF. Similarly to the counting of particles in a region  $dr$  in the RDF, the Van Hove function can be interpreted as the number of particles  $j$  in a region  $dr$  at a time  $t$  provided that there was a particle  $i$  at the origin at  $t = 0$ . To account for the possibility that  $i$  and  $j$  might be the same or different particles, the function is usually split into a self and a distinct part [6].

The van Hove function can be expressed in terms of the local density  $\rho(\vec{r}, t)$  and thus the ISF

can also be written in terms of the Fourier components of the density as

$$F(\vec{k}, t) = \frac{1}{N} \langle \rho_{\vec{k}}(t) \rho_{-\vec{k}}(0) \rangle. \quad (3.8)$$

Unless stated otherwise, this work usually means the self part of the function, which can be expressed as

$$F_s(\vec{k}, t) = \frac{1}{N} \sum_{i=1}^N \cos [\vec{k}(\vec{r}_i(t) - \vec{r}_i(0))] \quad (3.9)$$

This part of the ISF can be interpreted as the probability of still finding a particle at its original spot after a time  $t$  has passed. In this context, the same ‘spot’ is defined depending on length scale determined by the vector  $\vec{k}$ . A typical choice in MD for this length scale is the interparticle spacing. In the context of isomorph theory it is important to compare the ISF at constant reduced  $\vec{k}$  values.

# 4

## *Computational methods for Metals*

---

Computer simulations and associated methods and techniques are the main tool used in this work. The previous chapter gave an introduction to molecular dynamics simulations. To describe how the particles interact with each other, any simulation requires a definition of these interactions. As mentioned in the previous chapter, metals can not be accurately described by pair-potentials alone.

The two methods used to model the particle interactions in this work are the *effective medium theory*-potential and *density functional theory*. Both models are many-body type potentials. Density functional theory (DFT) is an *ab initio* method that in theory determines interactions from first principles. The effective medium theory (EMT) potential is a semi-empirical potential that is in part derived from DFT. The most significant difference between the two models is that DFT treats the electrons explicitly and quantum mechanically, whereas EMT involves only the atoms' coordinates and a potential energy which is an explicit function of them. However, before we turn to these two methods, the first section illuminates some essential features of interacting electrons and electronic structure calculations using the homogeneous electron gas (HEG).

The main problem when dealing with a many-body system is the complexity arising from all constituents in the system interacting with each other, all at the same time and while being influenced by its interactions. While there exist special cases that have solutions involving three and four particles, the interacting many-body system can generally not be solved analytically for more than two particles. To conquer this, usually one or more approximations are necessary. For atomic systems, the first step to simplify the problem is usually the Born-Oppenheimer approximation [59]. It assumes that the motions of an atomic nuclei and its orbiting electrons are decoupled, i.e. the atomic nuclei are frozen and can be regarded as a static, external potential from the point of view of the electrons. The Born-Oppenheimer approximation removes the kinetic term for the nuclei and the term giving the interaction between electrons and nuclei. The remaining many-body Hamiltonian of an

atomic many-body system is then given by

$$\hat{H} = \underbrace{\sum_i -\frac{1}{2}\nabla_i^2}_{\text{kinetic}} + \underbrace{\frac{1}{2}\sum_{i\neq j} \frac{1}{|\mathbf{r}_i - \mathbf{r}_j|}}_{\text{e-e interaction}} - \underbrace{\sum_{i,\alpha} \frac{Z_\alpha}{|\mathbf{r}_i - \mathbf{R}_\alpha|}}_{\text{nuclei potential}}. \quad (4.1)$$

where  $\mathbf{r}$  denotes the electron positions and  $\mathbf{R}$  denotes the positions of a nucleus with atomic number  $Z$ . Any system whose Hamiltonian is known, can be described by solving the Schrodinger equation

$$\hat{H}\Psi(\mathbf{r}_1 \dots \mathbf{r}_n) = E\Psi(\mathbf{r}_1 \dots \mathbf{r}_n) \quad (4.2)$$

where  $\Psi(\mathbf{r}_1 \dots \mathbf{r}_n)$  is the many-electron wavefunction. Even though part of the interaction terms was removed through the decoupling of electrons and nuclei, because of the remaining interaction term involving the coordinates  $\mathbf{r}_i$  and  $\mathbf{r}_j$  of two particles, this problem cannot be separated into a series of single-particle equations. Further simplification of the system is required in order to be able to find a solution.

## 4.1 Electron gas and simple metals

Some models that are related to the two models used for the simulations in this work are the homogeneous electron gas, the Hartree-Fock system and Sommerfeld's theory for charge carriers in metals. All models attempt to simplify the description of interacting and correlating electrons in front of a background field of the ions.

The homogeneous electron gas enables the analytic calculation of all independent-particle terms which makes it the ideal model to illustrate consequences arising from electron correlation. A homogeneous electron gas is obtained by replacing the nuclei with a uniform positively charged background. The model is also called a uniform electron gas or Jellium model in reference to the positive background "jelly" that replaces the nuclei. The advantage of this system is that while it is much simpler than the full system including nuclei, the system still includes interactions both between electrons as well as between electrons and the background. This means that the model correctly reproduces many features associated with materials being *metallic* [60].

In the Hartree atomic units where  $\hbar = m_e = e = 4\pi\epsilon_0^{-1} = 1$ , the Hamiltonian of the electron gas is given by replacing the nuclei term in Eq. (4.1) with a uniform background resulting in the expression:

$$\hat{H} = \sum_i -\frac{1}{2}\nabla_i^2 + \frac{1}{2} \left[ \sum_{i\neq j} \frac{1}{|\mathbf{r}_i - \mathbf{r}_j|} - \int d^3r d^3r' \frac{n^2}{|\mathbf{r} - \mathbf{r}'|} \right], \quad (4.3)$$

where  $n$  is the density  $n = N_e/\Omega$  and the last term now represents the average background.

Accordingly, the total energy expression for the system is

$$E = \langle \hat{H} \rangle = \langle \hat{T} \rangle + \langle \hat{V}_{int} \rangle - \frac{1}{2} \int d^3r d^3r' \frac{n^2}{|\mathbf{r} - \mathbf{r}'|} \quad (4.4)$$

where  $\langle \hat{T} \rangle$  is the kinetic energy of the interacting electrons and  $\langle \hat{V}_{int} \rangle$  is the potential energy of the interacting system. Taken together, the last two terms in Eq. (4.4) give the difference between the potential energy of the real interacting system and the self-interaction of a classical uniform negative charge density. This difference is dubbed the exchange-correlation energy that will become relevant later. For the homogeneous system, a parameter  $r_s$  can be defined which gives the average distance between electrons, also known as the Wigner-Seitz radius:

$$r_s = \left( \frac{3}{4\pi} \frac{\Omega}{N} \right)^{1/3}. \quad (4.5)$$

This radius can be used to rescale the Hamiltonian in Eq. (4.3) in terms of  $\tilde{\mathbf{r}} = \mathbf{r}/r_s$ . The rescaled Hamiltonian reads:

$$\hat{H} = \left( \frac{a_0}{r_s} \right)^2 \sum_i \left[ -\frac{1}{2} \tilde{\nabla}_i^2 + \frac{1}{2} \frac{r_s}{a_0} \left( \sum_{i \neq j} \frac{1}{|\tilde{\mathbf{r}}_i - \tilde{\mathbf{r}}_j|} - \frac{3}{4\pi} \int d^3\tilde{\mathbf{r}} \frac{1}{|\tilde{\mathbf{r}}|} \right) \right] \quad (4.6)$$

which illustrates how the interacting gas can be understood as a function of density [60].

The exchange-correlation energy contribution can be separated into two parts by comparison of the electron gas energy with the same system in the Hartree-Fock approximation. In the Hartree-Fock approximation, all correlation between electrons are neglected except the part required by the Pauli exclusion principle. The difference between the full HEG and the same system in the Hartree-Fock approximation is the correlation part of the exchange-correlation. The Hartree-Fock energy of the HEG has an exact solution and thus the exchange of the HEG can be calculated analytically [61]. An important feature of Hartree-Fock is that there is no self-interaction. The interaction of any electron with its own field is cancelled by a term with the opposite sign that appears naturally in the exchange.

Simple metals are metals that have a partially filled *sp* shell as their outermost shell, with the simplest being the alkalis with only one electron per atom. These outermost valence electrons are only weakly bound to their atom's core and are therefore aptly described by a HEG plus attraction from the positive cores. This is what inspired the idea of the pseudopotential which will be used later. The basic idea is that the strong interaction of the atomic nucleus that tightly binds the electrons in the inner shells is replaced by an effective potential between a *frozen* core – consisting of nucleus plus core electrons – and its screened interaction with the valence electrons.

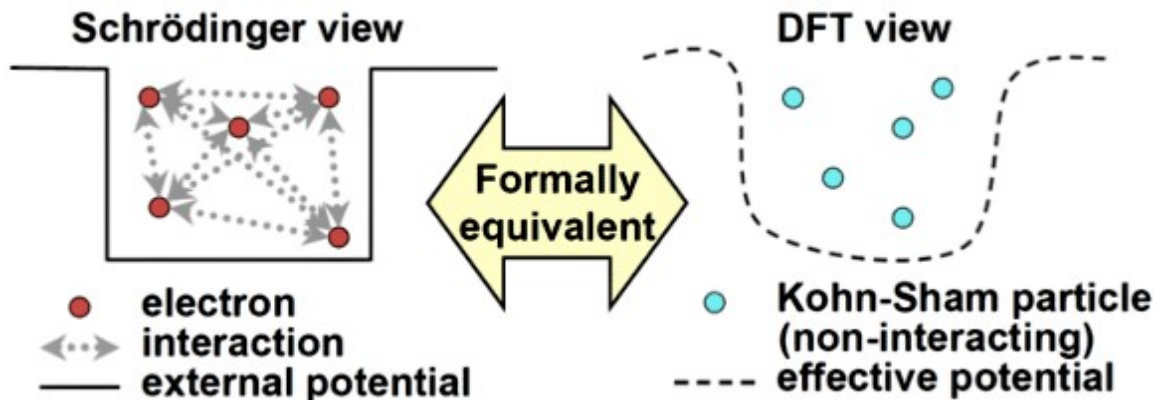


Figure 4.1: Schematic of the ansatz of DFT taken from Ref. [66]. The DFT picture of non-interacting KS particle in an effective potential is a formally exact representation of the full interacting many particle Schrödinger equation

## 4.2 Density functional theory

Density functional theory is a state of the art *ab-initio* method for electronic structure calculations, which in theory gives the exact solution to the many-body Hamiltonian [60]. Modern DFT simplifies the many-body problem significantly by mapping the interacting many-electron system into an auxiliary system with independent particles moving in an effective potential. The result is an energy functional that depends explicitly only on the electron density  $n(\mathbf{r})$ .

Although there are earlier types of DFT, like the Thomas-Fermi model [62, 63], in the modern context of computer simulations, DFT usually refers to the version by Hohenberg, Kohn and Sham [64, 65]. The Thomas-Fermi model was an important step in the theoretical development but the result was lacking in accuracy. The concept of simplifying the  $N$  electron Schrödinger equations to a “functional that depends only on density” is the common to all DFTs and also inspired the method’s name. The mapping specific to the Kohn-Sham ansatz of DFT is illustrated in Figure 4.1.

### 4.2.1 Hohenberg-Kohn-Sham

Modern DFT is made possible by the definition of the two famous theorems by Hohenberg and Kohn [67]. The theorems apply to any system of interacting electrons moving in an external potential which can consist solely of the static potential caused by the nuclei as well as include any additional external potential. In the original form, the theorems did not apply to e.g. degenerate ground state systems or for systems in a magnetic field, but it has since been extended to also include these [68, 69]. The theorems read as follows [67] accompanied by the corollary that can be deduced from them, taken from Ref. [60]:

**Theorem I:** For any system of interacting particles in an external potential  $v_{\text{ext}}(\mathbf{r})$ , the external potential is uniquely determined by the ground state density  $n_0(\mathbf{r})$  (except for a constant).

**Corollary I:** Since the ground state density fully determines the Hamiltonian from which both ground and excited states can be determined, all properties of the system are completely determined given only the ground state density  $n_0(\mathbf{r})$

**Theorem II:** A universal functional for the energy  $E[n(\mathbf{r})]$  can be defined in terms of the density  $n(\mathbf{r})$ . The density of the exact ground state is the global minimum of the energy functional.

**Corollary II:** Only the functional  $E[n(\mathbf{r})]$  is necessary to determine the exact ground state density and energy.

The proofs of both theorems are surprisingly simple. This recap of the proofs is based on Ref. [60]. To prove the first theorem one assumes that the theorem is wrong and that two external potentials  $v_{\text{ext}}^{(1)}(\mathbf{r})$  and  $v_{\text{ext}}^{(2)}(\mathbf{r})$  that differ by more than a constant do lead to the same ground state density. Two different external potentials have two different Hamiltonians  $\hat{H}^{(1)}$  and  $\hat{H}^{(2)}$  with a ground state wavefunction  $\Psi^{(1)}$  and  $\Psi^{(2)}$  each. The wavefunction  $\Psi^{(2)}$  is not the ground state wavefunction of  $\hat{H}^{(1)}$  which means that

$$E^{(1)} = \langle \Psi^{(1)} | \hat{H}^{(1)} | \Psi^{(1)} \rangle < \langle \Psi^{(2)} | \hat{H}^{(1)} | \Psi^{(2)} \rangle \quad (4.7)$$

by the fact that any other state must give a higher expectation value of the Hamiltonian than the ground state. For the strict inequality to hold, it is assumed that the ground state is non-degenerate. The right-hand side term above can be rewritten as

$$\begin{aligned} \langle \Psi^{(2)} | \hat{H}^{(1)} | \Psi^{(2)} \rangle &= \langle \Psi^{(2)} | \hat{H}^{(2)} | \Psi^{(2)} \rangle + \langle \Psi^{(2)} | \hat{H}^{(1)} - \hat{H}^{(2)} | \Psi^{(2)} \rangle \\ &= E^{(2)} + \int d^3r \left[ v_{\text{ext}}^{(1)}(\mathbf{r}) - v_{\text{ext}}^{(2)}(\mathbf{r}) \right] n_0(\mathbf{r}). \end{aligned} \quad (4.8)$$

Inserting this into the inequality above implies that

$$E^{(1)} < E^{(2)} + \int d^3r \left[ v_{\text{ext}}^{(1)}(\mathbf{r}) - v_{\text{ext}}^{(2)}(\mathbf{r}) \right] n_0(\mathbf{r}). \quad (4.9)$$

Considering the opposite case, i.e. starting from the wavefunction  $\Psi^{(1)}$  is not the ground state wavefunction of  $\hat{H}^{(2)}$ , results in an expression where the superscripts are interchanged:

$$E^{(2)} < E^{(1)} + \int d^3r \left[ v_{\text{ext}}^{(2)}(\mathbf{r}) - v_{\text{ext}}^{(1)}(\mathbf{r}) \right] n_0(\mathbf{r}). \quad (4.10)$$

Combining Eqs. (4.9) and (4.10) results in the contradicting inequality that  $E^{(1)} + E^{(2)} < E^{(1)} + E^{(2)}$  and thus proves the theorem. Two different external potentials cannot result in the same non-degenerate ground state density.

The second theorem requires a definition of what is meant by a functional of the density. This is restricted in Hohenberg and Kohn's original work to the densities  $n(\mathbf{r})$  that are the ground state densities of any system with a Hamiltonian that includes some external potential  $v_{\text{ext}}$ . In this space, a total energy functional of the following form can be written

$$\begin{aligned} E_{\text{HK}}[n] &= T[n] + E_{\text{int}}[n] + \int d^3r v_{\text{ext}}(\mathbf{r})n(\mathbf{r}) + E_{II} \\ &\equiv F_{\text{HK}} + \int d^3r v_{\text{ext}}(\mathbf{r})n(\mathbf{r}) + E_{II} \end{aligned} \quad (4.11)$$

where  $E_{II}$  is the ion-ion interaction energy, and all energies of the electronic system are absorbed into the functional  $F_{\text{HK}}$ . The functional

$$F_{\text{HK}} = T[n] + E_{\text{int}}[n] \quad (4.12)$$

is by construction universal, i.e. it is the same for every electronic system, since the external potential nuclei part is excluded. As shown in the first theorem, there is a ground state energy  $n(\mathbf{r})$  which has a corresponding wavefunction  $\Psi^{(1)}$  that minimizes Eq. (4.11) for a particular potential  $v_{\text{ext}}(\mathbf{r})$ . This means necessarily that any other wavefunction  $\Psi^{(2)}$  results in an energy  $E^{(2)}$  which is greater than the ground state energy  $E^{(1)}$ :

$$E^{(1)} = \langle \Psi^{(1)} | \hat{H}^{(1)} | \Psi^{(1)} \rangle < \langle \Psi^{(2)} | \hat{H}^{(1)} | \Psi^{(2)} \rangle = E^{(2)} \quad (4.13)$$

From this, it follows that if the functional was known, the ground state is determined by finding the density that minimizes the energy of the system.

In summary, it can be proven from the theorems that, if the the ground state density  $n(\mathbf{r})$  is known, the potential and therefore all properties of the system, including the many-body wavefunction, are uniquely determined. This means in particular, that there exist a HK functional, defined as

$$F_{\text{HK}}[n(\mathbf{r})] = T[n(\mathbf{r})] + U[n(\mathbf{r})], \quad (4.14)$$

which is a *universal* functional of density only i.e. it does not depend explicitly on the external potential. Furthermore, the systems energy is at its absolute minimum, its ground state, when the electron density is that of the ground state. Thus, for a given distribution of electrons  $n(\mathbf{r})$  in a potential  $v_{\text{ext}}(\mathbf{r})$ , a density functional  $F[n(\mathbf{r})]$  exists such that the energy functional,

$$E_{\text{HK}}[n(\mathbf{r})] = F[n(\mathbf{r})] + \int d\mathbf{r} v_{\text{ext}}(\mathbf{r}) n(\mathbf{r}), \quad (4.15)$$

has the ground state as its global minimum. While powerful - the theorems prove the existence

and uniqueness of the functional - they are no recipe to finding the ground state.

Kohn and Sham addressed this shortcoming in their subsequent contribution [70], where they developed approximation methods to find the ground state from a set of self-consistent equations. To obtain the set of equations, the KS energy functional first needs to be re-expressed including more detail:

$$E_{\text{HK}}[n(\mathbf{r})] = \underbrace{T_0[n(\mathbf{r})]}_{\text{non-interacting, kinetic energy}} + \underbrace{\int d\mathbf{r} n(\mathbf{r}) v_{\text{ext}}(\mathbf{r})}_{\text{External potential (nuclei)}} + \underbrace{E_H[n(\mathbf{r})]}_{\text{classical Coulomb}} + \underbrace{E_{xc}[n(\mathbf{r})]}_{\text{Everything else}}. \quad (4.16)$$

introducing the exchange-correlation energy functional  $E_{xc}[n(\mathbf{r})]$  that contains all non-trivial contributions to the energy, like the effect of the Pauli exclusion principle. Varying the energy functional with respect to the orbitals of the fictive non-interacting particles, also called KS quasi-particles, yields the effective KS potential  $v_{\text{eff}}[n(\mathbf{r})] = v_{\text{ext}}(\mathbf{r}) + v_H[n(\mathbf{r})] + v_{xc}[n(\mathbf{r})]$ . Subsequently, an equation analogous to the Schrodinger equation for the KS particles moving in the effective potential, is given by

$$\left( -\frac{\hbar^2}{2m} \nabla^2 + v_{\text{eff}}(\mathbf{r}) \right) \psi_i(\mathbf{r}) = \varepsilon_i \psi_i(\mathbf{r}) \quad (4.17)$$

where  $\varepsilon_i$  is the orbital energy of the Kohn–Sham orbital  $\psi_i$ . The orbitals are related to the density of the  $N$  particle system via  $n(\mathbf{r}) = \sum_i^N |\psi_i(\mathbf{r})|^2$ .

The self-consistent scheme now requires only an initial guess for the electron density  $n(\mathbf{r})$ . Then the effective potential for this density can be calculated and used to solve Eq. (4.17). From the obtained orbitals, a new density  $n'(\mathbf{r})$  can be calculated. The scheme is converged when the difference of  $E[n(\mathbf{r})]$  and  $E[n'(\mathbf{r})]$  has become small enough to be within a predefined limit. If the limit is not yet reached, the calculated density  $n'(\mathbf{r})$  becomes the new initial density  $n(\mathbf{r})$  to repeat the scheme with. A flowchart illustrating the self-consistent scheme is shown in Figure 4.2 (taken from Ref. [60]).

Following from the theorems and the self-consistent scheme to solve the equations defined by the theorems, DFT could in principle provide an exact solution. In practice however, it involves an approximation for  $E_{xc}$  and thus  $v_{xc}$ , the part of the energy functional and potential that contains the non-trivial contributions due to interactions and quantum mechanics. The next section gives an overview over some of the standard approximations that have been developed to approximate the exchange-correlation functional.

### 4.2.2 Exchange-correlation functionals

DFT is one of the most popular methods used in condensed matter physics, computational physics and chemistry alike. If the exact exchange-correlation functional was known, all systems could be accurately modeled with regards to all quantities of interest by the same, exact functional. In the absence of the exact exchange-correlation functional, the method its

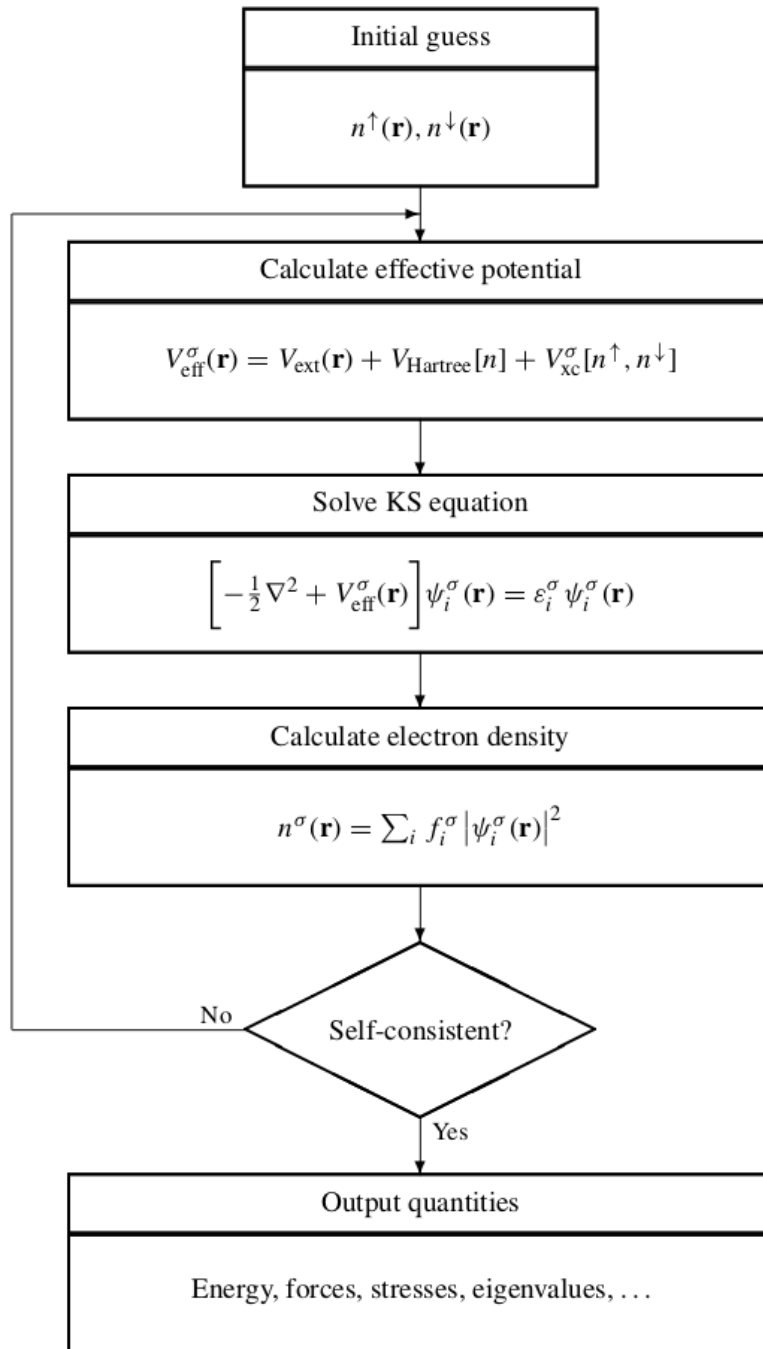


Figure 4.2: Flowchart giving a schematic representation of the self-consistent loop to solve the KS equations. Starting from an initial guess for the density, the effective potential is calculated and subsequently used to solve the KS equations in the given effective potential. From this a set of wavefunction is found and the density corresponding to the wavefunctions determined. The resulting density is compared to the initial guess and the loop is considered self-consistent if the deviation is small enough. Otherwise the calculated density takes on the role of the guessed density for the next round. The figure was taken from Ref. [60].

still suitable for a variety of problems due to the different approaches one can take to arrive at an approximation for the exchange-correlation functional. These can range from general consideration based on fundamental physics (favoured by physicists) at one end, to fits to specific properties (popular for chemistry applications). This makes it a powerful tool for a variety of applications, where the problem dictates the type of approximation that should be chosen.

The name exchange-correlation (XC) is a combination of the two main energy contributions that cannot be expressed exactly as a functional of the electron density. The *exchange* part refers to the effect coming from the anti-symmetry of the fermionic wavefunction under exchange of indistinguishable particles, a consequence of which is the Pauli exclusion principle. The forbidden region around a given fermion that, for the same reason, cannot be occupied by another fermion is dubbed the *exchange hole*. The correlation part contains both contributions to the potential as well as to the kinetic energy. The kinetic part accounts for difference in kinetic energy between the non-interacting and the interacting system since the kinetic part of the KS functional only contains the non-interacting part. In addition to the name giving contributions, the XC functional ideally also includes corrections, for example, to offset the self interaction error. The following will review some of the most relevant types of functionals, the rationale behind them and what application they are best suited for.

The local-density approximation (LDA) and the slightly more general local spin density approximation (LSDA) are the simplest and earliest approximations to the XC functional. As Kohn and Sham already pointed out in their DFT paper [70], solids can often be approximated as uniform, homogeneous electron gas also known as Jellium. It is known that the exchange and correlation contributions of Jellium depend only on the one parameter present, namely the density. In this case, the XC energy is simply given by the integral where the energy at each point is the same as that of a homogeneous electron gas with the same density. Thus, the XC energy in the LSDA approximation is defined as

$$E_{\text{XC}}^{\text{LSDA}}[n_{\uparrow}, n_{\downarrow}] = \int d^3r n(\mathbf{r}) \epsilon_{\text{XC}}^{\text{LSDA}}(n_{\uparrow}(\mathbf{r}), n_{\downarrow}(\mathbf{r})) \quad (4.18)$$

and the related expression for the LDA can be found from the LSDA by setting

$$n_{\uparrow}(\mathbf{r}) = n_{\downarrow}(\mathbf{r}) = n(\mathbf{r})/2, \quad (4.19)$$

where  $n_{\uparrow}(\mathbf{r})$  and  $n_{\downarrow}(\mathbf{r})$  are spin densities and  $n(\mathbf{r})$  is the total density. The energy can be separated in an exchange and a correlation contribution. The exchange contribution is usually based on calculations of the homogeneous electron gas and can be calculated exactly as  $\epsilon_x \sim n(\mathbf{r})^{1/3}$  [71], resulting in

$$E_x^{\text{LDA}}[n(\mathbf{r})] = -\frac{3}{4} \left(\frac{3}{\pi}\right)^{1/3} \int n(\mathbf{r})^{4/3} d\mathbf{r}. \quad (4.20)$$

for the LDA and similarly for the LSDA

$$E_x^{\text{LSDA}}[n(\mathbf{r})] = -\frac{3}{2} \left(\frac{3}{\pi}\right)^{1/3} \int d\mathbf{r} [n_{\uparrow}(\mathbf{r})^{4/3} + n_{\downarrow}(\mathbf{r})^{4/3}], \quad (4.21)$$

which naturally includes only interaction between parallel spin pairs. The correlation effects cannot be calculated exactly but several parameterized versions exist that are obtained from quantum Monte Carlo simulations of the HEG at different densities [72–74].

The main drawback of the L(S)DA is the unphysical self-interaction term. The presence of the self-interaction overestimates the electron-electron energy and is not completely cancelled by the exchange-correlation term. A possible fix to this can be added in form of a correction, but this makes the exchange correlation dependent on orbitals instead of density only [75]. Without corrections, the remaining contribution from the self-interaction is small (only about 5% is left over for example for the hydrogen atom) especially in systems close to the homogeneous gas but large in inhomogeneous or confined systems. Thus, the L(S)DA works best for systems that are close to the Jellium model, e.g. solids with nearly free electrons, and in general systems where density varies only slowly. This makes the L(S)DA not best model for systems where the electron density varies rapidly, like the inside of atoms or molecules. However, the L(S)DA still performs remarkably well in most applications. This is in part due to the fact that, while the shape of the exchange-correlation hole from the L(S)DA is not correct, it satisfies overall sum rules correctly. This means that if the exchange-correlation hole is viewed as the conditional probability  $P_{XC}(\mathbf{r}, \mathbf{r}')$  of finding another electron at  $\mathbf{r}'$  given that there is an electron at  $\mathbf{r}$ , the probability should normalize to exactly one electron. The LS(D)A fulfills this condition [76, 77].

Another reason is that, while the exchange part is underestimated by the L(S)DA, the correlation part is usually overestimated, leading to a considerable reduction of the overall error on the energy. This enables the L(S)DA to model overall behaviour fairly accurately, while absolute values are off. As a consequence, known problems of the L(S)DA are underestima-

| Crystal | LDA  | Exper. | Crystal             | LDA | Exper. | Crystal            | LDA  | Exper. |
|---------|------|--------|---------------------|-----|--------|--------------------|------|--------|
| Ne      | 11.4 | 21.4   | C                   | 4.1 | 5.5    | Ar                 | 8.3  | 14.2   |
| Si      | 0.56 | 1.17   | Kr                  | 7.0 | 11.6   | Ge                 | 0.65 | 0.76   |
| LiF     | 9.9  | 14.2   | NaCl                | 5.3 | 9.0    | GaAs               | 0.71 | 1.5    |
| CsCl    | 5.0  | 8.3    | MgO                 | 4.5 | 7.7    | CuAlS <sub>2</sub> | 2.1  | 3.5    |
| CaS     | 2.6  | 5.4    | BaS                 | 1.8 | 3.9    | CuGaS <sub>2</sub> | 1.3  | 2.4    |
| ZnS     | 2.3  | 3.8    | CuGaSe <sub>2</sub> | 0.5 | 1.7    | ZnSe               | 1.8  | 2.8    |
| NiO     | 0.3  | 4.3    | AIP                 | 1.6 | 2.5    | CdS                | 2.0  | 2.6    |

Table 4.1: Fundamental gaps of insulators calculated from the band structure as predicted by the L(S)DA versus the experimental values. The table is an excerpt from values collected in Ref. [78].

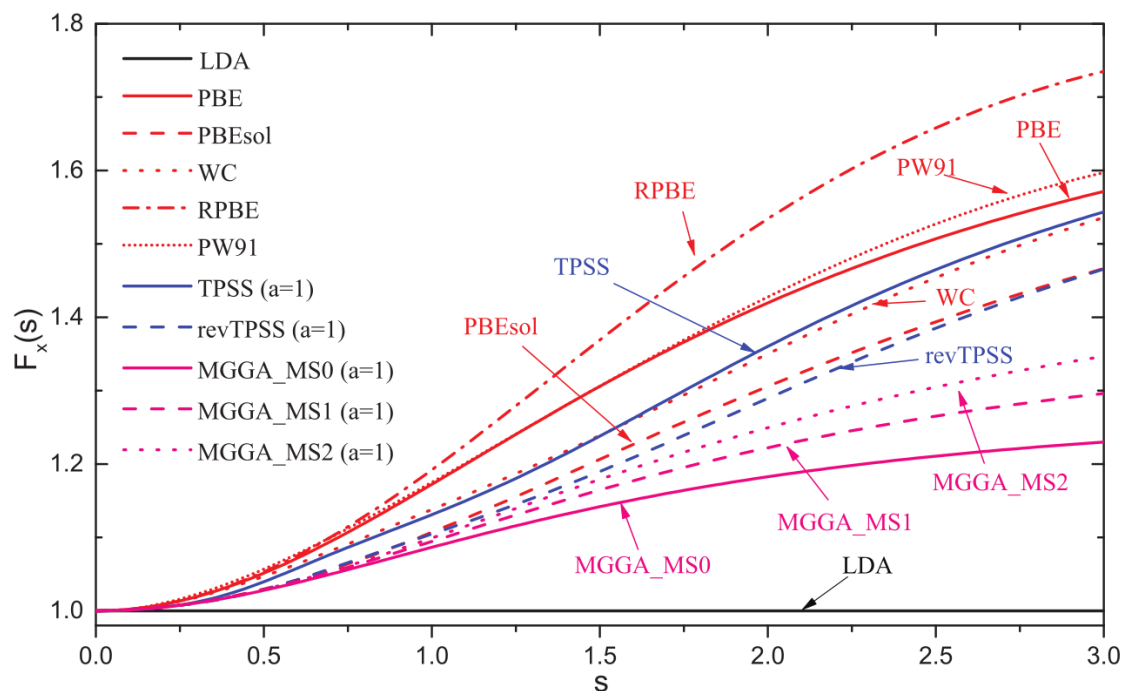


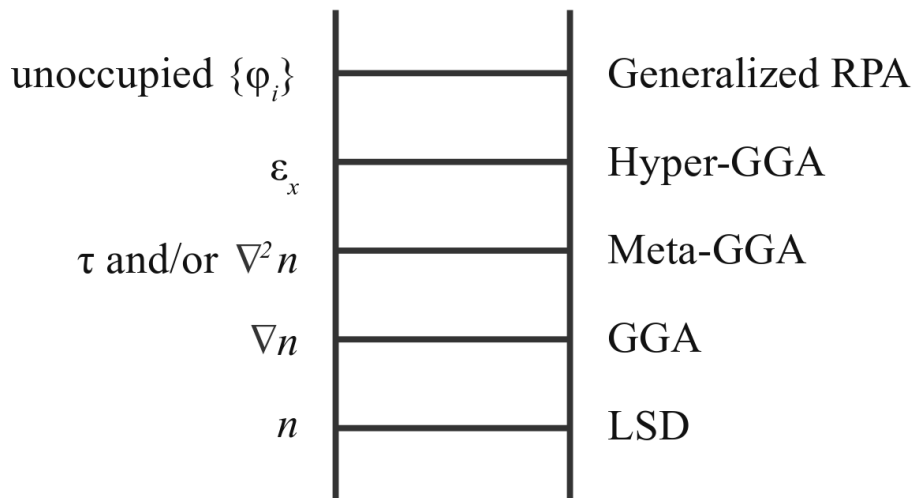
Figure 4.3: The enhancement factor  $F$  for a host of different GGA functionals as a function of the reduced density gradient  $s$ . Figure taken from Ref. [82]

tion of band gaps and too high binding energies resulting in overbinding. An excerpt of a comparison between the band gaps of different materials as predicted by the LDA versus their experimental values taken from Ref. [78] is given in Table 4.1.

In addition to the L(S)DA being an adequate approximation on its own, it is also the ideal starting point from which to develop improved approximations. In the framework of Thomas and Fermi, the predecessor of KS DFT, it has been shown by Lieb and Simon [79–81] that the LDA works not only for slowly varying, homogeneous systems but provides also an asymptotic limit for the case of large nuclear charges. While this has been proven with rigour only for Thomas-Fermi calculations, a similar statement can be made about KS DFT calculations [64] which states that the error of the L(S)DA vanishes with increasing atomic number making it the universal limit of all electronic systems.

This built-in ability of the L(S)DA to satisfy overall constraints and recovering the correct limiting behaviour is no easy feat and hard to achieve when trying to construct a XC functional from arbitrary approximations instead. This makes the L(S)DA the ideal starting point to build more sophisticated approximations from. Since the *local* density approximation is purely local, the next piece of information to include are non-local contributions. Cue the generalized-gradient approximation (GGA) which is technically semi-local rather than non-local. As the name suggests, the GGA takes also the gradient of the electron density  $\nabla n(\mathbf{r})$  as well as the electron density  $n(\mathbf{r})$  at each point into account. A problem that arises from including the gradient in form of a low-order expansion as suggested by Kohn and Sham is that gradients in real materials can get so large that the expansion breaks down. The *generalized*-gradient

## HEAVEN OF CHEMICAL ACCURACY



## HARTREE WORLD

Figure 4.4: The 'Jacobs ladder' to illustrate the hierarchy of composition of different types of functionals and the quantities taken into account for evaluating them. The ladder metaphor should be understood that a functional on a given rung includes all ingredients listed on the same rung plus everything from the rungs below. The figure is an adaptation of a figure that appeared in Ref. [83]

therefore denotes several possible ways of including a modified gradient to circumvent the break down of the expansion. GGA type functionals can be written in the form

$$E_{\text{XC}}^{\text{GGA}}[n] = \int \epsilon_{\text{XC}}^{\text{GGA}}(n, \nabla n) n(\mathbf{r}) d^3\mathbf{r} \quad (4.22)$$

where the explicit spin density is dropped from now on. Following from the philosophy of constructing the GGA from the LDA rather than as a completely new functional,  $\epsilon_{\text{XC}}^{\text{GGA}}(n, \nabla n)$  and  $\epsilon_{\text{XC}}^{\text{LSDA}}(n)$  are related to each other by an enhancement factor  $F$ , which is a function that scales the exchange energy of the LDA:

$$\epsilon_{\text{XC}}^{\text{GGA}}(n) = \epsilon_{\text{XC}}^{\text{LDA}}(n, \nabla n) F_{\text{XC}}(r_s, s) \quad (4.23)$$

where  $r_s \sim n^{-1/3}$  is the Wigner-Seitz radius (Eq. (4.5)) and  $s = (|\nabla n|)/(2k_F(\mathbf{r})n(\mathbf{r}))$  the dimensionless reduced density gradient in terms of the Fermi wave vector  $k_F$ . The enhancement factor as a function of the parameter  $s$  for a host of different GGAs is shown in Figure 4.3 [82]. These functionals are obtained from fitting to different features, properties and limits resulting in many, slightly different realisations of GGA functionals.

Modern GGAs improve over the L(S)DA type functionals by correcting the overbinding of the L(S)DA and show overall better agreement with experiments. The three most widely used

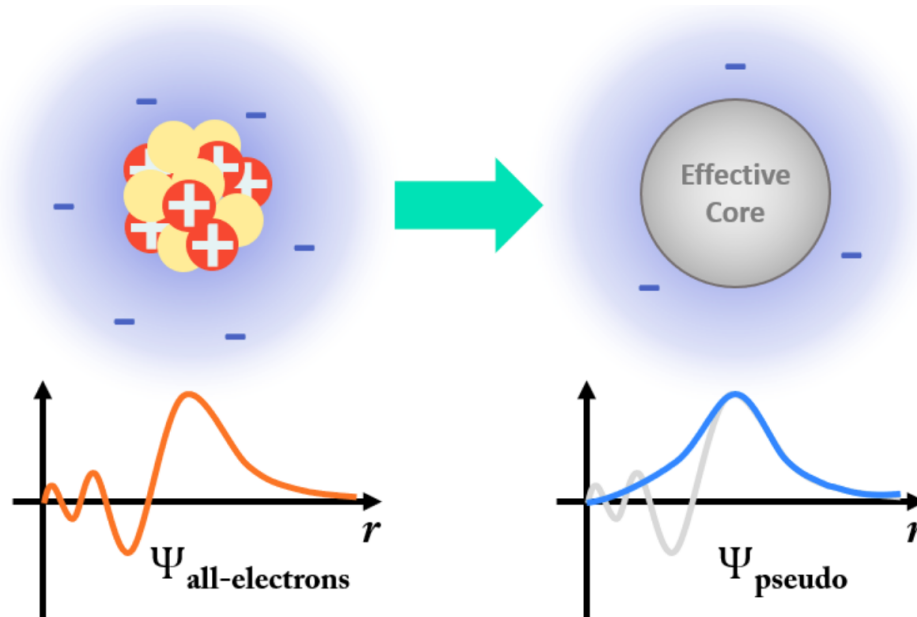


Figure 4.5: Schematic that illustrates the idea of the pseudopotential. The core electrons and the nucleus with all its tight binding interactions is replaced by an effective core. The resulting wavefunction for the valence electrons is smooth within the core region and equal to the all electron wavefunction outside the core region. Figure taken from Ref. [90]

GGA functionals are the ones developed by Becke (B88) [84], Perdew and Wang (PW91) [85] and Perdew, Burke and Enzerhof (PBE) [86].

More classes of functionals exist, that include more information beyond density and its gradient. One possibility is to extend the GGA like the GGA extends the L(S)DA, in a modular fashion including more and more information. The ‘Jacobs ladder’, a metaphor taken from Ref. [83], illustrates this. The ladder should be understood as such that the functional on a given rung of the ladder includes all ingredients on the left of the same rung and everything below. At the top of the ladder is the random-phase approximation (RPA). While the RPA is the most exact, it is also by far the most computationally expensive. Instead of including more and more details into the functional, a different approach has been taken in the development of hybrid functionals. A hybrid functional is a combination of an explicit density functional like a L(S)DA or a GGA together with Hartree-Fock exchange energy. When it comes to energetics, these functionals are the most accurate which makes them the most popular for chemistry applications. The most favoured functionals in this group are the B3LYP [87], a GGA hybrid, and the M05-2X [88] and M06-2X [89], which are both hybrid meta-GGA’s.

This work is interested in the general behaviour of metals over a somewhat large part of the phase diagram including both the liquid and the solid state. We therefore use the GGA-PBE functionals which fits the bill of being an good choice for physics applications that are aimed at the accurate modeling of overall behaviour without particular interest in extremely exact calculations of numerical values.

The potentials used are pseudopotentials as mentioned briefly in the previous chapter. The

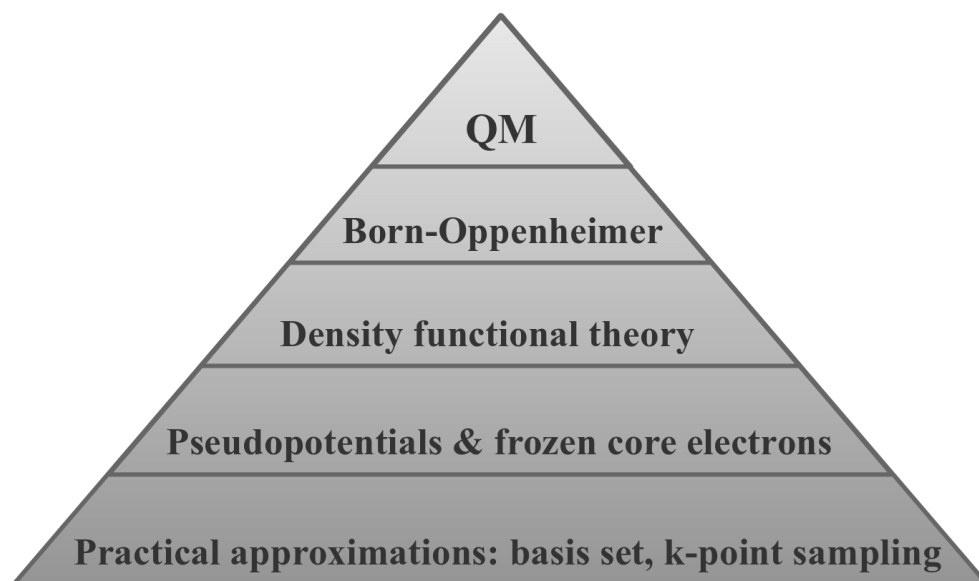


Figure 4.6: The pyramid illustrates the hierarchy of the approximations used for the DFT simulations of this work. At the top is the fully quantum-mechanical treatment of nuclei and all electrons. In the Born-Oppenheimer approximation the nuclei are treated classically. DFT on the middle layer is in principle exact, but effectively an approximation since the exact functional is unknown. Below is the pseudopotential where no longer all, just the valence electrons are treated explicitly. The practical approximations used to carry out concrete calculations of the electronic structure form the bottom layer.

core electrons around an atomic nucleus are tightly bound to the nucleus and rarely partake in chemical binding and interactions. Their main job is to screen and thereby weaken the interaction between the core and the valence electrons. Therefore the core electrons are effectively frozen around the core and only the effective interaction of the frozen core with the valence electrons is considered [60, 91]. This simplifies the wavefunction for the valence electrons as sketched in Figure 4.5. The real wavefunction of the valence electron includes a strongly varying behaviour in the atomic core. Since the valence electron is virtually never actually this far inside the core (at least not in a physical meaningful situation) the wavefunction is replaced by a function that is smooth inside the core region and matches the real wavefunction outside of the core region. This makes for more efficient simulations since it simplifies the wavefunction and more importantly, instead of all electrons surrounding an atom, only the valence electrons need to be considered explicitly.

The DFT simulations of this work are carried out using the Vienna Ab-initio Simulation Package (VASP) [92–94]. The simulations use a basis set for the wave functions that consist of plane waves and the projector-argument-wave (PAW) method [95]. Except for one simulation discussed in appendix A.2, only the  $\Gamma$  point is used for the k-point sampling. The k-point sampling specifies the Bloch vectors (k-points) that will be used to sample the Brillouin zone in calculations. The (first) Brillouin zone is the Wigner-Seitz cell of the reciprocal lattice and the  $\Gamma$  point is the center point of the first Brillouin zone. Due to the high symmetry at

the center point, using the  $\Gamma$  point only is usually a sufficient and efficient choice [96, 97]. Figure 4.6 illustrates the hierarchy of all the approximations involved in the calculation.

### 4.2.3 Simpler potentials derived from DFT considerations

The effective medium potential that will be introduced in the next section is not the only attempt at creating a potential from DFT considerations. The idea of developing empirical potentials from DFT is born from the aim to be similar in accuracy while reducing the computational costs. Similar efforts resulted in a host of different potentials that try to translate DFT results into a form that translates density functional considerations into a function that only depends on atomic positions and does not treat electrons explicitly. They have the following general expression for their total energy in common,

$$E = \sum_{i,j} U(r_{i,j}) + \sum_i F(\rho_i) \quad \text{where} \quad \rho_i = \sum_j \rho(r_{i,j}). \quad (4.24)$$

where the energy is split into a pair potential part  $U$  and  $F$ , a function depending on the density  $\rho$ . This common parent form for the potential derives from the shared concept of including the electronic structure environment as some function  $F$  in addition to the pair-interaction  $U$ . Since the main difference is how the environment is included, this usually inspired the name for the potentials, just like the positive charged “jelly” background inspired the name of the Jellium system. Besides the effective medium potential, this includes the embedded atom method [98, 99], the glue potential [100] and the Finnis-Sinclair [30] potential.

The embedded atom method (EAM) is the most widely used of the potentials above. A comprehensive review of the model and its applications can be found in Ref. [101]. In the EAM the function  $F$  is called an embedding function (hence the name), since it gives the energy to *embed* an atom  $i$  in the combined electron density consisting of contributions from each of the atoms neighbouring atom  $i$ . This follows from the ansatz of Daw and Baskes [98, 99] to view the cohesive energy in a metallic solid as decomposed into the embedding energy and the electrostatic interactions, also referred to as electron cloud contribution. From fitting to properties of the bulk metal, separate, empirical functions for each contribution are obtained. For a single element system three such functions need to be specified; the embedding function, the electron cloud and the pair-wise interaction. What makes the EAM unfit for this work is the fact that these functions are typically provided in tabulated format which is not easily includable in RUMD [102], our group’s MD code. We therefore turn to a close relative of the EAM, the effective medium theory potential.

## 4.3 Effective medium theory

The effective medium theory (EMT) potential [51, 103, 104] was constructed from the same consideration as the potentials above, from the need for a potential that describes metals at a similar level of the accuracy of DFT at lower computational costs. What sets the EMT

potential apart is that the EMT potential realizes this in a semi-empirical way. This means that instead of fitting to experimental properties of the bulk solid like the EAM, some of the parameters in the EMT potential are calculated directly from DFT in the local-density approximation. Ref. [51] gives a detailed derivation of the potential and its parameters. Some relations between the EAM and the EMT potential are discussed in Refs. [103, 104].

The core of the EMT potential is a well chosen reference system, the *effective medium*. The total energy of the system is then obtained as the energy of the reference system and an estimate of the difference between the real system. Thus the total energy  $E$  can be written as

$$E = \sum_i E_{c,i} + \left( E - \sum_i E_{c,i} \right) \quad (4.25)$$

with  $E_{c,i}$  being the *cohesive energy*, the energy of atom  $i$  in the reference system and the difference is given by  $(E - \sum_i E_{c,i})$ . The difference term should be small enough so it can be treated within perturbation theory, so the goal for choosing the reference system is to find a system as close as possible to the real system. The real and the reference system are linked to each other by a tuning parameter. In the first version of the EMT potential, the homogeneous electron gas has been used as the reference system [105, 106]. In the version of Ref. [51] that we are using for this work, a perfect fcc crystal is used as the reference system. The lattice constant then serves as the tuning parameter and is used to adjust the environment of an atom so that the average electron density surrounding the atom matches that of the real system.

The EMT potential is defined in terms of seven parameters:  $E_0$  the negative of the cohesive energy, a density parameter  $n_0$ , the Wigner-Seitz radius  $s_0$  (here defined in terms of atomic not electronic density), the parameter  $\eta$  quantifying the influence of the density tail surrounding an neighbouring atom, the parameter  $\lambda$  determined from the bulk modulus and the product of parameters  $V_0(\beta\eta_2 - \kappa)$  determined together from the shear modulus. The density related parameters  $n_0$  and  $\eta$  are calculated from self consistent calculations using the homogeneous electron gas. The other parameters are determined from experimental data. The following will summarize the discussion given in Ref. [51] on how the values for these parameters can be obtained for system with an ideal FCC crystal as the reference system.

The form for the correction term has been derived from DFT to be a combination of the *atomic-sphere correction* and the *one-electron correction*. The former term corrects for the difference in electrostatic and exchange-correlation between real and reference system. This is approximately equal to the difference in pair-interactions of the two systems. The one-electron correction is given by the difference of sums over one-electron energies. These contributions do not require any fitting input from experiments and can be calculated fully *ab initio* [107]. While this would yield an accuracy level comparable to DFT, it is also similarly computationally expensive. To circumvent this, the one-electron contribution is momentarily neglected. Including only the cohesive and the atomic-sphere correction parts, the total energy

expression can be simplified to

$$E = \sum_i \left( E_{c,i} + \Delta E_{AS}(i) \right) \quad (4.26)$$

$$= \sum_i \left( E_{c,i}(n_i) + \frac{1}{2} \left[ \sum_{i \neq j} V_{ij}(r_{ij}) - \sum_{i \neq j}^{ref} V_{ij}(r_{ij}) \right] \right) \quad (4.27)$$

where the atomic sphere correction  $\Delta E_{AS}(i)$  has been expressed as the difference between pair potentials  $V_{ij}$  between the real and the reference system. The neglected one-electron contribution is not necessarily small enough to be neglected, but it is possible to include this contribution as a small adjustment to the potential  $V_{ij}$ .

The density argument  $n_i$  of the cohesive energy  $E_{c,i}$  is the parameter that connects the environment around a given atom  $i$  in the real system with the reference system. This so-called embedding density  $n_i$  is obtained from adding the contributions from the surrounding atoms

$$n_i = \sum_{i \neq j} \Delta n_j(s_i, r_{ij}). \quad (4.28)$$

The density tail  $\Delta n_j(s_i, r_{ij})$  is assumed to have the following exponential form:

$$\Delta n(s_i, r_{ij}) = \Delta n_0 \exp \left[ \eta_1(s_i - s_0) - \eta_2(r_{ij} - \beta s_0) \right] \quad (4.29)$$

where  $s_0$  is the equilibrium Wigner-Seitz radius,  $s_i$  is the neutral sphere radius at non-zero pressure and  $\beta$  is a geometric factor related to the nearest-neighbour distance  $d_{nn}$  via  $\beta s = d_{nn}$ , meaning that  $\beta = (16\pi/3)^{1/3}/\sqrt{2} \approx 1.81$ . As mentioned before, the electron density  $n_0$  for each atom was determined from calculations of a homogeneous electron gas which are carried out at densities that are considered typical for metals.

For the concrete case of using an FCC lattice as the reference system, the atomic sphere correction can be expressed as

$$\Delta E_{AS}(i) = \frac{1}{2} \left[ \sum_{j \neq i} v(r_{ij}) - 12v(\beta s_i) \right] \quad (4.30)$$

where the second term corresponds to the FCC lattice having 12 nearest neighbours at distance  $r = \beta s_i$ . The potential is given by:

$$v(r) = -V_0 \exp -\frac{\kappa}{\beta}(r_{ij} - \beta s_0) \quad (4.31)$$

Input from experiments is required to determine the remaining parameters describing the elastic and structural properties of metals. The cohesive energy and the parameter  $\lambda$  are related to the bulk modulus  $B$  via

$$B = \frac{-E_0 \lambda^2}{12\pi s_0} \quad (4.32)$$

and the product  $V_0(\beta\eta_2 - \kappa) = V_0\delta$  can be found from the shear modulus  $C_{44}$  from the expression

$$C_{44} = \frac{sV_0\delta\kappa}{8\pi s_0}. \quad (4.33)$$

Eqs. 4.32 and 4.33 are only true for the nearest-neighbour approximation but Ref. [51] explains how to include more neighbours using a cutoff implemented using a Fermi-function. The standard choice, that is also the one used for this work, corresponds to the edge of the Fermi-function being between the 3rd and 4th neighbour shell of the equilibrium FCC crystal.

This gives all parameters to describe a pure metals. For two component systems, some generalization of the energy expression is required which is also discussed in Ref. [51]. The specific values for the pure metals and the CuZr alloy used in this thesis are given in chapter 5.1 and 5.2 where the results are presented.

# 5

## *Hidden Scale Invariance in Metals*

---

Several model liquids have been shown to be 'simple' in the isomorph theory interpretation of the word and obey hidden scale invariance to good approximation (see Chapter 2). Further studies have confirmed the simplicity to extend into the crystal phase of the Lennard-Jones system [22] as well. DFT calculations [29] of a state point close to the triple point of several elements in the periodic table have hinted that most metals also belong to the group of simple materials. The purpose of this chapter is to continue the study of simplicity in realistic models of metals.

Therefore this chapter investigates invariance of structure and dynamics in six mono-atomic metallic crystals as well as the well-known glass-former CuZr in the liquid regime. The semi-empirical EMT potential is used to represent the metallic interactions for these systems. A similar study is also conducted using DFT to investigate invariance in (Na,) Mg and Al in the solid and liquid regime along isomorphs close to melting.

### *5.1 Mono-atomic crystals (Ni, Cu, Pd, Ag, Pt, Au)*

The results presented in this section have been published in the first accompanying paper [39]. The study of metallic crystals is oriented at the study performed on Lennard-Jones crystals in [22]. The crystals are modeled using the EMT potential. The elements considered were determined by available potentials to be: Ni, Cu, Pd, Ag, Pt, Au. All have a face-centered cubic crystal structure. The parameters for the EMT potential are listed in Table 5.1, details of the potential are summarized in section 4.3.

For each of the metals, three curves were simulated: one isomorph, one isotherm and one isochore. The state point along the isomorphs were found using the DIC (see Sec. 2.3) with density steps of 10% of the initial density up to a total increase of 100%. The start point for the isomorphs were chosen to resemble a crystal at room temperature density at 1293 K (1000°C) which corresponds to a pressure of about 10 GPa. Atomic masses and densities are taken from [108]. At each state point the NVT ensemble was simulated using periodic

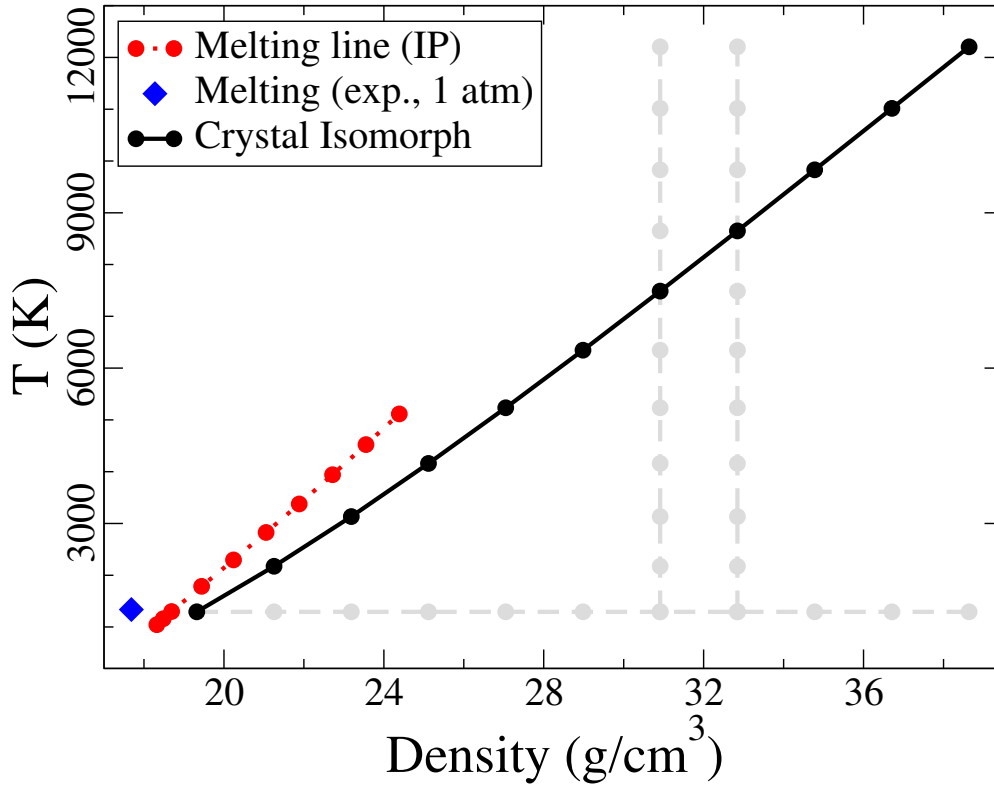


Figure 5.1: Phase diagram of Au showing the crystal isomorph with the melting line as reference. The red dot melting line has been obtained from interface pinning and one experimental point is included as well. It can be seen that the isomorph is fairly close to the melting line. The grey lines indicate the reference isotherm and isochores. A version of this figure appeared in Ref. [39]

boundary conditions and a Nosé-Hoover thermostat. The simulated systems consist of 4000 particles organized on a  $10 \times 10 \times 10$  fcc lattice with periodic boundary conditions. The simulations were carried out in RUMD[102]. For comparison, state points along an isochores and an isotherm were simulated as well.

Figure 5.1 shows the relevant part of the phase diagram using Au as an example including the iso-lines relative to the melting line for this system. The melting line was determined using the interface pinning method [109]. Also one point from the experimental melting curve is

| Material | $s_0$ (Å) | $E_0$ (eV) | $\lambda$ (Å $^{-1}$ ) | $\kappa$ (Å $^{-1}$ ) | $V_0$ (eV) | $n_0$ (Å $^{-3}$ ) | $n_2$ (Å $^{-1}$ ) |
|----------|-----------|------------|------------------------|-----------------------|------------|--------------------|--------------------|
| Ni       | 1.37586   | -4.44      | 3.68119                | 5.20997               | 3.673      | 0.0695078          | 3.15395            |
| Cu       | 1.41290   | -3.51      | 3.60182                | 5.17785               | 2.476      | 0.0614098          | 3.12183            |
| Pd       | 1.51874   | -3.90      | 4.07236                | 5.87138               | 2.773      | 0.0464285          | 3.43552            |
| Ag       | 1.59282   | -2.96      | 3.57536                | 5.27234               | 2.132      | 0.0369134          | 3.12183            |
| Pt       | 1.53461   | -5.85      | 4.14228                | 5.94319               | 4.067      | 0.0541216          | 3.42418            |
| Au       | 1.58753   | -3.80      | 4.12338                | 5.42918               | 2.321      | 0.0474408          | 3.16340            |

Table 5.1: EMT parameters for mono-atomic crystals. All numbers are taken from Ref. [51]

pictured which lies somewhat higher in temperature than the melting curve from simulation. This slight difference is not surprising given that the EMT model has not been explicitly fitted to melting data.

The isotherm is along the  $T = 1293\text{K}$  line, thus shares the initial point with the isomorph. Initially also the isochore was intended to share the starting point but the isomorph is too close to the melting line to maintain a crystalline phase along that isochore. To avoid melting, the isochore therefore starts at a higher density,  $\rho = 32.84\text{ g/cm}^3$  for the investigation of structural and dynamical invariance (Sec. 5.1.1) and  $\rho = 30.91\text{g/cm}^3$  for the vacancy study (Sec. 5.1.3).

### 5.1.1 Invariance of structure and dynamics

The RDFs from simulations in Au are shown in Figure 5.2. All three panels show the RDFs in reduced units for eleven state points each, with the top panel being state points along an isomorph. In comparison to the RDFs of the state points along isotherm and isochore, it can be clearly seen that only the structure along the isomorph collapses near perfectly onto one single line. A slightly less perfect collapse can be seen for the dynamics, shown in Figure 5.3 using again Au as the prototype. The figure shows VAF and VDOS for the same eleven state points as in Figure 5.2, again along isomorph, isochore and isotherm. Some variations can be seen after the first minimum but the collapse is still very clearly visible when comparing to the isotherm and isochore.

Leaving aside the isochores and isotherms and focusing on the isomorphs only, Figure 5.4 shows a summary for the five remaining metals that were included in this study. All show very similar behaviour as Au. The invariance of structure is obeyed as evidenced by all RDFs collapsing perfectly onto a single line. The dynamics in all metals deviate slightly but collapse still reasonably well onto one line.

Unlike in other systems, the scaling exponent  $\gamma$  is strongly state point dependent when using the EMT potential. Figure 5.5 shows how  $\gamma$  depends on density and temperature along isotherms (left) and isochores (right). The variation of  $\gamma$  along isomorphs is shown in the main panel of Figure 5.6 together with the correlation coefficient  $R$  in the bottom panel. While it is evident that the change in  $\gamma$  is dominated by changes in density, it does depend on temperature as well. As explained in Section 2,  $\gamma$  depending on both, temperature and density, is one of the new predictions of the generic extension of isomorph theory. However, as a first order approximation,  $\gamma$  can be regarded as depending on density only, which is in agreement also with the prediction from the original version of isomorph theory. The bumps in the low  $\gamma$ , high density region most obviously visible in the cases of Ni and Cu, is an artifact due to the cutoff in the EMT potential being at a fixed distance. The bumps occur when the density is increased so much that a new neighbor shell is pushed through the cutoff distance. Details of this are explained in the next section (5.1.2).

Given that the correlation coefficient  $R$  is well above 0.98 across all metals and all state points along all isomorphs, a good collapse is expected according to the theory. To summarize, this

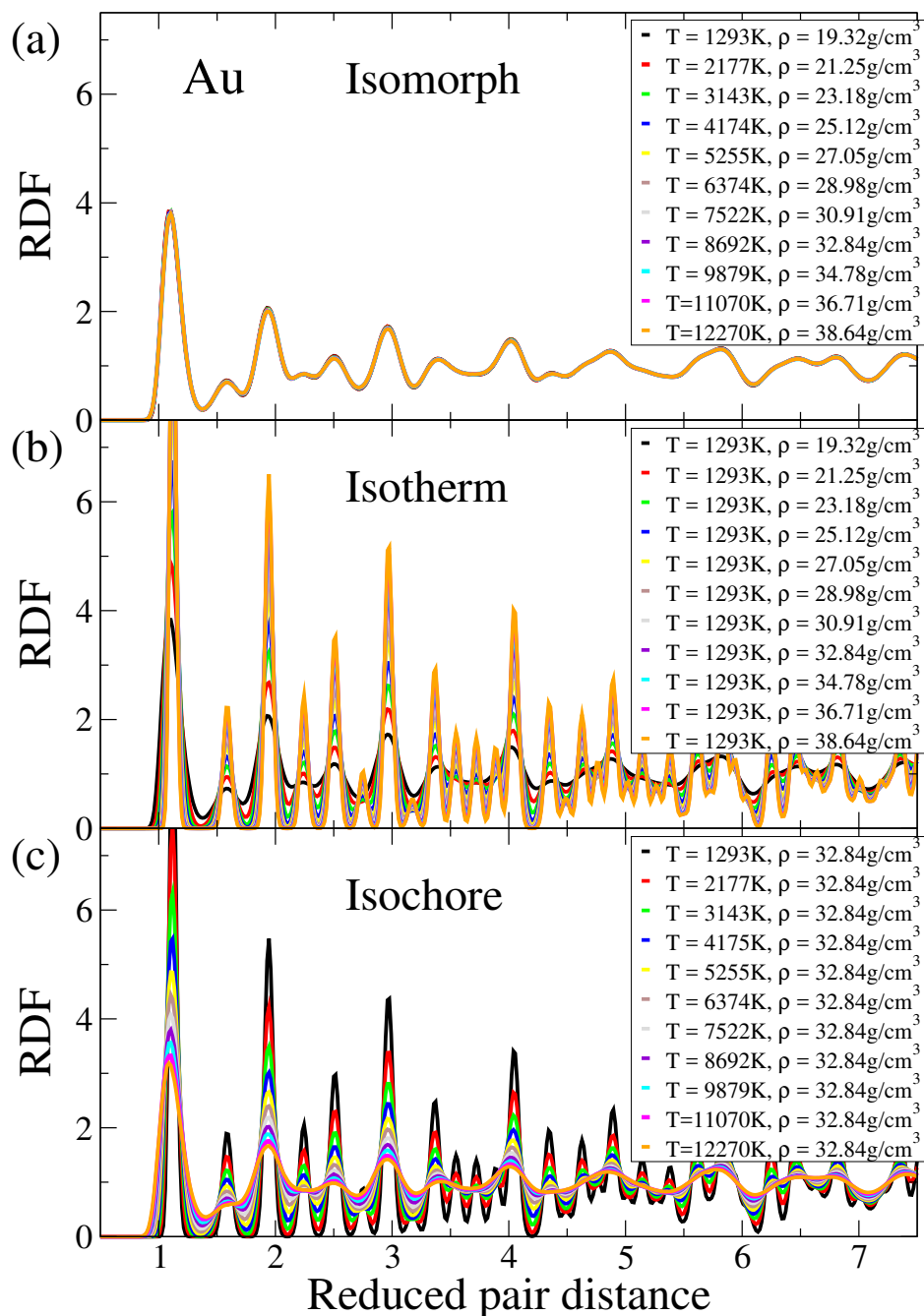


Figure 5.2: Invariance of structure and dynamics along an isomorph in Au. For comparison an isochore and isotherm are pictured as well along which no collapse of data can be seen. The figure appeared in Ref. [39].

part of this work validates that EMT metals have indeed good isomorphs. While a lot of liquid systems have been studied in the context of isomorph theory and also confirmed to be R-simple, this is only the second time isomorphs were studied in crystals and the first time in crystals of a realistic system. The first was the aforementioned study investigating isomorphs in Lennard-Jones crystals by Ref. [22].

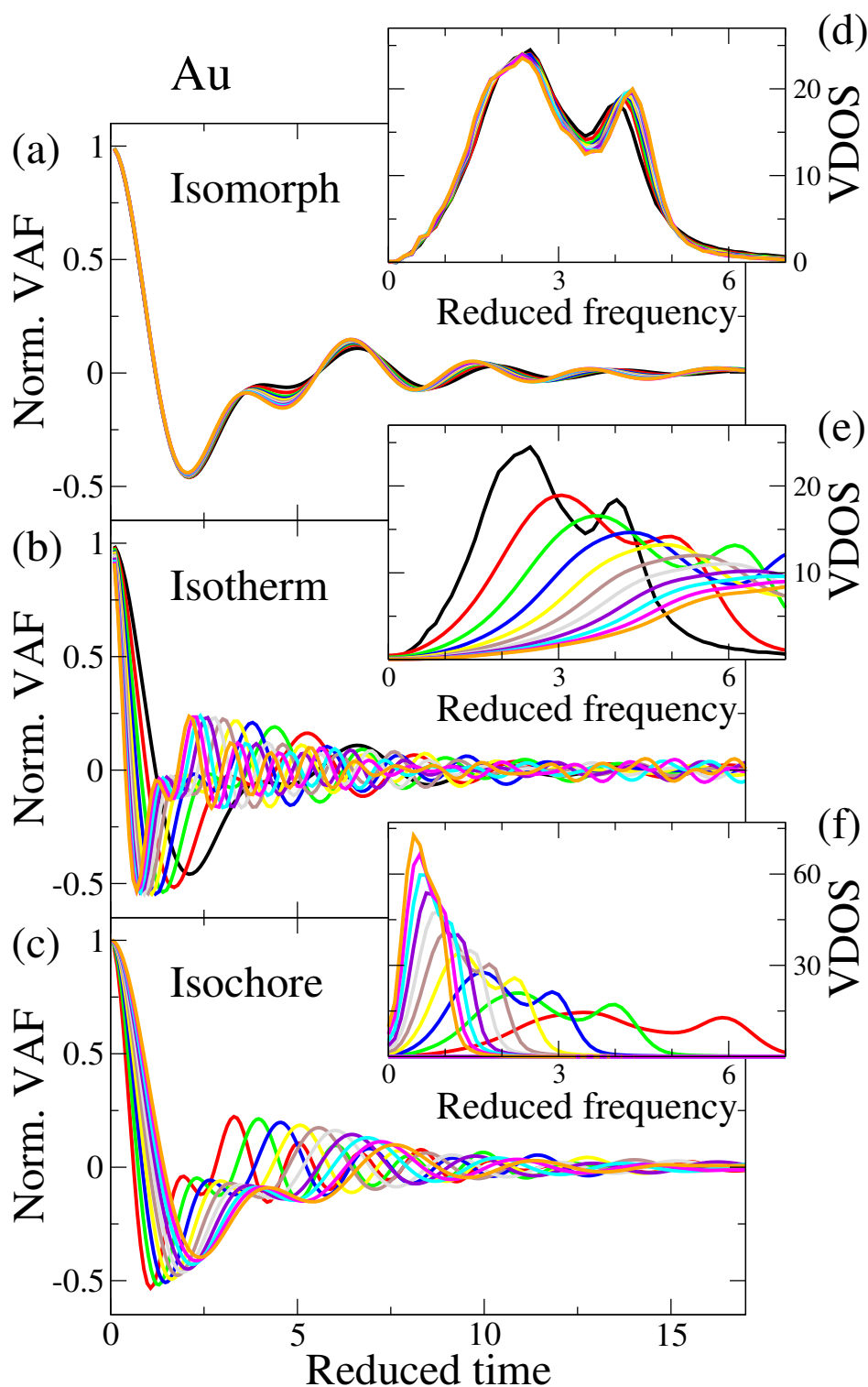


Figure 5.3: Invariance of structure and dynamics along an isomorph in Au. For comparison an isochore and isotherm are pictured as well along which - as expected - no collapse of data can be seen. This figure also appeared in Ref. [39].

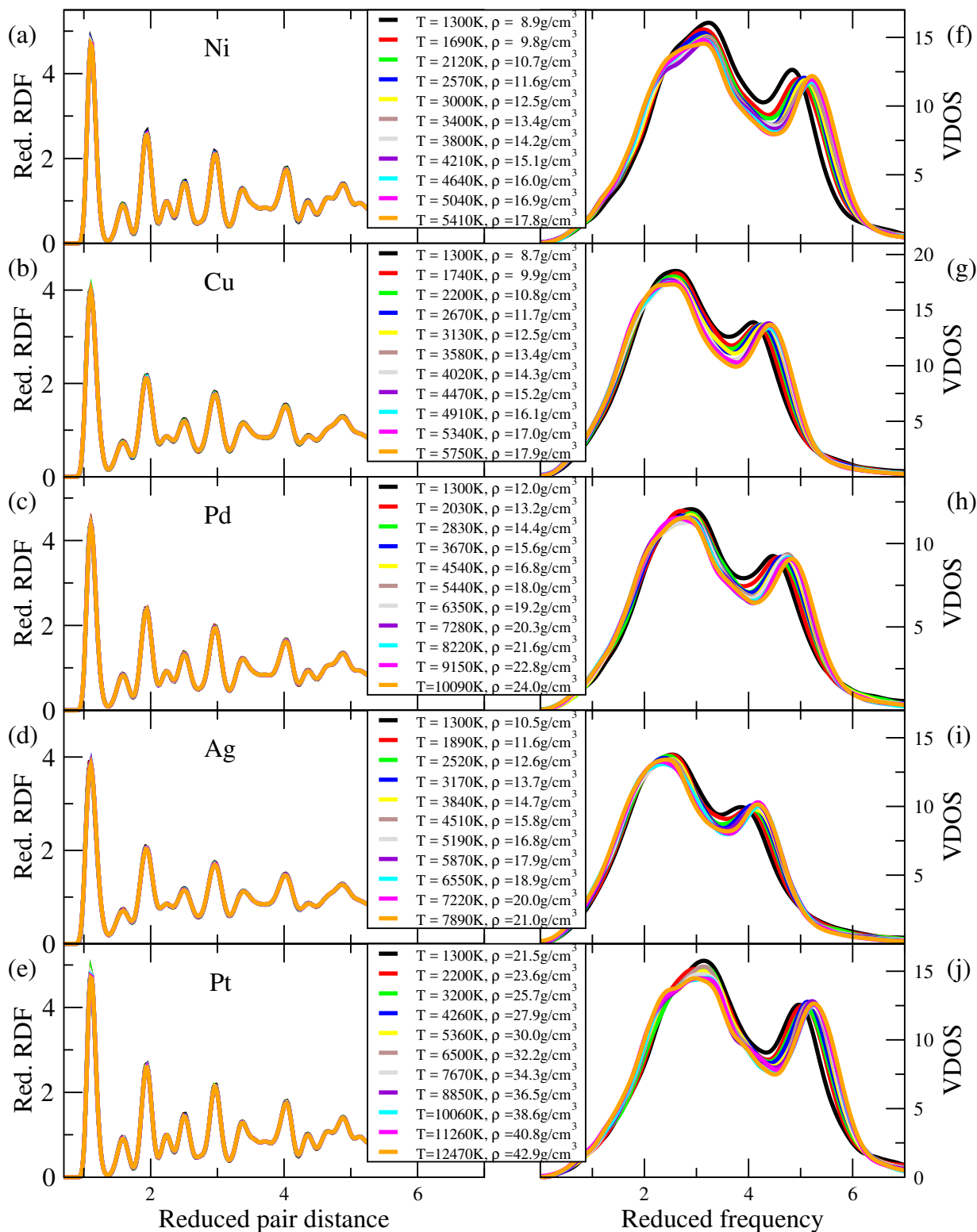


Figure 5.4: RDFs ((a)-(e)) and VDOSs ((f)-(j)) for the five other elements: Ni, Cu, Pd, Ag, Pt. All materials show a collapse similar to the one presented in Au. The structural invariance is near perfect for all cases, while there are slight deviations in the collapse of the dynamics. A version of this figure appeared in Ref. [39].

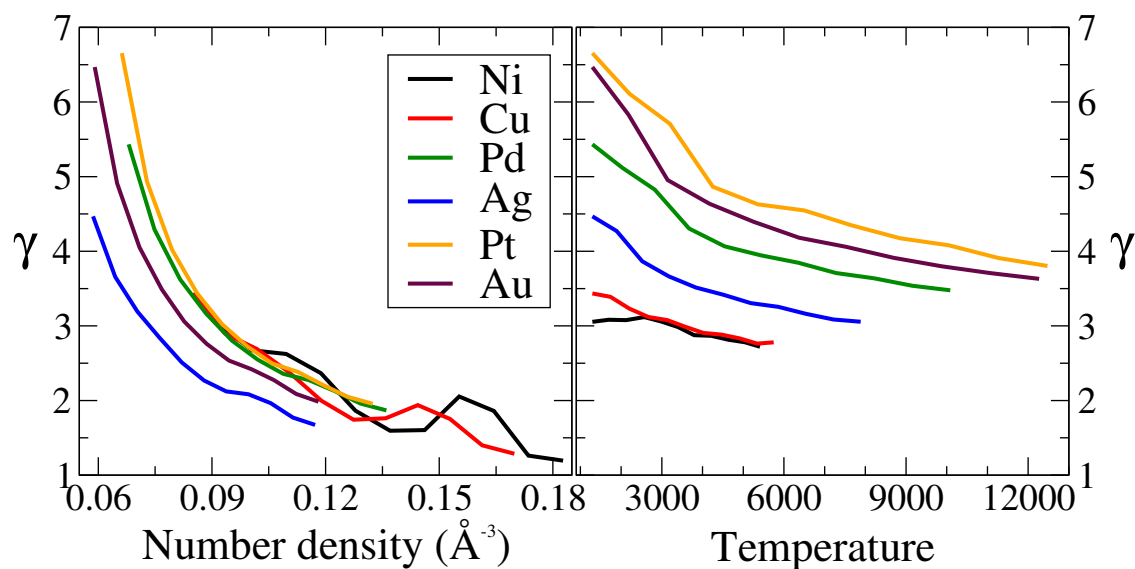


Figure 5.5: The variation of the scaling exponent  $\gamma$  along an isotherm (left) and an isochore (right) for the six metals. It is apparent that  $\gamma$  varies more with changing density than with temperature. A version of this figure appeared in Ref. [39].

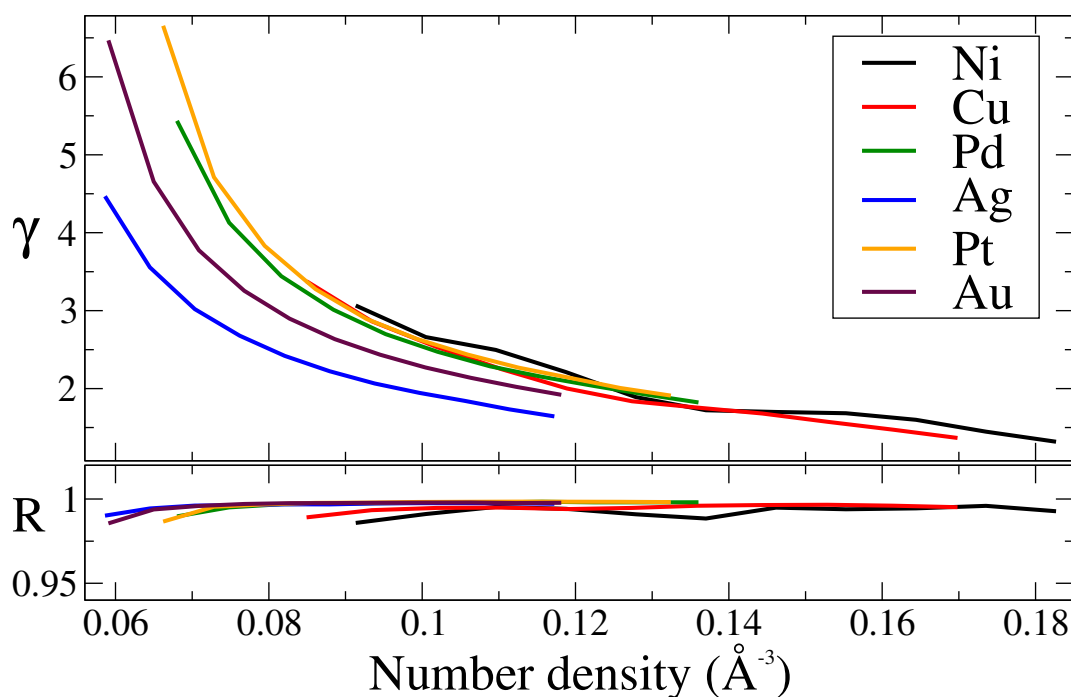


Figure 5.6: The variation of the scaling exponent  $\gamma$  along isomorphs in the six metals in the main panel. The bottom panel shows the correlation coefficient  $R$ , which is well above the  $R > 0.9$  criterion. A version of this figure appeared in Ref. [39].

### 5.1.2 EMT-cutoff bumps

This section addresses the oscillatory behaviour of the density dependence of  $\gamma$  in particular noticeable for Cu and Ni in Figure 5.5 of section 5.1.1. The bump-like artifacts can be

traced back to the implementation of the cutoff as a fixed distance in the EMT potential. The bumps occur when increasing the density pushes successive neighbor-shells through the cutoff distance.

Using the nearest neighbour distance  $d_1 = a/\sqrt{2}$  where  $a$  is the lattice constant, the distance to the  $n$ -th shell of neighbouring atoms,  $d_n$ , is given by  $d_n = \sqrt{n}d_1$ . The cutoff distance is implemented using a smoothed step function (like a Fermi function) modulating the interactions. The half-way point of the step function cutoff  $r_c$  is defined to be in the middle between the neighboring shells  $n$  and  $n + 1$  at:

$$r_c = \frac{d_n + d_{n+1}}{2} = d_1 \frac{(\sqrt{n} + \sqrt{n+1})}{2}. \quad (5.1)$$

The fcc lattice unit cell, a cube of volume  $a^3$ , contains 4 atoms. In terms of the number density  $\rho = N/V$ , the lattice constant  $a$  can be expressed as:

$$\rho = \frac{4}{a^3} \Leftrightarrow a = (4/\rho)^{1/3}. \quad (5.2)$$

Using Eq. (5.2), the distance to the  $n$ -th shell can be rewritten in terms of the density:

$$d_n = \sqrt{n}d_1 = \sqrt{n} \frac{a}{\sqrt{2}} = \sqrt{\frac{n}{2}} \left(\frac{4}{\rho}\right)^{1/3}. \quad (5.3)$$

The implementation puts the cutoff between the third and fourth neighbouring atom shells at  $r_c$  ( $n = 3$ ). Equating the distance to the  $n$ -th shell, Eq. (5.3), with Eq. (5.1) at  $n = 3$ . The resulting expression is given by

$$\sqrt{\frac{n}{2}} \left(\frac{4}{\rho}\right)^{1/3} \equiv r_c(n=3) = d_1 \frac{(\sqrt{3} + \sqrt{4})}{2}. \quad (5.4)$$

Rewriting the above expression, the densities at which subsequent neighbouring shells are passing through the cutoff distance can be found as

$$\rho(n > 3) = 4 \left( \frac{\sqrt{2}}{d_1} \frac{\sqrt{n}}{\sqrt{3} + \sqrt{4}} \right)^3. \quad (5.5)$$

The material dependent nearest neighbor distances are listed in Ref. [51] as  $d_1^{Ni} = 2.49\text{\AA}$  and  $d_1^{Cu} = 2.56\text{\AA}$ . Plugging these values into Eq. (5.5) yields the following densities for the 4th and 5th shell to coincide with the middle point of the cutoff:

$$\text{Ni:} \quad \rho(n=4) = 0.113 \text{\AA}^{-3} \quad \rho(n=5) = 0.158 \text{\AA}^{-3} \quad (5.6)$$

$$\text{Cu:} \quad \rho(n=4) = 0.104 \text{\AA}^{-3} \quad \rho(n=5) = 0.145 \text{\AA}^{-3} \quad (5.7)$$

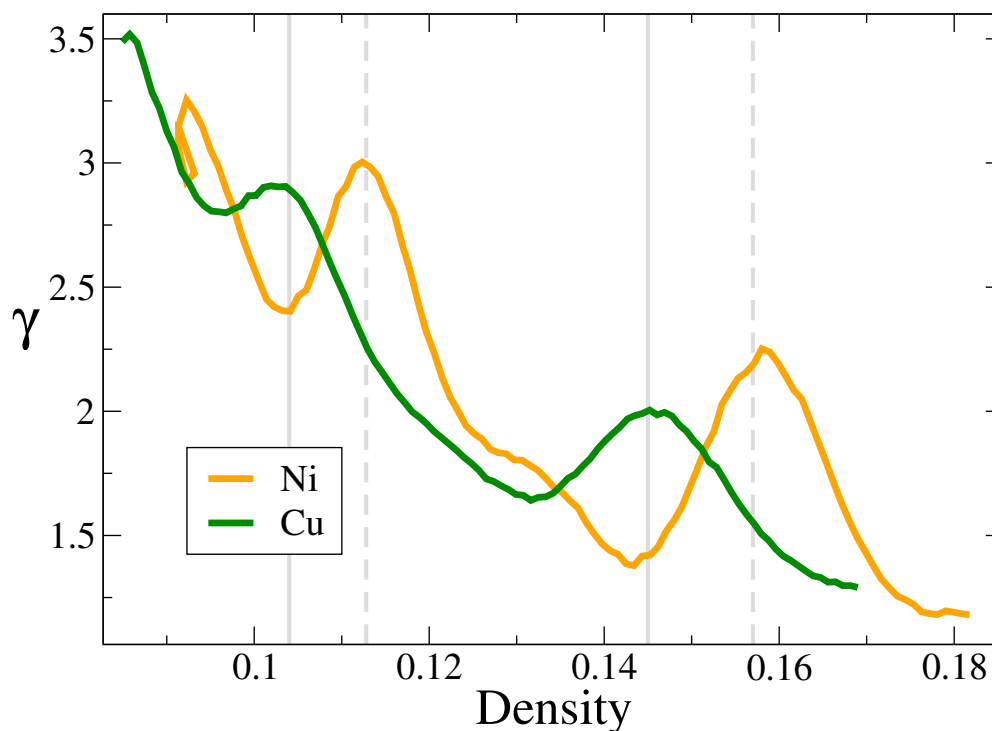


Figure 5.7: Bump-like artifacts occurring in the density dependence of  $\gamma$  for Cu and Ni due to the cutoff. The behaviour can be explained by the cutoff implementation of the EMT potential as a fixed distance. The light grey lines (solid for Cu, dashed for Ni) indicate the densities at which the radius of the fourth and fifth shell of neighbouring atoms is exactly in the middle of passing through the cutoff which coincides with the bumps in  $\gamma$ .

Figure 5.7 shows the density dependence in Ni and Cu (same curves as in Figure 5.5). The densities found for the 4th and 5th neighbouring shells to pass through the cutoff are marked by light grey lines (solid for Cu and dashed for Ni). It can be seen that the grey lines coincide perfectly with the bumps in  $\gamma$ . This effect is most striking in Cu and Ni because of the comparable low  $\gamma$  values for these materials. Interpreting  $\gamma$  in the context of an effective inverse power law exponent (see sec. 2.4.1), a small  $\gamma$  implies that the effective interaction is relatively long ranged. This makes the contributions from distant neighbouring atoms more significant for materials with smaller  $\gamma$  like Ni and Cu when compared to the other metals.

### 5.1.3 Other isomorph related studies

Now that it is established that our EMT metals in question are R-simple, other predictions from isomorph theory are investigated as well. One of these prediction concerns the *isomorph jump*. Recall from Chapter 2, that isomorph theory predicts instantaneous equilibration after a sudden change, a so-called jump, from one state point to another on the same isomorph. The theory implies that if the system was in equilibrium at the first state point should be in equilibrium right away after the jump. This prediction has been validated for viscous liquids [16], as well as in Lennard-Jones crystals [22].

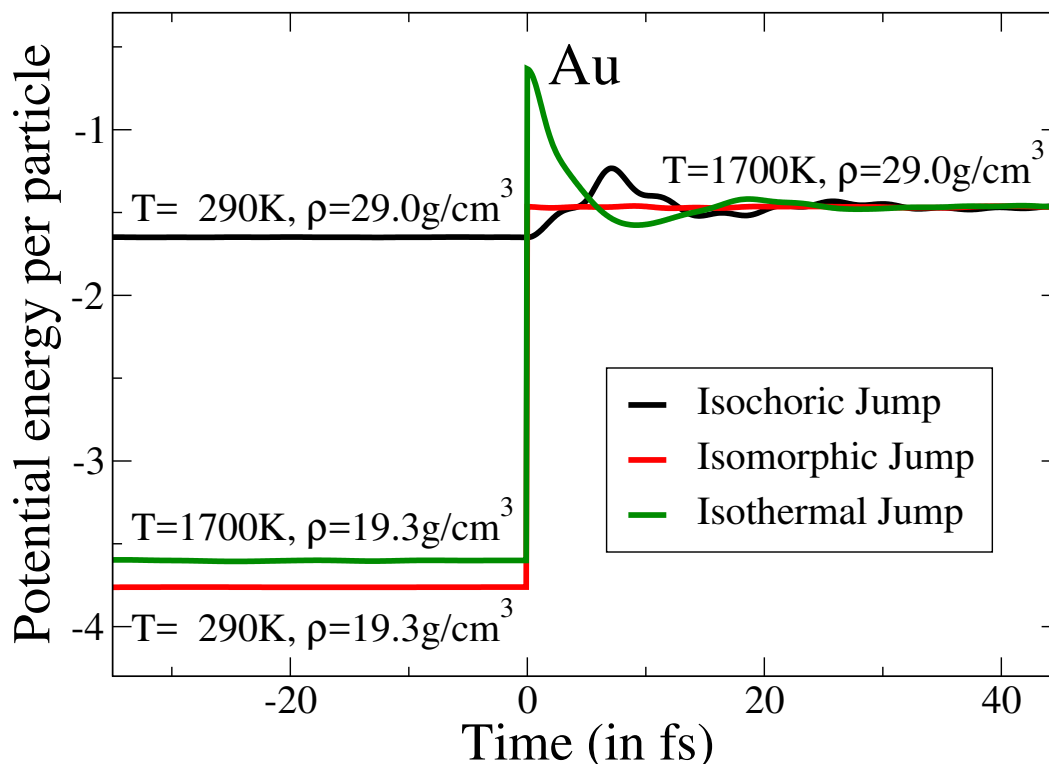


Figure 5.8: Per particle potential energy before and after jumps (at  $t = 0$ ) to a common target state point from state points that are, respectively, isochoric (black), isomorphous (red) and isothermal (green) to the target state point. All initial state points were in equilibrium pre-jump ( $t < 0$ ) as indicated by the flat lines. After the jump ( $t > 0$ ), the isothermal and isochoric jumps are out of equilibrium and oscillate towards the new level, while the isomorphous jump remains continuous as a flat line validating the predicted instantaneous equilibration. A version of this figure appeared in Ref. [39]

The jump along an isomorph shown in Figure 5.8 corresponds to a jump from the start point in the phase diagram of Fig. 5.1 to a point of 50% change of the initial density. The isochoric jump starts from a state point with the same density as the target point and only requires the temperature to be changed from the starting to the target temperature. The isothermal jump correspondingly starts at the target temperature and changes only the density from initial to target point.

The resulting time-series of the potential energy per particle before and after the jump are shown in Figure 5.8. To this end, the simulations at the initial state points have been run for an adequate amount to ensure equilibration. At the jump, the system is uniformly scaled to the new density, the temperature is changed to the new temperature and the velocities are scaled accordingly (if applicable). Subsequently the simulation continues at the target state point. On the scale of Figure 5.8, a system in equilibrium exhibits no visible fluctuations in its per particle potential energies. It can be seen that this is the case for all initial state points. After the jump it is only the isomorphous jump that remains a flat line right away while the potential energies after the isochoric and isothermal jumps oscillate towards the new level.

The second feature investigated is the diffusion of vacancies in the R-simple crystals. Many mechanical properties of crystals are associated with defects of the lattice. These properties are expected to be invariant in R-simple materials. A possible type of defect in the lattice are vacancies. A vacancy is an empty spot on the lattice from which the atom has been removed. The empty lattice spot enables neighbouring atoms to hop into the empty spot, effectively resulting in the vacant spot moving through the lattice. This introduces a new kind of dynamic to the crystal. Therefore crystals of all six EMT metals have been simulated with  $n = 1, 4, 16$  vacancies.

Figure 5.9 shows a snapshot of an 'inverted' configuration of the 16 vacancies study. Inverted here means that the red spheres resemble the vacancies while the actual particles are removed. The white spheres are positioned at the corners of the simulation box as guide to the eye. From snapshots manipulated in this way, it can be seen that for the case of 16 vacancies, all vacancies cluster together early on and do not disperse again, thus inadvertently simulated a cavity rather than the diffusion of vacancies.

Figure 5.10 shows the MSD for  $n = 1$  (left) and  $n = 4$  (right) vacancies along an isomorph in all six metals. The isomorph were re-determined by re-running the DIC for systems with

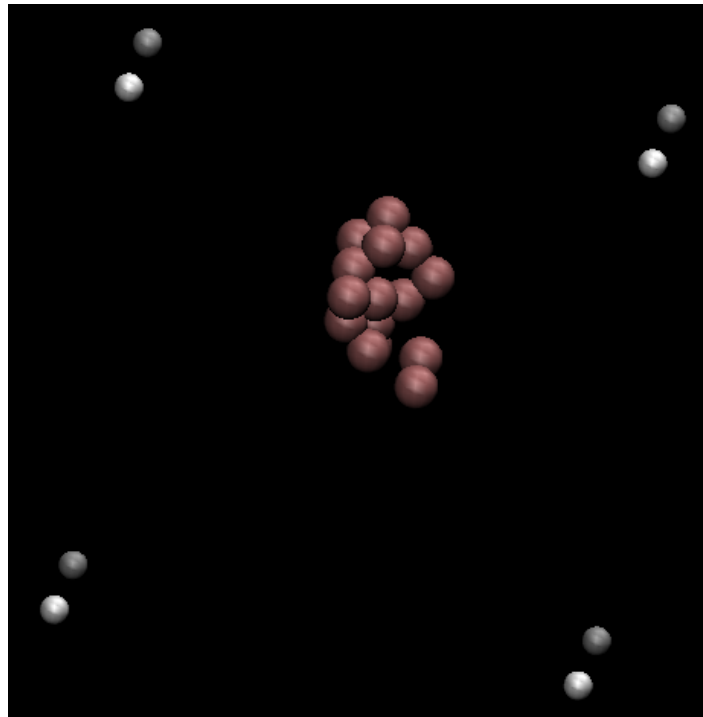


Figure 5.9: The figure shows a snapshot of an 'inverted' crystal to visualize the vacancies behaviour. The particles are removed and the red spheres indicate the position of the vacancies. The white spheres are a guide to the eye and indicate the corners of the simulation box. From similar analysis of snapshots at different times in the simulation, it can be seen that the vacancies cluster together early on and do not disperse again throughout the simulation. The snapshot also appeared in Ref. [39].

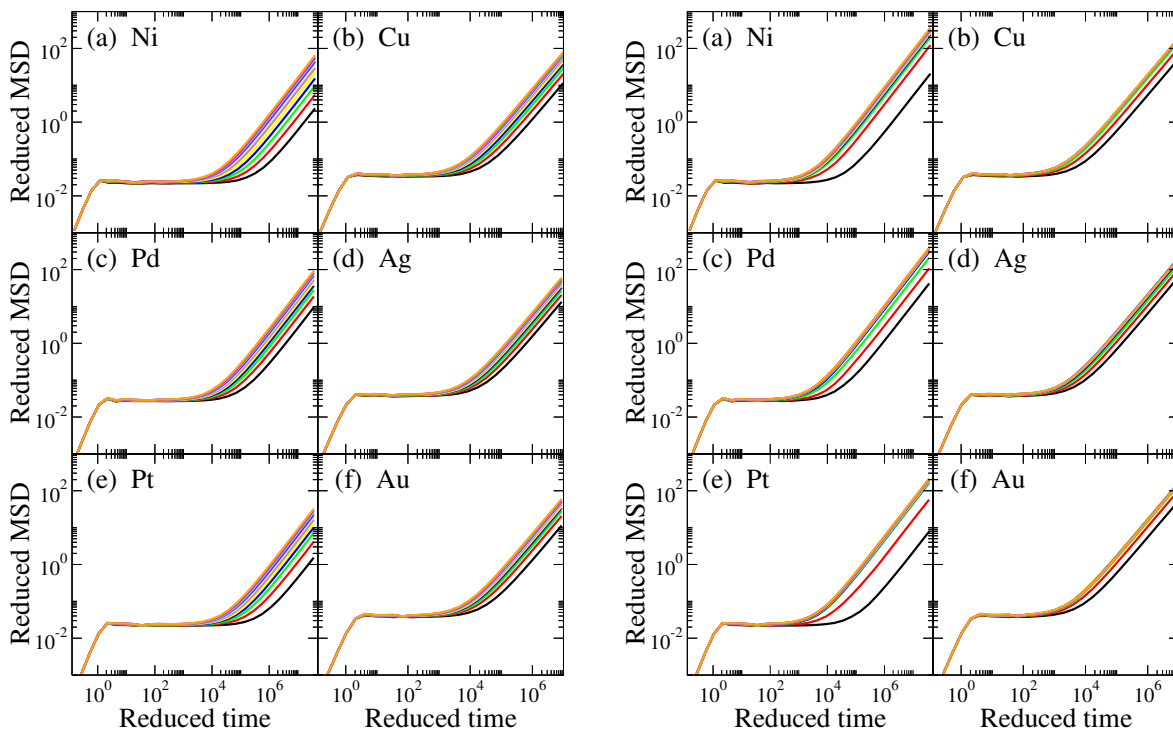


Figure 5.10: MSD of the six EMT metals with one (left) and four (right) vacancies in the crystal. To obtain the vacancies, one respective four randomly selected particles have been removed from the crystal configurations. The MSDs collapse nicely in the ballistic part and on the plateau. While collapse in the ballistic regime is a trivial consequence of using reduced units, the invariance of the height and onset of the plateau is not trivial and follows from R-simplicity. The invariance of the diffusive part is poorer than for the Lennard-Jones crystals of Ref. [22]. This can be partly attributed to the fact that the starting point is closer (in density) to the triple point. The figures also appeared in Ref. [39].

vacancies, leading to slightly different temperatures. To put the number of vacancies into perspective, four vacancies in a 4000 atom cube of Au corresponds to a vacancy concentration of  $10^{-3}$ . In experimental Au close to melting, the concentration is only slightly lower, at  $7 \times 10^{-4}$  [110].

The MSDs can be separated into three distinct phases, the ballistic regime, the plateau and the diffusive part. The collapse of the diffusive part is noticeable poorer than in the other two parts. However, only the collapse of the height and onset of the plateau is non-trivial and somewhat validates isomorph invariance of the vibrational dynamics. The collapse in the ballistic regime is simply a consequence of the fact that using reduced units re-expresses this part of the MSD as proportional to time squared.

The failure of collapse in the diffusive part for the case of one vacancy (left panel of Fig. 5.10) is consistent with Albrechtsen and Olsen's findings for LJ crystals with only one vacancy [111]. This is possibly due to the fact that the relevant energies of a configuration where an atom is in the middle of the vacancy hopping process scales differently than energies of a perfect crystal. For details, see discussion section of Ref. [39].

While poorer than the collapse seen in Ref. [22] for the case of four vacancies (right panel of Fig. 5.10), the collapse is better compared to the one vacancy case. This is especially the case for the higher density/temperature points of the isomorph, thus when disregarding the two lowest density/temperature points along the isomorph (black and red lines in every panel). This outlier behaviour is common in all six metals and particularly pronounced in the panels on the left hand side of the figure, namely Ni, Pd and Pt. These three metals have incomplete d-shells which corresponds to stronger bonding and having a higher melting point. Given that all isomorphs were started from the same temperature, this means that the three left hand metals are further below their respective melting lines.

Overall we find a very similar level of collapse among all six EMT metals. Also the state point dependence of  $\gamma$  shows a qualitative similar behaviour and looks like the curves can somehow be scaled onto each other. There is however also no a priori prescription of how such a scaling should look like and in terms of which quantities the scaling should be done. With the exception of Ag and Au, the  $\gamma$  values for the remaining four metals do in fact already almost follow the same curve.

## 5.2 Liquid CuZr

Metallic systems are a very important category of glass former due to their possible applications in material science as well as their suitability as a model system to study the glass transformation in simulations. As a natural extension of the study of invariance of structure and dynamics in mono-atomic crystals, the next interesting possible application of isomorph theory are compound systems. The results shown in this section were presented on a poster in 2019 at the *XV International Workshop on Complex Systems* in Andalo. A reprint of the poster can be found in Appendix D. A paper to publish the results is planned but not written.

This chapter studies different compositions of the well-known binary glass former CuZr in the context of isomorph theory using the different compositions  $\text{Cu}_x\text{Zr}_{100-x}$  ( $x = 64, 50, 36$ ). The experimental phase diagram for CuZr with respect to different proportions of Zr content is shown in Figure 5.11. The figure shows that the liquidus temperature (the lowest temperature at which a material is completely liquid) varies by a few hundred degrees depending on the composition. Since this work is focused on studying isomorphs in the liquid regime, the simulations were carried out well into the liquid part of the phase diagram. Furthermore, the phase diagram shown is at ambient pressure while our study will be conducted at a higher pressure to ensure a non-negative virial, i.e. avoiding a starting point where isomorph theory does not work since the system is not dense enough. Therefore, the low temperature starting

| Material | $s_0$ (Å) | $E_0$ (eV) | $\lambda$ (Å <sup>-1</sup> ) | $\kappa$ (Å <sup>-1</sup> ) | $V_0$ (eV) | $n_0$ (Å <sup>-3</sup> ) | $n_2$ (Å <sup>-1</sup> ) |
|----------|-----------|------------|------------------------------|-----------------------------|------------|--------------------------|--------------------------|
| Cu       | 1.41      | -3.51      | 3.693                        | 4.943                       | 1.993      | 0.0637                   | 3.039                    |
| Zr       | 1.78      | -6.30      | 2.247                        | 3.911                       | 2.32       | 0.031                    | 2.282                    |

Table 5.2: EMT parameters for the CuZr alloy. The parameters were taken from Ref. [113]

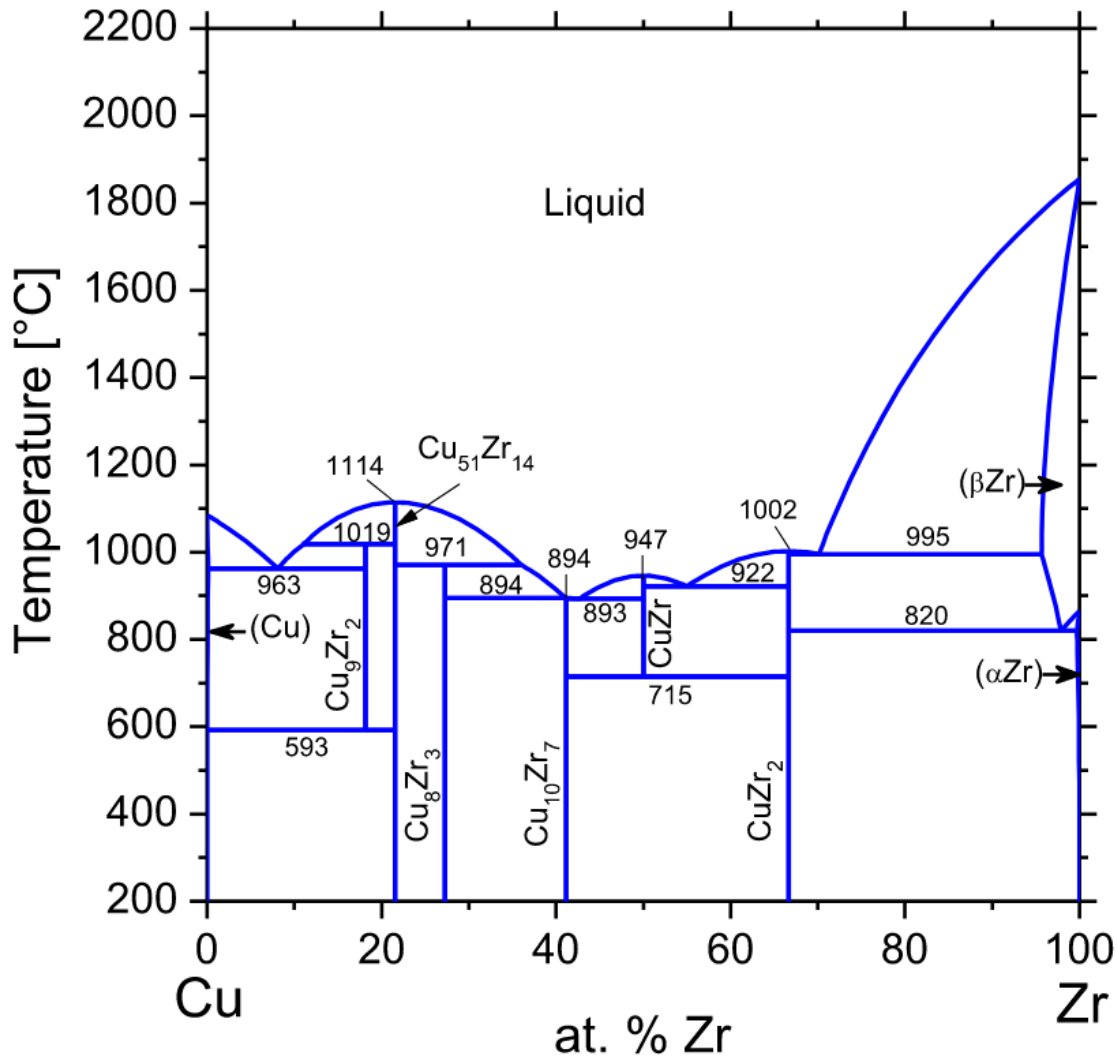


Figure 5.11: Part of the phase diagram of CuZr at different compositions in terms of the Zr content. Figure taken from Ref. [112]

points for the isomorphs were chosen to be at 1500K, fairly far above the freezing temperature for all compositions (see Fig. 5.11). Additionally, the start point density for each composition was adjusted so that the pressure is roughly the same, around 17 GPa.

From the start point, isomorphs were traced out using the DIC. Ten state points were determined for each composition, in steps of 10% of the initial density up to a total density change of 100%. Subsequently, a simulation was carried out at each of the obtained state points. All simulations were carried out in RUMD [102] using the NVT ensemble with a total of 1000 particles. The initial configurations were constructed in RUMD, starting from a simple cubic crystal with randomly assigned particle types according to the given ratio that was subsequently melted. The runs consist of  $10^4$  MD steps of equilibration followed by  $10^6$  MD steps of production run with a time step of 0.5 in RUMD simulation units<sup>1</sup>. Pressure, density

<sup>1</sup>RUMD units are derived from Å, eV and atomic mass units.

| $T$ [K] | $\rho$ [ $\frac{0.01}{\text{\AA}^3}$ ] | $P$ [GPa] | $T$ [K] | $\rho$ [ $\frac{0.01}{\text{\AA}^3}$ ] | $P$ [GPa] | $T$ [K] | $\rho$ [ $\frac{0.01}{\text{\AA}^3}$ ] | $P$ [GPa] |
|---------|--|-----------|---------|--|-----------|---------|--|-----------|
| 1500    | 5.85                                   | 17.2      | 1500    | 6.40                                   | 17.2      | 1500    | 7.00                                   | 17.1      |
| 1745    | 6.14                                   | 24.6      | 1747    | 6.72                                   | 25.2      | 1749    | 7.35                                   | 25.6      |
| 1999    | 6.45                                   | 33.2      | 2005    | 7.06                                   | 34.5      | 2009    | 7.72                                   | 35.7      |
| 2266    | 6.77                                   | 43.2      | 2274    | 7.41                                   | 45.4      | 2283    | 8.10                                   | 47.6      |
| 2540    | 7.11                                   | 54.8      | 2555    | 7.78                                   | 58.0      | 2568    | 8.51                                   | 61.3      |
| 2828    | 7.47                                   | 68.0      | 2850    | 8.17                                   | 72.5      | 2867    | 8.93                                   | 77.3      |
| 3122    | 7.84                                   | 83.0      | 3151    | 8.58                                   | 89.2      | 3177    | 9.38                                   | 95.6      |
| 3428    | 8.23                                   | 100.1     | 3464    | 9.01                                   | 108.1     | 3499    | 9.85                                   | 116.6     |
| 3746    | 8.64                                   | 119.5     | 3795    | 9.46                                   | 129.7     | 3834    | 10.34                                  | 140.7     |
| 4070    | 9.08                                   | 141.3     | 4128    | 9.93                                   | 154.2     | 4179    | 10.86                                  | 168.0     |
| 4404    | 9.53                                   | 165.8     | 4473    | 10.42                                  | 181.8     | 4533    | 11.40                                  | 199.0     |

Table 5.3: Values for temperature, number density and pressure along the isomorphs. The vertical lines divide the compositions shown in the following order:  $\text{Cu}_{36}\text{Zr}_{64}$ ,  $\text{Cu}_{50}\text{Zr}_{50}$ ,  $\text{Cu}_{64}\text{Zr}_{36}$

and temperature for each of the isomorph state points simulated are given in Table 5.3. Note that in addition to the density that changes by a factor of two along the isomorph by construction, there is also a significant range of temperature and pressure along the isomorph. The final temperature is roughly a factor three, the final pressure a factor of ten larger than their counterparts at the starting state point.

Like the previous section, this investigation focuses on the existence and quality of isomorphs, employing the EMT potential to simulate the metallic interactions (for details see section 4.3 or [51]). The parameters for the CuZr EMT potential are listed in Table 5.2. Note that some of the parameters for Cu as part of a compound differ from the parameters for pure Cu. This is because the potential including the Cu parameters was re-fitted to better match mixtures of Cu and Zr.

The structure is quantified using the RDF and dynamics is studied by means of the intermediate scattering function and the mean squared displacement plotted in reduced units. For a binary system, three different RDFs can be calculated, two between the two types of particles with other particles of the same type and a third between opposite types. Figure 5.12 shows all three types of RDF for each of the three compositions. Each panel includes eleven RDFs, one for each of the state points listed in Table 5.3 (with the black line corresponding to the lowest density/temperature state point and orange to the highest). All lines collapse reasonably well on top of each other. To evaluate the quality of the collapse, recall that the isomorphs in all three compositions includes a density change of a factor of two which corresponds to about a factor of three in temperature and a factor of ten in pressure change (see Table 5.3). The collapse seen here is comparable to what is typically observed in Lennard-Jones systems [16], even though most Lennard-Jones studies do not cover an isomorph with a similarly large density range. A counter example to this statement however can be found in Ref. [114] which shows a collapse of similar quality for the Lennard-Jones system but with a much larger change in density of roughly a factor of ten.

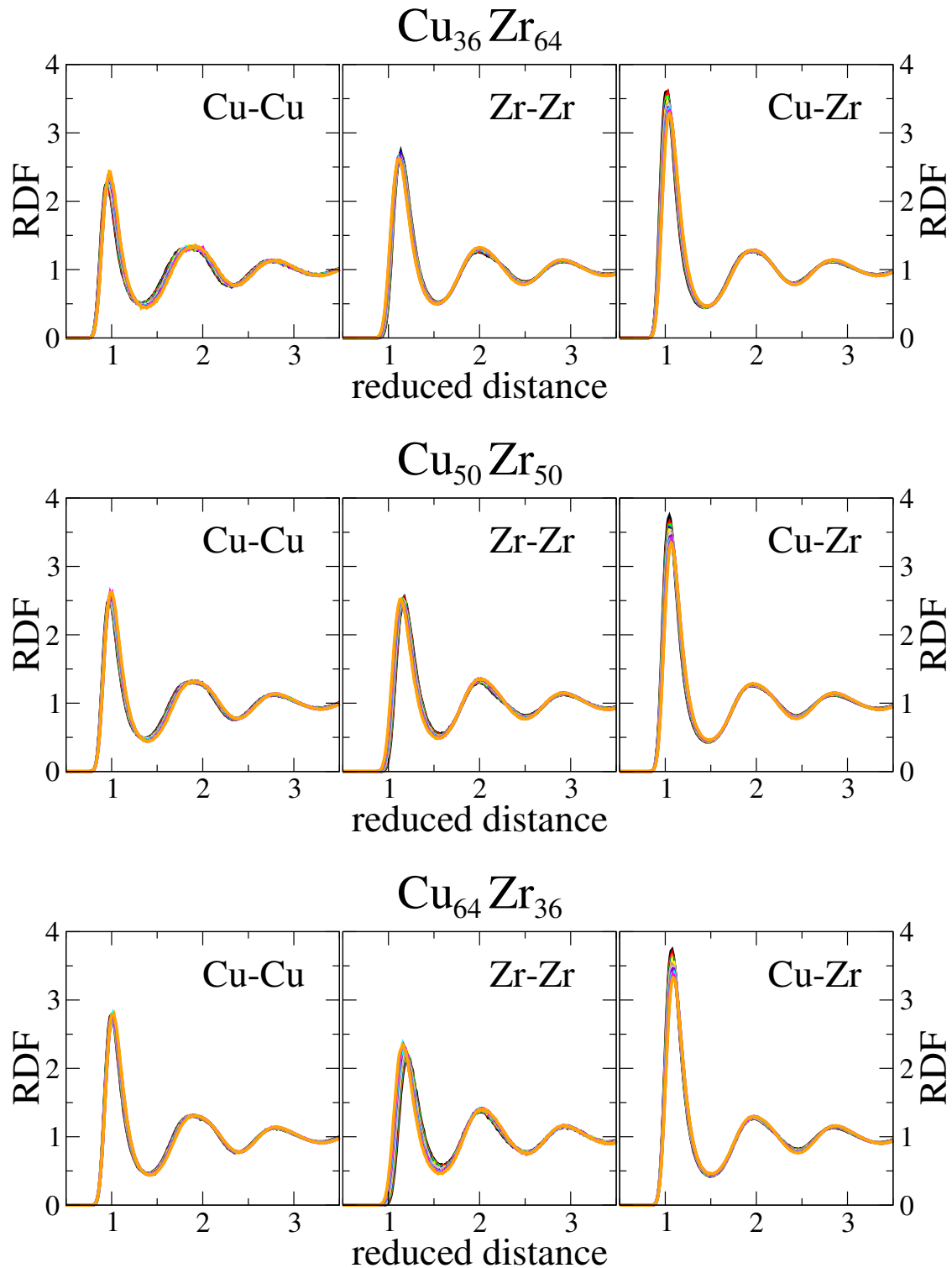


Figure 5.12: The three panels, from left to right, show the radial distribution function between same type particles, namely Cu-Cu, Zr-Zr and between opposite particle types. Each row corresponds to one composition as noted at the top of each row. Each graph shows 11 curves with each curve corresponding to one of the state points given in Table 5.3 where the orange curve on top corresponds to the state point highest in density, temperature and pressure.

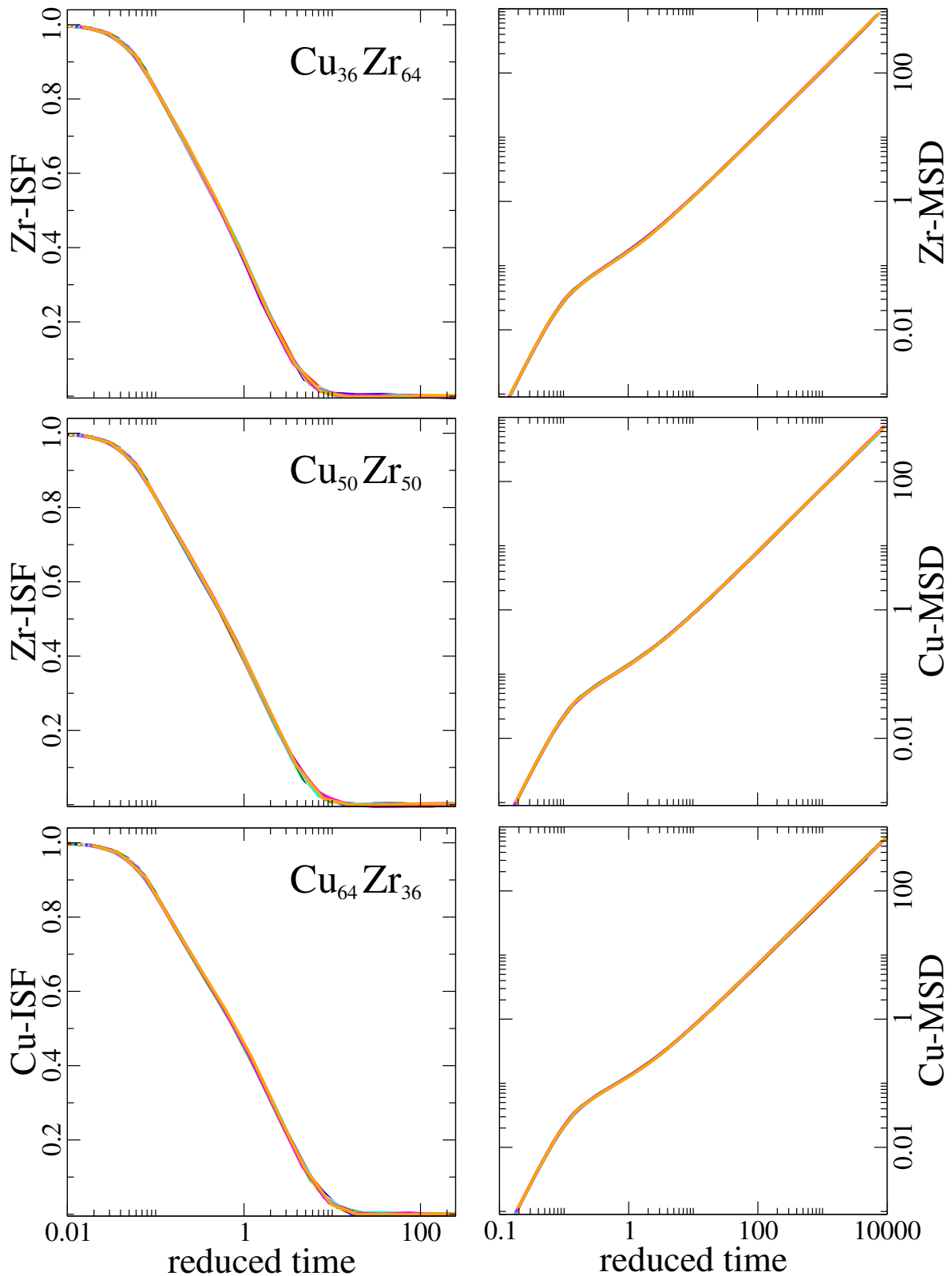


Figure 5.13: Each row shows the intermediate scattering function (ISF) on the left and the mean squared displacement (MSD) on the right for the composition indicated in the left panel of the row. The first row and the first panel in the second row, i.e. the first three panels in reading direction, show data for the Zr atoms and the other half shows the Cu atoms as indicated by the Cu- and Zr- before MSD and ISF on the y-axis.

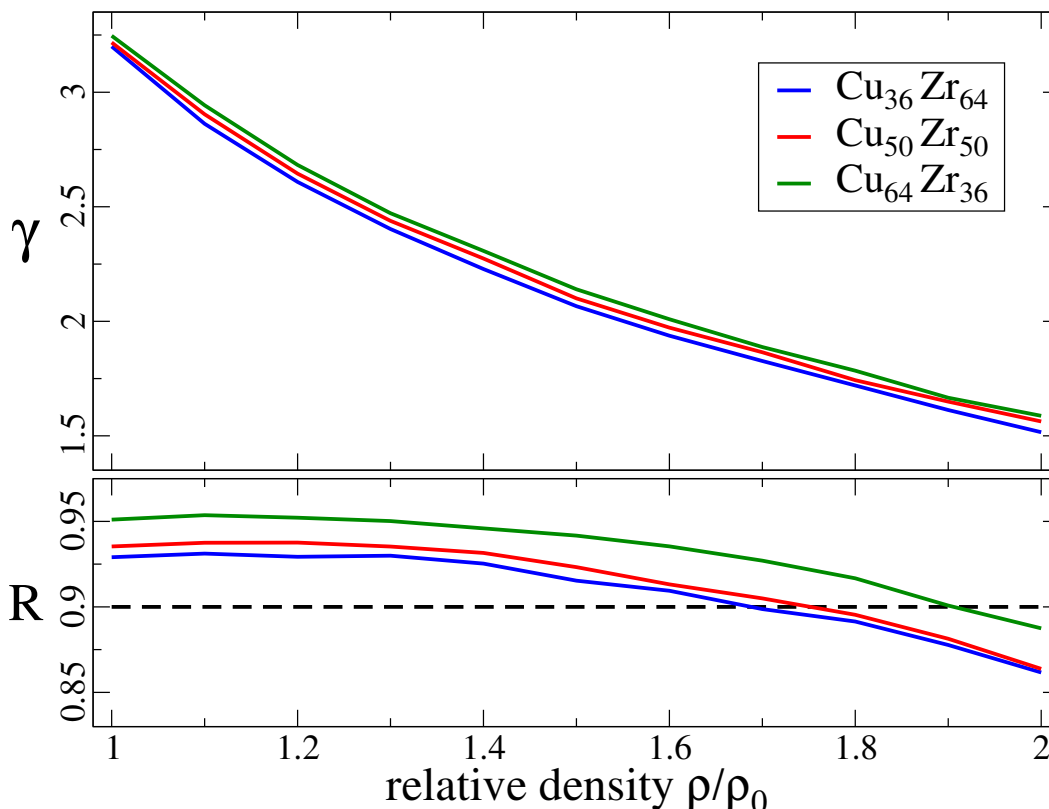


Figure 5.14: The scaling exponent  $\gamma$  and correlation coefficient  $R$  along the isomorphs. Different colors correspond to the three different compositions. The black dashed line in the lower panel indicates the  $R > 0.9$  criterion.

Small systematic deviations can be seen at the first peak of the opposite type RDFs, with the peak height decreasing for state points at higher temperature and pressure. Other panels that exhibit some deviations are the Zr-Zr RDF of the  $\text{Cu}_{64}\text{Zr}_{36}$  and the Cu-Cu RDF of the  $\text{Cu}_{36}\text{Zr}_{64}$ . This means that the minority element with itself as well as the opposite particle RDFs do not exhibit a collapse as good as the majority element with itself. A similar behaviour can be seen in a Kob-Anderson binary Lennard-Jones mixture. In this system the majority particles are A type particles and the minority are B type particles. Also this system exhibits a good collapse in all compositions, but the collapse among AA particle curves is better than for the AB and BB curves (seen e.g. in Fig. 2 of [16]). Thus the behaviour agrees well with our CuZr results down to where the deviations occur, i.e. also the AB RDFs deviate strongest around the first maximum just like the Cu-Zr RDFs, while the BB and minority element curves deviate slightly but in an overall fashion.

The dynamic observables are single-particle quantities, thus only one for each type can be calculated and there is no cross term. Additionally, the quality of the collapse between the Cu and Zr ISF or MSD is so identical, that only one ISF and MSD for each composition is shown. Figure 5.13 shows the results, the MSD on the left and the ISF on the right of each row. Each row corresponds to one composition. All curves collapse nearly perfectly onto each other and the overall quality of the collapse is much better than for the structure. The good collapse of

dynamics is consistent with a recent study of excess entropy scaling [115] that investigated some isomorph-type aspects of dynamic properties in different binary system including EMT CuZr.

All in all the DIC seems to have determined a good isomorph. One could speculate if a better determined isomorph, i.e. using a step-wise method would have located the isomorph even better. This could have resulted in a better collapse of the structure. But presumably it would have also resulted in a slightly less good collapse for the dynamics. This is however only a speculation based on the fact that most isomorphs located using the step-wise method exhibit a better collapse for the structure than for the dynamics and we see the opposite here. It needs to be mentioned though, that recent results suggest that CuZr is not the only case where a better collapse for dynamics than for structure is observed.<sup>2</sup>

Compared to the mono atomic crystals from the previous section, we find a similar level of collapse among the RDFs. The dynamics cannot be compared directly as different quantities were considered. However, there is no reason to believe that the invariance of dynamics should be better in one particular quantity than another. Therefore, it can still be noted that the collapse of the CuZr data is much better than it was the case for the VACF of the mono atomic crystals. Noteworthy is also the fact, that the different compositions do not seem to influence the quality of the collapse at all.

The scaling exponent  $\gamma$  and the correlation coefficient  $R$  along the isomorphs are shown in Figure 5.14 with different colors corresponding to the different compositions. The dashed black line indicates the  $R = 0.9$  criterion. While the correlation coefficient is typically lower in a liquid than in solid,  $R$  drops very low with the last two or three state points at the high pressure/temperature end of the isomorphs. This is perhaps surprising given the extremely good collapse that would suggest a higher degree of correlation. It should be mentioned that the  $R = 0.9$  criterion was chosen arbitrarily as a convenient way to quantify what *strong* means in the context of strong correlations between  $W$  and  $U$ . Good isomorphs are expected in the limit of perfect correlations, where  $R \rightarrow 1$ . So  $R > 0.9$  was chosen as a good guess of where to expect the collapse of isomorph invariant quantities to deteriorate but the value is not motivated in a rigorous way. Thus the  $R > 0.9$  criterion should not actually be regarded as a one size fits all and the actual  $R$  criterion indicating a good collapse can be higher or lower depending on the system in question. It can be concluded that CuZr - independent of composition - supports this view.

The overall behaviour of  $R$  is typical for metals and similar to the behaviour seen for the EMT mono-atomic crystals, going down density increases. Also the behaviour of  $\gamma$  is similar. Just like in the case of the mono atomic crystals,  $\gamma$  decreases with increasing pressure and temperature along the isomorphs. What is interesting is how close the values of  $\gamma$  are among the three compositions. One of the research questions to consider regarding isomorph theory in compound systems was how the combination of two elements with different  $\gamma$  influences the resulting  $\gamma$ . According to the periodic table of isomorph theory (Fig. 1.4) the values for  $\gamma$

---

<sup>2</sup>At the time of writing no published results are available to support this statement. This is based on internal sharing of ongoing work.

at the triple point of Cu and Zr are 4.1 and 2.2 respectively. This could suggest that the Zr heavy composition should have a smaller  $\gamma$ , i.e. a value closer to the value of pure Zr, and similarly a higher value for the Cu heavy composition. This is indeed reflected in the tendency the  $\gamma$ 's in Fig. 5.14 exhibit, although the difference is somewhat unexpectedly small.

### 5.3 DFT metals

The large scale study using *ab-initio* simulations [29] that resulted in the periodic table of isomorph theory suggests that most metals have isomorphs at least in the vicinity of their triple point. In this last section we will explore the hidden scale invariance along isomorphs in two metals simulated using DFT. The candidate metals for this study are Al and Mg. This time a state point at solid-liquid coexistence is chosen as the reference point. From this state point two isomorphs, one solid and one liquid, are generated. For comparison, also some points along an isotherm and isochore in each phase are included as well.

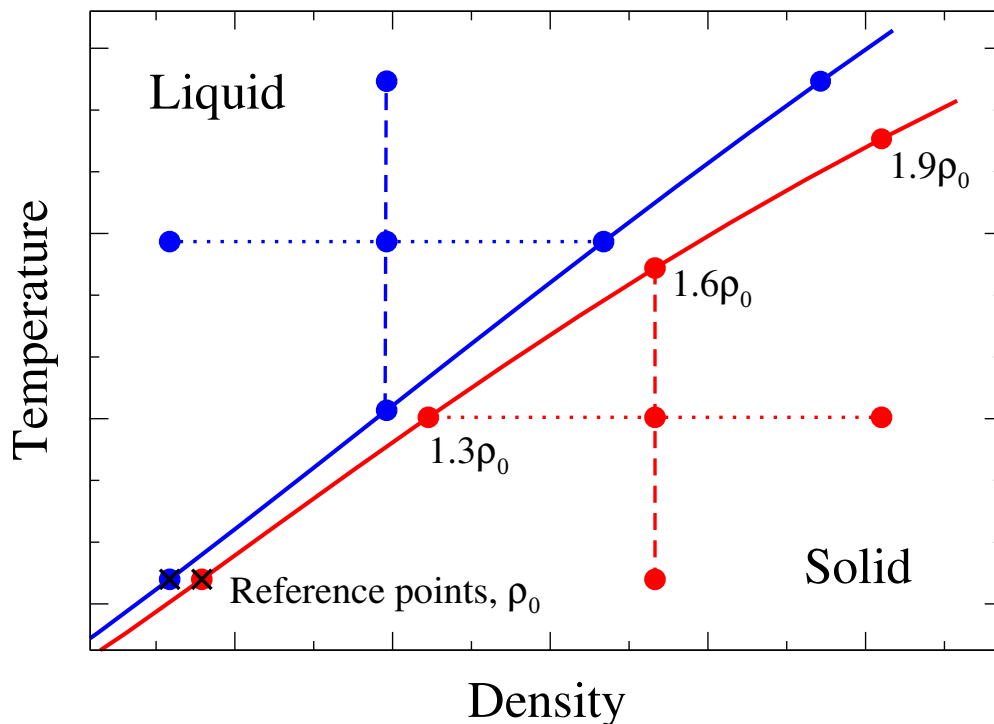


Figure 5.15: Sketch of the relevant part of the phase diagram marking all points of interest. The solid lines denote isomorphs generated from the reference point marked by an x. Additional simulations were carried out at the state points marked by filled circles. Liquid state points are blue and solid state points are in red. State points along the isomorphs are labeled according to the relative change with respect to the reference point density. The points connected by the dotted (dashed) line are on the same isotherm (isochore).

A sketch of the phase diagram is shown in Figure 5.15. The lines represent the isomorphs found from applying the DIC to data from a simulation at the reference points marked by the

x. The other points noted in the figure correspond to state points where additional simulations have been carried out. Including the reference points, this means a total of four isomorph state points and three state points that are isothermal or isochoric to state points along the isomorph for each phase were simulated. Isomorph state points are referred to by their label according to the change in density relative to the reference point as denoted in the figure.

The simulations were carried out in VASP, using only the  $\Gamma$  point to sample the reciprocal space. The initial choice for the energy cutoff for the plane-waves is discussed in appendix B.3. In order to avoid discontinuities, the number of plane waves is kept constant, which means that for the density changes of the DIC, the energy cutoff is scaled as

$$E_{\text{cut}}(\rho) = E_{\text{cut}}(\rho_i) \left( \frac{\rho}{\rho_i} \right)^{1/3} \quad (5.8)$$

where  $\rho_i$  and  $E_{\text{cut}}(\rho_i)$  are the initial density and the energy cutoff chosen for that density. Some more technical details are discussed in the next chapter. Each simulation run includes 50000 steps with a time step of 2 fs. For the DIC, every 100th frame sampled from the last 30000 steps is used in the scaling procedure<sup>3</sup>. The new density is obtained from scaling the initial density by factors (0.8, 0.9, 1.1, 1.2, ...1.9, 2.0). While the DIC can also determine thermodynamic average quantities at the scaled points, data describing structure and dynamics is not available. The radial distribution functions would be invariant by construction if calculated from the scaled configurations. The thermodynamic average quantities however, can be determined from the static calculation carried out for each scaled configuration which actually evaluate pressure and energies at the given state point and thus include non-trivial information about how energy and pressure vary along the isomorph. To obtain data to evaluate structure and dynamics, selected points at the relative density changes of (1.3, 1.6, 1.9) are simulated at the temperature predicted for the given density from the DIC. Again the simulations consist of 50000 steps with a time step of 2 fs. The last 20000 steps of the resulting simulation data is then used to calculate the radial distribution and velocity auto-correlation functions. Unlike in RUMD, these quantities are not readily available from VASP and need to be calculated manually.

Both candidate metals, Al and Mg, have relatively empty outer shells, containing only 3 and 2 electrons, respectively. This enables an efficient simulation using a frozen core type pseudo potential. This means that only the outer shell electrons are treated explicitly while the inner electrons are considered *frozen*. For both metals, the PBE frozen core pseudo potential is used.

The simulation box for Al contains 108 atoms for each phase. The number is determined by the crystal phase having an FCC structure which gives 108 atoms for a crystal size of  $3 \times 3 \times 3$  unit cells. Recall that a self consistent check of the DIC was derived in Chapter 2. For this

---

<sup>3</sup>The scaling procedure was initially, erroneously carried out on every 10th frame over the range of frame number 2000 to 5000. Both have been carried out correctly after the error was discovered, but there was not enough time to rerun all simulations at the corrected state points. The temperatures found for Al differ by 1% or less between the correct and the wrong interval and were therefore not rerun. The results for Mg are from rerun simulation at the correct state points.

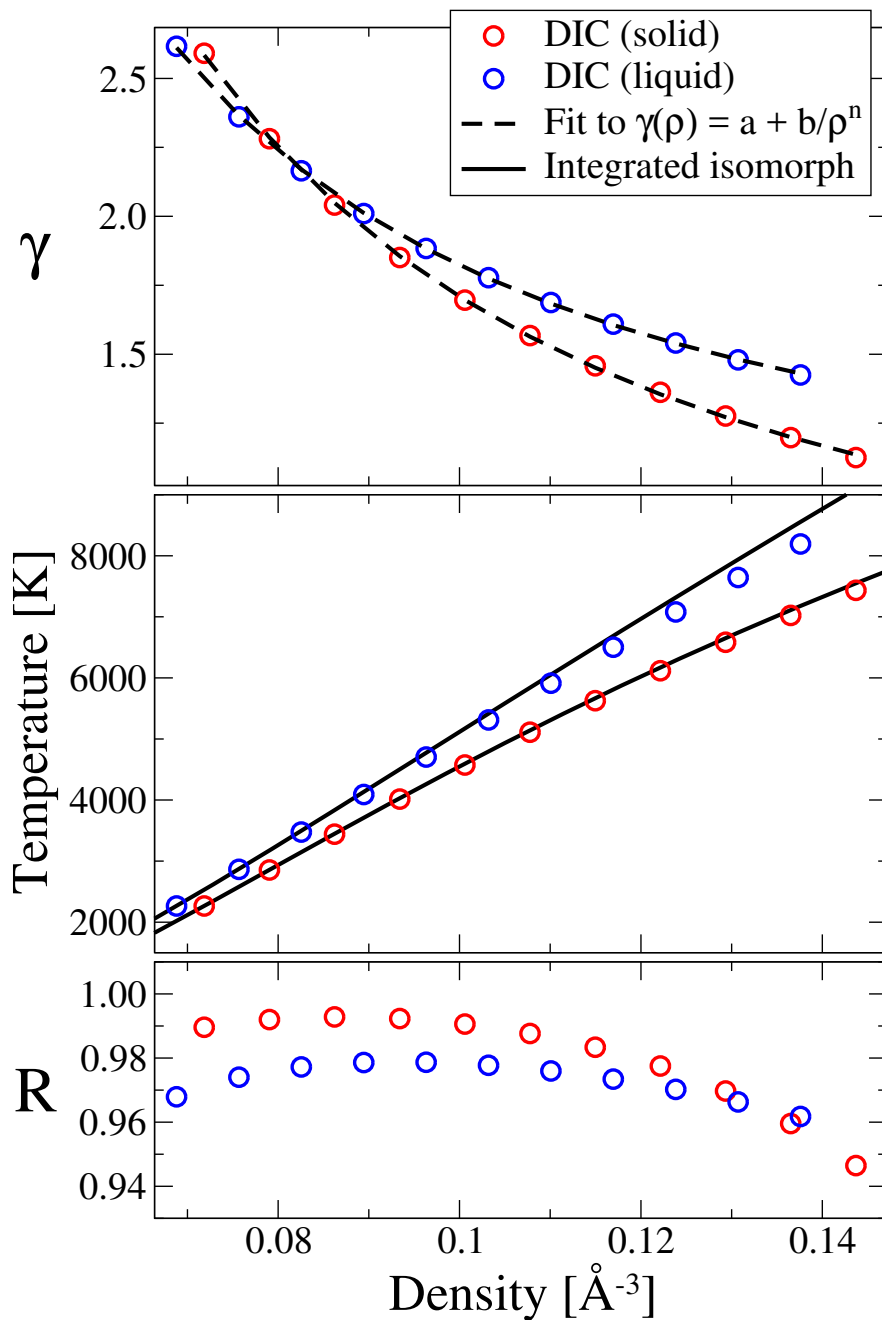


Figure 5.16: DIC self consistency check for Al. Open circles represent data for the isomorphs from DIC, red for the solid and blue for the liquid. The dashed line in the top panel was obtained from fitting to the DIC point. The parameter for the fitted expression for  $\gamma(\rho)$  are:  $a = 0.342247, b = 0.0433792, n = 1.49827$  for the solid and  $a = 0.818062, b = 0.0282633, n = 1.55063$  for the liquid isomorph. The resulting integrated isomorph is given by the solid line in the middle panel. The bottom panel shows the correlation coefficient for both isomorphs obtained from the DIC.

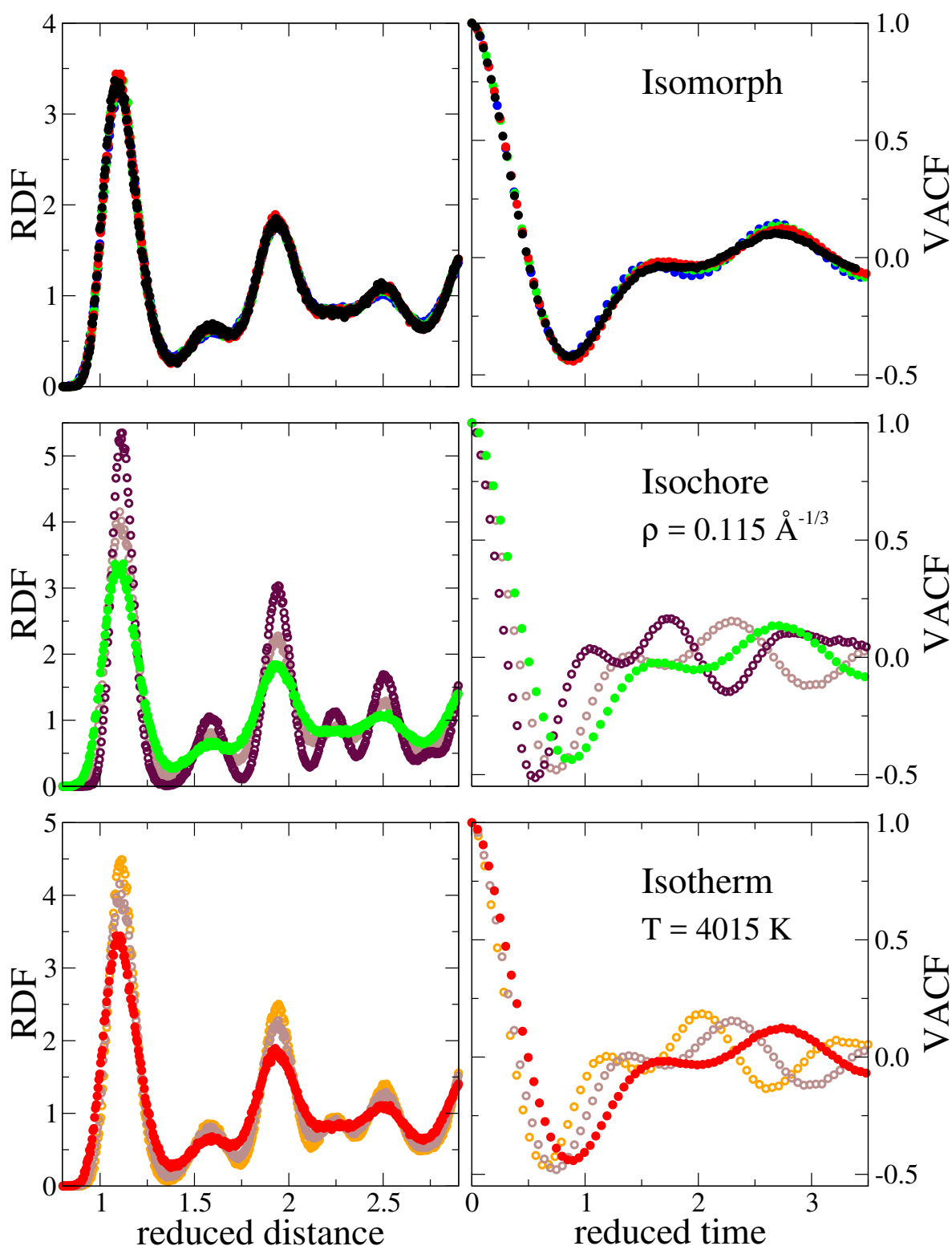


Figure 5.17: RDF and VACF along iso-lines in the solid side of the phase diagram of Al. Each panel shows the RDF on the left and VACF on the right for the same state points (Values are given in Table 5.4). The state points for the top row are along the same isomorph. State points shown in the middle and bottom panel are along an isochore and isotherm, respectively.

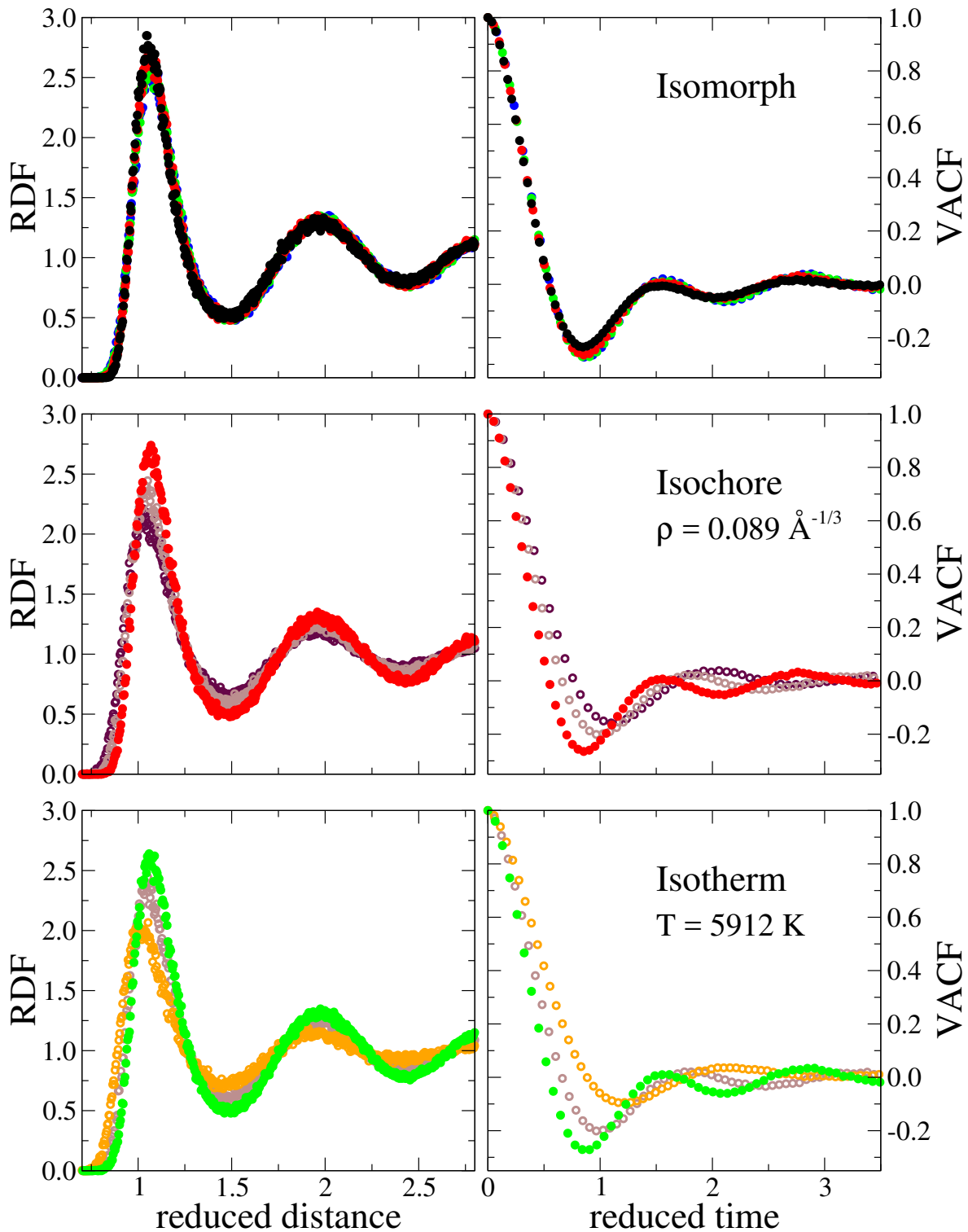


Figure 5.18: RDF and VACF along iso-lines in the liquid side of the Al phase diagram, similar to the presentation of the solid side in Figure 5.17. Each panel shows the RDF on the left and VACF on the right for the same state points. The state points for the top row are along the same isomorph. A legend is provided in Table 5.4. State points shown in the middle and bottom panel are along an isochore and isotherm, respectively.

check, the values of  $\gamma$  obtained from the DIC are fitted by  $\gamma(\rho) = a + b/\rho^n$ . The expression is then used to integrate the differential expression for state points along an isomorph;

$$\gamma(\rho, T) = \left( \frac{\partial \ln T}{\partial \ln \rho} \right)_{S_{ex}} .$$

Such a check has been carried out on the data obtained for Al and is present in Figure 5.16. The open circles in the top panel show  $\gamma$  from DIC data with the dashed lines given by the fit to them. The parameters for the fit are given in the figure caption. The middle panel shows the integrated expression for isomorph state points together with the state points obtained from the DIC. Since the DIC is not exact, and the reference point for the DIC and also the fitting is the lowest density and temperature state point, some small deviations between the fitted and the DIC state points can be expected at the high density and temperature end. In the example used for the deviation in Chapter 2 also a step-wise generated isomorph was available for comparison. We have seen there that the step-wise generated isomorph, which should be considered the most exact method, predicted points nearly identical to the DIC, with the consistency check being slightly off far away from the reference point. A step-wise isomorph for direct comparison is out of question when using DFT. But the deviation between the consistency check and the DIC points is similar to the example case from Ch. 2. This suggests that good isomorph invariance can be expected (we will see in the case of Mg that this check does not work as well, and the isomorphs there are not good). The same is suggested by the  $R$  values pictured in the lowest panel of Figure 5.16. The correlation coefficient is well above  $R = 0.9$  and shows the same behaviour as the other metallic systems studied in this work (see e.g. Fig. 5.14) of decreasing slightly as density and temperature increase. The similarity in the behaviour of  $\gamma$  and  $R$  between DFT and EMT is interesting and provides further evidence that the EMT potential, although simple compared to other many-body potentials, gives a good description of metallic interactions.

While the check gives a fair indication of good isomorphs, the most direct way to check for isomorph invariance is of course to look at structure and dynamics directly. For convenience, structure and dynamics of both phases are studied using the same functions: by means of RDF and VACF. As mentioned before, additional simulations at the state points from the DIC have only been carried out at the selected state points noted in Figure 5.15. This is done as an attempt of covering a similar range along the isomorph as for the EMT materials but keeping the computational cost associated with DFT somewhat in check. The resulting RDFs and VACFs along iso-lines are shown in Figure 5.17 for the solid side of the phase diagram and in Figure 5.18 for the liquid side. Table 5.4 serves as a legend to the Figures and gives pressure, temperature and densities of the state points that were simulated. The table also includes the  $\gamma$  and  $R$  values both as predicted from the DIC and the values measured after simulation at the given state point.

The first panel of both figures shows the structure and dynamics along the respective isomorphs. For comparison, also structure and dynamics along an isochore and isotherm are included in the middle and bottom panel. Thus, we expect a collapse of the curves shown in the top

panels and not in the other two. This is exactly what can be seen in both figures. While the deviations along the isotherm and isochore especially in the RDF of the liquid side (Fig. 5.18) are relatively small since the density or temperature difference between the state point is also somewhat small, there is a clear difference from the well collapsing RDFs along the isomorph. The difference is even clearer for the VACF, where on the isotherm and isochore the data clearly do not collapse while the VACFs along the isomorph only have small deviations, mostly with regards to the depth of the first minimum. The same can be said about the curves of the solid state points (Fig. 5.17). The RDFs of the solid isomorph collapse very well on top of each other while the VACF deviates slightly, this time especially around the second minimum. Again those deviations are small compared to the significantly varying curves for the state points along isotherm and isochore.

The values for pressure, temperature and density along the isomorphs are given Table 5.4. The table includes also the  $\gamma$  and  $R$  values predicted from the DIC together with the values measured in the simulation. There is good agreement between the predicted and the measured values. This supports the conclusion from the good collapse shown in the figures, that the DIC has in fact predicted good isomorphous state points.

In summary, we find a good collapse of both structure and dynamics along both isomorphs in Al, with a slightly better collapse of structure than for the dynamics. This is the same overall tendency that was seen for the EMT mono atomic crystals where the RDFs overlapped nearly perfectly. Also the slight deviations in the VACF along the solid isomorph show the same behaviour as in the case of the mono atomic EMT crystals, with the deviations starting only after passing through the first minimum.

Together with Al, Mg was studied with regards to how well structure and dynamics collapse along two isomorphs mapped from a reference point at coexistence. Just like for the study

| $\rho/\rho_0$ | Color | $T$ [K] | $P$ [kbar] | $\rho$ [ $\text{\AA}^{-3}$ ] | $\gamma_{DIC}$ | $R_{DIC}$ | $\gamma_{Sim.}$ | $R_{Sim.}$ |
|---------------|-------|---------|------------|------------------------------|----------------|-----------|-----------------|------------|
| 1.0 (l)       | black | 2265    | 278.2      | 0.0688                       |                |           | 2.616           | 0.9679     |
| 1.3           | red   | 4090    | 949.2      | 0.0894                       | 2.010          | 0.9786    | 1.935           | 0.9846     |
| 1.6           | green | 5912    | 1987       | 0.1101                       | 1.687          | 0.9760    | 1.558           | 0.9747     |
| 1.9           | blue  | 7644    | 3405       | 0.1307                       | 1.480          | 0.9663    | 1.338           | 0.9653     |
| 1.0 (s)       | black | 2265    | 276.7      | 0.0714                       |                |           | 2.591           | 0.9896     |
| 1.3           | red   | 4015    | 979.6      | 0.0934                       | 1.851          | 0.9923    | 1.843           | 0.9916     |
| 1.6           | green | 5626    | 2100       | 0.1150                       | 1.458          | 0.9834    | 1.464           | 0.9852     |
| 1.9           | blue  | 7022    | 3653       | 0.1365                       | 1.198          | 0.9596    | 1.169           | 0.9526     |

Table 5.4: Temperature, pressure and density of the state points simulated for Al with the colors corresponding to the color in Figures 5.18 and 5.17. The top half of the table is for the liquid isomorph and the bottom for the solid isomorph. The last four columns give the  $\gamma$  and  $R$  values as predicted from the DIC versus the values measured from simulation.

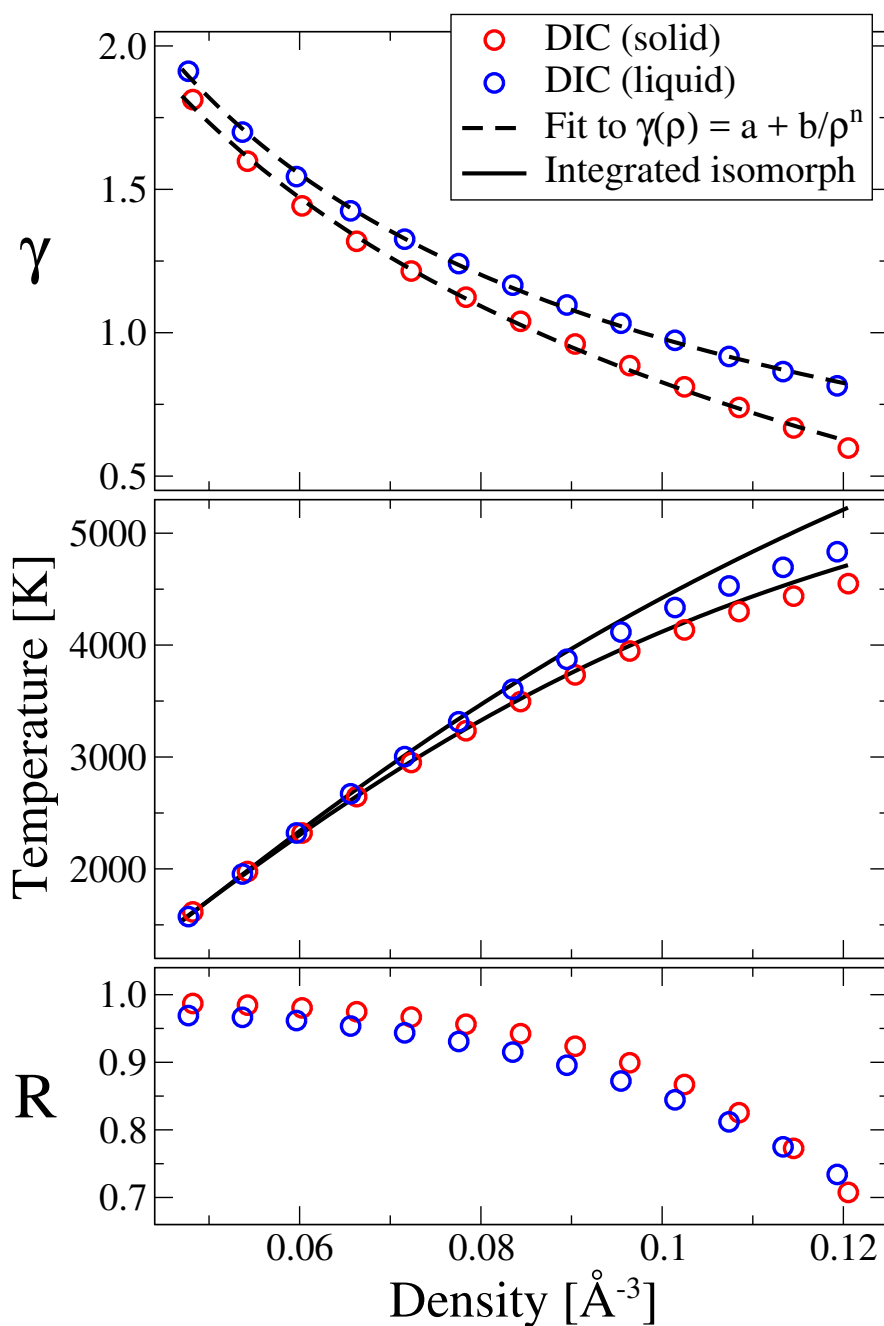


Figure 5.19: DIC self consistency check for Mg. Open circles represent data for the isomorphs from DIC, red for the solid and blue for the liquid. The dashed line in the top panel was obtained from fitting to the DIC points. The parameter for the fitted expression for  $\gamma(\rho)$  are:  $a = -2.16962, b = 1.24669, n = 0.380891$  for the solid and  $a = -0.182162, b = 0.190526, n = 0.785176$  for the liquid isomorph. The resulting integrated isomorph is given by the solid line in the middle panel. The bottom panel shows the correlation coefficient for both isomorphs obtained from the DIC.

of Al, the simplest pseudopotential is used which for Mg means two free electrons. Mg has an HCP crystal structure at low pressures giving a simulation box containing 180 particles in  $(5 \times 3 \times 3)$  unit cells and a liquid box containing the same number of particles. Due to the HCP unit cell not being cubic, also the resulting crystal cell is not exactly cubic. The unit cell ratio was chosen to obtain a simulation box that is at least close to cubic. Additionally there are two pressure related issues that require small changes of the side lengths of the box. Details are given in appendix B.4. The aspect ratio is kept constant in the scaling procedure of the DIC.

Also for Mg a consistency check was carried out and is shown in Figure 5.19. The points represent the state points found from the DIC, red for the solid and blue for the liquid isomorph. The bottom panel shows the correlation coefficient along both isomorphs and drops quite low – reaching 0.77 at the highest density; with the  $R$  values for the solid in particular decreasing steeply about halfway along the isomorph. This suggests that both isomorphs but especially the solid one may not be good isomorphs. The same suggests the middle panel of the figure where the state points are plotted in the  $(\rho, T)$  plane. It looks suspicious that the state points for both phases are so close together. Also the fitting procedure from the consistency check does not fit the data as well as usual.

The RDFs and VACFs along one isotherm, isochore and isomorph in Mg are shown in Figures 5.20 (liquid) and 5.21 (solid). The values for temperature, pressure and density along the isomorphs are given in Table 5.5. Like the  $R$  values and the look of the state points in Figure 5.19 suggested, the isomorph mapped from the solid reference point is not a good isomorph over the whole range. The top panel of Fig. 5.21 shows that only the two lowest state points simulated along the isomorph (black and red) are actually solid and somewhat collapsing onto each other. The higher temperature and pressure state points in green and blue seem liquid judging from their RDF and VACF. Interestingly, the dynamics of the two

| $\rho/\rho_0$ | Color | $T$ [K] | $P$ [kbar] | $\rho$ [ $\text{\AA}^{-3}$ ] | $\gamma_{DIC}$ | $R_{DIC}$ | $\gamma_{Sim.}$ | $R_{Sim.}$ |
|---------------|-------|---------|------------|------------------------------|----------------|-----------|-----------------|------------|
| 1.0 (l)       | black | 2321    | 279.7      | 0.0597                       |                |           | 1.545           | 0.9617     |
| 1.3           | red   | 3315    | 742.8      | 0.0776                       | 1.241          | 0.9308    | 1.147           | 0.9133     |
| 1.6           | green | 4117    | 1422       | 0.0955                       | 1.033          | 0.8722    | 0.823           | 0.8125     |
| 1.9           | blue  | 4695    | 2319       | 0.1134                       | 0.864          | 0.7750    | 0.539           | 0.5684     |
| 1.0 (s)       | black | 2320    | 279.1      | 0.0603                       |                |           | 1.442           | 0.9805     |
| 1.3           | red   | 3234    | 754.1      | 0.0784                       | 1.124          | 0.9563    | 1.037           | 0.9242     |
| 1.6           | green | 3947    | 1455       | 0.0964                       | 0.885          | 0.8992    | 0.786           | 0.7930     |
| 1.9           | blue  | 4437    | 2386       | 0.1145                       | 0.668          | 0.7726    | 0.534           | 0.5594     |

Table 5.5: Temperature, pressure and density of the state points along the liquid (top half) and solid (bottom half) isomorphs in Mg. Again the table serves as a legend and the colors correspond to those in Figures 5.20 and 5.21. The last four columns give the  $\gamma$  and  $R$  values as predicted from the DIC versus the values measured directly in the simulation.

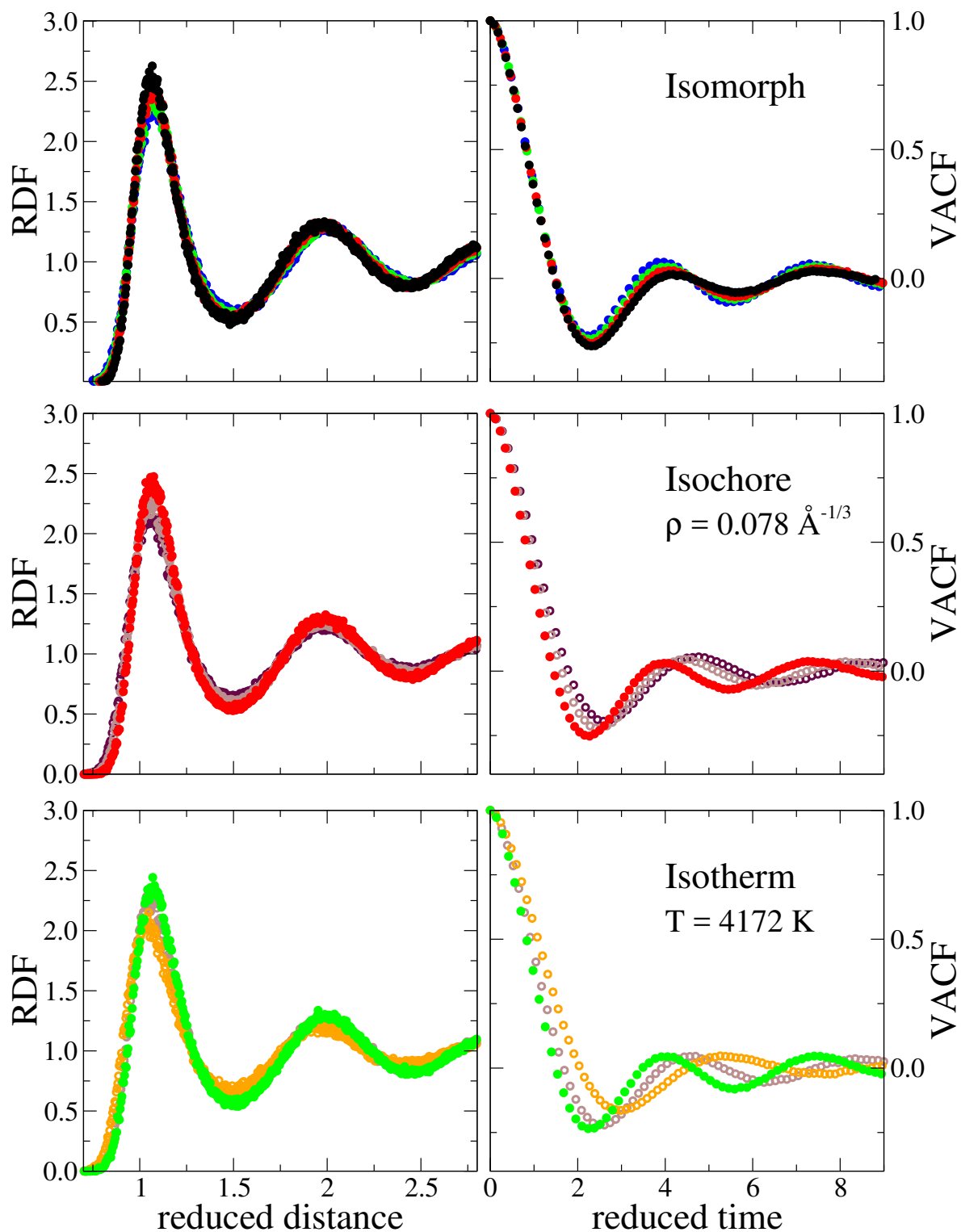


Figure 5.20: RDF and VACF along liquid iso-lines in the Mg phase diagram. Each panel shows the RDF on the left and VACF on the right for the same state points. The state points for each row in the top, middle and bottom panel are along an isomorph, isochore and isotherm, respectively, as indicated in the figure. The state points along the isomorph are given in Table 5.5.

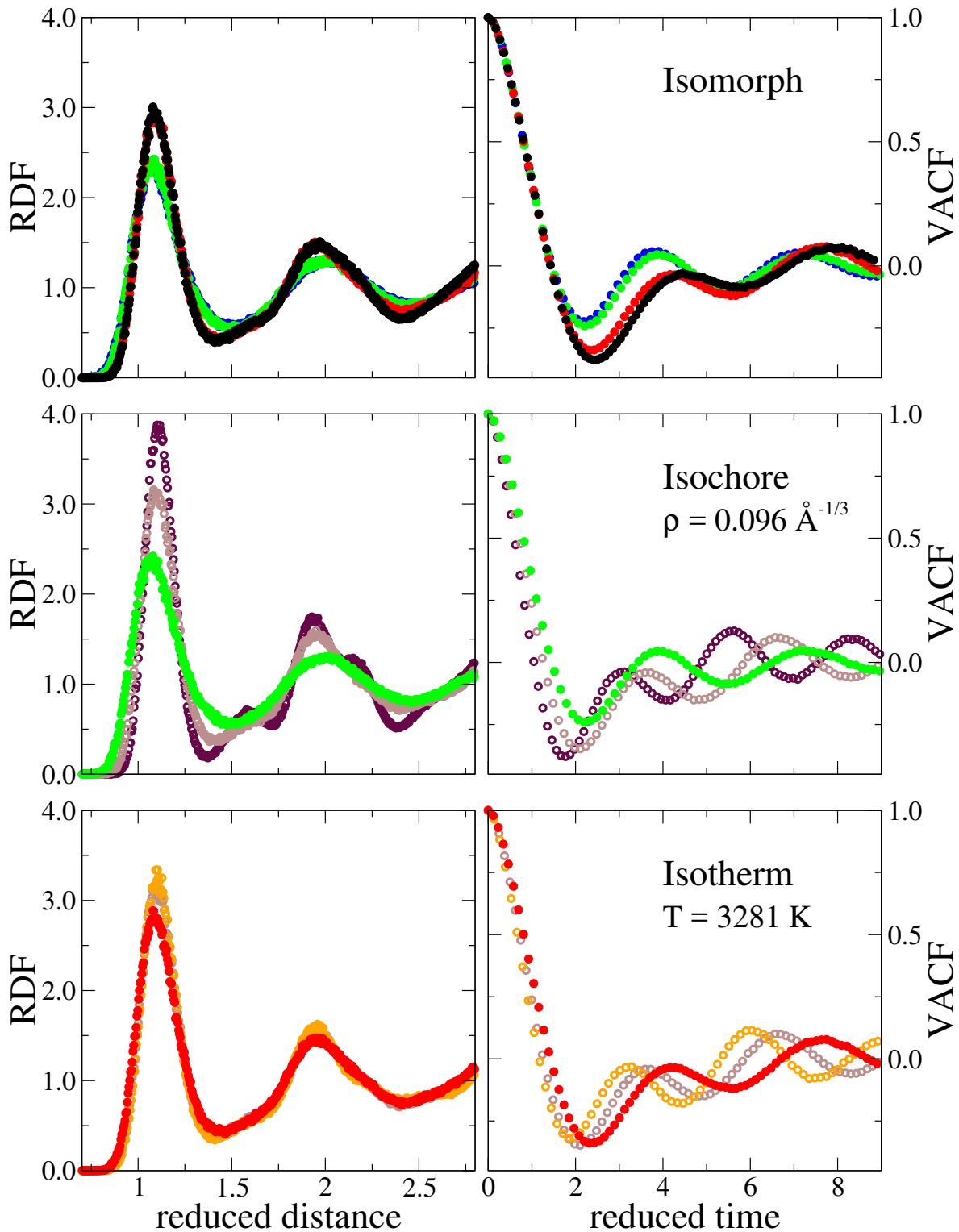


Figure 5.21: RDF and VACF along solid iso-lines in the Mg phase diagram. Each panel shows the RDF on the left and VACF on the right for the same state points. The state points for each row in the top, middle and bottom panel are along an isomorph, isochore and isotherm, respectively, as indicated in the figure. The state points along the isomorph are given in Table 5.5.

liquid state points on the solid isomorph seem to almost collapse better than the points along the liquid isomorphs.

Temperature, pressure and density and a comparison between the  $\gamma$  and  $R$  values predicted from the DIC and the ones measured from simulation is given in Table 5.5. The first thing to notice is how close the densities between the solid and the liquid reference point are. The difference is only about 1%. Unlike in Al, the values of  $\gamma$  and  $R$  as predicted by the DIC do not match the values from the actual simulation as well. Especially the highest pressure/temperature point for both phases, that were already low as predicted from the DIC are even lower in the simulation. This matches the behaviour of structure and dynamics, that high pressure/temperature state points are not on a good isomorph.

What possibly weakens the crystal structure is the fact that the preferred crystal structure of Mg above 500 kbar is BCC rather than the HCP at lower pressures. The starting point for the isomorph here is at 280 kbar, thus initially below the change in structure. The mapped isomorph however ends at a pressure of around 2700 kbar which means the majority of the isomorph is not in the desired structure. Since the HCP crystal structure results in a non-cubic box of only 180 particles, the melting could be the result of the HCP crystal being unstable but unable to reorganize into a BCC structure.

An observation from isomorph theory predicts a cross over  $\gamma$  of 2.5 [29] that marks the change in crystal structure where a larger  $\gamma$  value predicts HCP or FCC structure and lower values suggest that BCC is favoured. The Mg isomorph is already well below the 2.5 cross over value at the reference point and decreases further from there. This would also suggest that the isomorph has the wrong crystal structure. However, also the Al isomorphs are largely below the cross over value (see Tab. 5.4) and show no sign of that causing a problem. The cross over  $\gamma$  was determined at the triple point, thus may simply not be relevant at the high pressures and temperatures considered here.

To check if the problem is the crystal structure, the state point from which the solid isomorph was started, was additionally simulated as a BCC crystal in a cell containing 128 Mg atoms. The resulting RDFs are shown in Figure 5.22 and the associated values for temperature, pressure and density are given in Table 5.6. The obtained temperatures for roughly the same pressure are somewhat higher for the BCC points than for the HCP points, which is consistent with BCC being the more stable crystal structure. The RDFs show the same behaviour as the state points of the HCP isomorph, with the two high temperature/pressure state points becoming liquid. The  $R$  values are slightly higher for the BCC isomorph than for the HCP one but the difference is not large. Additionally, there is a large discrepancy between the DIC prediction and the  $\gamma$  and  $R$  values from the simulations similarly to the discrepancy along the HCP points. This suggests that the BCC isomorph is not a significantly better isomorph candidate.

It is therefore more likely that the problem is the fact that the maximum of the melting curve, the reentrant melting temperature is predicted to be around 3000 K which means that the isomorphs end roughly at the maximum of the melting curve. Assuming that the isomorphs stay relatively close to the melting curve,  $\gamma$  goes to zero around the maximum temperature

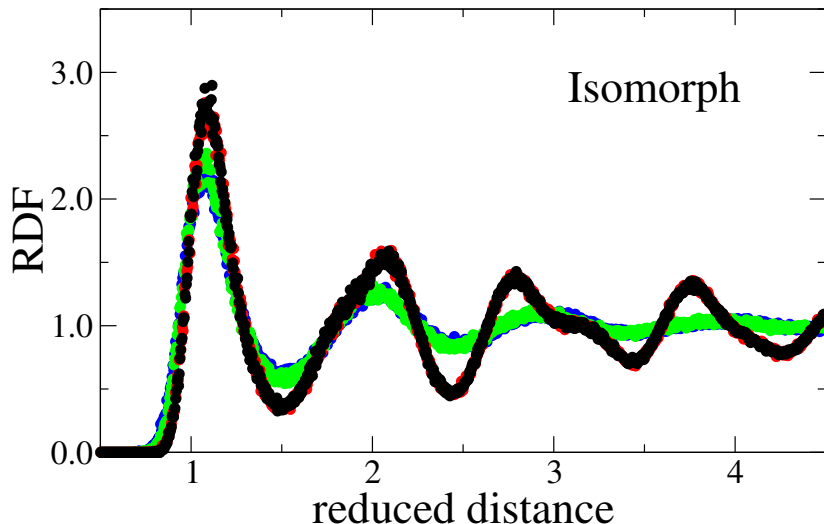


Figure 5.22: Solid isomorph generated from the same state point as the solid isomorph shown in Figure 5.21 but from a BCC crystal structure. Also this isomorph melts at the two state points higher in temperature in pressure (blue and green). Table 5.6 serves as a legend for the figure.

where the slope flattens out. Recall that from comparing Eqs. 2.1 and 2.2,  $\gamma$  going to zero necessarily means that also  $R$  goes to zero. This explains the low  $R$  and  $\gamma$  values along the state points predicted by the DIC.

In summary, much better collapse was observed along the solid and liquid isomorphs in Al than in Mg. Both structure and dynamics collapse well for Al. The same cannot be said about Mg that shows some deviations along the liquid isomorph. Additionally, the solid isomorph only somewhat collapse with regards to the two state points lowest in temperature and pressure while the higher state points become liquid in the simulation. The same is seen when the solid isomorph is started from a BCC rather than an HCP crystal structure to account for the change in crystal structure occurring in this region of the phase diagram. The difference in behaviour between Al and Mg can in part be attributed to the choice in reference points. With respect

| $\rho/\rho_0$ | Color | $T$ [K] | $P$ [kbar] | $\rho$ [ $\text{\AA}^{-3}$ ] | $\gamma_{DIC}$ | $R_{DIC}$ | $\gamma_{Sim.}$ | $R_{Sim.}$ |
|---------------|-------|---------|------------|------------------------------|----------------|-----------|-----------------|------------|
| 1.0 (s)       | black | 2321    | 281.1      | 0.0606                       |                |           | 1.6309          | 0.9667     |
| 1.3           | red   | 3379    | 755.8      | 0.0788                       | 1.2931         | 0.9498    | 1.2139          | 0.9567     |
| 1.6           | green | 4247    | 1458       | 0.0970                       | 1.0476         | 0.9075    | 0.8180          | 0.7276     |
| 1.9           | blue  | 4881    | 2394       | 0.1152                       | 0.8252         | 0.8110    | 0.5221          | 0.4908     |

Table 5.6: Temperature, pressure and density of the state points along the solid isomorph in Mg that started from the same reference point as the isomorphs of Table 5.5 but with a BCC crystal structure. Again the table serves as a legend and the colors corresponds to the color in Figure 5.22. The last four columns give the  $\gamma$  and  $R$  values as predicted from the DIC versus the values measured directly in the simulation.

to the relative position of the reference state in the respective phase diagram, the state point chosen for Mg turned out to be much closer to the re-entrant point at around 3000 kbar which is fairly close to the high temperature/pressure end of the Mg isomorphs. The maximum in Al is predicted to be around 35000 kbar which is well beyond the range of the isomorphs considered here.



# 6

## *Freezing and Melting in Metals*

---

The previous chapter has established that hidden scale invariance is obeyed in models of metals simulated using EMT as well as DFT. This chapter is dedicated to second focus of this work: the prediction of the freezing and melting curve in these metals based on nearby isomorphs.

Melting (and freezing) is the change in phase of a substance from solid to liquid (and vice versa). This change occurs at a well defined temperature under ambient conditions, which is usually referred to as the melting temperature. This temperature, however, is dependent on the pressure and the term melting curve refers to the curve that their functional dependency maps out through the phase diagram. As mentioned in the introduction, the melting and freezing curves look differently depending on which plane of the phase diagram is considered. Therefore sometimes the word melting curve encompasses both freezing and melting as these are indistinguishable in e.g. the  $(P, T)$  plane while in other planes freezing and melting are two separate curves. A state point on the melting curve or, if applicable, between the freezing and melting curve is at coexistence. At a state point at coexistence, a two phase system consisting of part liquid and part solid is stable and one phase is not overtaken by the other when simulated.

A multitude of methods exist to determine melting in experiments and simulations, that are either based on finding the stable state points in a two-phase system or observing the phase transition directly. A simple method that directly observes the phase transition is the *heat until it melts* (HUM) method. As the name suggests, the method mirrors the experimental approach of heating a solid sample until it melts. In simulations, this is not a very accurate way of determining the melting temperature. The lack of defects and open surfaces in a simulation results in an superheated crystal, thus the sample can remain crystalline at temperatures until far above the actual melting temperature [116–119]. To counteract the overestimation of the melting temperature, the HUM result is sometimes combined with a temperature obtained the opposite way. For similar reasons, the *cool until it freezes* approach results in an underestimation of the melting temperature. These two methods by themselves should be considered as providing an upper and lower bound not an accurate results. More reliable

but also computationally more expensive are two-phase methods. Here the simulation box consists of both phases interfacing. Exactly at coexistence the interface does not move and close to coexistence the speed of the interface of one phase taking over the other one can be used to infer by how much the temperature/pressure are off. In the conventional version, this requires a fairly large cell as the method requires several layers of atoms in each phase. Recent methods have tried to address this shortcoming. If a coexistence state point was determined for this work, the state point has been determined by interface pinning (IP). The IP method was devised in Ref. [109] as an improvement on the conventional two-phase type method. Here the two-phase system is stabilized using a bias field from which the state point of coexistence can be inferred in an iterative procedure. Since there is not interface movement to be monitored a much smaller cell can be used. More details on the method can be found in the reference and a summary is given in appendix A.1. Some DFT reference points used to compare our results to stem from a similar method addressing the same problem but using a different approach. The small cell coexistence method [120] utilizes several small coexistence cells with only a few layers of atoms in each phase. The error on the melting temperature is around 100 K for a cell with 100 atoms and decreases with increasing size. The method infers the melting temperature statistically from letting several instances of a small coexistence cell run at the same temperature and pressure and evaluating which phase wins how often. Experimental points from literature that are shown in this work were determined using a diamond anvil cell (DAC), a device that can compress a small sample of material and achieve extreme pressures. The highest pressure reached with this device was 770 GPa (7700 kbar) using Osmium [121]. The DAC setup is usually combined with laser heating [122] for high pressure high temperature measurements.

Based on isomorph theory, Ref. [28] developed a method to predict the melting pressure as well as the densities of freezing and melting curves from two reference isomorphs starting from a coexistence state point. A summary of the method is given in the first section of this chapter. The subsequent sections present the results found from applying the method to EMT-Cu and three DFT metals. This chapter also gives special attention to the previously believed uncommon phenomenon that is re-entrant melting. Re-entrant melting refers to a maximum in the melting temperature dependence of the pressure. Beyond the maximum pressure, the value of the melting temperature reduces again. While the melting curve having a maximum has been observed in a few materials e.g. in alkali metals. Until recently, this was considered the anomalous behaviour of a few materials. This view has been challenged in 2019 by Ref. [3] who found that re-entrant melting might actually be a universal feature common to all metals. In most metals re-entrant melting just occurs at such high temperatures and pressures that it has not been seen in experiments.

We have seen in the previous chapter that the scaling exponent  $\gamma$  decreasing with increasing pressure and temperature along an isomorph. This means that the slope of the isomorph tends to flatten. Assuming these isomorphs originate from a state point at coexistence as the method from Ref. [28] prescribes, this suggests that also the melting line between them flattens which is consistent with the melting line reaching a maximum. The last section of this chapter highlights some parallels between Ref. [3] and isomorph theory in more detail. However,

it should be noted that isomorph theory becomes less reliable around the maximum of the melting line, since as  $\gamma$  goes to zero, so does the correlation coefficient  $R$  (see Eqs. 2.4 and 2.3).

## 6.1 Method to predict freezing and melting curves

This section gives some details on the method for predicting the melting and freezing curve in materials from nearby isomorphs. The method was introduced in Ref. [28] where it was used to explore the phase diagram of the Lennard-Jones system.

The method relies on ideas from isomorph theory that were briefly mentioned at the end of chapter 2 connecting the melting and freezing curve to the nearby isomorphs. Recall that if structure and dynamics are invariant along a curve in the  $(\rho, T)$  phase space, this line should not be able to cross from one phase to another as this contradicts said invariance. This by extension would imply that the melting curve itself would be an isomorph. This is true in the limiting case of perfect correlation with perfect correlation,  $R = 1$ . For any other system this is only approximately true. In particular, isomorphs apply to single phase configurations better than two phase ones, not least because gamma in general depends on density: Assuming the liquid and crystal have different densities, the same temperature change would correspond to the two phases' densities changing by different factors if they were to both follow isomorphs. Thus, an isomorph starting from a reference point on the melting line does not actually trace along the melting curve, but slightly deviates moving away from the reference point. The method devised in Ref. [28] recovers the melting curve as a Taylor expansion using two isomorphs starting from coexistence, one on the liquid side and one the solid side.

At coexistence, the liquid and the solid state point have the same temperature and pressure, but different densities where the liquid density is typically lower than that of the corresponding solid. This means that the melting and freezing curves in the  $(P, T)$ -phase diagram are the same line while in the  $(\rho, T)$ -phase diagram the freezing curve and the melting curve are separated by a coexistence region. This is illustrated in Fig. 6.1 taken from Ref. [28]. The figure also shows the remarkable agreement of the prediction method with coexistence points found from interface pinning showing only the slightest deviation in the low density/temperature end far away from the reference point (indicated by arrows). Using that the freezing and melting curves coincide in the  $(P, T)$  plane, the first step of the method is to calculate the pressure along the melting curve as a function of temperature. A detailed review of the derivation can be found in Ref. [28]. The resulting expression for the melting pressure is

$$P_m(T) = \frac{U_s^I - U_l^I - \frac{T}{T^0} (U_s^0 - U_l^0) + Nk_B T \ln(\tilde{\rho}_s^I / \tilde{\rho}_l^I) + \frac{T}{T^0} (W_l^0 - W_s^0)}{V_l^I - V_s^I} \quad (6.1)$$

where the subscript indicates the phase, solid ( $s$ ) and liquid ( $l$ ), the superscript indicates whether the quantity is taken from the reference point ( $^0$ ) or as function of  $T$  along the isomorph ( $^I$ ) and  $\tilde{\rho}^I = \rho^I / \rho^0$  is the relative density along the isomorph with respect to the density at the reference point. Knowing the deviation of the pressure between the melting

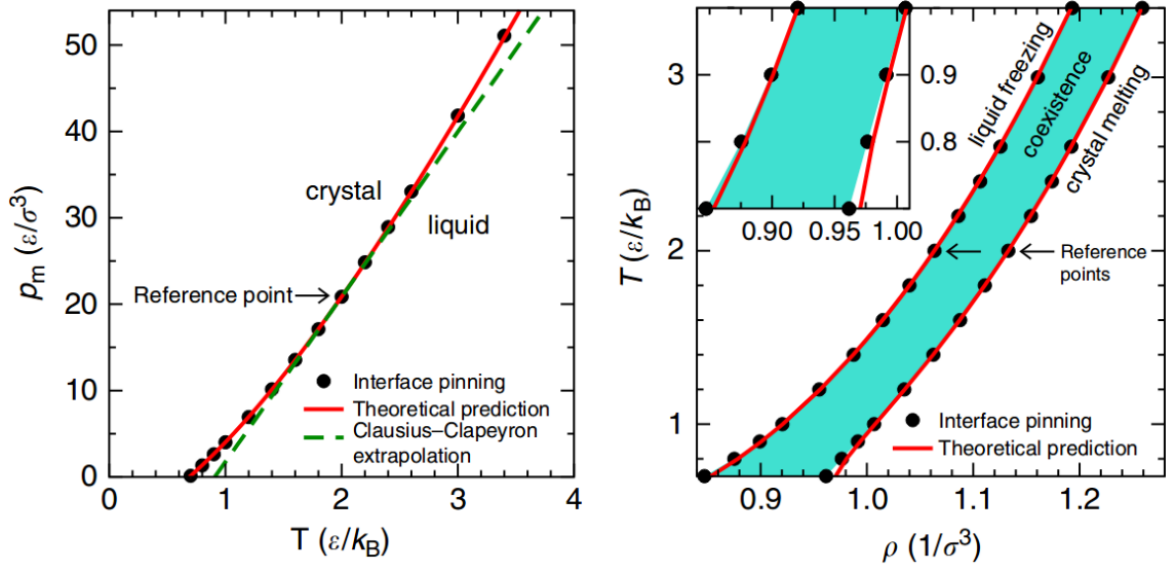


Figure 6.1: Figure taken from Ref. [28] showing the melting pressure in the  $(P, T)$  plane and the freezing and melting line separated by the region where solid and liquid can coexistence. The red line gives the prediction from the method presented in the reference and the dots are obtained from interface pinning.

curve and the reference isomorph, the density of the freezing or melting curve can be found from the difference of the calculated melting pressure  $P_m$  and the pressure along the respective isomorph via

$$\rho_{f/m}(T) = \rho_{l,s}(T) \left( 1 + \frac{P_m(T) - P_{l,s}^I}{K_{Tl,s}^I} \right) \quad (6.2)$$

where  $K_{Tl,s}^I$  is the isothermal bulk modulus along the isomorphs. Together, Eqs. (6.1) and (6.2) give a prediction for the melting curve in the  $(P, T)$  plane as well as the melting and freezing curves in the  $(\rho, T)$  plane using quantities along the isomorphs.

It can be seen from Eqs. (6.1) and (6.2) that the input quantities along the isomorphs are required to be evaluated at the same temperature. In Ref. [28] the method was applied to a Lennard-Jones type system where analytical expressions for thermodynamic quantities along the isomorphs exist. This is not the case for the models employed in this work. Additionally, the DIC finds temperature (and other thermodynamic quantities) for a specific density. Thus, the data along the two isomorphs is not readily available as the function of temperature that the method requires. This problem is solved by fitting the DIC data with polynomials that are subsequently evaluated at a set of temperatures. This procedure is a possible source of error and different orders of polynomials may be needed for the different quantities. Particularly the potential energies should be handled with care. Their contribution to Eq. (6.1) is the most significant (the other two terms are fairly constant) and even more important, their contribution emerges from small differences between large numbers.

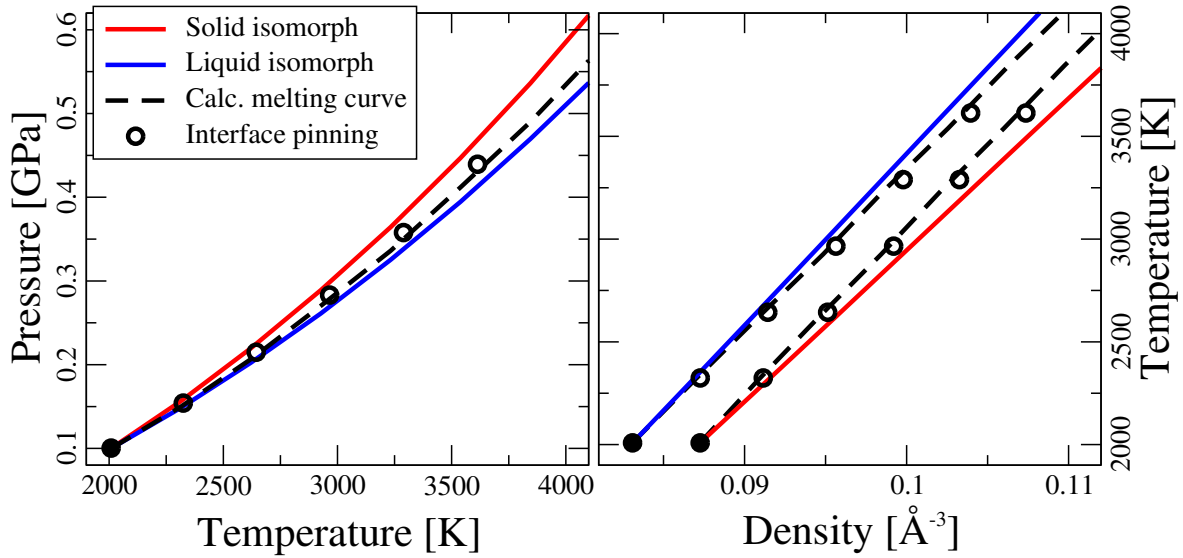


Figure 6.2: Application of the method to EMT-Cu together with coexistence state points from interface pinning. The reference point is marked by the full circle. The left panel shows the pressures along the solid and liquid isomorph generated from the reference point with the melting pressure calculated from that. The right panel shows the same curves in the  $(\rho, T)$  plane.

## 6.2 Melting curve of EMT-Cu

As a first proof of principle the method was applied to an EMT model of Cu. The two reference isomorphs were generated from a state point at coexistence. For the solid phase a simulation box with 2048 particles was simulated which corresponds to an FCC crystal with  $8 \times 8 \times 8$  unit cells. The same number of particles was used for the liquid side. Since the state point at coexistence was determined in interface pinning, the density and thus the volume for the simulation boxes for both phases was readily available. The isomorphs were determined using the direct isomorph check. The calculated melting pressure and resulting freezing and melting densities are shown in Figure 6.2. For comparison, coexistence state points for the same system determined using interface pinning (courtesy of my supervisor) are included in the figure as well.

The melting pressure predicted from the method agrees well with the interface points although not as perfectly as in the Lennard-Jones case of Ref. [28]. A small systematic shift can be observed with the calculated melting pressure being slightly below the interface results. The same statement is true also for the predicted densities of liquid freezing and solid melting.

The method has been successfully applied to the Lennard-Jones in the original paper. This work now demonstrates that the method works well also for systems where no analytic expressions are available for the isomorphs and for how thermodynamic quantities vary along them. It needs especially to be emphasized that all data required to produce this prediction has been obtained from simulations at only the reference state point. Combining the prediction

method with the DIC thus offers a possibility to predict the melting and freezing curves in systems where conventionally used methods are too computationally expensive.

### 6.3 Melting curves using DFT

After the first proof of principle, the method is applied to the even more realistic (and computationally much more costly) model of metals that are DFT metals. The initial plan was to conduct the same study as with EMT-Cu with DFT metals, meaning in particular to include interface pinning points also for the DFT materials. This would have ensured full model consistency between the prediction method and the state points used to validate them. Unfortunately, this plan had to be discarded on account of problems when running interface pinning using DFT. The problem arises from not negligible and anisotropic contributions to the pressure from the nearly free electrons in the metal when simulated in a non-cubic box. For more details see section A.2. Instead, literature data from both experiments and other DFT simulations is used as a reference point and to validate our predictions.

Literature data does not report volumes or densities for the two phases, only temperature and pressure at melting. The simulations were carried out in the  $NVT$  ensemble, thus the volume corresponding to the given pressure needs to be determined for each phase first. This is done by simulating a string of slight different box sizes. After the runs, the pressures for each box are measured and the desired box size can be inferred. A box at the desired box size is simulated and if the measured pressure agrees with the desired pressure to within fluctuations, the data is used for the DIC.

The isomorphs on the solid and the liquid side of the reference point are generated using the DIC. Both simulations are run for 50000 steps with a time step of 2 fs. Although the samples are pre-equilibrated, only every 100th frame of the last 30000 steps are used for the DIC. The 300 independent configurations are then scaled to a set of different densities. The densities were scaled by the following factors relative to the initial density: (0.8, 0.9, 1.1, 1.2, 1.3, ..., 1.9, 2.0). VASP potentials require an energy cutoff that translates to the shortest wavelength for the plane waves used by the code. This in turn determines the number of plane waves used in the calculations. Scaling the simulation box to the densities specified at a constant energy cutoff would therefore lead to different numbers of plane waves used for each density. Additionally, to the scaling of the DIC, we also carry out much smaller scaling around the specified densities to determine the hypervirial from a numerical derivative. Especially for the numerical derivative but also for the scaling for the DIC, any discontinuities arising from different numbers of plane waves used could be problematic. Therefore the energy cutoff is scaled as a function of density  $E_{\text{cut}}(\rho)$  so that the number of plane waves stays constant:

$$E_{\text{cut}}(\rho) = E_{\text{cut}}(\rho_i) \left( \frac{\rho}{\rho_i} \right)^{1/3} \quad (6.3)$$

where  $\rho_i$  and  $E_{\text{cut}}(\rho_i)$  are the initial density and the energy cutoff chosen for that density. The initial energy cutoffs for Al and Mg are given in B.3. The hypervirial  $H_{\text{vir}}$  from the numerical derivative is necessary to estimate the bulk modulus  $K_T$  along the isomorph from using

$$K_T^I = \frac{1}{V^I} \left( Nk_B T^I + W^I + H_{\text{vir}}^I - \frac{\text{Var}[W^I]}{k_B T^I} \right) \quad (6.4)$$

where  $\text{Var}[W^I]$  is the variance of the virial  $W^I$  along the isomorph.

The elements chosen – Al, Mg and Na – are all expected to be reasonably fast to simulate using DFT. Due to their almost empty outer shells, the simplest potentials for these elements have only a few electrons that need to be treated explicitly while the core electrons in the inner shells remain *frozen*. Technically, such a frozen core potential is a pseudopotential, but the word potential is used in this work to refer to them as well.

Although Al, Mg and Na are by far not the most computationally intensive materials to simulate, especially when most shells are considered frozen, it is still necessary to simulate a much smaller box than what could be achieved with EMT. Small here means that the box contains, depending on the crystal structure achieved, between 108 (fcc) to 180 (hcp) particles. Such small boxes give large fluctuations on average thermodynamic quantities which causes another pressure related problem. The problem here is that the expression to predict the pressure (Eq. (6.1)) gets a distinct offset at the starting point if the pressures measured on the liquid and the solid side do not exactly match the coexistence pressure. The NVT simulation boxes for solid and liquid at the reference point are chosen to be at the same pressure to within its error. The small deviation between set and measured pressure from this are magnified when plugged into Eq. (6.1) resulting in the offset. This is fixed by correcting the virial so that the pressures at the reference point match. More details are given in section B.1.

### 6.3.1 Aluminium

The first candidate metal is Al which was simulated using the PBE frozen core potential with three free electrons. The simulation boxes for each phase contain 108 atoms which means a  $(3 \times 3 \times 3)$  FCC crystal for the solid phase. The resulting phase diagram in the  $(P, T)$  plane is shown in Figure 6.3. The phase diagram also includes coexistence state points (red, open circles) determined by experimental methods [123, 124] and by other simulation techniques using DFT [3, 125] (orange symbols). The latter DFT method, depicted by the orange triangles in the phase diagrams for Al and Mg, is the method that we expect to be most consistent with this work since the authors also use VASP and the PBE approximation.

The state point that served as the reference point for the isomorphs is marked by an x and an arrow. The points along the isomorphs found using the DIC are marked by the colored crosses with the dashed line given by the polynomial fitted to the data. The DIC points are the same as shown in the previous section. The small panel on the right-hand side of Fig. 6.3 shows the scaling exponent  $\gamma$  and the correlation coefficient  $R$  along the isomorphs. The

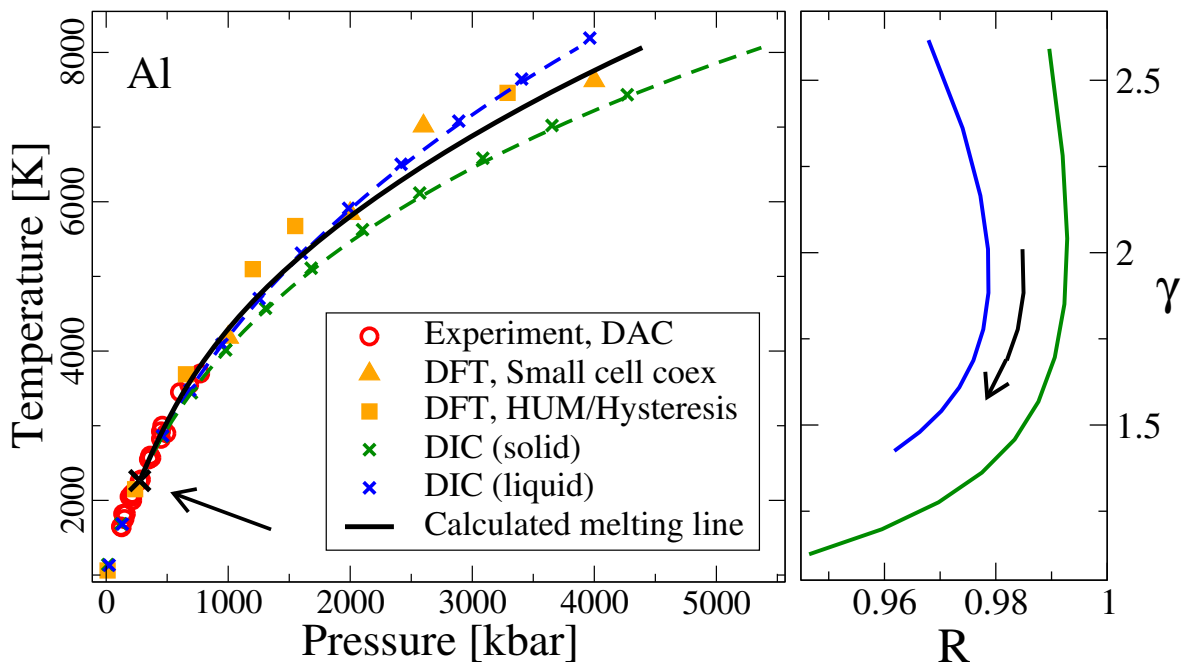


Figure 6.3:  $(P, T)$  phase diagram of Al. The experimental points are taken from [123] which includes points from [124], both references determine melting in a diamond anvil cell (DAC). The DFT points are taken from [125] (HUM/Hysteresis) and [3] (Small cell coexistence method). The experimental point marked by the x and arrow was used as reference point to generate the isomorphs from. The predicted melting pressure from the method is given by the solid black line and agrees well with both experimental and DFT data. The small panel on the right shows the correlation coefficient  $R$  and scaling exponent  $\gamma$ . The curved arrow points along the curves in the direction of increasing pressure/temperature along the isomorph.

scaling exponent  $\gamma$  goes down monotonically with increasing pressure/temperature along the isomorph. This behaviour is consistent with experience from the EMT metals [39] and seems to be a fairly general feature of metals. The correlation coefficient is well above the  $R > 0.9$  criterion. This means good isomorphs in this part of the phase diagram can be expected and the invariance of structure and dynamics has been validated along them in the last section. It is expected that  $R$  goes down as  $\gamma$  goes down, since the correlation necessarily goes to zero when  $\gamma$  does too (see Eqs. 2.1 and 2.2). The virial becomes close to zero at the state point lowest in temperature and density. A low virial is a sign that the liquid-gas coexistence is close, where correlation break down, see e.g. Fig. 1 of Ref. [7]. This explains why  $R$  also goes down slightly at the high  $\gamma$  end.

The points marked by the small colored crosses in Figure 6.3 mark the isomorph state points found from the DIC. The associated dashed lines are given by a fit to the DIC data. The fitting is required to calculate the melting curve pressure and densities. The method takes data from the two isomorphs at the same temperature, whereas the DIC produces data at given density.

There is no rigorous argument for why the solid isomorph lies to the right of the liquid in the  $(p, T)$  phase diagram. It is however possible to give a hand-waving argument as to why

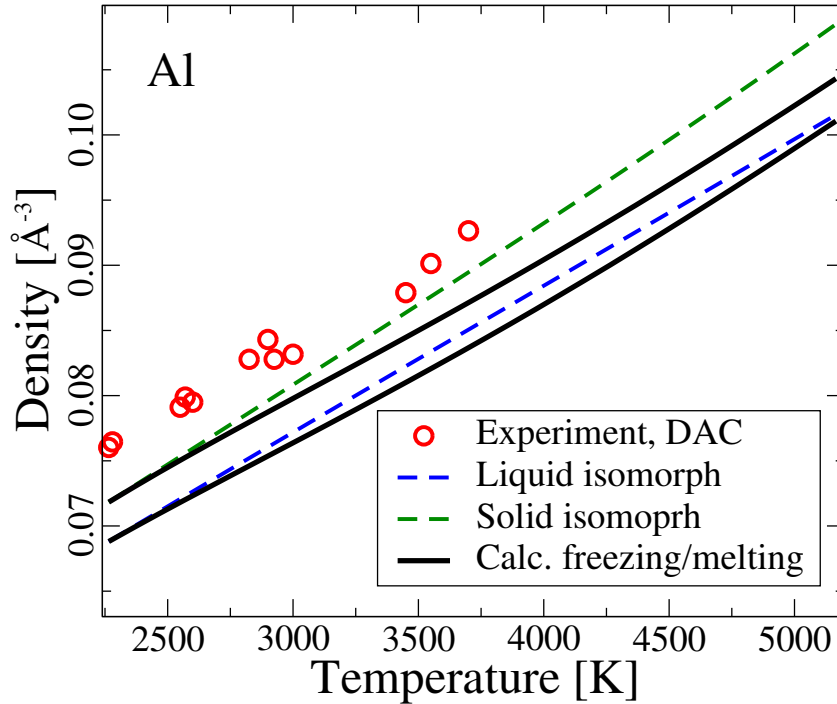


Figure 6.4:  $(\rho, T)$  phase diagram of Al. Note that the axis are switched compared to the usual textbook way of plotting  $(\rho, T)$  diagrams. This is because the method calculates densities as a function of temperature. The calculated melting pressure shown in Figure 6.3 can be translated into the densities at which the liquid freezes and the solid melts via Eq. (6.2). The resulting densities are given by the solid black lines. The dashed lines mark the associated isomorphs. Reference [123] report one volume for each point (it is unclear for which phase) shown in Fig. 6.3. The red circles are obtained by converting these volumes to a density.

the liquid isomorph should be at a higher pressure than the solid at the same temperature provided that both started from the same state point. The solid (usually) has a larger density than the liquid and correspondingly a lower  $\gamma$  than the liquid at the same temperature. For a given common temperature increase the solid therefore requires a larger fractional density change. Assuming the bulk modulus of the solid is at least as large as that of the liquid implies a greater pressure change. It is intuitive to assume the solid's bulk modulus would be larger than the liquid's but this has not been checked.

The melting curve calculated from the two isomorphs is given by the solid black line in Figure 6.3. Our calculated melting pressure agrees well with both the experimental and the DFT points. As expected, our calculations are closer to the DFT points taken from Ref. [3]. The hysteresis method combines data from the *heat until it melts* (HUM) method with the opposite method, *freeze until it cools*, to counteract that the HUM method alone is well known for overestimating the melting curve due to superheating effects [116]. The resulting combined melting curve is much better fit than HUM alone but often still somewhat too high. This is consistent with our findings.

Figure 6.4 shows the densities calculated using Eq. (6.2) together with the densities along the

reference isomorphs. Unfortunately, there are no densities reported together with the DFT pressures from Refs. [125] and [3] shown in Fig. 6.3. Ref. [123] reports one volume for each point which were translated to a density to obtain the red circles shown in the Figure. It is not clear in the reference whether the volume is for the liquid or the solid phase, but from the figure one could guess that the volumes correspond to the solid phase.

### 6.3.2 Magnesium

The second candidate metal of this study is Mg. Similar to Al the simplest PBE frozen core potential is used; in the case of Mg this means two free electrons. Mg has an HCP crystal structure at low pressures resulting in a simulation box containing 180 particles in  $(5 \times 3 \times 3)$  unit cells and a liquid simulation box with the same number of particles. As described in the previous chapter, the crystal cell is not exactly square but very close to it in an attempt to avoid anisotropic pressure (see appendix B.4).

The relevant part of Mg phase diagram in the  $(P, T)$  plane is shown in the main panel of Figure 6.5. The experimental points (red circles) are taken from Ref. [126] and the DFT points are provided from the same reference as for Al [3]. The state point marked by the black x and arrow is the point simulated for this work. The points obtained from the DIC are marked by the colored x's and the dashed lines are from the fitted data. The solid black line gives the calculated melting pressure. The small panel of Figure 6.5 shows  $\gamma$  and  $R$  along the isomorphs.

The  $R$  value along both isomorphs decreases to rather low values well below the 0.9 criterion. The point where  $R$  drops below 0.9 is indicated by the grey dashed line in the main panel of Figure 6.5. In Chapter 5 it was showed that especially the solid isomorph is not a good isomorph. Structure and dynamics are only invariant for the lower temperature/pressure state points while the simulations at the higher temperature/pressure state points melted. Also the overall collapse along the liquid isomorph was qualitatively less convincing than along the Al isomorphs. This is presumably due the relative closeness of the maximum in the melting temperature curve. The maximum is reported by Ref. [3] to occur around  $\sim 3000$  kbar and 4500 K (included in the figure). Recall that the same reference predicts the re-entrant point of Al to be around  $\sim 35000$  kbar and 20000 K. This means that the reference point used for the isomorphs in Mg is much closer to the maximum of the melting curve than it was in Al. This is consistent with the much lower  $\gamma$  and the fact that the system becomes uncorrelated before the maximum of the melting curve is reached [127].

The calculated melting line exhibits an odd slope right around the reference point. A similar behaviour was initially seen in Al. In Al, this was due to the fitting procedure being not accurate enough for the potential energies so that their difference entering Eq. (6.1) became non-monotonous. For Al this could be alleviated by increasing the order of the fit polynomial. More details on this are given in appendix B.2. The same did unfortunately not work for Mg but it can still be assumed that this is unphysical and due to the relative closeness of the two isomorphs immediately after the reference point and the fact that they enter as small

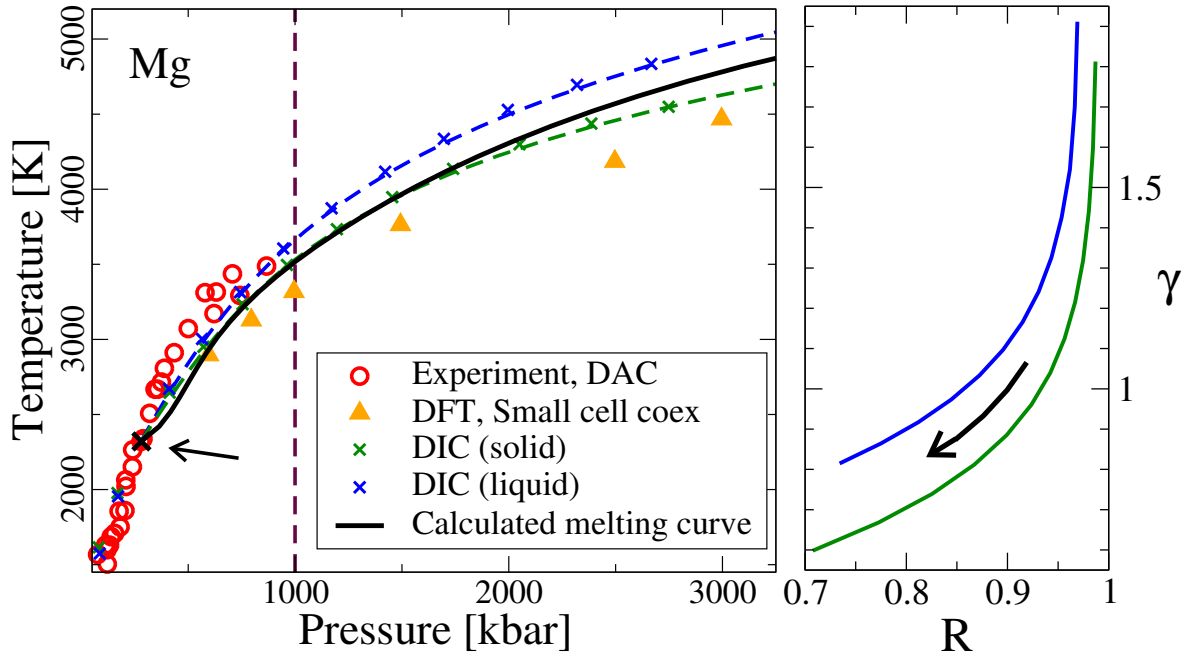


Figure 6.5: The main panel shows the phase diagram of Mg in the  $(P, T)$  plane. The red circles are experimental points taken from [126]. The reference reports a transition from HCP to BCC crystal structure above 500 kbar which corresponds to the six points highest in temperature and pressure. The orange triangles are DFT points taken again from Ref. [3]. The orange triangle at 3000 K is predicted to be the maximum of the melting curve. The reference point for the DIC points is marked by the black x and arrow. The blue and green lines are given by the isomorphs and the solid black line is the melting curve calculated from them. The small panel shows the correlation coefficient  $R$  and scaling exponent  $\gamma$ . The arrow points along the curves in the direction of increasing pressure/temperature along the isomorphs. The correlation coefficient falls below 0.9 along the isomorphs. This is indicated by the vertical dashed line in the main panel.

differences between big numbers into Eq. (6.1). Therefore, the first few points along the calculated melting curve immediately after the reference point should be ignored.

Overall, the melting line calculated from these less than ideal isomorphs fits well with the experimental and the DFT data included in Figure 6.5. Unlike in Al the experimental and the DFT points from literature do not fully agree in the range where points from both methods are available. Our melting line agrees reasonably well with both, it is slightly lower than the experimental prediction and slightly above the DFT prediction.

The study of structure and dynamics of the previous section suggests that the solid curve found from the DIC is too high in temperature since the two high pressure/temperature state points did not stay solid when simulated. It is thus maybe not surprising that the calculated melting curve is so close to the supposedly solid line. This is also consistent with the DFT points from Ref. [3] being lower, suggesting that our melting curve might be somewhat overestimated given the problematic solid DIC it is based on.

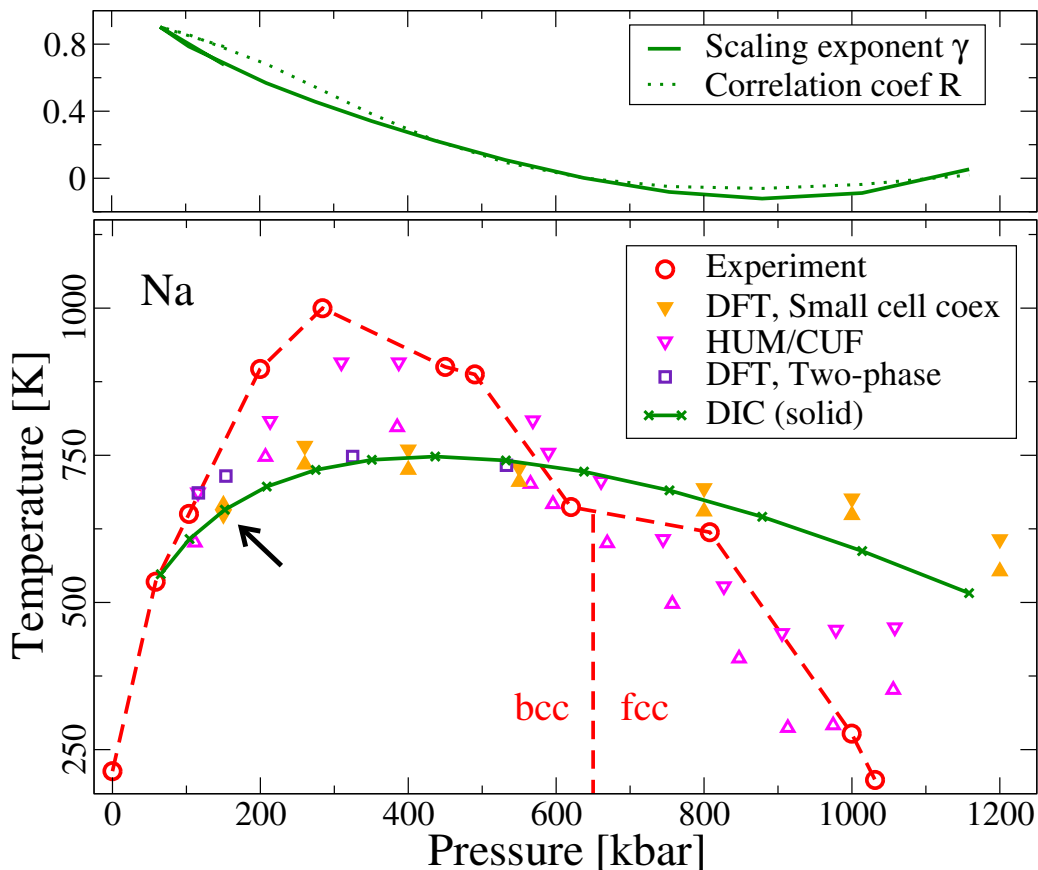


Figure 6.6: Phase diagram in the  $(P, T)$  plane for Na. The experimental points (open circles) are taken from [128]. The region determined by the heat until it melts/freezes until it cools method (open triangles) is taken from [118]. Points from two DFT methods are shown as well; the two phase method [129] (open squares) and the small cell coexistence method [3] (filled triangles). The dashed vertical line denotes where the crystal structure transitions from BCC to FCC. The state point marked by the arrow has been simulated as the starting point for the DIC. Only a solid isomorph was generated from the starting point, which is given by the green line. The top panel shows  $R$  and  $\gamma$  for the DIC points separately. Values for temperature, pressure, density,  $\gamma$  and  $R$  are given in Table 6.1

### 6.3.3 Sodium

The third metal in this series is Na. While re-entrant melting in the two previous candidates is only hypothesised based on simulation data, Na is one of the few materials where re-entrant melting has been observed in experiments. The  $(P, T)$  phase diagram is shown in Figure 6.6. The experimental points, taken from Ref. [128], show that the melting temperature has a maximum of 1000 K at around 300 kbar. Upon increasing the pressure further, it drops down to 200 K at 1000 kbar. Along the way, the crystal structure transitions from BCC to FCC above 650 kbar. The DFT data taken from Ref. [3] predicts a change in crystal structure at the same pressure. The results from both DFT methods also agree with the pressure region at which the maximum occurs, but the maximum temperature predicted by the DFT methods is

lower than the experimental value. Both DFT methods are in close agreement with each other.

The frozen core PBE approximation used for Na is the computationally simplest, including only one free electron per atom. Since Na has a BCC crystal structure in the lower pressure part of the phase diagram, our simulation box contains 128 atoms which corresponds to a  $(4 \times 4 \times 4)$  unit cell system.

The state point used as the initial point for the DIC is marked by an arrow. The top panel in Figure 6.6 shows  $R$  and  $\gamma$  at the state points found from the DIC. The values for temperature, pressure, density,  $\gamma$  and  $R$  are given in Table 6.1. The correlation coefficient  $R$  is below 0.9 over the entire range. This means that the curve given by the DIC is at best a configurational adiabat, rather than an isomorph. Recall that the scaling exponent  $\gamma$  is expected to vanish around the maximum in the melting curve. And accordingly, also  $R$  goes to zero (see 2.2 and 2.1). It is therefore not a surprise that the DIC from a point this close to the maximum does not result in a good isomorph in terms of the  $R > 0.9$  criterion. No additional simulations along the isomorph were carried out, so there is no data available confirming the collapse of structure and dynamics or lack thereof. Unfortunately, there was also not enough time to map a liquid isomorph from the same reference point. The results for Al and Mg suggest that the isomorphs alone are already a rather good indication of the melting curve's position and one could expect that the predicted melting line would be only slightly higher in temperature than the solid isomorph shown in Figure 6.6.

What is noteworthy about the curve found from the DIC is that, even though there is no reason

| $\rho/\rho_0$ | $T$ [K]      | $P$ [kbar]   | $\rho$ [ $\text{\AA}^{-3}$ ] | $\gamma_{DIC}$ | $R_{DIC}$     |
|---------------|--------------|--------------|------------------------------|----------------|---------------|
| 0.8           | 553.0        | 65.2         | 0.0396                       | 0.8676         | 0.8888        |
| 0.9           | 610.9        | 104.1        | 0.0445                       | 0.7421         | 0.8306        |
| <b>1.0</b>    | <b>657.5</b> | <b>151.7</b> | <b>0.0495</b>                | <b>0.6228</b>  | <b>0.7409</b> |
| 1.1           | 692.7        | 208.5        | 0.0544                       | 0.5034         | 0.6122        |
| 1.2           | 716.0        | 274.8        | 0.0593                       | 0.3810         | 0.4485        |
| 1.3           | 727.2        | 350.7        | 0.0643                       | 0.2556         | 0.2739        |
| 1.4           | 725.8        | 436.4        | 0.0692                       | 0.1296         | 0.1201        |
| 1.5           | 711.3        | 532.2        | 0.0742                       | 0.0094         | 0.0073        |
| 1.6           | 683.5        | 637.9        | 0.0791                       | -0.0917        | -0.0583       |
| 1.7           | 642.1        | 753.6        | 0.0841                       | -0.1524        | -0.0794       |
| 1.8           | 586.7        | 879.1        | 0.0890                       | -0.1401        | -0.0603       |
| 1.9           | 517.1        | 1014.5       | 0.0940                       | -0.0144        | -0.0052       |
| 2.0           | 433.4        | 1159.3       | 0.0989                       | 0.2637         | 0.0813        |

Table 6.1: Temperature, pressure and density as well as  $\gamma$  and  $R$  of the state points found from the DIC for solid Na. The row in bold gives the data at the reference point.

to expect for isomorph theory to work, the DIC points nonetheless agree very nicely with the other DFT points. The shape follows the other DFT coexistence points with a maximum in the same region. Since we use a very similar system as Ref. [3] we expect their results to be the closest match, but it is still surprising that the DIC points follow their melting point results so well.

## 6.4 Re-entrant melting and R-simplicity

Reentrant melting has been suggested by Ref. [3] to be far more common than previously thought. The difference between the materials known to have a maximum temperature along the melting curve as function of pressure is simply that this maximum occurs at much lower temperatures and pressures and thus has been observed in experiments. Their simulation work finds reentrant melting also in other metals, just well above the pressures that can be archived in experiments. To pinpoint the reentrant point, Ref. [3] suggest a quick method to screen materials instead of carrying out several simulations throughout the phase diagram to determine the melting curve and its maximum point by point. The method is surprisingly simple and more interesting: inadvertently related to isomorph theory.

It is generally assumed that the cause of the melting slope becoming negative is that the ratio between the specific volumes for the solid and the liquid phase inverts. According to the Clausius-Clapeyron relation, the slope of the melting curve is given by

$$\frac{dP}{dT_m} = \frac{\Delta H}{T_m \Delta V} \quad (6.5)$$

where  $\Delta H$  is the specific heat of fusion and  $\Delta V = V_l - V_s$  is the difference in specific volume. The slope becomes negative, when  $\Delta V$  does, i.e. when  $V_s > V_l$ . Ref. [3] indeed found in simulations of Na and Mg that the maximum of the melting temperature  $T_m$  coincides with the sign of  $\Delta V$  changing. The screening method thus relies on finding the point where  $V_s$  becomes larger than  $V_l$ .

The proposed method takes one randomly selected snapshot from the trajectories of simulation of a solid and a liquid simulation. This snapshot is used to represent each phase. The snapshots are then compressed by scaling all lattice vectors uniformly. From this the pressure-volume relation is estimated for each phase, and the pressure where the sign of  $\Delta V$  changes can be found from comparison. The method thus provides a well informed guess where the melting curve maximum can be expected. The interesting relation to isomorph theory is that the scaling involved in the method is essentially the same as the scaling used for the DIC, however the DIC includes several configurations to identify correlations between the scaled configurations.

A possible method for a similarly educated guess derived from isomorph theory directly could be based on  $\gamma$ . The connection between  $\gamma$  going to zero and the maximum of the melting is more than a hand-waving argument of the slope flattening out. In the Lindemann law [130]

for melting, the melting curve is described by the function

$$\frac{d\ln T_m}{dP} = \frac{2\left(\gamma_m - \frac{1}{3}\right)}{B_m}, \quad (6.6)$$

where  $B_m$  is the bulk modulus of the solid and  $\gamma_m$  is the Grüneisen melting parameter. The law is often used to interpolate the melting curve to high pressures from low pressure data. Typical values for  $\gamma_m$  in metals at low pressure are around 2 and higher [131], thus yielding a melting curve with a positive slope.

The relation between the Grüneisen melting parameter  $\gamma_m$  and the scaling exponent  $\gamma$  from isomorph theory has been discussed in Ref. [29], and is (using the Dulong-Petit approximation) given by:

$$\gamma = 2\left(\gamma_m - \frac{1}{3}\right) \quad (6.7)$$

According to Eq. (6.6), the slope of the melting curve becomes negative when  $\gamma_m < 1/3$  which, as can be seen from Eq. (6.7), is equivalent to the scaling exponent becoming zero. It can be seen that in fact  $\gamma_{\text{Na}}$  (Tab. 6.1) becomes negative slightly after the maximum of the melting curve. There is also the problem of  $R$  going to zero when  $\gamma$  does meaning that isomorph theory is not predicted to work in this region. However, Figure 6.6 suggests that the DIC state points nonetheless nicely follow the DFT coexistence points from [3].

A similar behaviour of  $\gamma$  was observed in the EXP potential [8, 127]. In the EXP potential particles interact via a purely repulsive exponentially decaying function of the form

$$v_{\text{EXP}}(r) = \varepsilon e^{-r/\sigma} \quad (6.8)$$

The EXP potential is a simple model that can describe the complexity of metals surprisingly well. This can be traced back to e.g. the fact that the low-density limit of the Yukawa (screened Coulomb) potential system is well described by the EXP potential [8] which is an important ingredient in most models for metals.

As a prototype for metal and consistent with Ref. [3] hypothesis that re-entrant melting is a universal behaviour that all metals have, also the melting curve in the EXP potential has a maximum temperature. Contrary to our DFT observation,  $\gamma_{\text{EXP}}$  goes to zero slightly before the maximum is reached. Thus there seems to be a weak model dependence for the exact relation between  $\gamma$  going to zero and the re-entrant point. In both cases however the zero crossing of  $\gamma$  occurs close to the melting curve maximum. A criterion based on fitting and interpolating the zero crossing of  $\gamma$  could therefore be used similarly to the volume screening method to outline the region where the maximum of the melting curve should be expected. A possible advantage over the volume screening method would be that using the  $\gamma$  interpolation method can be done from scaling of only one phase rather than both – although it uses information from more than one configuration.



# 7

## *Concluding Remarks*

---

This work has investigated the invariance of structure and dynamics predicted by isomorph theory in EMT mono-atomic metals, different compositions of EMT CuZr alloy and DFT metals. With the exception of Mg all metals exhibit good collapse of both structure and dynamics at all state points studied. Additionally, a method to predict the melting curve from nearby isomorphs derived from isomorph theory has been successfully applied to EMT Cu and the DFT metals. This includes Mg even though the method was in this case not based on good isomorphs.

A natural system to compare the results of this work, in particular the EMT results, is the EXP potential briefly mentioned in the last chapter. The EXP potential with its purely repulsive, exponentially decaying interaction is in many ways the archetype model for models of metals, especially other models that also include exponential functions, e.g. the Buckingham [132] or the Morse potential [133]. The EXP potential has only recently been studied on its own [8, 127, 134, 135] previous studies usually focused on the aforementioned models that include an exponential function but only in addition to other terms. The study of the EXP potential alone has shown that the system has exceptionally good isomorphs that even extend into the gas phase. The EMT potential is closely related to the EXP potential, since it essentially consists of several exponential functions. Given this connection, it is perhaps not too surprising that the EMT model also has good isomorph with well collapsing structure and dynamics along them, just like its relative the EXP potential has.

To evaluate the quality of the isomorphs in the DFT-metals, it is important to keep the relative position of the reference points for the isomorphs in the respective phase diagram in mind. The isomorphs studied with regards to the invariance of structure and dynamics are the same isomorphs that are used to predict the melting curve. This means that they start from a reference point at coexistence and also the points found from the DIC are close to the phase transition. Additionally, the reference point used for Mg is very close to the maximum of the melting curve around which the correlations defining isomorphs necessarily break down. The reference point for Al is roughly at the same absolute temperature as the one for Mg, however the maximum of the melting curve in Al is much further away. This explains why

there is a good collapse along the isomorphs in Al. The same cannot be said for Mg, where especially the points found from the solid side of the reference state point are not isomorphic. This makes the successful application of the method to calculate the melting curve all the more impressive. For both Al and Mg, the calculated melting pressure fits very well with experimental data and also melting points found from other simulation techniques. Limited conclusions can be drawn from only two materials studied, but it seems like the agreement of the calculated melting pressure with literature data is hardly impacted by the quality of the isomorphs used as the basis for the method. Isomorphs and calculated melting curve remain close to each other also far away from the reference point, meaning that for a quick guess of where the melting curve should be expected, the mapping of one isomorph might be sufficient.

One of the reasons why the EMT potential was used in this work is that the relatively simple functional form of the potential could help reveal a direct dependence of  $\gamma$  on density from the form of the potential. This is subject of ongoing research and requires further work. As a general observation on the behaviour of  $\gamma$ , it can be stated that  $\gamma$  goes down with increasing density along an isomorph. This behaviour is common to both the EMT and DFT simulations of this work and was also seen in the EXP potential. A decreasing  $\gamma$  is associated with a softening of the potential and more directly suggests the slope of the melting curve reaching zero. Although the details of the behaviour of  $\gamma$  are not well understood, the observation of decreasing  $\gamma$  with increasing density lends weight to the hypothesis of Ref. [3]: that re-entrant melting could very well be a universal feature of all metals.

A possible method to constrain the region where the melting curve reaches its maximum using the scaling exponent  $\gamma$  has been outlined in this work, build upon predicting the point where  $\gamma$  goes to zero which happens in close vicinity of the maximum of the melting curve. The method however lacks refinement and is not rigorously motivated by isomorph theory, as the isomorph defining correlations also go to zero around the maximum. Nonetheless, the simulation of Na suggests that the DIC prediction for  $\gamma$  can be used to narrow down the region of the melting curve maximum even with vanishing correlations. The advantage of this method would clearly be that only one isomorph from one phase is needed which cuts down on simulation time. A problem could be the validity of the the DIC over very large density changes. This is not studied well but one can assume that the error becomes bigger with larger density steps. Alternatively, the  $\gamma$  values from a DIC that does not directly observe  $\gamma$  going to zero could be used to infer the zero crossing from fitting  $\gamma$  with an appropriate function.

At the top of the list of possible improvements and extension to this work would be to include a model consistent method to determine temperature, pressure and densities of coexistence state points to compare the calculated DFT freezing and melting curves to. For the EMT-Cu simulations comparison points where available from interface pinning. This method was unfortunately not suitable for the small DFT simulation boxes used in this work. The possibility to determine temperature, pressure and density for our DFT systems for several points at coexistence would be especially interesting for the density temperature plane. As shown in the results, temperature and pressure data for points on the melting curve are relatively easy to find in the literature from both simulations and experiments. The densities

of the freezing and melting curve on the other hand are rarely reported. A good candidate for such a method that works well with DFT could for example be the small-cell coexistence method [120] that was used for the DFT literature data.

Also the possibility of a direct comparison of EMT and DFT results would be interesting to include. The EMT model provides parameter for six d-metals. Although there exist different interpretations which elements exactly are included in this group, this group of elements is sometimes also called noble metals. This is done in reference to the noble gases due to the metals having (almost) filled outer orbital shells. Conversely, the DFT metals chosen are from the sp-metal group due to their almost empty outer orbital. This makes them fairly efficient to simulate using a frozen core potential with a maximum of 3 electrons treated explicitly (Al). A frozen core potential for Cu however has for example 11 electrons and the other d-metals are similarly expensive. Since simulation time scales with the number of electrons cubed, simulating the DFT metals selected for this work was the most practical choice with regards to efficient simulation for a project with a time restriction.

Something that would make the comparison of isomorph quantities between metals within the same model more meaningful would be a different choice of reference point for the isomorphs. The reference points selected for this work are similar in absolute terms, e.g. at the same temperature and pressure. The better option would probably have been to use reference points that are similar in their relative position in the respective phase diagram of the metals.

Lastly, the usual suggestion to improve on isomorphs generated from the DIC would be to use a more accurate method to trace out isomorphs. For the DFT simulations those methods were dismissed due to the extreme computational costs associated with them but they are of course possible to use. With regards to the DIC points of Na that reproduced the melting curve surprisingly well through the maximum of the melting curve, it would be interesting to see if a step-wise isomorph would do better here. Given that the correlations vanish at the maximum, a step-wise isomorph might actually do poorer than the DIC did. The DIC was based on a state point with fairly good correlations, which will not be the case for the intermediate points used to find the next point for the more accurate, small-step methods.

To wrap up, this work has established good isomorphs in (most of) the metals studied. The EMT mono-atomic crystals especially contribute to the study of isomorphs in crystals, whereas most previous studies of isomorphs usually focus on the liquid phase. The study of CuZr has added to the understanding of the scaling exponent  $\gamma$  in compound systems, insofar that the rather different values of  $\gamma$  for the individual components do not seem to influence the value of the compound system. Also the DFT metals have good isomorphs in both liquid and solid phase if the isomorph does not get too close to the maximum of the melting curve. A possible application of  $\gamma$  as a tool to predict where the melting curve maximum occurs, should be investigated further. The overall behaviour of  $\gamma$  observed in all metals suggest that all the materials studied in this work should have such a maximum, but also this needs to be investigated further.



# A

## *Problems with Interface pinning and DFT*

---

Initially coexistence state points on the melting curve were planned to be determined using the interface pinning method just like it was done for EMT-Cu. However, it turned out that the interface pinning method was not working well together with DFT simulations. This is due to anisotropic contributions to the pressure from the electrons in a non cubic box. This effect is amplified by the relatively small box size that is required by DFT. In this chapter, first a quick recap of the method is given followed by a more detailed discussion of the problem with the electrons.

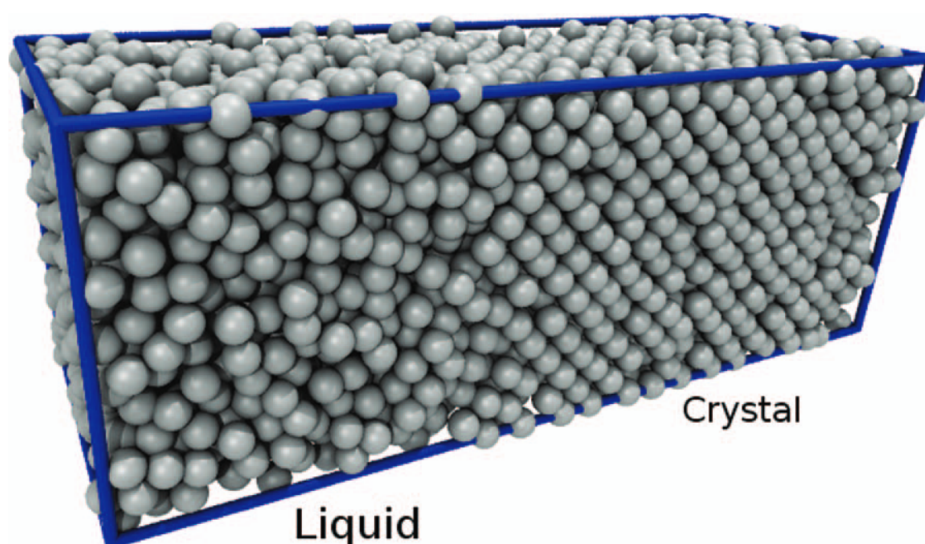


Figure A.1: Setup of the simulation box for the interface pinning method. A two-phase system consisting of the liquid and solid phase directly interfacing each other is simulated in an elongated box using periodic boundary conditions. Figure taken from Ref. [109].

## A.1 Interface Pinning Procedure

Interface pinning method was first devised in Ref. [109]. A review of the theory behind the method is given in this section. The interface pinning method is a development from the conventional large cell coexistence method. As the name suggests, the large cell coexistence method requires a large simulation cell so that the simulation cell has room for the interface between the solid and liquid phase to move until equilibrium has been achieved without the system going completely over to one or the other phase. The IP method includes a bias potential to keep the simulation cell in its two phase state, thus the interface is pinned in place.

For the control of the bias potential, the method requires the use of an order parameter to distinguish between the phases. This work uses the  $q_6$  parameter of the Steinhardt-Nelson's bond orientational order parameters [136]. The order parameters are based on the spherical harmonics  $Y_{l,m}$  as follows

$$q_l(i) = \left( \frac{4\pi}{2l+1} \sum_{m=-l}^l |q_{lm}(i)|^2 \right)^{1/2} \quad (\text{A.1})$$

where  $l, m$  are integers given by  $m \in (-l, l)$  and  $q_{lm}$  is defined as

$$q_{lm}(i) = \frac{1}{N(i)} \sum_{j=1}^{N(i)} Y_{lm}(\mathbf{r}_{i,j}) \quad (\text{A.2})$$

with  $N(i)$  the number of neighbours of particle  $i$  and  $\mathbf{r}_{i,j}$  the vector between particles  $i$  and  $j$ .

Using the bias potential, state points at coexistence are determined iteratively based on the following considerations. Difference of the chemical potential is the difference in Gibbs free energy per particle

$$\Delta\mu = \Delta u + P\Delta v - T\Delta s \quad (\text{A.3})$$

with  $P, T$  being the pressure and temperature of the simulation and the  $\Delta$  quantities being the per particle difference between solid and liquid phase of the respective quantity. The order parameter  $Q$  with bias potential enabled is Gaussian distributed with expectation value and variance being

$$\langle Q \rangle = A - \frac{\Delta\mu}{\kappa\Delta q} \quad \text{and} \quad \langle Q^2 \rangle - \langle Q \rangle^2 = \frac{k_B T}{\kappa} \quad (\text{A.4})$$

respectively, where  $A$  is the value of the desired order parameter (Specified using the OFIELD\_A-tag in VASP) and  $\Delta q$  being the difference in average order parameter of the two phases,  $\Delta q = \frac{\langle Q \rangle_{\text{solid}}}{N} - \frac{\langle Q \rangle_{\text{liquid}}}{N}$ . Combining Eqs. (A.3) and (A.4), the latent entropy per particle  $\Delta s$  can be determined from the simulation from:

$$\Delta s = \frac{\Delta u + P\Delta v - \Delta\mu}{T} = \frac{\Delta u + P\Delta v - \kappa\Delta q(A - \langle Q \rangle)}{T} \quad (\text{A.5})$$

Coexistence points are defined by the difference of the chemical potential vanishing,  $\Delta\mu = 0$ . The derivatives along the isotherm and the isobar are given by:

$$\left(\frac{\partial(\Delta\mu)}{\partial P}\right)_T = \Delta v \quad \text{and} \quad \left(\frac{\partial(\Delta\mu)}{\partial T}\right)_P = -\Delta s, \quad (\text{A.6})$$

respectively. The correction from the current state point towards the state points on the coexistence line,  $(T, P_m)$  and  $(T_m, P)$ , can be found by iteration from

$$T^{(i+1)} = T^i + \frac{\Delta\mu}{\Delta s} \quad \text{and} \quad P^{(i+1)} = P^i - \frac{\Delta\mu}{\Delta v} \quad (\text{A.7})$$

assuming that the change between the simulated and the new state points is small enough, so that the change in  $\Delta$  quantities can be neglected. The procedure is repeated until the difference in chemical potential  $\Delta\mu$  vanishes within statistical accuracy. For more details on the method, see Ref. [109].

## A.2 Free electrons in a non-cubic box

To set-up an interface pinning simulation one needs a half solid, half liquid configuration. In order to get there, one first separately finds the volumes that correspond to same pressure for the cube of solid and liquid each. These two volumes taken together give the volume from which the interface pinning simulation should be started with the barostat set to the pressure used to determine the single phase volumes. The problem that occurs here when doing interface pinning with DFT is that the liquid solid combined configurations now exhibits a significant pressure anisotropy. The pressure components  $P_x$ ,  $P_y$  and  $P_z$  taken at every time step for such a simulation is shown in Figure A.2 where the outlier pressure  $P_z$  is the pressure along the long axis that is perpendicular to the interface. The interface configuration was pre-equilibrated using RUMD, therefore the system only needs a few hundred additional time steps to equilibrate in VASP. The additional equilibration explains the larger fluctuation at the beginning but not the subsequent behaviour of the pressure components.

This is not an effect that stems from the interfacing configuration or the bias field belonging to the method. Instead this is due to contributions of the electrons to the pressure. To illustrate this, we take away the liquid part and simplify the system to something that will be referred to as a ‘‘double crystal’’. The double crystal is simply the single phase version of the interface pinning configuration meaning it as crystal with an aspect ration of 1 : 1 : 2 as illustrated in Figure A.3 where again the  $z$  axis is taken to point along the long side.

The pressure anisotropy where the pressure component along the long axis is lower than the short axis pressure components is also exhibited by the double crystal system. Hence, the anisotropy is - as stated before - not an effect that is due to the interface pinning itself but to the non-cubic shape of the system. As a naive solution, the first attempt to alleviate the pressure anisotropy was to slightly change the aspect ratio for the double crystal while keeping the volume constant. To quantify the change of aspect ratio the parameter  $\alpha$  is introduced.

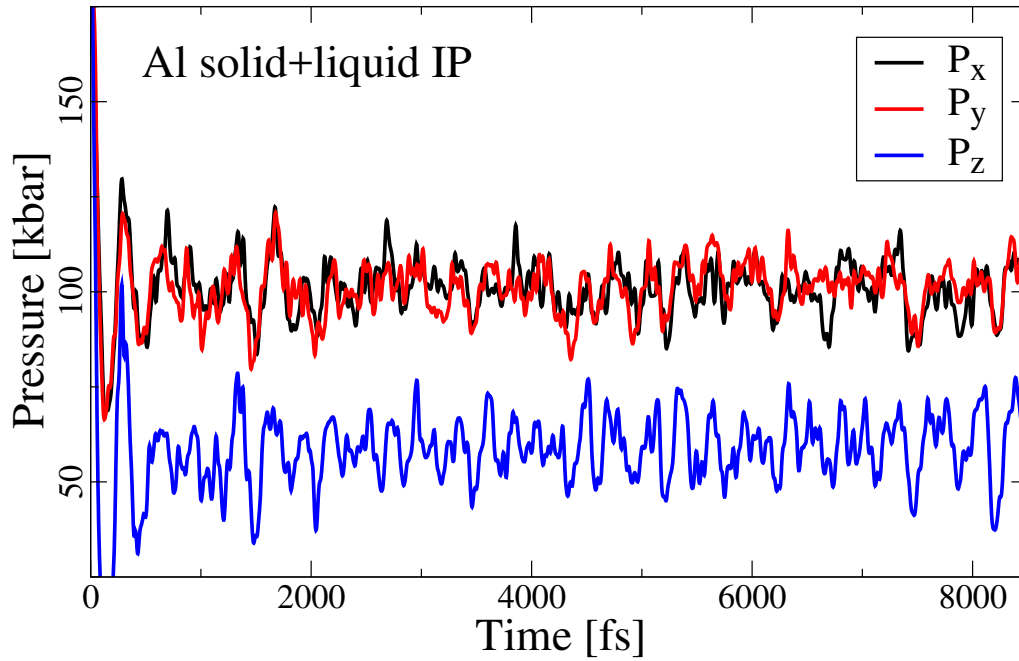


Figure A.2: Pressure by components in the  $x$ ,  $y$  and  $z$  direction (which means the diagonal components of the pressure tensor) of a simulation of an interface pinning configuration. The configuration is half liquid and half solid interfacing with each other. The  $z$  direction and thus the pressure component that is lower compared to the other two components is the direction perpendicular to the interface.

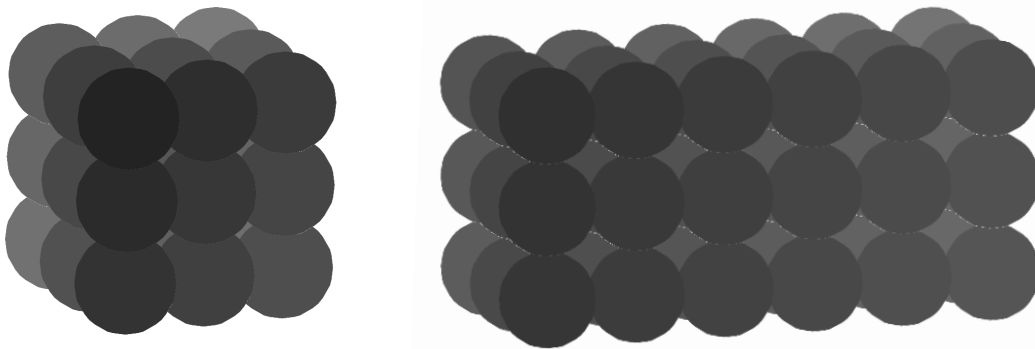


Figure A.3: A regular crystal cube with volume  $V$ ,  $N$  particles and pressure  $P$  is shown on the left. The right illustrates the “double crystal” with volume  $2V$  and  $2N$  particles obtained by doubling the cubic system along one side. The coordinate system is placed with the  $z$  axis pointing along the long side. When going from a cubic crystal to a double cube, the pressure becomes anisotropic even though density stays constant.

The new box lengths are now given by

$$l_x = l_y = \frac{l_0}{\sqrt{\alpha}} \quad l_z = 2l_0 \alpha. \quad (\text{A.8})$$

with  $\alpha = 1$  recovering the double crystal. A perfect double crystal configuration is taken and scaled according to  $\alpha$  going from 0.9 to 1.05 recording the three pressure components  $P_x, P_y, P_z$ . Since the components in the two short directions,  $P_x$  and  $P_y$ , are roughly the same while  $P_z$  is the outlier, the anisotropy is expressed as  $P_z - (P_x + P_y)/2$ . Together with the average of the components, this is shown in Figure A.4 for three different sizes of double crystal.

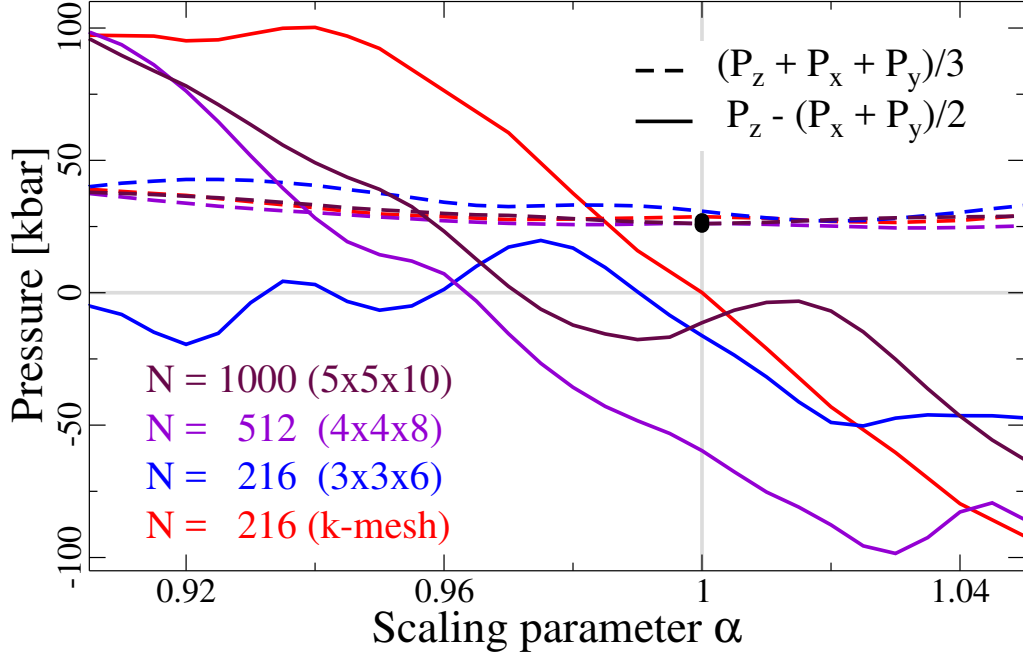


Figure A.4: The average pressure (dashed) and the anisotropy as the difference between  $P_z$  and  $(P_x + P_y)/2$  in four three different systems when changing the aspect ratio of the double crystal box while maintaining constant volume in terms of  $\alpha$ . The system size is given in terms of particle numbers and the corresponding number of FCC unit cells for three of the systems. The fourth (red) is the same as the blue but additionally uses a  $2 \times 2 \times 1$  k-point mesh.

The anisotropy is depicted by the solid line and the average pressure by the dashed lines. The blue and purple-ish sets of lines correspond to the different sizes of crystals as indicated in the figure by number of particles and in terms of the corresponding number of FCC unit cells. The fourth set of lines, the red lines, are a special case using a  $2 \times 2 \times 1$  k-point mesh which will be explained shortly. The vertical grey line indicates the original double crystal with  $\alpha = 1$ . The horizontal grey line is at zero pressure, thus crossings of the horizontal grey line and the solid colored lines mean no anisotropy.

It can be seen that the anisotropy is not linear but has a zig-zag shape and especially the smallest cell has multiple crossings of the zero pressure line. The red line on the other hand is quite linear over a range of  $\alpha$  and the anisotropy vanishes right were  $\alpha = 1$ . The k-point mesh used here is a  $2 \times 2 \times 1$  mesh. The mesh dictates how the Brillouin zone is sampled. Except for this case where we use the mesh, all sampling usually uses only the  $\Gamma$  point. Note that the mesh is the ‘opposite’ shape of the box’s aspect ratio. This results in the electronic system

essentially corresponding to the electronic system of  $6 \times 6 \times 6$  unit cell cube sampled using only the  $\Gamma$  point. Thus it alleviates the pressure anisotropy for the double crystal because the electronic system feels cubic.

The pressure data shown in Figs. A.2 and A.4 are from simulations of Al. Al is considered a prototype simple metal. A simple metal is not to be confused with the simple materials of this work in the sense of R-simple. Instead a simple metal is characterized by its band structure having very small gaps and all energy bands being very close to free-electron bands [61]. A fairly small number of free electrons in a non-cubic box can have a rather dramatic effect on the pressure.

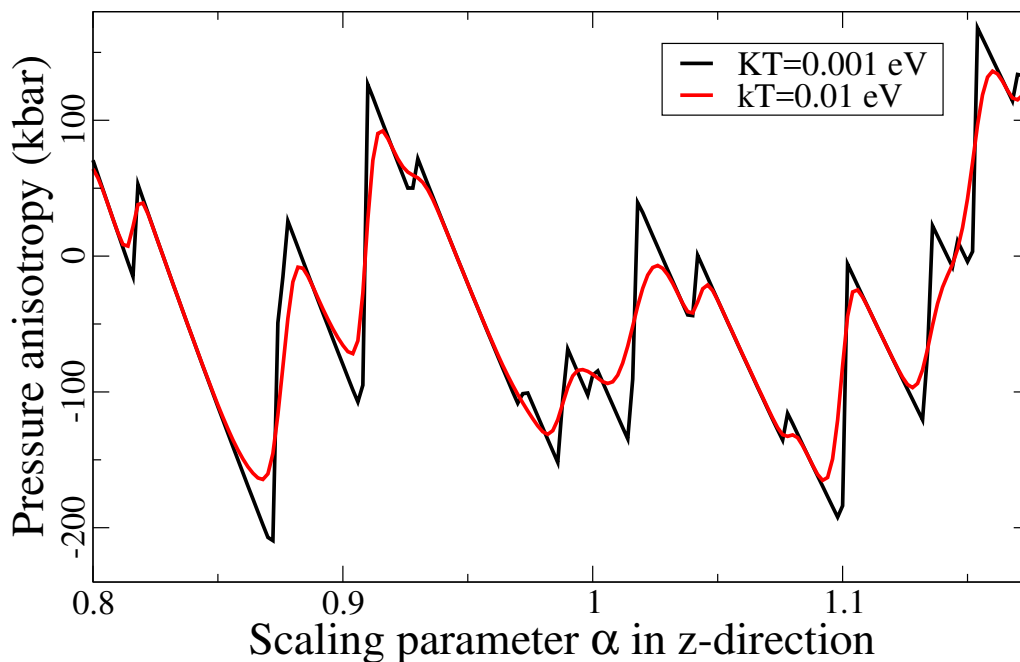


Figure A.5: Pressure anisotropy upon varying the box aspect ratio of a free electron box corresponding to the system shown in blue in Figure A.4. The two curves correspond to two different temperatures

To illustrate this effect, one can perform a similar scaling of the aspect ratio as above without the ionic system. Since the potential used for Al has 3 explicitly treated electrons, the small double crystal with 216 atoms is replaced by 648 free electrons in a box. The resulting pressure anisotropy when changing the aspect ratio of the free electron box (courtesy of my supervisor) are shown in Figure A.5.

The filling of the orbitals varies strongly with minute changes to the box shape. These discontinuous changes in orbital filling causes the stark changes in the anisotropy visible in Fig. A.5. The two lines in the figure correspond to two temperatures. One can see that the extreme sharp spikes that the ground state exhibits get smeared for the increased temperature since the effect of the degeneracy in the ground state becomes less dramatic. Going back to the full system including the nuclei, the degeneracy is alleviated further. However, especially the smallest system shown in blue in Fig. A.4 exhibits a wavy behaviour that is reminiscent of

the sharp spikes for the free electron box.

Including the k-point mesh alleviates the pressure effects from electrons in a non-cubic box because this makes the electronic system of the double cube *feel* cubic again. This is however of limited help for the IP box. Since the specific volume of the liquid is larger than the solid, the IP box is even longer than the double crystal in the long direction. Thus also with a k-mesh, there is an anisotropy present in the IP box. Additionally the author perceives the barostat of VASP as behaving odd. This could of course be a user error, but especially at high pressures we have observed that the average pressure is often off by several kbar from the pressure the barostat was set to (around 5% of the set value). We have therefore opted to avoid simulations in the  $NPT$  ensemble in VASP. Since this means we cannot carry out simulations to determine solid-liquid coexistence ourselves, the reference points for the isomorphs starting from coexistence are taken from literature data.



# B

## Other details

---

This section discusses some issues that occurred during the work on this thesis.

### B.1 Fixing pressure for melting pressure start point

When using the procedure to calculate the melting pressure from nearby isomorphs as detailed in Section 6.1 a problem arises from the fact that the simulations are carried out in the NVT ensemble. This is necessary in order to map out isomorphs but causes a problem because the simulation should also run at a particular pressure. However, the pressure is only indirectly fixed by specifying a volume which means that the simulation runs at the intended pressure to within statistical uncertainty. These uncertainties introduce an offset to the calculated melting pressure. This section shows where this offset originates and explains how the procedure was modified to remove the unphysical offset again.

The expression to calculate the melting pressure given in Ref. [28] is given by:

$$P_m(T) = \frac{\left[ \left( U_s^I - \frac{T}{T_0} U_s^0 \right) - \left( U_l^I - \frac{T}{T_0} U_l^0 \right) + Nk_B T \ln \left( \frac{\rho_s^I / \rho_s^0}{\rho_l^I / \rho_l^0} \right) + \frac{T}{T_0} (W_l^0 - W_s^0) \right]}{V_l^I - V_s^I} \quad (\text{B.1})$$

Considering the above expression at the reference point, i.e. where  $T = T_0$ ,  $U_s^I(T = T_0) = U_s^0$  and  $TU_l^I(T = T_0) = U_l^0$  the expression simplifies to:

$$P_m(T = T_0) = \frac{W_l^0 - W_s^0}{V_l^I - V_s^I} = \frac{P_l^0 V_l^0 - P_s^0 V_s^0}{V_l^0 - V_s^0} \quad (\text{B.2})$$

where in the last step the definition of the virial  $W = PV - Nk_B T$  was used. The starting point was chosen to be at coexistence thus that  $P_m(T = T_0) = P_l = P_s$ . This is where the problem originates from. Since the pressure is not a fixed quantity, the actually measured pressures in the simulation have a small uncertainty  $\sigma$ . Thus we need to instead insert

$P_l^0 = P_m + \sigma_l$  and  $P_s^0 = P_m + \sigma_s$  in Eq. (B.2) which results in:

$$P_m(T = T_0) = \frac{(P_m + \sigma_l)V_l^0 - (P_m + \sigma_s)V_s^0}{V_l^0 - V_s^0} = P_m + \sigma_l \frac{V_l^0}{V_l^0 - V_s^0} + \sigma_s \frac{V_s^0}{V_l^0 - V_s^0} \quad (\text{B.3})$$

Thus, the small and unavoidable deviation of the measured pressure from the intended pressure is amplified by being multiplied by a large number, the volume, and divided by a small number, the difference between liquid and solid volume. In the results shown in this work this is fixed by correcting both virials at the reference point, so that  $W_{\text{corr.}}^0 = P_m V N k_B T^0$ . Since only the reference point virial enters the expression for the melting pressure and no  $W^I$  appears there is no need to translate this shift along the isomorph. The contribution from the correction to the virials does slightly vary due to the volume difference in the denominator changing along the isomorph.

The impact of the correction is illustrated using data for Al in Figure B.1. The solid black lines are the isomorphs from which the melting curve was calculated. The red solid line is the corrected melting curve and the dashed red curve is the un-shifted result from the method. Correcting the virial as described above removes the offset, 165 kbar for Al, from the small pressure error. The intended pressure  $P_m(T = T_0)$  was 275 kbar, the average pressures and their standard deviation obtained from the simulations are  $278 \pm 7$  (liquid) and  $271 \pm 6$  (solid). The ‘magnifying factor’ from the volumes divided by the differences in volume are 23 and 22.

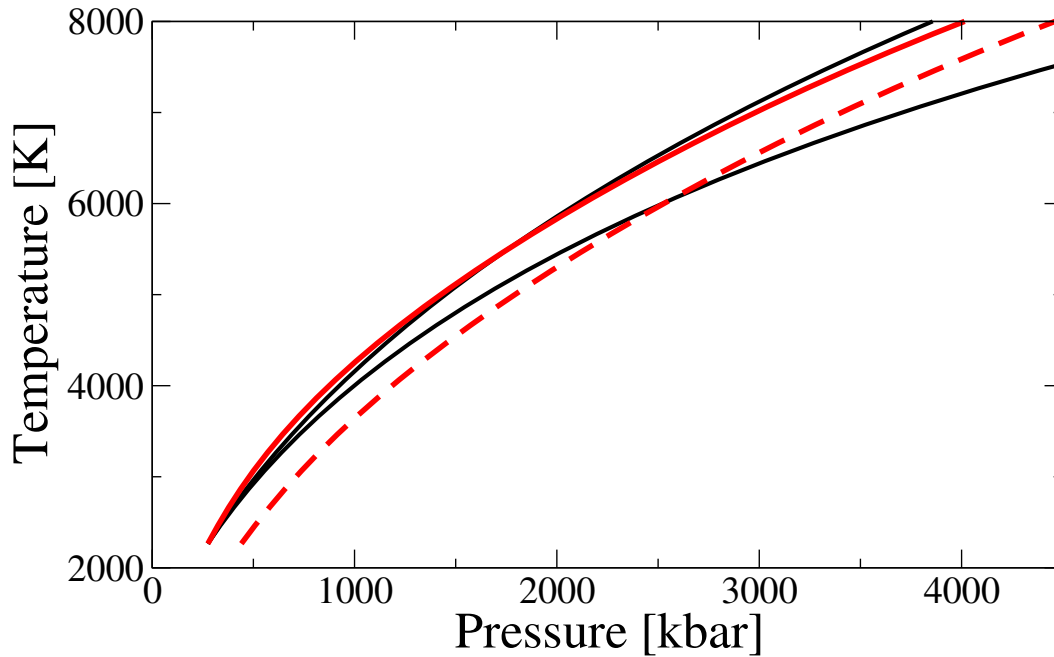


Figure B.1: The figure shows the corrected and the uncorrected melting curve calculated from isomorphs in Al. The isomorphs are denoted by the black lines. The corrected melting curve reported in this work is the solid red curve, the red, dashed curve is the uncorrected melting curve. The offset at the reference point of the uncorrected melting curve is 165 kbar.

## B.2 Polynomial fits to the DIC data

The method to calculate the melting pressure from nearby isomorphs given in Eq. (B.1) takes all input quantities as function of temperature. However, the DIC provides all the required quantities along isomorphs at a set of fixed densities, including a temperature for each density. The data is therefore fitted to polynomials to construct analytical functions of temperature for all input quantities.

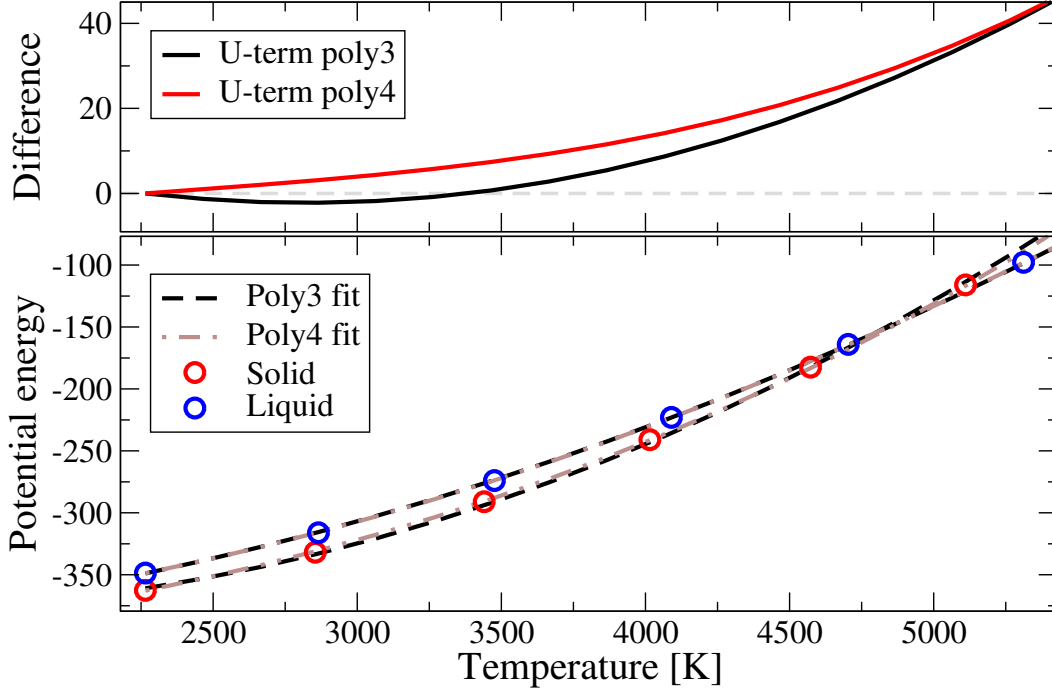


Figure B.2: The bottom panel shows a third and a fourth order fit to the potential energies obtained from the DIC. The top panel shows the effect slightest deviations of the fit functions can have on the resulting term entering into Eq. (B.1)

For most fits, a third order polynomial is sufficient as most curves only deviate slightly from a linear function of temperature. Problems arise where small differences of big numbers enter into the melting pressure calculation method, which happen in the case of the potential energies. In this case a tiny deviation can contribute an odd behaviour to the calculated melting curve results. This is illustrated in Figure B.2. The bottom panel shows the data obtained along the Al solid and liquid isomorph as the red and blue open circles. The third degree polynomial fit is given by the black dashed line and a fit to a fourth order polynomial is given by the brown dot-dash line. To the eye, both fits seem good and do not appear to deviate from each other or the data. The top panel shows the potential energies difference term from Eq. (B.1):

$$\left( U_s^I - \frac{T}{T_0} U_s^0 \right) - \left( U_l^I - \frac{T}{T_0} U_l^0 \right) \quad (\text{B.4})$$

Using the third order fit, this difference first becomes slightly negative before it starts to

rise, while the difference calculated from the fourth order fit has no such non-monotonous behaviour. Since both other terms, the one involving the virials and the the one involving the densities, are nearly constant, the non-monotonous behaviour was translated to the resulting melting curve, giving a melting pressure that first decreased briefly with increasing temperature.

### B.3 Pulay stress

The VASP user manual explains the Pulay stress as follows: *“The Pulay stress arises from the fact that the plane wave basis set is not complete with respect to changes of the volume. Thus, unless absolute convergence with respect to the basis set has been achieved - the diagonal components of the stress tensor are incorrect. This error is often called ”Pulay stress”. The error is almost isotropic (i.e. the same for each diagonal component), and for a finite basis set it tends to decrease volume compared to fully converged calculations (or calculations with a constant energy cutoff).”* [137]

Vasp potentials include a recommended range of ENMIN to ENMAX for the energy cutoff that translates to the number of plane waves used for the given box size. This section explains how to estimate the relation between the Pulay stress and the energy cutoff. If the relation is known, a smaller energy cutoff can be used where the difference in pressure between the smaller energy cutoff and the pressure for the fully converged system is offset by an external pressure via the PSTRESS-tag.

The relation between stress and cutoff is found from varying both box size and cutoff. Figure B.3 illustrates the method for a unit cell of FCC Al. For a set of different cutoffs, the box size of the simulation box is varied given in the figure by the length of the side of one unit cell. The left panel of the figure shows the free energy as a function of the varied box size around the minimum in the free energy. The right panel shows the pressure for the same systems, the minimum in the free energy roughly corresponds to zero pressure. The extremely high cutoffs of 500 and 1000 are included to resemble the fully converged situation as evident by the fact that both curves are on top of each other. The value for the offset pressure is given by the difference of the converged pressure and the pressure for the smaller cutoff we intend to use. The difference is evaluated around the minimum in free energy which roughly corresponds to zero pressure, indicated by the red dashed line in the figure. The point does not

|    | ENMIN   | ENMAX   | ENCUT | PSTRESS |
|----|---------|---------|-------|---------|
| Mg | 100     | 200     | 150   | -0.1    |
| Al | 240.300 | 180.225 | 220   | 1.1     |

Table B.1: The table lists the recommended range for the energy cutoff taken from the respective VASP potential for Al and Mg together with the chosen value and the corresponding pressure offset.

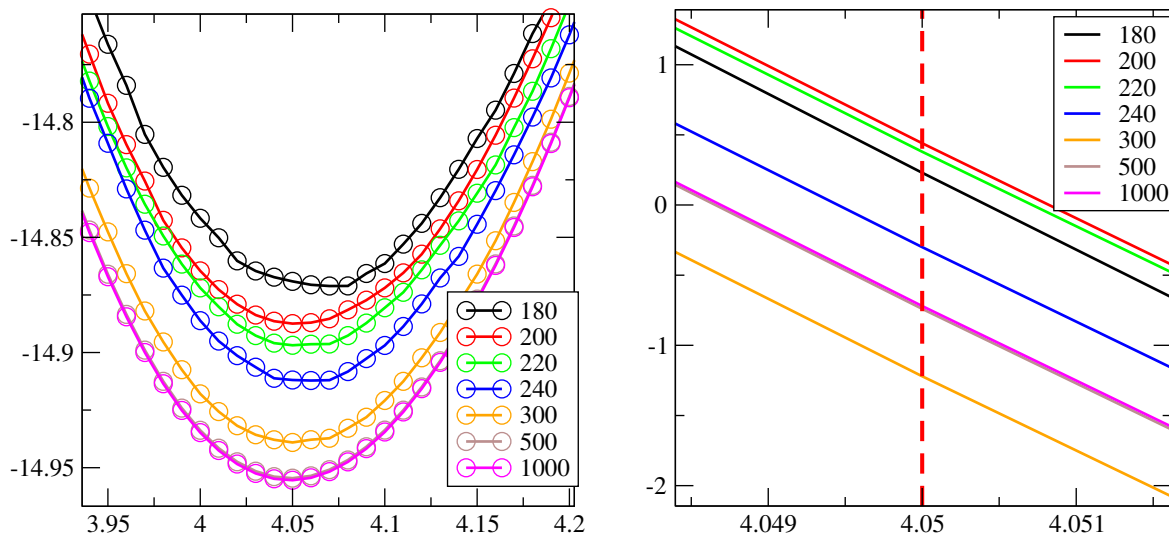


Figure B.3: Estimation of external stress to compensate for using a smaller ENCUT than necessary for full convergence. The figure shows free energy (left) and pressure (right) as a function of the side length of the cubic simulation box. The different colored curves correspond to different values for ENCUT, i.e. the energy cutoff for the plane waves used by VASP. The curves for ENCUT = 500, 1000 are on top of each other meaning this is the limit where a larger ENCUT does not increase accuracy anymore.

need to be exactly at the minimum. The pressures for the different ENCUT values have the same slope around the minimum, which means that the difference between them is constant. For Al, ENCUT= 220 was chosen, giving a pressure difference of 1.1 kbar to the converged ENCUT that needs to be compensated by the PSTRESS-tag. Table B.1 summarizes the results for both Al and Mg. The ENMIN and ENMAX values are taken from the recommendation made in the respective potentials. The cutoff used for the simulations in this work is given in the ENCUT column side by side with the associated PSTRESS value. For both materials the PSTRESS tag was set, but the pressure is so small, it could as well have been neglected especially for Mg.

## B.4 Pressure anisotropy in the HCP DFT crystal

There are two causes for the pressure anisotropy in the HCP crystal used in this work. The pressure by components for an Mg crystal without any corrections to the side lengths is shown in Figure B.4. It can be seen that all three differ from each other. The initial setup of the crystal used the ideal  $c/a$  ratio. The HCP crystal consists of hexagonal layers stacked in an ABAB pattern. The  $c/a$  ratio relates the height between same layers  $c$  to the distance between atoms in the same layer  $a$ . The geometry is illustrated in Figure B.5. To obtain ideal close packing, the ratio is given by  $c/a = \sqrt{8/3} \approx 1.633$ .

Real materials do not pack according to the ideal ratio. The ratio for Mg determined in experiments is very close but slightly smaller than the ideal ratio,  $(c/a)_{\text{exp}} = 1.632$ . Our small

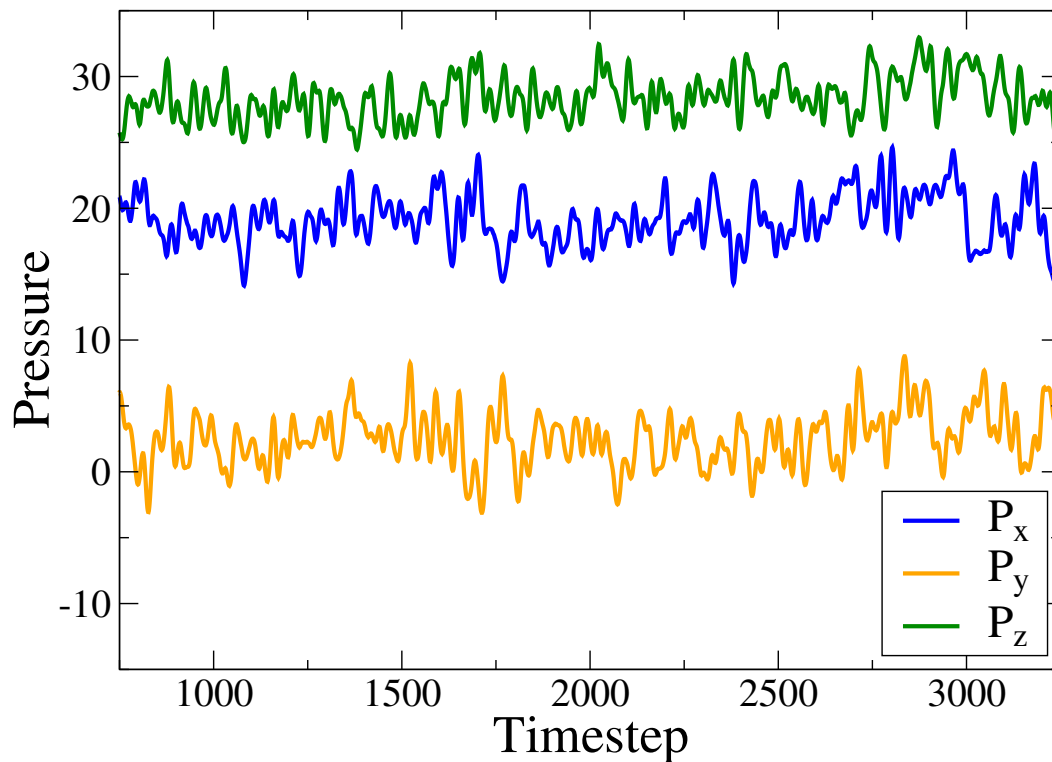


Figure B.4: Pressure by components of an HCP crystal with unchanged side lengths. The  $c/a$  ratio corresponds to the ideal ratio and the hexagonal pattern in the  $xy$  plane is not distorted.

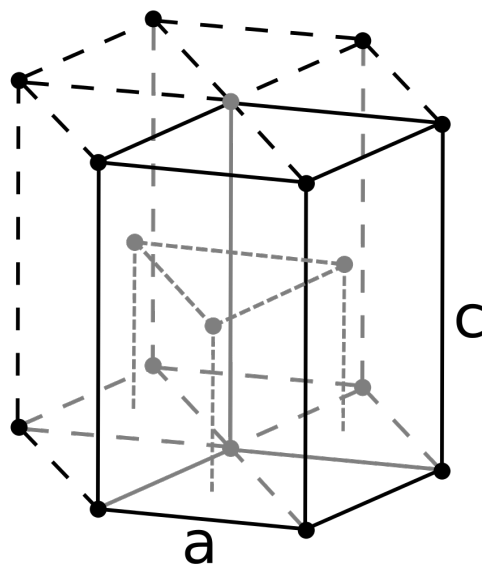


Figure B.5: Geometry of the HCP crystal. The lengths characterizing the crystal are  $a$ , the interparticle distance within the hexagonal layers, and  $c$ , the height between two of the same layers. The layers of the HCP crystal are stacked in an ABAB pattern.

simulation box does not reproduce the experimental ratio which is not surprising given the small size of the simulation box. instead we find a ratio of  $(c/a)_{\text{dft}} = 1.646$ . This still leaves the fact that also the hexagonal layers in the plane contribute to the anisotropy. The hexagonal lattice in the layer is in principle determined by symmetry. But since the box is small and quadratic, the relevant symmetry transformation for the hexagonal lattice cannot be applied to the system. This results in the additional pressure anisotropy that is relieved by tweaking the ratio of the x and y box lengths.

The final aspect ratio we find for the  $(5 \times 3 \times 3)$  unit cell box to give an isotropic pressure is  $(1.001075 \times 1.015684 \times 0.983599)$  (normalized to give a volume of 1). For comparison, the corresponding ratio for the ideally closed packed HCP crystal of the same size is given by  $(0.993995 \times 1.032989 \times 0.973913)$ .



C

*Reprints of articles*

---

**Hidden scale invariance at high pressures in gold and five other face-centered-cubic metal crystals**Laura Friedeheim,<sup>\*</sup> Jeppe C. Dyre, and Nicholas P. Bailey*“Glass and Time,” IMFUFA, Department of Science and Environment, Roskilde University, P.O. Box 260, DK-4000 Roskilde, Denmark*

(Received 18 October 2018; published 27 February 2019)

Recent density functional theory simulations showed that metals have a hitherto overlooked symmetry termed “hidden scale invariance” [Hummel *et al.*, *Phys. Rev. B* **92**, 174116 (2015)]. This scaling property implies the existence of lines in the thermodynamic phase diagram, so-called isomorphs, along which structure and dynamics are invariant to a good approximation when given in properly reduced units. This means that the phase diagram becomes effectively one-dimensional with regard to several physical properties. This paper investigates consequences and implications of the isomorph theory in six metallic crystals: Au, Ni, Cu, Pd, Ag, and Pt. The data are obtained from molecular dynamics simulations employing many-body effective medium theory (EMT) to model the atomic interactions realistically. We test the predictions from isomorph theory for structure and dynamics by means of the radial distribution and the velocity autocorrelation functions, as well as the prediction of instantaneous equilibration after a jump between two isomorph state points. Many properties of crystals tend to be dominated by defects, and many of the properties associated with these defects are expected to be isomorph invariant as well. This is investigated in this paper for the case of vacancy diffusion. In regard to the perfect crystal properties, we find the predicted invariance of structure and also, though less perfectly, of dynamics. We show results on the variation of the density-scaling exponent  $\gamma$ , which can be related to the Grüneisen parameter, for all six metals. We consider large density changes up to a factor of two, corresponding to very high pressures. Unlike systems modeled using the Lennard-Jones potential where the density-scaling exponent  $\gamma$  is almost constant, this quantity varies substantially when using the EMT potential and is also strongly material dependent.

DOI: [10.1103/PhysRevE.99.022142](https://doi.org/10.1103/PhysRevE.99.022142)**I. INTRODUCTION**

The most common state of metals as used by humans is the solid (crystal) phase. Investigation of the properties of pure crystalline metals has played a huge role in the development of solid state physics [1], and the mechanical properties of pure metals and alloys have historically been the most important topic in materials science [2]. It might therefore be thought that all of the basic physics of pure crystalline metals have been well understood and documented. However, recent work has demonstrated the existence of a previously unknown approximate scale invariance in a range of model systems, including metals, in both the liquid and crystal phases. Specifically, in the part of the phase diagram corresponding to the condensed phases there exist curves, termed *isomorphs*, along which a large set of physical properties, namely, those relating to structure and microscopic dynamics, as well as some thermodynamic properties and some transport coefficients, are approximately invariant when expressed in appropriately scaled units [3]. Recent *ab initio* simulations [4] have confirmed that many pure metals belong to the class of systems which have good isomorphs, a class known as Roskilde or R-simple systems. It is the purpose of this paper to document isomorph invariance of structure and dynamics of perfect metallic crystals, specifically the fcc metals Au, Ni, Cu, Pd, Ag, and Pt. The work was inspired by a bachelor’s

degree student project which investigated isomorphs in the liquid state for the same six metals [5].

An early paper [6] presented some evidence that metallic systems belong to the class of R-simple systems. Hu *et al.* have also reported results for a simulated metallic glass [7]. Recently, Hummel *et al.* confirmed using density functional theory (DFT) methods that most metals are R-simple close to their triple point [4]. Because of the large computational cost of DFT methods, other state points were not studied, so the variation of, for example, the density-scaling exponent  $\gamma$  has not been studied. Moreover, the cost of DFT calculations limits what aspects of thermodynamics and structure can be studied and essentially prohibits the study of dynamics and transport coefficients. It is of great interest to investigate and document expected isomorph variances in metallic crystals, liquids, and amorphous structures (metallic glasses) using many-body empirical potentials, which offer a reasonable compromise between computational efficiency and accuracy. In addition, metals form an interesting class of R-simple systems because they are not described by pair interactions (as evidenced by the violation of the Cauchy relations for the elastic constants) [8]; while a good understanding of the density-scaling properties of systems with pair interactions exists [9–11], many-body systems present a challenge: are they R-simple?

In this work we use the effective medium theory (EMT) semiempirical many-body potential [12]. It is considered semiempirical because it is derived from DFT, and some of the parameters are drawn directly from DFT calculations. The expression for the total potential energy is similar in structure

<sup>\*</sup>lauraf@ruc.dk

to other commonly used many-body potentials for metals, such as the embedded atom method (EAM), involving pair sums and some nonlinear “embedding” function. Unlike many EAM potentials, EMT is based on fairly simple functional forms, rather than complex functions which require heavy fitting to large data sets and are typically tabulated. This means that (1) EMT has been relatively straightforward to implement in our graphical processing unit (GPU) molecular dynamics software RUMD [13] and (2) we can hope to understand analytically the existence of strong virial potential-energy correlation in this potential and moreover find an analytic expression for how  $\gamma$  depends on density. We use the simplest version of EMT presented in Ref. [12], which provides all parameters necessary to simulate EMT models of Ni, Cu, Pd, Ag, Pt, and Au.

We restrict our investigation of the isomorph scaling properties of metallic systems to the crystal phases of pure systems, the metal elements listed above. These all have a face-centered-cubic (fcc) ground state at zero pressure. A previous work considered the isomorph scaling properties of classical crystals consisting both of spherical particles interacting via pair potentials, as well as simple molecular systems, and found that simple measures of structure and dynamics are invariant along isomorphs, as expected [14]. We consider the same properties as those authors: we investigate structure as quantified by the radial distribution function (RDF) and dynamics as quantified by the velocity autocorrelation function (VAF), which can be related to the phonon spectrum [15]. Mechanical properties of crystalline materials tend to be dominated by defects, specifically vacancies, interstitials, dislocations, stacking faults, and grain boundaries [16]. Many properties associated with defects are expected to be isomorph invariant—for example, defect mobilities—when expressed in reduced units. As in Ref. [14] we investigate in this work a simple case, namely vacancy diffusion. We also check one of the dramatic predictions of isomorph theory, instantaneous equilibration when a system is brought rapidly from one state point to another on the same isomorph [3].

## II. ISOMORPH THEORY AND HIDDEN SCALE INVARIANCE

Isomorph theory has been developed throughout a series of papers [3,6,17–19] starting from first establishing the existence and subsequently developing a theoretical understanding of strong correlations between the equilibrium fluctuations of the configurational parts of pressure and energy. The correlations are deemed strong when  $R > 0.9$  where  $R$  is the (Pearson) correlation coefficient

$$R = \frac{\langle \Delta W \Delta U \rangle}{\sqrt{\langle (\Delta W)^2 \rangle \langle (\Delta U)^2 \rangle}} \quad (1)$$

with the sharp brackets denoting the canonical constant-volume (NVT) averages, and where  $W$  and  $U$  are the virial and the potential energy, respectively. Systems with these strong correlations are also referred to as R-simple systems to (1) account for the ambiguity of the term “strongly correlated” in physics and chemistry, (2) stress the fact that these systems exhibit a particularly simple behavior in terms of structure and dynamics, and (3) show that this behavior is not limited to

liquids only but extends to the solid phase as well since the strong correlations generally appear when the system is dense [6,17].

Paper IV [3] of the series mentioned above introduced the concept of *isomorphs*. Isomorphs are curves in the phase diagram along which certain static, dynamic, and thermodynamic quantities are invariant when given in appropriately reduced units. Any configuration can be described in terms of the particle coordinates as

$$\mathbf{R} = (\mathbf{r}_1, \mathbf{r}_2, \dots, \mathbf{r}_N) \quad (2)$$

where  $\mathbf{r}_i$  is the coordinate vector of the  $i$ th particle. The reduced unit version is given by  $\tilde{\mathbf{R}} = \rho^{1/3} \mathbf{R}$ , where  $\rho \equiv N/V$  is the number density. If two configurations from different state points have the same reduced coordinates,

$$\rho_1^{1/3} \mathbf{R}_1 = \rho_2^{1/3} \mathbf{R}_2, \quad (3)$$

then Roskilde simplicity implies they have approximately proportional configurational NVT Boltzmann factors

$$\exp \left[ -\frac{U(\mathbf{R}_1)}{k_B T_1} \right] \cong C_{12} \exp \left[ -\frac{U(\mathbf{R}_2)}{k_B T_2} \right], \quad (4)$$

where the constant  $C_{12}$  depends only on the state points  $(T_1, \rho_1)$  and  $(T_2, \rho_2)$  and not on the configurations. This means that the potential energy of a given configuration  $U(\mathbf{R}_i)$  at density  $\rho_i$  can be scaled to a different density on the same isomorph as follows:

$$U(\mathbf{R}_2) \cong \frac{T_2}{T_1} U(\mathbf{R}_1) + k_B T_2 C_{12}, \quad (5)$$

or, considering fluctuations about the respective mean values:

$$\Delta U(\mathbf{R}_2) \cong \frac{T_2}{T_1} \Delta U(\mathbf{R}_1). \quad (6)$$

The shape of an isomorph is characterized in terms of the density-scaling exponent  $\gamma$  defined as the logarithmic derivative of temperature with respect to density along a curve of constant excess entropy. Statistical mechanics provides an expression in terms of fluctuations for this derivative [3], giving

$$\gamma \equiv \left( \frac{\partial \ln T}{\partial \ln \rho} \right)_{S_{\text{ex}}} = \frac{\langle \Delta W \Delta U \rangle}{\langle (\Delta U)^2 \rangle}. \quad (7)$$

“Excess” quantities are defined in reference to the respective quantity for the ideal gas at the same temperature and density, e.g.,  $S_{\text{ex}} = S - S_{\text{id}}$ . Equation (7) allows one to map out isomorphs in a stepwise manner by evaluating  $\gamma$  at each state point. Another way to trace isomorphs is the so-called direct isomorph check (DIC), which exploits the connection between the energies and temperatures of two state points of Eqs. (5) and (6). Hence, plotting the potential energies of the initial microscopic configurations at  $\rho_1$  versus the potential energies of the configurations scaled to another density  $\rho_2$  results in a scatter plot where the slope of the best fit line is given by the ratio of the temperatures,  $T_2/T_1$ . An example of such a scatter plot is shown in Fig. 1. The advantage of the direct isomorph check is that this method allows a whole isomorph to be generated from a single simulation at one reference state point. We have checked that the generated temperatures differ by at most 0.5% from isomorphs generated in the stepwise manner by Eq. (7) (see Appendix A).

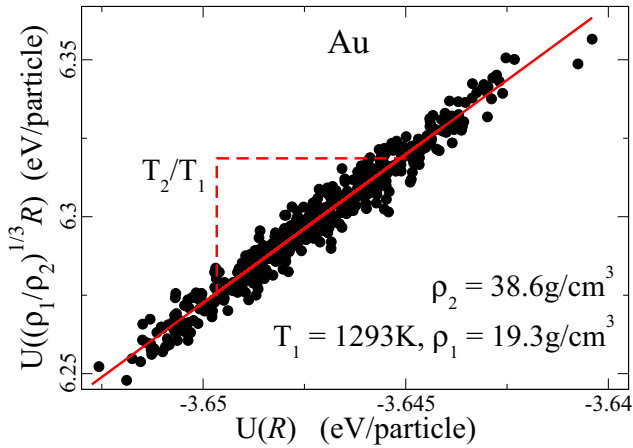


FIG. 1. The direct isomorph check for gold: a scatter plot of potential energies of configurations drawn from a simulation at a given density  $\rho_1$  and temperature  $T_1$  versus the potential energies of the configurations scaled to another density  $\rho_2$ . The red line is the best fit line and has the slope  $T_2/T_1$ , so the temperature  $T_2$  for a state point with density  $\rho_2$  on the same isomorph as the initial state point can be identified from linear regression. The same initial configuration can be scaled to different densities, thus allowing one to map out several isomorph points from a single simulation.

The existence of isomorphs yields the profound simplification of effectively reducing the  $(T, \rho)$ -phase diagram by one dimension. The one-to-one correspondence between state points as illustrated above also explains why many quantities are invariant along isomorphs when given in reduced units. Using the length unit  $l_0$ , time unit  $t_0$ , and an energy unit  $e_0$  defined as follows:

$$l_0 = \rho^{-1/3}, \quad t_0 = \rho^{-1/3} \sqrt{m/k_B T}, \quad e_0 = k_B T, \quad (8)$$

all quantities can be expressed in a dimensionless form to compensate for the trivial scaling of lengths by average interparticle spacing and energies by the temperature.

As pointed out in paper IV [3], systems with strong correlations have isomorphs and vice versa, i.e., these two features are equivalent. It was found later that they are both manifestations of an underlying approximate *hidden scale invariance*. Indeed, isomorph theory has been refined in Ref. [20] by defining R-simple systems directly from a scale invariance of the potential-energy function. It is based on the following scaling behavior:

$$U(\mathbf{R}_a) < U(\mathbf{R}_b) \Rightarrow U(\lambda \mathbf{R}_a) < U(\lambda \mathbf{R}_b), \quad (9)$$

where  $U(\mathbf{R}_i)$  is the potential energy of a configuration  $\mathbf{R}_i$  and  $\lambda$  is a scaling parameter. Thus, a uniform scaling of configurations does not change the ordering of potential energies. For most systems this scale invariance is approximate and dubbed “hidden” since it is not obvious from the mathematical expression for the potential. This approximate scaling is illustrated in Fig. 2, where the potential energies of 20 configurations from an equilibrium simulation have been scaled to different densities. For clarity the energies have been shifted and scaled using the mean value and standard deviation at each density. For perfectly isomorph systems—with correlation

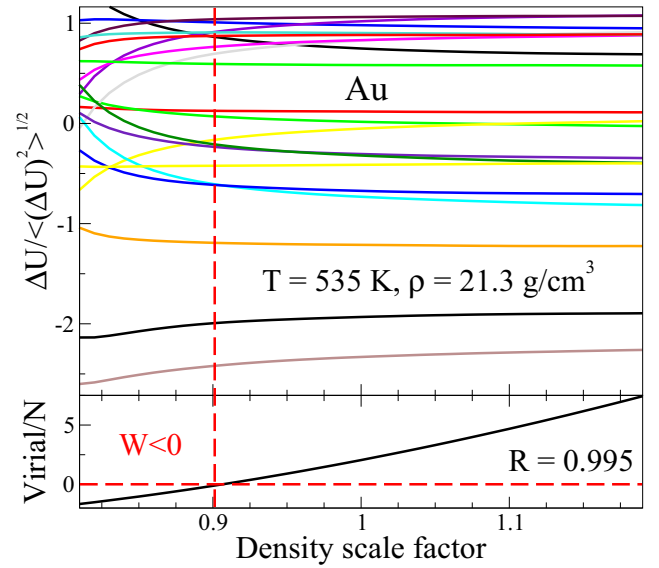


FIG. 2. Gold’s potential energy per particle after subtracting the average and scaling by the standard deviation of 20 configurations taken from an equilibrium simulation, which were subsequently scaled uniformly by 20% up and down in density and plotted as a function of the density-scaling factor. The lines obtained in this way illustrate the hidden scale invariance of R-simple systems and cannot cross each other in the ideal ( $R = 1$ ) case. The configurations used for generating this figure are taken from equilibrium simulations at a state point close to ambient conditions at which  $R = 0.995$ . The bottom panel shows the average virial for the scaled configurations. The strongly diverging lines in the left part of the figure are due to the virial becoming negative (indicated by the red dashed lines).

coefficient  $R = 1$ —the lines cannot cross each other. The red dashed line indicates where the virial becomes negative, which leads to a breakdown of the scaling properties as seen by the sudden diverging of the lines.

The updated definition preserves the property that isomorphs are the configurational adiabats of the phase diagram, curves along which structure, dynamics, and the excess entropy  $S_{\text{ex}}$  are invariant together with the simplification of effectively reducing the phase diagram by one dimension. Subtle differences between the versions of isomorph theory emanate from the fact that the original formulation is a first-order approximation of the more accurate updated theory of Ref. [20]. This can be illustrated, for example, using the case of the isochoric heat capacity  $C_V$ . If exactly obeyed, Eq. (4) implies that  $C_V$  is invariant along isomorphs, which is often a good approximation but not exact. The slight variation of  $C_V$  along isomorphs can, however, be accommodated using the more recent formulation of isomorph theory, with which Eq. (6) can be derived without requiring Eq. (4) or (5) [20].

One of the more fundamental consequences of the update concerns the density-scaling exponent  $\gamma$ . Initially the density-scaling exponent  $\gamma$  was interpreted as being related to an effective inverse power law exponent, which (assuming it to be constant) yields the form  $\rho^\gamma/T = \text{const}$  for isomorphs, consistent with experimental determinations of isochrones [10,21–26]. Determination of  $\gamma$  from fluctuations in simulations shows variation with state point, however [6]. It was

TABLE I. Comparison of correlation coefficient  $R$  and density-scaling exponent  $\gamma$  calculated using DFT and using EMT. A liquid state point near the triple point is used in each case. The DFT values are taken from Ref. [4].

| Sym. | Z  | T (K) | $\rho$ ( $\frac{\text{g}}{\text{cm}^3}$ ) | $R_{\text{EMT}}$ | $R_{\text{DFT}}$ | $\gamma_{\text{EMT}}$ | $\gamma_{\text{DFT}}$ |
|------|----|-------|---|------------------|------------------|-----------------------|-----------------------|
| Ni   | 28 | 2000  | 8.19                                      | 0.96             | 0.92(0.03)       | 3.62(0.01)            | 3.5(0.3)              |
| Cu   | 29 | 1480  | 8.02                                      | 0.95             | 0.90(0.02)       | 4.15(0.02)            | 4.1(0.2)              |
| Pd   | 46 | 1900  | 10.38                                     | 0.91             | 0.92(0.04)       | 6.47(0.03)            | 4.9(0.5)              |
| Ag   | 47 | 1350  | 9.32                                      | 0.93             | 0.90(0.03)       | 5.35(0.02)            | 4.8(0.4)              |
| Pt   | 78 | 2200  | 18.53                                     | 0.87             | 0.87(0.06)       | 7.88(0.05)            | 6.0(1.4)              |
| Au   | 79 | 1470  | 16.69                                     | 0.88             | 0.86(0.14)       | 7.93(0.05)            | 7.9(1.6)              |

shown in Ref. [11] that the assumption of constant  $C_V$  along isomorphs implies that  $\gamma$  can depend only on density, which is a fairly good approximation. The most recent definition of hidden scale invariance allows, however, temperature dependence of  $\gamma$  also to be handled within the theory [20].

We find, in fact, that for metals—at least when using the EMT potential— $\gamma$  does vary significantly, both for a given metal and between metals. Table I shows a comparison of the DFT and EMT values of the parameters  $R$  and  $\gamma$  for the liquid phase near the triple point. There is reasonable agreement between the  $R$  and  $\gamma$  values, especially noting that the latter vary quite widely (more than a factor of two). From this we can conclude that EMT gives a reasonably accurate description of the thermodynamic scaling properties of these metals. A version of this table appeared in Ref. [5].

### III. SIMULATION RESULTS

The results presented in this paper for the fcc metals Ni, Cu, Pd, Ag, Pt, and Au have been obtained from simulations carried out in RUMD [13,27] using the effective medium theory (EMT) potential. The potential is based on a reference system modified with a correction term. The reference system is chosen to give a close to accurate description while still being a simple, well-known system which can be fitted through some built-in scaling parameter. For metal crystals this can be achieved with an ideal fcc lattice where the lattice constant serves as the scaling parameter. The correction term accounts for the difference between the real and the reference system and is based on a pair potential. A detailed description of the potential and the respective material-specific parameters is given in Ref. [12].

The simulated systems consist of 4000 particles organized on a  $10 \times 10 \times 10$  fcc lattice with periodic boundary conditions. Atomic masses and densities are taken from Ref. [28].

For each metal, we simulate at least three curves: one isomorph, one isotherm, and one isochore. The state points for the isomorph have been determined using a single simulation and the direct isomorph check, as described in the previous section. We obtain isomorph points corresponding to steps of 10% density change in terms of the reference density up to a total increase of 100% in density. The state points for the isochore (isotherm) are chosen so that they match the temperatures (densities) of the points along the isomorph. The initial state point for each metal is chosen to resemble a crystal with room temperature density,  $\rho_{rt}$ . ([28]), at 1293 K

TABLE II. Pressure  $P$ , virial  $W$ , correlation coefficient  $R$ , and density-scaling exponent  $\gamma$  along the studied isomorph for gold.

| T (K)  | $\rho$ ( $\frac{\text{g}}{\text{cm}^3}$ ) | P (GPa) | $W$ ( $\frac{eV}{\text{particle}}$ ) | R     | $\gamma$ |
|--------|---|---------|--------------------------------------|-------|----------|
| 1293   | 19.32                                     | 10      | 0.86                                 | 0.986 | 6.47     |
| 2177   | 21.25                                     | 30      | 3.03                                 | 0.994 | 4.66     |
| 3143   | 23.18                                     | 70      | 5.58                                 | 0.996 | 3.77     |
| 4175   | 25.12                                     | 110     | 8.50                                 | 0.997 | 3.25     |
| 5255   | 27.05                                     | 160     | 11.73                                | 0.998 | 2.90     |
| 6374   | 28.98                                     | 220     | 15.25                                | 0.998 | 2.63     |
| 7522   | 30.91                                     | 300     | 19.03                                | 0.998 | 2.44     |
| 8692   | 32.84                                     | 380     | 23.05                                | 0.998 | 2.27     |
| 9879   | 34.78                                     | 480     | 27.29                                | 0.998 | 2.14     |
| 11 073 | 36.71                                     | 590     | 31.71                                | 0.998 | 2.02     |
| 12 270 | 38.64                                     | 710     | 36.32                                | 0.998 | 1.92     |

for gold, corresponding to a pressure of 10 GPa. The isotherm is along  $T = 1293.15$  K and thus shares the initial point with the isomorph. To avoid melting on isochores, they start at higher densities,  $\rho = 32.84$  g/cm<sup>3</sup> for the investigation of structural and dynamical invariance and  $\rho = 30.91$  g/cm<sup>3</sup> for the vacancy study.

For each state point the NVT ensemble was simulated using periodic boundary conditions and a Nosé-Hoover thermostat. Table II shows the temperatures and densities for the isomorph simulated for Au, while Fig. 3 shows the isomorph together with the melting curve for this system. The latter was determined using the interface pinning method [29]. A single point from the experimental melting curve is included, showing that it lies somewhat higher in temperature than the model curve. A slight discrepancy between model and experiment is expected if the model has not explicitly been fitted to the melting temperature. Melting is identified as the point where the Gibbs free energies of the solid and the liquid phase are equal, thus a precise prediction for the melting

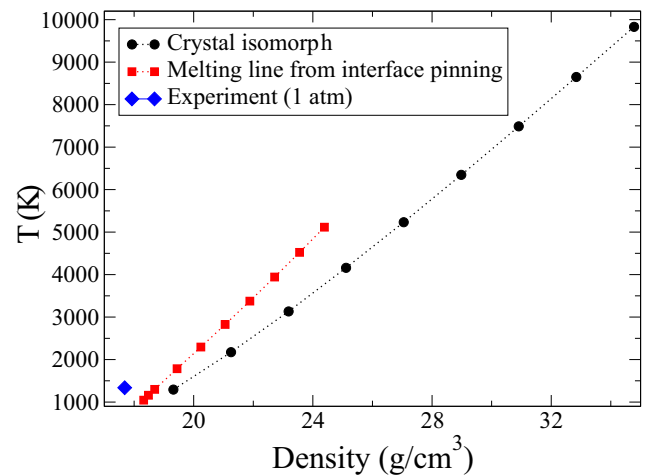


FIG. 3. A density-temperature phase diagram of EMT-Au showing the melting curve determined by the interface-pinning method [29] and the crystal isomorph studied in this work. One point from the experimental melting curve is also included [30]. The isomorph for Au studied in this work is quite close to the melting curve.

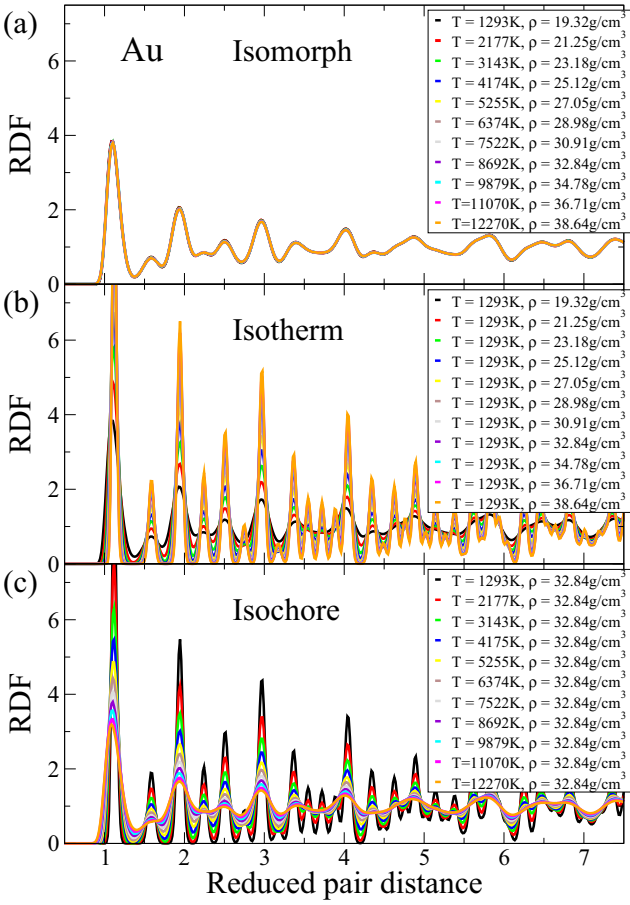


FIG. 4. The radial distribution functions (RDFs) plotted in reduced units [see Eq. (8)] for the case of gold. From top to bottom, the panels show the RDFs for state points that are respectively isomorph, isothermal, and isochore to each other. The top panel shows the data collapse along an isomorph as predicted by isomorph theory. Isomorph and isotherm share the state point indicated by the black line, while isochore and isomorph match at the purple line (this is done to avoid melting of the crystal along the isochore; the highest temperature is probably above the melting temperature, however, meaning that this is a superheated state).

temperature requires a model that describes both phases with the same accuracy, which is usually not the case [31].

#### A. Isomorph invariance of structure and dynamics

We start with the results on structure and dynamics. For brevity, the results shown here in detail are from simulations for gold; the other five materials exhibit the same behavior and will be presented in a summarized fashion. A phase diagram is shown in Fig. 3 indicating the isomorph simulated along with the melting curve for the model, to give an idea of where in the phase diagram our focus lies. Some numerical data for gold along the isomorph are shown in Table II. The structure of a system can be quantified by the radial distribution function (RDF), also called pair-correlation function  $g(r)$ , which is a measure of the probability of finding a particle at a distance  $r$  away from a given reference particle. Figure 4 shows the RDF for the reduced pair distance  $\tilde{r} = \rho^{1/3}r$  for the state points indicated in the panels, thus along an isomorph, an isotherm,

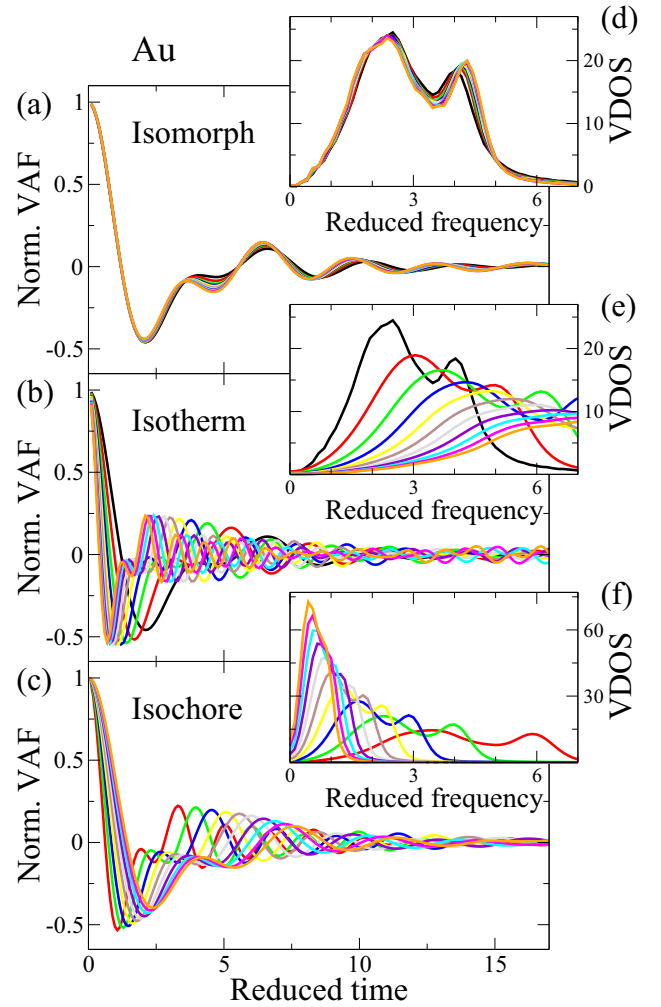


FIG. 5. The figure shows the normalized velocity autocorrelation function (VAF) for the same state points as in Fig. 4. The insets depict the respective phonon or vibrational densities of states (VDOS) obtained from the Fourier transform of the VAF [Eq. (10)]. The predicted data collapse along the isomorph is obeyed, although not as well as in the RDF case.

and an isochore, respectively. The peak positions are expected to remain the same also along the isotherm and isochore as a trivial consequence of the reduced pair distance being scaled by  $\rho^{1/3}$ . Isomorph theory predicts that the structure along an isomorph is invariant, thus we expect all isomorph RDFs to collapse onto a single curve. Figure 4 validates this to a good approximation, even for large density changes, for the case of gold.

In addition to the structure, also the dynamics of isomorph state points are predicted to be invariant. The dynamics are studied here by means of the velocity autocorrelation function (VAF). Figure 5 shows the normalized reduced-unit single-particle VAFs obtained from the same simulations and state points of gold as the RDF data. The top, middle, and bottom panels show the VAFs for state points along isomorph, isotherm, and isochore, respectively. The isomorph curves exhibit a reasonable collapse but with some deviation, especially compared to the near perfect agreement in the RDF

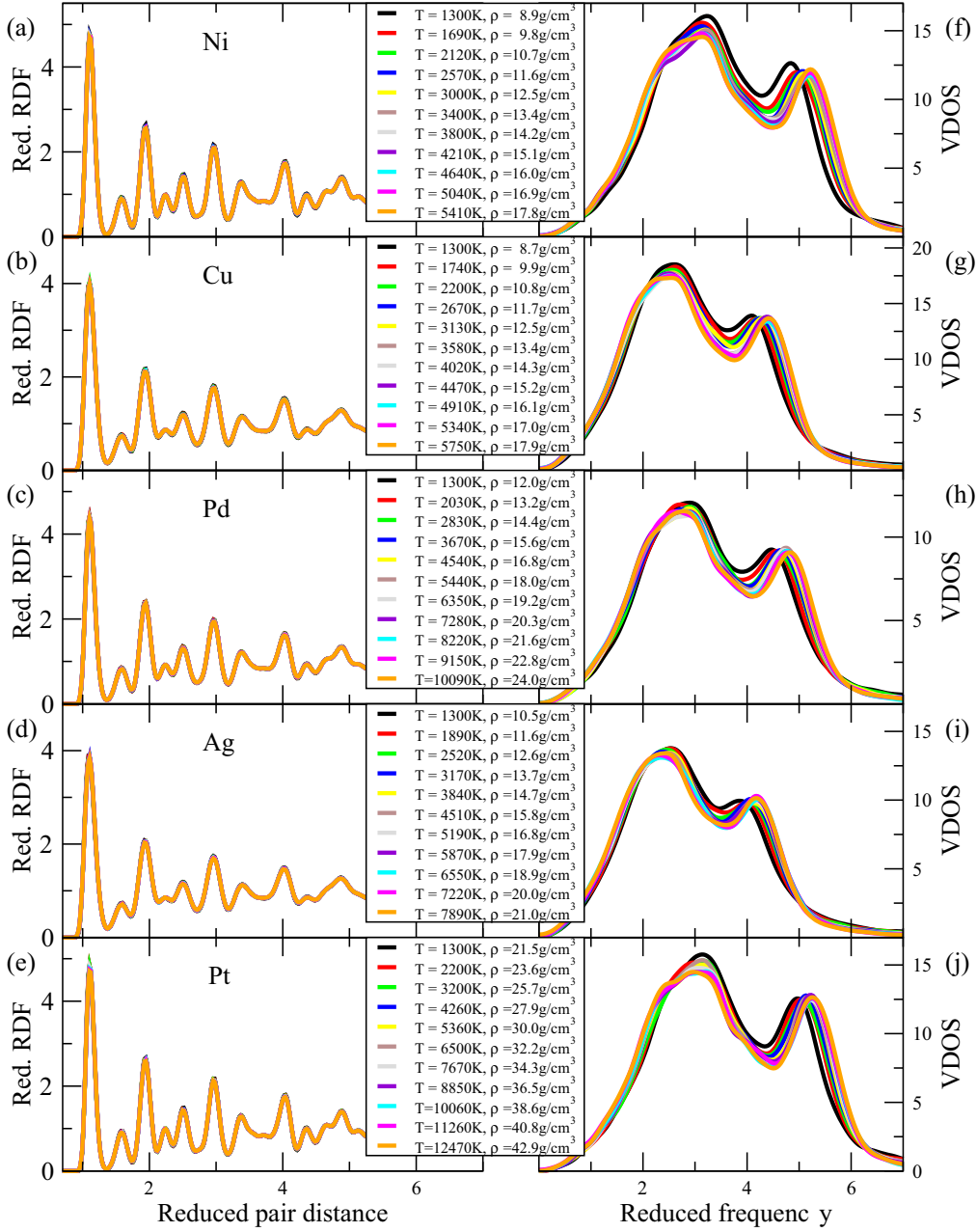


FIG. 6. Radial distribution functions (RDFs) and vibrational densities of states (VDOS) along isomorphs for Ni, Cu, Pd, Ag, Pt. The other five metals confirm the findings for gold, i.e., a near perfect collapse for the structure and a less perfect, but reasonable collapse for the dynamic. The most notable deviations are for the first state point(s).

case. The insets of Fig. 5 show the phonon (vibrational) density of states of their respective curves. The spectrum is related to the Fourier transform of the velocity autocorrelation function via [15]

$$\rho(\omega) = \frac{1}{3NTk_B} \int_{-\infty}^{\infty} \sum_{i=1}^N \langle v_i(t)v_i(0) \rangle C(t) e^{i\omega t} dt, \quad (10)$$

where we include a Gaussian function  $C(t) = \exp[-(t/t_c)^2]$  (with  $t_c$  chosen to be fixed in reduced units) to smoothly truncate the integrand, which otherwise decays very slowly compared to the data-sampling window.

We obtained similar results for the structure and dynamics of the five other materials simulated, *viz.*, Ni, Cu, Pd, Ag, and Pt; see Fig. 6. Each row shows the RDF on the left and the phonon density on the right, along an isomorph for one metal. All metals demonstrate a comparably good collapse to that found for gold.

### B. Other implications of isomorph theory

Another prediction from isomorph theory concerns *isomorph jumps*, which refer to a sudden change in density via a uniform scaling of all particle coordinates and temperature

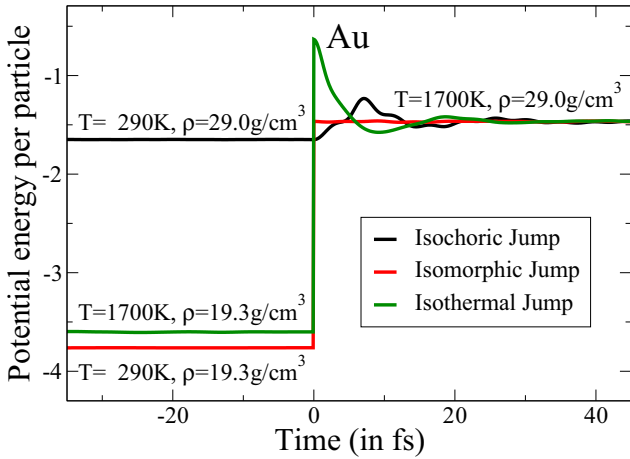


FIG. 7. Potential energy per particle before and after instantaneous jumps at  $t = 0$  between the state points indicated. The black and the green lines depict jumps between state points that are, respectively, isochoric and isothermal to each other. Only the red line shows instantaneous equilibration—the line stays flat and does not visibly fluctuate—after the jump.

between state points on the same isomorph. Isomorph theory implies that such a sudden change from a well-equilibrated initial state point should not require further equilibration post jump, predicting the system to be instantaneously in equilibrium at the final state point [3], because the Boltzmann probabilities are unchanged by a jump along an isomorph. This prediction has been validated for viscous liquids, as well as for perfect Lennard-Jones crystals.

The simulations start with runs at the respective starting point to make sure the systems are in equilibrium. At the jump, the density is changed by uniformly scaling all particle coordinates, the temperature for the thermostat is set to the new value, and all velocities are scaled accordingly. The results for gold can be found in Fig. 7, showing the potential energy per particle before ( $t < 0$ ) and after ( $t > 0$ ) jumps to the point indicated in the figure. The initial points have been chosen to be isothermal (green), isochoric (black) and isomorph (red) to the final state point. The red line validates the prediction as it shows no visible fluctuations in the potential energy post jump. The system is instantaneously in equilibrium as evidenced by the red line staying perfectly flat (apart from normal equilibrium fluctuations, not visible here). In contrast to this, the black and the green lines are clearly not in equilibrium, and the potential energies oscillate towards the new level after the jump.

Since many mechanical properties in crystals are associated with the existence of defects in the lattice and these properties are also expected to be isomorph invariant, we examine this in the following for the case of vacancy diffusion. A vacancy in the lattice is an empty spot from which the atom has been removed. This introduces a new kind of dynamics to the crystal since atoms can now jump to the new, empty positions on the lattice, resulting in the vacancies moving around. Vacancy diffusion is quantified by means of the mean-square displacement (MSD) of the atoms [14,32]. Figure 8 shows the MSD along isomorph, isochore and isotherm for

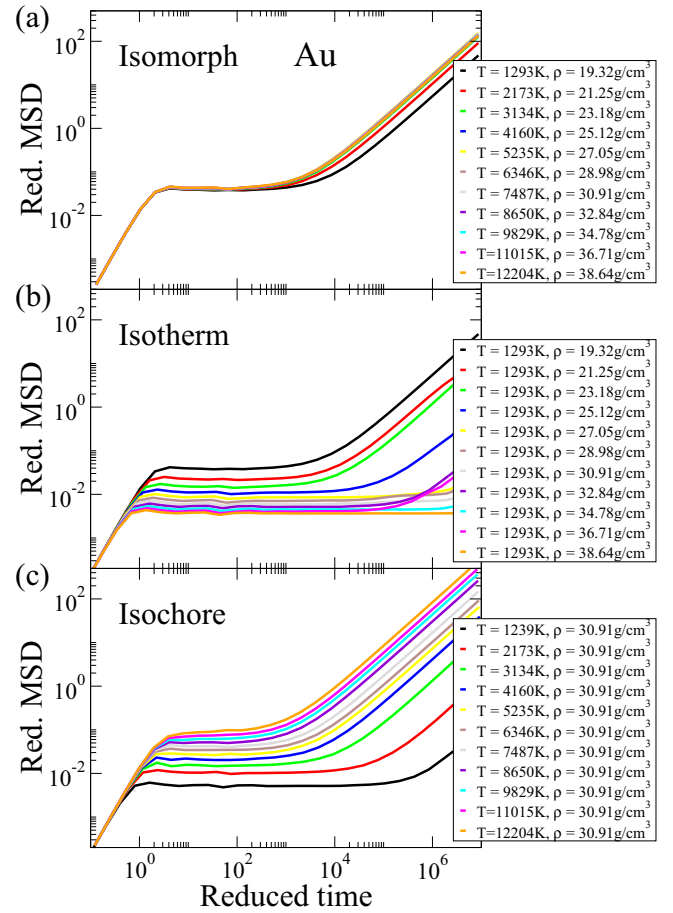


FIG. 8. Mean-squared displacement (MSD) for the state points indicated. To generate vacancies, four randomly selected atoms have been removed from the initial crystal. The collapse exhibited along the isomorph is good in the ballistic regime (trivial) and the plateau (less trivial), while the diffusive part shows some deviations, especially for the lowest density state point. (Note that the isochore has a slightly different density than that of Fig. 4.)

the case of four particles removed from a  $10 \times 10 \times 10$  fcc crystal of gold, corresponding to a vacancy concentration of  $10^{-3}$ , which is only slightly higher than the experimental concentration close to melting,  $7 \times 10^{-4}$  [33]. The isomorph used for studying diffusion was redetermined using the DIC, leading to slightly different temperatures.

The figure shows an approximate collapse along the isomorph, although there is a noticeable deviation for the first two curves (the lowest two densities). The collapse is poorer than that seen for the Lennard-Jones crystal in Ref. [14]. This can be partly explained by observing that the starting state point in the present case is closer (in density) to the triple point than was the case for the Lennard-Jones results, although the pressure in our simulations is still large by experimental standards (see Table II). The pre-diffusive parts of the curves collapse well. For the initial ballistic regime the MSD is proportional to time squared, which is a trivial consequence of the use of reduced units and has nothing to do with isomorph invariance (this is seen also for the isochore and isotherm). But the invariance of the height and

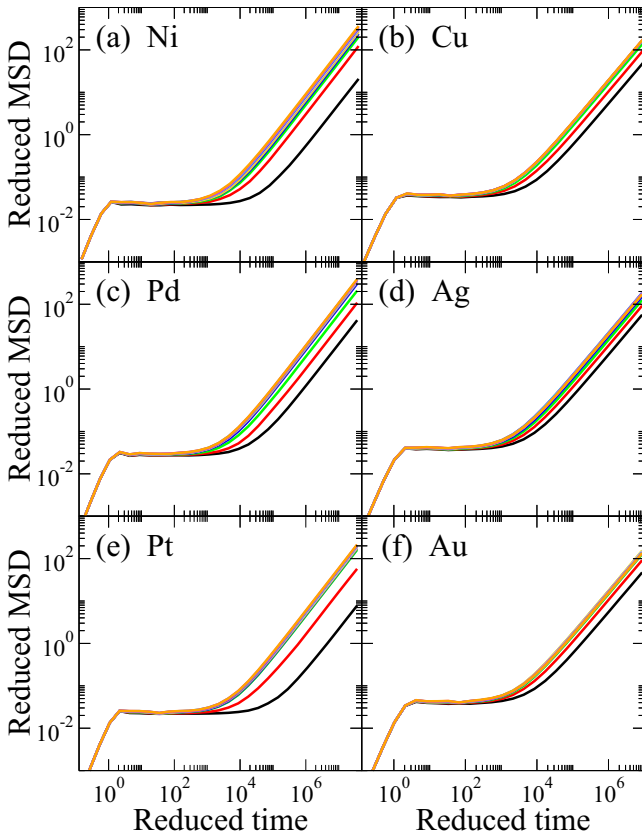


FIG. 9. Mean-squared displacement along isomorphs for the six metals with four vacancies (the bottom right panel depicting gold shows the same data as the top panel of Fig. 8).

the location of the onset of the plateau are nontrivial aspects of the vibrational dynamics. The diffusivity (corresponding in the double-logarithmic representation to the height of the long-time part of the MSD curves) is presumably determined by a single energy barrier associated with vacancy hopping. The poor collapse of the curves here therefore implies that this energy barrier scales in a slightly different manner than the potential energy surface near the ground state—it is the latter which controls vibrational dynamics whose fluctuations determine the isomorph.

Figure 9 shows the MSD along an isomorph in all six fcc metals with each crystal having four vacancies. The bottom right panel shows the same gold isomorph as in the previous figure. The same overall behavior is observed in the other metals, i.e., that the higher density and temperature points collapse well while the first (two) curve(s) exhibit an outlier behavior. This is more notable for the materials on the left-hand side; these have incomplete d-shells, corresponding to stronger bonding and higher melting points, therefore the simulated isomorphs (which all start at the same temperature) are further below the melting line in these cases.

Results for a single vacancy and 16 vacancies in the same  $10 \times 10 \times 10$  fcc crystal of the six metals can be found in Appendix B. Both cases exhibit a much worse collapse than the case of four vacancies. For 16 vacancies, visualization (snapshot included in Appendix B) shows that the vacancy

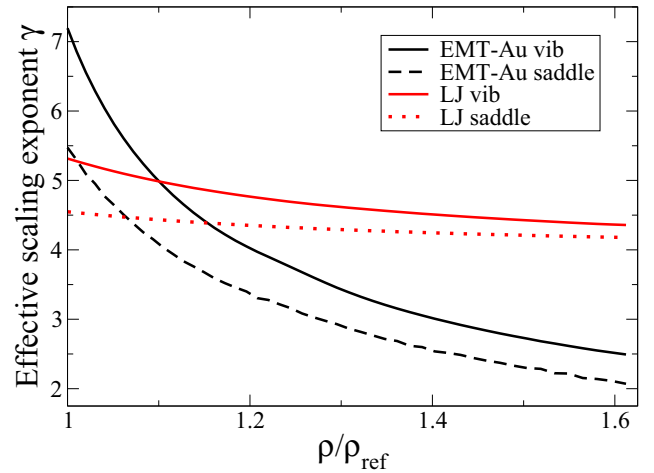


FIG. 10. Effective scaling exponent for specific configurations determined using EMT potential for gold and the Lennard-Jones (LJ) potential. The vibrational configurations, one for each system, were sampled from an NVT run of the perfect crystal at density  $\rho_{\text{ref}} = 19.3 \text{ g/cm}^3$  and temperature 1300 K for Au, density  $\rho_{\text{ref}} = 1.05\sigma^{-3}$ , and temperature  $0.630 \epsilon/k_B$  for LJ. The potential energy relative to the perfect lattice was determined for a range of densities (scaling both the perfect lattice and the vibrational configuration). The saddle configurations are the unrelaxed saddle point between vacancy hopping, constructed by moving a neighbor atom of the vacancy in an otherwise perfect crystal halfway towards the vacant site. The energy difference between the unrelaxed saddle point and the unrelaxed vacancy was determined for the same range of densities. The effective scaling exponents given by the logarithmic derivatives  $d \ln U / d \ln \rho$  are plotted against the reduced densities  $\rho / \rho_{\text{ref}}$ .

concentration is too high, which causes them to cluster together early on in the simulation runs. We thus in this case inadvertently probed void migration rather than vacancy diffusion. Especially interesting is the case of one vacancy where clustering is not an issue. We found a failure to collapse much like Albrechtsen and Olsen found for Lennard-Jones crystals with only one vacancy [34]. This case seems especially sensitive to departures from isomorph invariance (see also the discussion of Fig. 10), but at present we do not have a good explanation of this deviation.

#### IV. DISCUSSION

The overall results presented here are consistent with expectations from the work of Hummel *et al.*, which showed that most metals in the liquid state have a high virial potential-energy correlation coefficient  $R$  [Eq. (1)] and are therefore R-simple. As such they are expected to have good isomorphs. The present work has concentrated on the crystal phase at moderate and high temperatures to avoid quantum effects. The analysis is similar to that undertaken by Albrechtsen *et al.* for Lennard-Jones and other simple model systems including simple molecules [14].

The basic predictions of isomorph theory are invariance of structure and dynamics when the observables are expressed in reduced units: lengths in terms of the interparticle spacing  $\rho^{-1/3}$ , energies in terms of the temperature  $k_B T$ , and times in

terms of the time a particle with the thermal velocity would take to move an interparticle spacing [Eq. (8)]. With these units we find an excellent collapse of the radial distribution function. For the dynamics of the perfect crystal we studied the velocity autocorrelation function (VAF) and its Fourier transform, which can be interpreted as an effective vibrational density of states (VDOS). Here we observed an approximate collapse, clearly worse than the RDF, and also worse than the collapse seen for the Lennard-Jones crystal in Ref. [14]. We validated the prediction of instantaneous equilibration for isomorph jumps. To study dynamics beyond vibrations we simulated a system with vacancies and monitored the mean squared displacement. The collapse here was also approximate, in fact poorer than for the VAF, suggesting that the relevant energies (around the saddle point of the vacancy hopping process) scale somewhat differently with density than energies near ground state (perfect crystal), which are relevant for vibrations. In particular one can imagine that the local density experienced by the hopping atom at the top of the energy barrier is quite different from the densities of the surrounding atoms, corresponding to different effective  $\gamma$ .

The combination of locally high density at the saddle point for the hopping atom and the strong density dependence of the density-scaling exponent for EMT systems suggests a scenario like this. As a crude test we consider the energy of the “unrelaxed saddle point” relative to that of the unrelaxed vacancy, as well as the energy of a typical vibrational configuration of the defect-free lattice, drawn from a simulation at a specific temperature, relative to that of the perfect lattice. The unrelaxed vacancy is the perfect lattice with one atom removed. The unrelaxed saddle point is the configuration obtained by displacing a neighbor of the removed atom exactly halfway towards the empty site. The logarithmic derivatives of these energy differences give a kind of “configuration-specific” density-scaling exponent  $\gamma$ , plotted in Fig. 10. There is a significant reduction in the effective scaling exponent for the unrelaxed saddle-point energy compared to that of the vibrational energy (5.5 versus 7.2 at the initial density). Since vibrational fluctuations dominate the determination of the  $\gamma$  used to generate isomorphs, the lower scaling exponent for saddle points means these configurations have a lower energy than expected as one moves along the isomorph, which is why the diffusivity in reduced units is higher than than for the reference state point. The contrast between the energy fluctuations used to determine the isomorph and those relevant for the dynamics is greater for a defective crystal than for a liquid or amorphous solid, allowing such deviations from perfect isomorph scaling to arise. The figure includes also results of the same calculation for the Lennard-Jones crystal, where there is also a difference, albeit smaller than in the EMT case. The presence of this difference is consistent with the lack of collapse for a single vacancy noted in Ref. [34], while its small size explains the generally better collapse found in Ref. [14]. It remains unclear why including several vacancies then gives a better collapse; it presumably involves the interactions between them (including vacancy binding and unbinding) reducing the contrast between the energy fluctuations used to determine the isomorph and the relevant saddle-point energy which governs vacancy dynamics. In a sense it is not that surprising that the specific parts of the potential

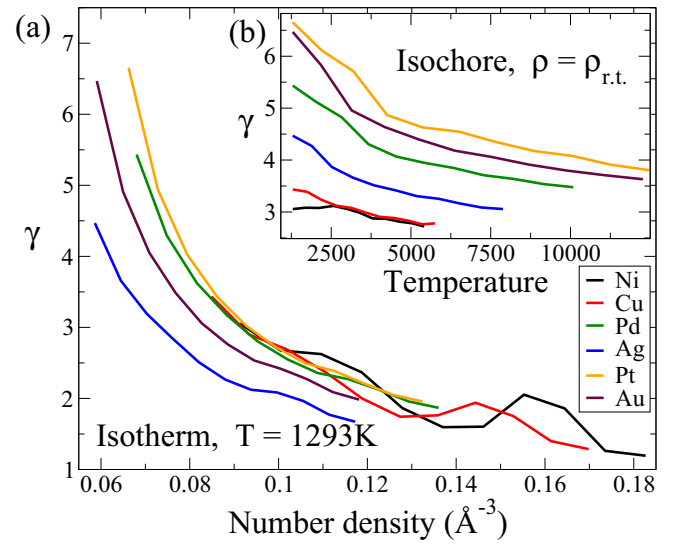


FIG. 11. Variation of  $\gamma$  for the six fcc metals along the  $T = 1293$  K isotherm in the main panel (a). The inset (b) shows the same variation along isochores where  $\rho = \rho_{r.t.}$  is the respective room temperature density of the metal. The  $\gamma$  variations are clearly dominated by changes in density. The bumps visible in the low  $\gamma$  regime, most notable in the Cu and Ni isotherms, are due to the cutoff as detailed in Appendix C.

energy function associated with vacancy hopping behave differently under density changes compared to those related to vibrations. Thus, while less pronounced in the Lennard-Jones case, the same deviations occur in both systems. This kind of nonuniform scaling could possibly also be the root of the failure to get a good collapse of the VAF, although in that case we do not see quite the same “outlier” behavior for the low density (temperature) data, except perhaps for Ni.

The general degree of isomorph invariance is similar for the different metals (see Fig. 6 for the radial distribution functions and phonon density of states, and Fig. 9 for the vacancy diffusion), which is not surprising since the same functional form of interatomic interactions is used for all of them. In the future, it is important to investigate isomorph invariance of these metals using other types of potentials, for example, EAM.

Unlike in other systems, the density-scaling exponent  $\gamma$  is strongly state point dependent when using the EMT potential. The main panel in Fig. 11 shows the variation of  $\gamma$  for the six fcc metals with changing density at constant temperature. The behavior for increasing temperature at fixed density can be seen in the inset. It is evident that the change in  $\gamma$  is dominated by changing density and only mildly decreasing with temperature. Thus, the variation of  $\gamma$  along an isomorph (not pictured) displays a similar behavior to that of the isotherms. The oscillatory behavior along the isotherms in the low  $\gamma$  region, most obvious in the cases of Ni and Cu, is an artifact due to the cutoff and occurs when increasing the density pushes a new neighbor shell through the cutoff distance (see Appendix C).

Next we discuss briefly the connection between the density-scaling exponent  $\gamma$ , of the two most important parameters (together with  $R$ ) in isomorph theory and the Grüneisen

TABLE III. Comparison of experimental Grüneisen parameters with EMT values at ambient pressure and temperature.

| Sym. | $\gamma_G$ (exp.)                          | $\gamma_G$ (EMT) |
|------|--|------------------|
| Ni   | 1.88 <sup>(a)</sup>                        | 1.9              |
| Cu   | 1.96 <sup>(a)</sup><br>1.99 <sup>(b)</sup> | 2.1              |
| Pd   | 2.33 <sup>(c)</sup>                        | 3.4              |
| Ag   | 2.40 <sup>(a)</sup><br>2.33 <sup>(b)</sup> | 2.8              |
| Au   | 2.94 <sup>(b)</sup>                        | 4.2              |
| Pt   | 2.54 <sup>(a)</sup>                        | 4.3              |

<sup>(a)</sup>Ref. [35].

<sup>(b)</sup>Ref. [36].

<sup>(c)</sup>Ref. [37].

parameter  $\gamma_G$ , which is an important thermodynamic parameter in the study of solids. The latter plays a fundamental role in the Mie-Grüneisen equation of state, often used to model metals at high pressures. Pandya *et al.* [38] argue that the Grüneisen parameter, involving as it does third derivatives of the potential, is a stringent test of a model of a solid. Reference [39] discusses the use of a pressure-dependent Grüneisen parameter to estimate the melting curves of silver, gold, and copper at high pressure. Insight from isomorph theory and the study of the isomorph properties of metals can help to understand the density dependence of  $\gamma$  and by extension  $\gamma_G$ . The microscopic definition of  $\gamma_G$  involves the density dependence of normal mode frequencies, but we focus on the macroscopic or thermodynamic definition

$$\gamma_G \equiv V \frac{\alpha_P K_T}{C_V} \quad (11)$$

where  $\alpha_P$  is the thermal expansion coefficient,  $K_T$  the isothermal bulk modulus, and  $C_V$  the isochoric specific heat. The relation

$$\gamma_G = \frac{\gamma C_V^{\text{ex}} + Nk_B}{C_V} \quad (12)$$

between  $\gamma$  and  $\gamma_G$ —where  $C_V^{\text{ex}}$  is the excess part of the isochoric heat capacity  $C_V$ —was derived in Ref. [18] and is exact within the classical approximation. Typically  $\gamma$  is greater than  $\gamma_G$  by around a factor of two. Using Eq. (12), Hummel *et al.* compared values of  $\gamma$  determined from the experimental values of  $\gamma_G$  for liquid metals to values determined from their DFT calculations (see their Fig. 5). In Table III we compare values of  $\gamma_G$  determine for the crystal phase at ambient temperature and pressure to values determined for EMT. We find good agreement for Cu and Ni, while the other values are significantly overestimated compared to experiment. From Table I for the comparison of  $\gamma$  between EMT and DFT for the liquid, and from the work of Hummel *et al.* who compared DFT results for  $\gamma$  with values inferred from experimental Grüneisen parameters, we can infer that for Au and Ag the EMT values match the DFT values reasonably well, but both overestimate the experimental values of  $\gamma$  and  $\gamma_G$ . For Pd and Pt the DFT results match experiment, but the EMT results are too high.

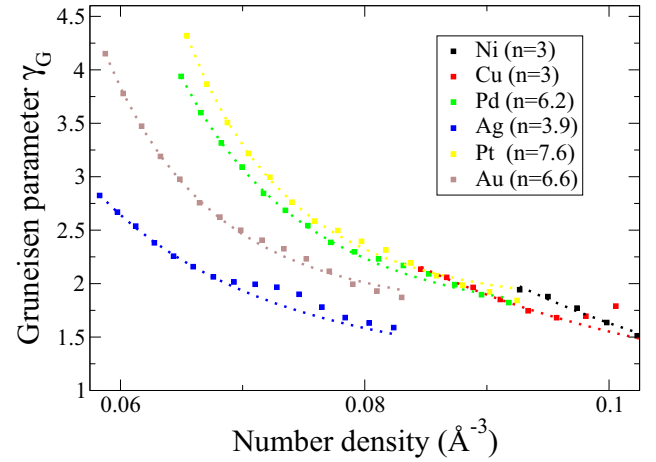


FIG. 12. Grüneisen parameter  $\gamma_G$  for the six metals as a function of (number) density at temperature 300 K (squares). The dotted lines show fits to the functional form  $a + b/\rho^n$ , with the exponent  $n$  indicated for each metal in the legend. The data show small bumps associated with the cutoff artifact mentioned above for the fitting only the data at small densities were used. For Cu and Ni allowing the exponent to vary leads to negative values of the additive constant  $a$  and here the exponent was fixed at  $n = 3$ .

There is interest in the literature in the density dependence of  $\gamma_G$ , for example, for understanding the state of matter deep in the earth’s interior [36,38]. A frequently used empirical model for the density dependence is  $\gamma_G \rho = \text{const}$ , i.e., the Grüneisen parameter decreases inversely with density. This is consistent with our observation that  $\gamma$  is mainly a function of density and for EMT metals decreases strongly with density; however, our data do not support a  $1/\rho$  dependence of  $\gamma_G$  (see Fig. 12). A closer look at the functional form of the EMT potential should provide some clues for the density dependence of both  $\gamma$  and  $\gamma_G$ .

Finally we discuss implications for the thermodynamics of melting and freezing of metals. An early prediction of the isomorph theory was that the melting curve follows an isomorph for R-simple systems [3]. This follows from the general idea that the structure is invariant. Considering constant volume conditions in the coexistence region, ensuring the presence of a fixed amount of each phase, a broad interpretation of “structure” would include “degree of crystallization,” and would have the consequence that the melting curve must follow an isomorph (otherwise the degree of crystallization along an isomorph would vary). However, for realistic systems isomorph invariance applies to a single phase, but not a system containing two phases with different densities. In the latter case terms in the free energy which depend on density only become relevant, affecting the position of the melting curve while having no relevance for the structure and dynamics of a single phase. This has been studied in detail in Refs. [40] and [41]. In particular the theory developed in Ref. [40] allows calculation of the freezing and melting lines using isomorphs as the basis for a perturbative approach. Computer simulations confirmed the predictions for the Lennard-Jones case. The data in Fig. 3 for the melting curve seem not to coincide with crystal isomorph, though data for the freezing line for

the same system (not shown) coincide very closely with a liquid isomorph. The methods of Ref. [40] should allow both to be calculated from simulations at a single temperature. Applied to more computationally demanding first-principles methods, such as DFT, this gives the possibility to make accurate melting curve determinations at high pressures.

In summary, we have shown that isomorph theory applies well to fcc metals simulated using the effective medium theory many-body potential. We find the expected invariance of structure and, slightly less perfectly, of vibrational dynamics. Instantaneous equilibration following an isomorph jump is also seen. Slightly larger deviations emerge when studying defect dynamics. This was argued to be a consequence of, on one hand, the contrast between the configurations governing (in this case) vacancy hopping and those dominating the fluctuations, and on the other hand, the strong density dependence of  $\gamma$ .

#### ACKNOWLEDGMENTS

We thank the anonymous reviewer who suggested the self-consistency check for the direct isomorph check and the analytical fit used in Fig. 12. The work was supported by the VILLUM Foundation's *Matter* Grant (No. 16515).

#### APPENDIX A: VALIDATION OF THE DIRECT ISOMORPH CHECK

We present two different ways of validating the direct isomorph check. The first is to compare with an isomorph generated by numerical integration of Eq. (7) using density steps of 1%. This is an accurate method for generating isomorphs [3], but is computationally demanding if large density changes are considered. The second validation method requires no extra simulation; instead it checks for self-consistency of the DIC

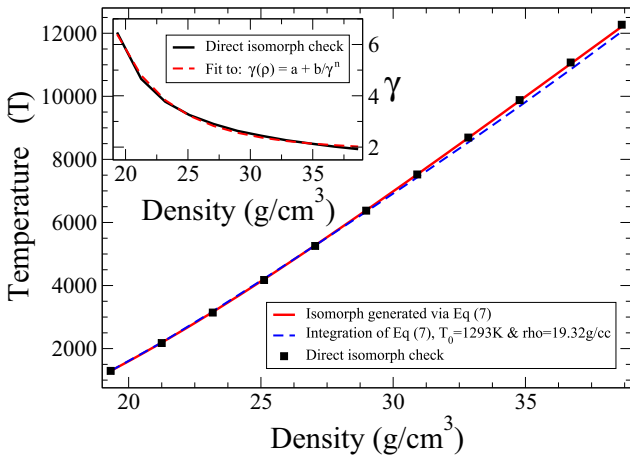


FIG. 13. Comparison between the isomorphic state points generated from the direct isomorph check and integration of Eq. (7) for Au. The inset shows a fit to  $\gamma(\rho) = a + b/\rho^n$  with parameters  $a = 1.823$ ,  $b = 2.977 \times 10^6$ ,  $n = 4.520$ ; analytic integration of Eq. (7) using this functional form starting from the lowest density yields the dashed curve. Numerical integration of Eq. (7) from the lowest density using the  $\gamma$  values determined along the way yields the smooth red curve.

isomorph: After generating the isomorph and simulating those state points, the actual  $\gamma$  values can be plotted as a function of density and fitted to a simple function  $\gamma(\rho) = a + b/\rho^n$ . An example of such a fit is shown in the inset of Fig. 13. Integration of this yields the form  $\ln T = \ln T_0 + a \ln \rho/\rho_0 + b(1/\rho^n - 1/\rho_0^n)/n$  for some starting point  $\rho_0, T_0$ . Both this and the numerical step-by-step generation of the isomorph are shown in Fig. 13. The stepwise-generated isomorph has a temperature within 0.5% of the DIC isomorph at the highest density. The analytic integration based on the fitting procedure underestimates it by about 2%, probably due to the small deviations between of the fit from  $\gamma(\rho)$  visible in the inset. Had the stepwise isomorph not been available, this could be considered a reasonable validation of the DIC.

#### APPENDIX B: TESTING DIFFERENT NUMBERS OF VACANCIES

The failure of the diffusive part of the mean-squared displacement to collapse along an isomorph is shown in Fig. 14 for the case of one vacancy and in Fig. 15 for 16 vacancies. Reasons that spoil isomorph invariance in the respective cases are discussed in the main text. Figure 16 shows a snapshot of the clustered vacancies in the 16 vacancies case; here the larger, pink spheres indicate the empty lattice positions while the actual particles were removed for better visibility,

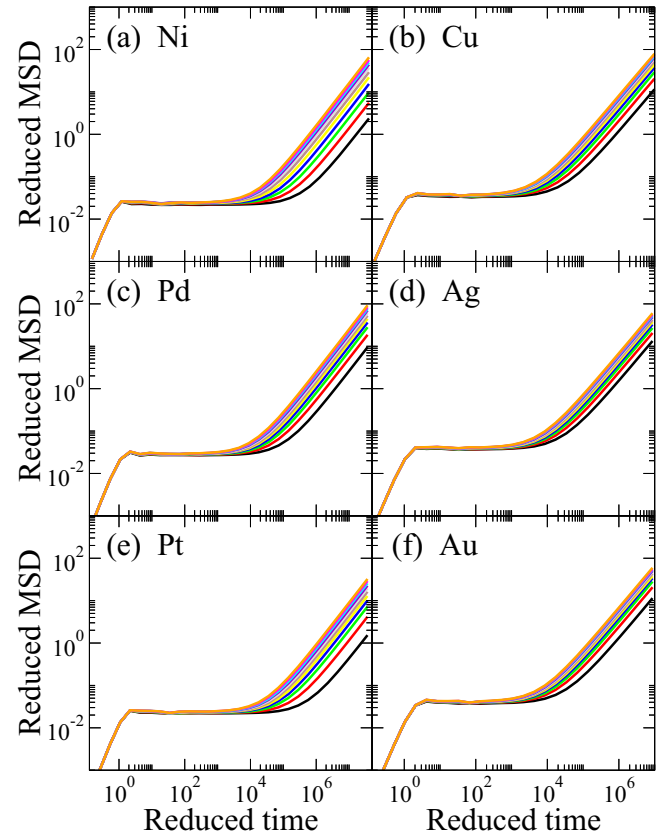


FIG. 14. MSD along isomorphs after removing one out of 4000 particles.

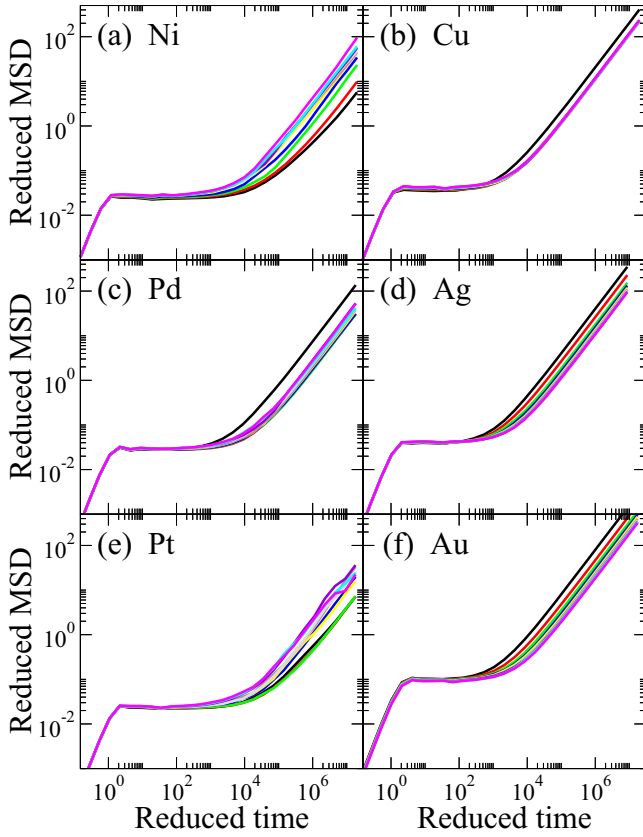


FIG. 15. MSD along isomorphs after removing 16 out of 4000 particles.

while the gray spheres are a guide to the eye and indicate the corners of the simulation box. The movie obtained from several of these “inverted” configurations shows that these

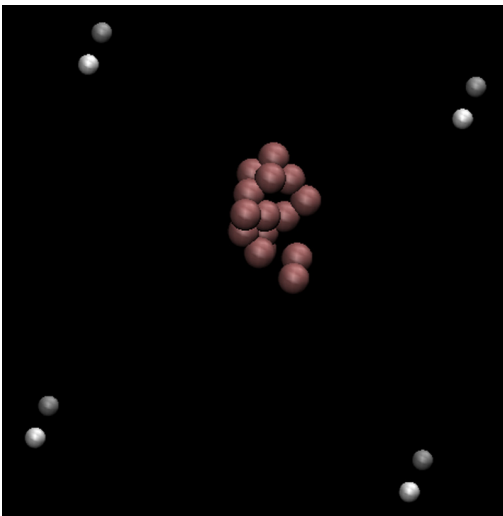


FIG. 16. Snapshot of the clustering of 16 vacancies in gold. The picture shows a “negative” of the simulation. The pink spheres indicate the vacant lattice points, and the actual particles have been removed. The gray spheres indicate the corners of the simulation box.

kind of clusters form early on in the simulation and do not disperse again.

### APPENDIX C: CUTOFF ARTIFACT

An explanation is given here as to how the bumplike artifacts in the density dependence of  $\gamma$  for Cu and Ni (Fig. 11) arise. They occur when successive neighbor shells pass through the cutoff. The latter is implemented in the form of a smoothed step function (a Fermi function) modulating the interactions: Noting that the distance to the  $n$ th shell of the zero-pressure, zero-temperature fcc lattice,  $d_n$ , is given by  $d_n = \sqrt{n}d_1$ , where  $d_1 = \frac{a}{\sqrt{2}}$  is the nearest neighbor distance, then the half-way point of the Fermi function is set to lie between the neighboring shells  $n$  and  $n + 1$  at

$$r_c = d_1 \frac{(\sqrt{n} + \sqrt{n+1})}{2} \quad (\text{C1})$$

with the default choice  $n = 3$ . The fcc lattice constant  $a$  can be expressed in terms of the number density  $\rho$  as follows:

$$\rho a^3 = 4 \Leftrightarrow a = (4/\rho)^{1/3}. \quad (\text{C2})$$

This yields the distance to the  $n$ th shell in terms of the density:

$$d_n = \sqrt{n}d_1 = \sqrt{n} \frac{a}{\sqrt{2}} = \sqrt{\frac{n}{2}} \left( \frac{4}{\rho} \right)^{1/3}. \quad (\text{C3})$$

The densities at which the  $n > 3$  shells pass through the middle of the cutoff, can be found through equating Eqs. (C3) and (C1) setting  $n = 3$  in the latter:

$$\sqrt{\frac{n}{2}} \left( \frac{4}{\rho} \right)^{1/3} = d_1 \frac{(\sqrt{3} + \sqrt{4})}{2}, \quad (\text{C4})$$

$$\rho = 4 \left( \frac{\sqrt{2}}{d_1} \frac{\sqrt{n}}{\sqrt{3} + \sqrt{4}} \right)^3. \quad (\text{C5})$$

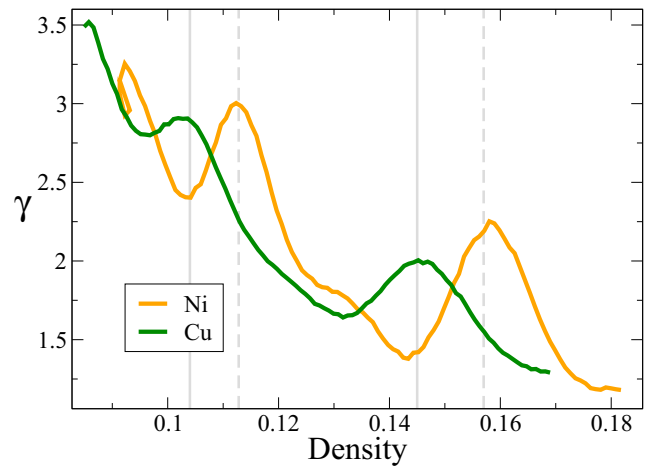


FIG. 17. Oscillatory behavior of density dependence of  $\gamma$  for Cu and Ni due to the cutoff. The light gray lines (solid for Cu, dashed for Ni) indicate the densities at which the radius of the fourth and fifth shells is exactly in the middle of passing through the cutoff.

Insertion of the material dependent nearest-neighbor distances:  $d_1^{Ni} = 2.49 \text{ \AA}$ ,  $d_1^{Cu} = 2.56 \text{ \AA}$  from the EMT parameters in Ref. [12] yields the following densities:

$$\text{Ni: } \rho_{n=4} = 0.113 \text{ \AA}^{-3}, \quad \rho_{n=5} = 0.158 \text{ \AA}^{-3} \quad (\text{C6})$$

$$\text{Cu: } \rho_{n=4} = 0.104 \text{ \AA}^{-3}, \quad \rho_{n=5} = 0.145 \text{ \AA}^{-3} \quad (\text{C7})$$

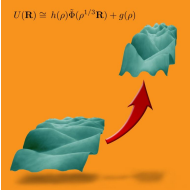
These densities are marked by light gray lines (solid for Cu and dashed for Ni) in Fig. 17 and coincide with the bumps in the variation of  $\gamma$ . The reason this effect is most visible for these metals is that  $\gamma$  reaches quite small values, which implies (interpreting  $\gamma$  as arising from an effective inverse power law exponent) a relatively long-ranged effective interaction and that contributions from distant neighbors are more significant than is the case for higher values of  $\gamma$ .

- 
- [1] N. W. Ashcroft and N. D. Mermin, *Solid State Physics* (Saunders College, Orlando, Florida, 1976).
- [2] G. Gottstein, *Physical Foundations of Materials Science* (Springer, Heidelberg, Germany, 2004).
- [3] N. Gnan, T. B. Schröder, U. R. Pedersen, N. P. Bailey, and J. C. Dyre, *J. Chem. Phys.* **131**, 234504 (2009).
- [4] F. Hummel, G. Kresse, J. C. Dyre, and U. R. Pedersen, *Phys. Rev. B* **92**, 174116 (2015).
- [5] A. L. Jensen, C. Køneke, C. Kjeldbjerg, F. S. Mahler, J. Olsen, and M. Bennetsen, Pävísning af isomorfer i metalliske væsker, Bachelor's thesis, Roskilde University, 2017.
- [6] N. P. Bailey, U. R. Pedersen, N. Gnan, T. B. Schröder, and J. C. Dyre, *J. Chem. Phys.* **129**, 184507 (2008).
- [7] Y.-C. Hu, B.-S. Shang, P.-F. Guan, Y. Yang, H.-Y. Bai, and W.-H. Wang, *J. Chem. Phys.* **145**, 104503 (2016).
- [8] D. C. Wallace, *Thermodynamics of Crystals* (Courier Corporation, Mineola, New York, 1998), pp. 104–105.
- [9] H. C. Andersen, J. D. Weeks, and D. Chandler, *Phys. Rev. A* **4**, 1597 (1971).
- [10] C. M. Roland, S. Bair, and R. Casalini, *J. Chem. Phys.* **125**, 124508 (2006).
- [11] T. S. Ingebrigtsen, L. Bøhling, T. B. Schröder, and J. C. Dyre, *J. Chem. Phys.* **136**, 061102 (2012).
- [12] K. W. Jacobsen, P. Stoltze, and J. K. Nørskov, *Surf. Sci.* **366**, 394 (1996).
- [13] N. P. Bailey, T. S. Ingebrigtsen, J. S. Hansen, A. A. Veldhorst, L. Bøhling, C. A. Lemarchand, A. E. Olsen, A. K. Bacher, L. Costigliola, U. R. Pedersen, H. Larsen, J. C. Dyre, and T. B. Schröder, *SciPost Phys.* **3**, 038 (2017).
- [14] D. E. Albrechtsen, A. E. Olsen, U. R. Pedersen, T. B. Schröder, and J. C. Dyre, *Phys. Rev. B* **90**, 094106 (2014).
- [15] C. Lee, D. Vanderbilt, K. Laasonen, R. Car, and M. Parrinello, *Phys. Rev. B* **47**, 4863 (1993).
- [16] A. Kelly and K. M. Knowles, *Crystallography and Crystal Defects* (John Wiley & Sons, Chichester, West Sussex, 2012).
- [17] N. P. Bailey, U. R. Pedersen, N. Gnan, T. B. Schröder, and J. C. Dyre, *J. Chem. Phys.* **129**, 184508 (2008).
- [18] T. B. Schröder, N. P. Bailey, U. R. Pedersen, N. Gnan, and J. C. Dyre, *J. Chem. Phys.* **131**, 234503 (2009).
- [19] T. B. Schröder, N. Gnan, U. R. Pedersen, N. P. Bailey, and J. C. Dyre, *J. Chem. Phys.* **134**, 164505 (2011).
- [20] T. B. Schröder and J. C. Dyre, *J. Chem. Phys.* **141**, 204502 (2014).
- [21] A. Tölle, H. Schober, J. Wuttke, O. G. Randl, and F. Fujara, *Phys. Rev. Lett.* **80**, 2374 (1998).
- [22] A. Tölle, *Rep. Prog. Phys.* **64**, 1473 (2001).
- [23] R. Casalini and C. M. Roland, *Phys. Rev. E* **69**, 062501 (2004).
- [24] G. Tarjus, D. Kivelson, S. Mossa, and C. Alba-Simionesco, *J. Chem. Phys.* **120**, 6135 (2004).
- [25] C. Alba-Simionesco, A. Cailliaux, A. Alegria, and G. Tarjus, *Europhys. Lett.* **68**, 58 (2004).
- [26] R. Casalini, U. Mohanty, and C. M. Roland, *J. Chem. Phys.* **125**, 014505 (2006).
- [27] RUMD software is freely available at <http://rumd.org>.
- [28] W. Haynes, *CRC Handbook of Chemistry and Physics*, 95th ed. (CRC Press, Boca Raton, Florida, 2014).
- [29] U. R. Pedersen, *J. Chem. Phys.* **139**, 104102 (2013).
- [30] P. W. Mirwald and G. C. Kennedy, *J. Geophys. Res.* **84**, 6750 (1979).
- [31] D. Alfe, L. Vočadlo, G. Price, and M. Gillan, *J. Phys.: Condens. Matter* **16**, S973 (2004).
- [32] J. Vaari, *Solid State Ion.* **270**, 10 (2015).
- [33] R. O. Simmons and R. W. Balluffi, *Phys. Rev.* **125**, 862 (1962).
- [34] D. E. Albrechtsen and A. E. Olsen, Undersøgelse af isomorfer i krystaller, Master's thesis, Roskilde University, 2013.
- [35] C. Kittel, *Introduction to Solid State Physics*, 2nd ed. (Wiley, New York, 1956).
- [36] F. Quareni and F. Mulargia, *Phys. Earth Planet. Inter.* **55**, 221 (1989).
- [37] T. F. Smith and G. K. White, *J. Phys. F* **7**, 1029 (1977).
- [38] C. Pandya, P. Vyas, T. Pandya, and V. Gohel, *Bull. Mat. Sci.* **25**, 63 (2002).
- [39] H. K. Hieu and N. N. Ha, *AIP Adv.* **3**, 112125 (2013).
- [40] U. R. Pedersen, L. Costigliola, N. P. Bailey, T. B. Schröder, and J. C. Dyre, *Nat. Commun.* **7**, 12386 (2016).
- [41] U. R. Pedersen, K. Adrjanowicz, K. Niss, and N. P. Bailey, *SciPost Phys.* **2**, 022 (2017).

*D*

*Reprints of posters*

---



# ISOMORPHS IN METAL CRYSTALS AND GLASS-FORMING ALLOYS

LAURA FRIEDEHEIM, JEPPE C. DYRE AND NICHOLAS P. BAILEY  
“Glass and Time”, INM, Roskilde University, Denmark



## BACKGROUND

Most materials with non-directional bonding (like metals) exhibit a particular (Roskilde) simple behaviour which can be explained by the **Isomorph theory** [1].

The theory predicts curves with invariant structure and dynamics, so-called isomorphs, to be present in the phase diagram when

$$R = \frac{\langle \Delta W \Delta U \rangle}{\sqrt{\langle (\Delta W)^2 \rangle \langle (\Delta U)^2 \rangle}} > 0.9 \quad (1)$$

Isomorphs can be traced out by:

$$\gamma(\rho, T) \equiv \left( \frac{\partial \ln T}{\partial \ln \rho} \right)_{S_{ex}} = \frac{\langle \Delta W \Delta U \rangle}{\langle (\Delta U)^2 \rangle} \quad (2)$$

Structure and dynamics such as relaxation times are invariant along isomorphs when expressed in appropriately **reduced units** [2]:

$$\tilde{r} = r/\rho^{-1/3}, \quad \tilde{t} = t / \left( \rho^{-1/3} \sqrt{m/k_B T} \right). \quad (3)$$

The **effective medium theory** (EMT) [3] potential combines some simple reference system which is already close to the real system (perfect fcc crystal for metals) with a small correction term:

$$E = \sum_i E_c(s_i) + \Delta E_{AS,i} \quad (4)$$

**Properties:**

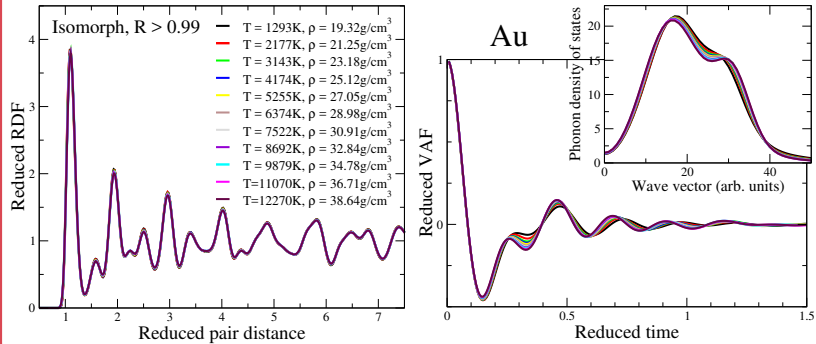
- Similar to the embedded atom method (EAM), but analytic expression
- More realistic model than Lennard-Jones

## CONCLUSION

- Results of the isomorph collapse for all metals are consistent with the expectation from isomorph theory.
- Gamma varies substantially with density, the value is material dependent and decreases monotonically.
- The onset of the plateau in the ISF of EMT CuZr is consistent with the expected experimental  $T_g$ .

## I: ISOMORPHS IN METAL CRYSTALS

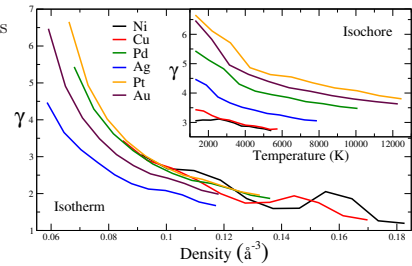
Collapse of **structure** and **dynamics** as predicted by isomorph theory shown for EMT gold



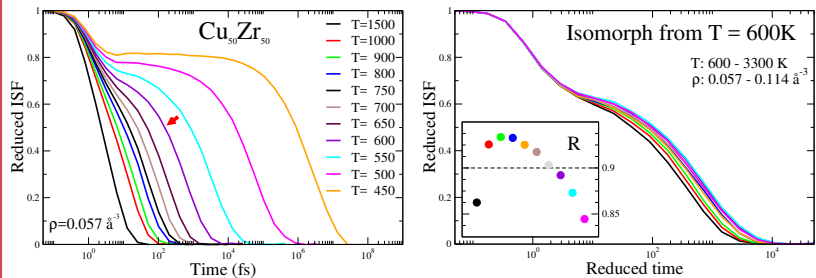
## II: $\gamma$ VARIATION IN METAL CRYSTALS

**Variation of  $\gamma$**  along isochores and isotherms for six EMT metal crystals

- As in LJ systems,  $\gamma$  depends more on density than temperature
- Dependence on density stronger than LJ
- The kinks in the isochore indicate melting
- The ‘bumps’ visible particularly at low densities in Cu and Ni are artifacts from the cut-off



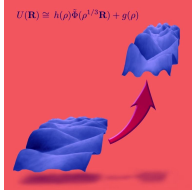
## III: SUPERCOOLED LIQUID CUZR



- The onset in CuZr is expected around 600 – 700K, the experimental value is  $T_g = 670$ K.
- Preliminary results show an approximate collapse of dynamics along an isomorph
- Ongoing work will consider other concentrations and potentials

## REFERENCES

- [1] F. Hummel, G. Kresse, J. C. Dyre, and U. R. Pedersen. *Hidden scale invariance of metals*. Phys. Rev. B **92**, 174116 (2015).
- [2] N. Gnan, T. B. Schröder, U. R. Pedersen, N. P. Bailey, and J. C. Dyre, *Pressure-energy correlations in liquids. IV. “Isomorphs” in liquid phase diagrams*. The Journal of Chemical Physics **131**, 234504 (2009).
- [3] K. Jacobsen, P. Stoltze, and J. Norskov, *A semi-empirical effective medium theory for metals and alloys*. Surface Science **366**, 394 (1996).
- [4] N. P. Bailey, T. S. Ingebrigtsen, J. S. Hansen, A. A. Veldhorst, L. Bøhling, C. A. Lemarchand, A. E. Olsen, A. K. Bacher, L. Costigliola, U. R. Pedersen, H. Larsen, J. C. Dyre, T. B. Schröder. *RUMD: A general purpose molecular dynamics package optimized to utilize GPU hardware down to a few thousand particles*. SciPost Phys. **3**, 038 (2017).



# HIDDEN SCALE INVARIANCE IN LIQUID CUZR

LAURA FRIEDEHEIM, JEPPE C. DYRE & NICHOLAS P. BAILEY  
“Glass and Time”, INM, Roskilde University, Denmark



## OBJECTIVE

Materials with non-directional bonding, such as metals, have recently been shown to exhibit a (Roskilde) simple behavior due to a hidden scale invariance as described by the isomorph theory [1, 2].

This work studies different compositions of the well-known binary glass former CuZr in the context of isomorph theory.

We investigate the existence and quality of isomorphs, employing the effective medium theory (EMT) potential [3], a realistic many-body potential, to simulate the metallic interactions

## ISOMORPH THEORY

Isomorphs are curves in the phase diagram along which structure and dynamics are invariant when given in appropriately reduced units:

$$l_0 = l \rho^{-1/3}, \quad t_0 = t \rho^{-1/3} \sqrt{m/k_B T}.$$

Isomorphs are present in the phase diagram when the instantaneous fluctuation of potential energy and virial are strongly correlated:

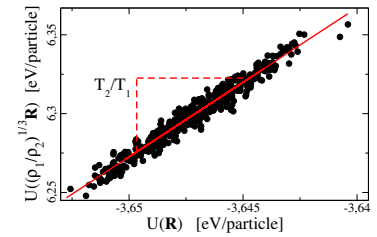
$$R = \frac{\langle \Delta W \Delta U \rangle}{\sqrt{\langle (\Delta W)^2 \rangle \langle (\Delta U)^2 \rangle}} \gtrsim 0.9.$$

This is due to an (approximate) scaling behavior of the potential energy landscape, preserving the potential energy ordering

$$U(\mathbf{R}) < U(\mathbf{R}') \rightarrow U(\lambda \mathbf{R}) < U(\lambda \mathbf{R}').$$

Isomorph state points can be found using, e.g. the direct isomorph check, that exploits that configurations on the same isomorph have the same reduced coordinates:

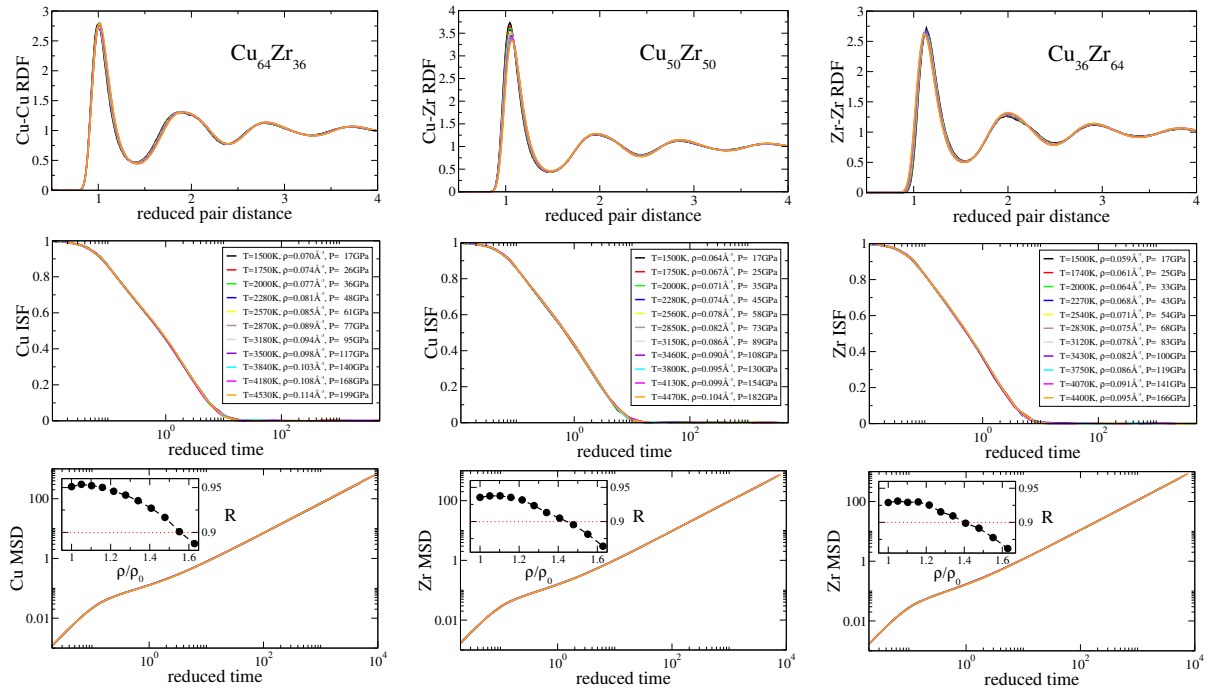
$$\rho_1^{-1/3} \mathbf{R}_1 = \rho_2^{-1/3} \mathbf{R}_2.$$



## SIMULATION RESULTS FOR $\text{Cu}_x\text{Zr}_{100-x}$ ( $x = 64, 50, 36$ )

Investigation of structure and dynamics along isomorphs in liquid CuZr up to density changes of well beyond 50%, studied by means of the radial distribution function (RDF), the intermediate scattering function (ISF), and the mean squared displacement (MSD).

GOOD COLLAPSE OF STRUCTURE AND DYNAMICS AS EXPECTED FROM ISOMORPH THEORY



All simulations were carried out using the Roskilde University Molecular Dynamics (RUMD) software package [rumd.org].

## REFERENCES

- [1] T. B. Schröder and J. C. Dyre. *Simplicity of condensed matter at its core: Generic definition of a Roskilde-simple system*. J. Chem. Phys., 141, 204502 (2014).
- [2] F. Hummel, G. Kresse, J. C. Dyre, and U. R. Pedersen. *Hidden scale invariance of metals*. Phys. Rev. B **92**, 174116 (2015).
- [3] K. Jacobsen, P. Stoltze, and J. Nørskov. *A semi-empirical effective medium theory for metals and alloys*. Surface Science **366**, 394 (1996).



## Bibliography

---

- [1] Carl McBride. *Phase diagrams: Pressure-temperature plane*, SklogWiki. [Online; accessed 16-November-2020]. (2007). URL: [http://www.sklogwiki.org/SklogWiki/index.php/Phase\\_diagrams:\\_Pressure-temperature\\_plane](http://www.sklogwiki.org/SklogWiki/index.php/Phase_diagrams:_Pressure-temperature_plane).
- [2] Carl McBride. *Phase diagrams: Density-temperature plane*, SklogWiki. [Online; accessed 16-November-2020]. (2007). URL: [http://www.sklogwiki.org/SklogWiki/index.php/Phase\\_diagrams:\\_Density-temperature\\_plane](http://www.sklogwiki.org/SklogWiki/index.php/Phase_diagrams:_Density-temperature_plane).
- [3] Q.-J. Hong and A. van de Walle. “Reentrant melting of sodium, magnesium, and aluminum: General trend”. In: *Phys. Rev. B* 100 (14 2019), p. 140102. DOI: 10.1103/PhysRevB.100.140102.
- [4] G. A. Neece and B. Widom. “Theories of Liquids”. In: *Annu. Rev. Phys. Chem.* 20.1 (1969), pp. 167–190. DOI: 10.1146/annurev.pc.20.100169.001123.
- [5] J.-L. Barrat and J.-P. Hansen. *Basic Concepts for Simple and Complex Liquids*. Cambridge University Press, 2003. DOI: 10.1017/CBO9780511606533.
- [6] J. P. Hansen and I. McDonald. *Theory of Simple Liquids*. London: Academic, 1990.
- [7] N. P. Bailey et al. “Statistical mechanics of Roskilde liquids: Configurational adiabats, specific heat contours, and density dependence of the scaling exponent”. In: *J. Chem. Phys.* 139.18 (2013), p. 184506. DOI: 10.1063/1.4827090.
- [8] A. K. Bacher et al. “The EXP pair-potential system. IV. Isotherms, isochores, and isomorphs in the two crystalline phases”. In: *J. Chem. Phys.* 152.9 (2020), p. 094505. DOI: 10.1063/1.5144871.
- [9] A. G. Eguluz. “Electronic screening at the surface of an sp-bonded metal”. In: *Phys. Scr.* 36.4 (1987), pp. 651–668. DOI: 10.1088/0031-8949/36/4/008.
- [10] “Theory of Pair Potentials in Simple s-p Metals”. In: *Mechanical Properties of Metals*. WORLD SCIENTIFIC, 1999, pp. 231–250. DOI: 10.1142/9789810248581\_0007.
- [11] E. V. Chulkov et al. “Electronic Excitations in Metals and at Metal Surfaces”. In: *Chem. Rev.* 106.10 (2006), pp. 4160–4206. DOI: 10.1021/cr050166o.
- [12] A. Sommerfeld. “Zur Elektronentheorie der Metalle auf Grund der Fermischen Statistik”. In: *Z. Phys.* 47.1-2 (1928), pp. 1–32. DOI: 10.1007/bf01391052.
- [13] N. P. Bailey et al. “Pressure-energy correlations in liquids. I. Results from computer simulations”. In: *J. Chem. Phys.* 129.18 (2008), p. 184507. DOI: 10.1063/1.2982247.

## BIBLIOGRAPHY

- [14] N. P. Bailey et al. “Pressure-energy correlations in liquids. II. Analysis and consequences”. In: *J. Chem. Phys.* 129.18 (2008), p. 184508. DOI: 10.1063/1.2982249.
- [15] T. B. Schrøder et al. “Pressure-energy correlations in liquids. III. Statistical mechanics and thermodynamics of liquids with hidden scale invariance”. In: *J. Chem. Phys.* 131.23 (2009), p. 234503. DOI: 10.1063/1.3265955.
- [16] N. Gnan et al. “Pressure-energy correlations in liquids. IV. “Isomorphs” in liquid phase diagrams”. In: *J. Chem. Phys.* 131.23 (2009), p. 234504. DOI: 10.1063/1.3265957.
- [17] T. B. Schrøder et al. “Pressure-energy correlations in liquids. V. Isomorphs in generalized Lennard-Jones systems”. In: *J. Chem. Phys.* 134.16 (2011), p. 164505. DOI: 10.1063/1.3582900.
- [18] T. B. Schrøder and J. C. Dyre. “Simplicity of condensed matter at its core: Generic definition of a Roskilde-simple system”. In: *J. Chem. Phys.* 141.20 (2014), p. 204502. DOI: 10.1063/1.4901215.
- [19] A. A. Veldhorst et al. “Isomorphs in the phase diagram of a model liquid without inverse power law repulsion”. In: *Eur. Phys. J. B* 85.1 (2012). DOI: 10.1140/epjb/e2011-20506-2.
- [20] T. S. Ingebrigtsen et al. “Communication: Thermodynamics of condensed matter with strong pressure-energy correlations”. In: *J. Chem. Phys.* 136.6 (2012), p. 061102. DOI: 10.1063/1.3685804.
- [21] T. S. Ingebrigtsen, T. B. Schrøder, and J. C. Dyre. “Isomorphs in Model Molecular Liquids”. In: *J. Phys. Chem. B* 116.3 (2012), pp. 1018–1034. DOI: 10.1021/jp2077402.
- [22] D. E. Albrechtsen et al. “Isomorph invariance of the structure and dynamics of classical crystals”. In: *Phys. Rev. B* 90 (9 2014), p. 094106. DOI: 10.1103/PhysRevB.90.094106.
- [23] C. Alba-Simionesco et al. “Scaling out the density dependence of the  $\alpha$ -relaxation in glass-forming polymers”. In: *Europhys. Lett.* 68 (2004), pp. 58–64. DOI: 10.1209/epl/i2004-10214-6.
- [24] C. M. Roland et al. “Supercooled dynamics of glass-forming liquids and polymers under hydrostatic pressure”. In: *Rep. Prog. Phys.* 68.6 (2005), pp. 1405–1478. DOI: 10.1088/0034-4885/68/6/r03.
- [25] C. M. Roland. “Relaxation Phenomena in Vitrifying Polymers and Molecular Liquids”. In: *Macromolecules* 43.19 (2010). Publisher: American Chemical Society, pp. 7875–7890. ISSN: 0024-9297. DOI: 10.1021/ma101649u.
- [26] L. A. Roed, K. Niss, and B. Jakobsen. “Communication: High pressure specific heat spectroscopy reveals simple relaxation behavior of glass forming molecular liquid”. In: *J. Chem. Phys.* 143.22 (2015), p. 221101. DOI: 10.1063/1.4936867.
- [27] A. K. Bacher and J. C. Dyre. “The mother of all pair potentials”. In: *Colloid. Polym. Sci.* 292.8 (2014), pp. 1971–1975. DOI: 10.1007/s00396-014-3290-0.

- [28] U. R. Pedersen et al. “Thermodynamics of freezing and melting”. In: *Nat. Commun.* 7 (2016), p. 12386. DOI: 10.1038/ncomms12386.
- [29] F. Hummel et al. “Hidden scale invariance of metals”. In: *Phys. Rev. B* 92 (2015), p. 174116. DOI: 10.1103/PhysRevB.92.174116.
- [30] M. W. Finnis and J. E. Sinclair. “A simple empirical N-body potential for transition metals”. In: *Philos. Mag. A* 50.1 (1984), pp. 45–55. DOI: 10.1080/01418618408244210.
- [31] J. C. Dyre. “Isomorphs, hidden scale invariance, and quasiuniversality”. In: *Phys. Rev. E* 88.4 (2013). DOI: 10.1103/physreve.88.042139.
- [32] J. C. Dyre. “Hidden Scale Invariance in Condensed Matter”. In: *J. Phys. Chem. B* 118.34 (2014), pp. 10007–10024. DOI: 10.1021/jp501852b.
- [33] A. Tölle et al. “Fast relaxation in a fragile liquid under pressure”. In: *Phys. Rev. Lett.* 80 (1998), pp. 2374–2377. DOI: {10.1103/PhysRevLett.80.2374}.
- [34] A. Tölle. “Neutron scattering studies of the model glass former ortho-terphenyl”. In: *Rep. Prog. Phys.* 64 (2001), pp. 1473–1532. DOI: {10.1088/0034-4885/64/11/203}.
- [35] R. Casalini and C. M. Roland. “Thermodynamical scaling of the glass transition dynamics”. In: *Phys. Rev. E* 69 (2004), p. 062501. DOI: 10.1103/PhysRevE.69.062501.
- [36] G. Tarjus et al. “Disentangling density and temperature effects in the viscous slowing down of glassforming liquids”. In: *J. Chem. Phys.* 120 (2004), pp. 6135–6141. DOI: 10.1063/1.1649732.
- [37] C. M. Roland, S. Bair, and R. Casalini. “Thermodynamic scaling of the viscosity of van der Waals, H-bonded, and ionic liquids”. In: *J. Chem. Phys.* 125 (2006), p. 124508. DOI: 10.1063/1.2346679.
- [38] R. Casalini, U. Mohanty, and C. M. Roland. “Thermodynamic interpretation of the scaling of the dynamics of supercooled liquids”. In: *J. Chem. Phys.* 125 (2006), p. 014505. DOI: 10.1063/1.2206582.
- [39] L. Friedeheim, J. C. Dyre, and N. P. Bailey. “Hidden scale invariance at high pressures in gold and five other face-centered-cubic metal crystals”. In: *Phys. Rev. E* 99 (2019), p. 022142. DOI: 10.1103/PhysRevE.99.022142.
- [40] L. Friedeheim et al. “Melting curve predictions for DFT metals”. Manuscript in preparation.
- [41] J. C. Dyre. “Perspective: Excess-entropy scaling”. In: *J. Chem. Phys.* 149.21 (2018), p. 210901. DOI: 10.1063/1.5055064.
- [42] L. A. Roed et al. “Generalized single-parameter aging tests and their application to glycerol”. In: *J. Chem. Phys.* 150.4 (2019), p. 044501. DOI: 10.1063/1.5066387.
- [43] L. Verlet. “Computer ”Experiments” on Classical Fluids. I. Thermodynamical Properties of Lennard-Jones Molecules”. In: *Phys. Rev.* 159.1 (1967), pp. 98–103. DOI: 10.1103/physrev.159.98.

## BIBLIOGRAPHY

- [44] L. Verlet. “Computer ”Experiments” on Classical Fluids. II. Equilibrium Correlation Functions”. In: *Phys. Rev.* 165.1 (1968), pp. 201–214. DOI: 10.1103/physrev.165.201.
- [45] C. Runge. “Ueber die numerische Auflösung von Differentialgleichungen”. In: *Math. Ann.* 46.2 (1895), pp. 167–178. DOI: 10.1007/bf01446807.
- [46] W. Kutta. *Beitrag zur näherungsweise Integration totaler Differentialgleichungen*. Teubner, 1901.
- [47] W. H. Press et al. *Numerical Recipes in C: The Art of Scientific Computing*. USA: Cambridge University Press, 1988. ISBN: 052135465X.
- [48] M. P. Allen and D. J. Tildesley. *Computer Simulation of Liquids*. USA: Clarendon Press, 1989. ISBN: 0198556454.
- [49] D. Frenkel and B. Smit. *Understanding Molecular Simulation: From Algorithms to Applications*. Second. Vol. 1. Computational Science Series. San Diego: Academic Press, 2002.
- [50] D. C. Wallace. *Thermodynamics of crystals*. Courier Corporation, 1998, pp. 104–105.
- [51] K. Jacobsen, P. Stoltze, and J. Nørskov. “A semi-empirical effective medium theory for metals and alloys”. In: *Surf. Sci.* 366.2 (1996), pp. 394–402. ISSN: 0039-6028. DOI: 10.1016/0039-6028(96)00816-3.
- [52] J. W. Gibbs. *Elementary principles in statistical mechanics developed with especial reference to the rational foundation of thermodynamics /*. New York ,C. Scribner, 1902, p. 236.
- [53] D. Chandler and D. Wu. *Introduction to Modern Statistical Mechanics*. Oxford University Press, 1987. ISBN: 9780195042771.
- [54] Wikibooks. *Molecular Simulation/Radial Distribution Functions — Wikibooks, The Free Textbook Project*. [Online; accessed 19-November-2020]. (2020). URL: [https://en.wikibooks.org/w/index.php?title=Molecular\\_Simulation/Radial\\_Distribution\\_Functions&oldid=3710016](https://en.wikibooks.org/w/index.php?title=Molecular_Simulation/Radial_Distribution_Functions&oldid=3710016).
- [55] G. L. Dirichlet. “Über die Reduction der positiven quadratischen Formen mit drei unbestimmten ganzen Zahlen.” In: *J. reine angew. Math.* 1850.40 (1Jul. 1850), pp. 209–227. DOI: 10.1515/crll.1850.40.209.
- [56] A. Malins, J. Eggers, and C. P. Royall. “Investigating isomorphs with the topological cluster classification”. In: *J. Chem. Phys.* 139.23 (2013), p. 234505. DOI: 10.1063/1.4830416. URL: <https://doi.org/10.1063/1.4830416>.
- [57] S.-T. Lin, M. Blanco, and W. A. Goddard. “The two-phase model for calculating thermodynamic properties of liquids from molecular dynamics: Validation for the phase diagram of Lennard-Jones fluids”. In: *J. Chem. Phys.* 119.22 (2003), pp. 11792–11805. DOI: 10.1063/1.1624057.
- [58] L. Van Hove. “Correlations in Space and Time and Born Approximation Scattering in Systems of Interacting Particles”. In: *Phys. Rev.* 95 (1 1954), pp. 249–262. DOI: 10.1103/PhysRev.95.249.

- [59] M. Born and R. Oppenheimer. “Zur Quantentheorie der Molekeln”. In: *Ann. Phys.* 389.20 (1927), pp. 457–484. DOI: 10.1002/andp.19273892002.
- [60] R. Martin, R. Martin, and C. U. Press. *Electronic Structure: Basic Theory and Practical Methods*. Cambridge University Press, 2004. ISBN: 9780521782852.
- [61] W. Harrison. *Solid State Theory*. Dover Books on Physics. Dover Publications, 1980, pp. 90–92. ISBN: 9780486639482.
- [62] L. H. Thomas. “The calculation of atomic fields”. In: *Math. Proc. Cambridge Philos. Soc.* 23.5 (1927), pp. 542–548. DOI: 10.1017/s0305004100011683.
- [63] E. H. Lieb and B. Simon. “The Thomas-Fermi theory of atoms, molecules and solids”. In: *Adv. Math.* 23.1 (1977), pp. 22–116. DOI: 10.1016/0001-8708(77)90108-6.
- [64] A. Pribram-Jones, D. A. Gross, and K. Burke. “DFT: A Theory Full of Holes?” In: *Annu. Rev. Phys. Chem.* 66.1 (2015), pp. 283–304. DOI: 10.1146/annurev-physchem-040214-121420.
- [65] R. Jones. “Density functional theory: Its origins, rise to prominence, and future”. In: *Rev. Mod. Phys.* 87.3 (2015), pp. 897–923. DOI: 10.1103/revmodphys.87.897.
- [66] A. E. Mattsson et al. “Designing meaningful density functional theory calculations in materials science—a primer”. In: *Modell. Simul. Mater. Sci. Eng.* 13.1 (2004), R1–R31. DOI: 10.1088/0965-0393/13/1/r01.
- [67] P. Hohenberg and W. Kohn. “Inhomogeneous Electron Gas”. In: *Phys. Rev.* 136 (3B 1964), B864–B871. DOI: 10.1103/PhysRev.136.B864.
- [68] M. Levy. “Universal variational functionals of electron densities, first-order density matrices, and natural spin-orbitals and solution of the  $v$ -representability problem”. In: *Proc. Natl. Acad. Sci.* 76.12 (1979), pp. 6062–6065. ISSN: 0027-8424. DOI: 10.1073/pnas.76.12.6062.
- [69] G. Vignale and M. Rasolt. “Density-functional theory in strong magnetic fields”. In: *Phys. Rev. Lett.* 59 (20 1987), pp. 2360–2363. DOI: 10.1103/PhysRevLett.59.2360.
- [70] W. Kohn and L. J. Sham. “Self-Consistent Equations Including Exchange and Correlation Effects”. In: *Phys. Rev.* 140 (4A 1965), A1133–A1138. DOI: 10.1103/PhysRev.140.A1133.
- [71] J. C. Slater and J. C. Phillips. “Quantum Theory of Molecules and Solids Vol. 4: The Self-Consistent Field for Molecules and Solids”. In: *Phys. Today* 27.12 (1974), pp. 49–50. DOI: 10.1063/1.3129035.
- [72] U. von Barth and L. Hedin. “A local exchange-correlation potential for the spin polarized case. i”. In: *J. Phys. C: Solid State Phys.* 5.13 (1972), pp. 1629–1642. DOI: 10.1088/0022-3719/5/13/012.
- [73] O. Gunnarsson and B. I. Lundqvist. “Exchange and correlation in atoms, molecules, and solids by the spin-density-functional formalism”. In: *Phys. Rev. B* 13 (10 1976), pp. 4274–4298. DOI: 10.1103/PhysRevB.13.4274.

## BIBLIOGRAPHY

- [74] D. Ceperley. “Ground state of the fermion one-component plasma: A Monte Carlo study in two and three dimensions”. In: *Phys. Rev. B* 18 (7 1978), pp. 3126–3138. DOI: 10.1103/PhysRevB.18.3126.
- [75] J. P. Perdew and A. Zunger. “Self-interaction correction to density-functional approximations for many-electron systems”. In: *Phys. Rev. B* 23 (10 1981), pp. 5048–5079. DOI: 10.1103/PhysRevB.23.5048.
- [76] V. Sahni, K. -P. Bohnen, and M. K. Harbola. “Analysis of the local-density approximation of density-functional theory”. In: *Phys. Rev. A* 37 (6 1988), pp. 1895–1907. DOI: 10.1103/PhysRevA.37.1895.
- [77] R. O. Jones and O. Gunnarsson. “The density functional formalism, its applications and prospects”. In: *Rev. Mod. Phys.* 61.3 (1989), pp. 689–746. DOI: 10.1103/revmodphys.61.689.
- [78] J. P. Perdew. “Density functional theory and the band gap problem”. In: *Int. J. Quantum Chem.* 28.S19 (2009), pp. 497–523. DOI: 10.1002/qua.560280846.
- [79] E. H. Lieb and B. Simon. “Thomas-Fermi Theory Revisited”. In: *Phys. Rev. Letters* 31.11 (1973), pp. 681–683. DOI: 10.1103/physrevlett.31.681.
- [80] E. H. Lieb and B. Simon. “The Thomas-Fermi theory of atoms, molecules and solids”. In: *Adv. Math.* 23.1 (1977), pp. 22–116. DOI: 10.1016/0001-8708(77)90108-6.
- [81] E. H. Lieb. “Thomas-fermi and related theories of atoms and molecules”. In: *Rev. Mod. Phys.* 53.4 (1981), pp. 603–641. DOI: 10.1103/revmodphys.53.603.
- [82] B. Xiao et al. “Testing density functionals for structural phase transitions of solids under pressure: Si, SiO<sub>2</sub>, and Zr”. In: *Phys. Rev. B* 88.18 (2013). DOI: 10.1103/physrevb.88.184103.
- [83] J. P. Perdew et al. “Prescription for the design and selection of density functional approximations: More constraint satisfaction with fewer fits”. In: *J. Chem. Phys.* 123.6 (2005), p. 062201. DOI: 10.1063/1.1904565.
- [84] A. D. Becke. “Density-functional exchange-energy approximation with correct asymptotic behavior”. In: *Phys. Rev. A* 38.6 (1988), p. 3098.
- [85] K. Burke, J. P. Perdew, and Y. Wang. “Derivation of a Generalized Gradient Approximation: The PW91 Density Functional”. In: *Electronic Density Functional Theory: Recent Progress and New Directions*. Ed. by J. F. Dobson, G. Vignale, and M. P. Das. Boston, MA: Springer US, 1998, pp. 81–111. ISBN: 978-1-4899-0316-7. DOI: 10.1007/978-1-4899-0316-7\_7.
- [86] J. P. Perdew, K. Burke, and M. Ernzerhof. “Generalized Gradient Approximation Made Simple”. In: *Phys. Rev. Letters* 77.18 (1996), pp. 3865–3868. DOI: 10.1103/physrevlett.77.3865.
- [87] A. D. Becke. “Density-functional thermochemistry. III. The role of exact exchange”. In: *J. Chem. Phys.* 98.7 (1993), pp. 5648–5652. DOI: 10.1063/1.464913.

- [88] Y. Zhao, N. E. Schultz, and D. G. Truhlar. “Design of Density Functionals by Combining the Method of Constraint Satisfaction with Parametrization for Thermochemistry, Thermochemical Kinetics, and Noncovalent Interactions”. In: *J. Chem. Theory Comput.* 2.2 (2006), pp. 364–382. DOI: 10.1021/ct0502763.
- [89] Y. Zhao and D. G. Truhlar. “The M06 suite of density functionals for main group thermochemistry, thermochemical kinetics, noncovalent interactions, excited states, and transition elements: two new functionals and systematic testing of four M06-class functionals and 12 other functionals”. In: *Theor. Chem. Acc.* 120.1-3 (2007), pp. 215–241. DOI: 10.1007/s00214-007-0310-x.
- [90] M. E. Yu. *Pseudopotential for Efficient Simulation – Materials Square Tech Blog*. [Online; accessed 02-December-2020]. (2020). URL: <https://blog.virtuallab.co.kr/en/2019/10/02/19-pseudopotential-for-efficient-simulation>.
- [91] F. Giustino. *Materials Modelling Using Density Functional Theory: Properties and Predictions*. Oxford University Press, 2014. ISBN: 9780199662449.
- [92] G. Kresse and J. Hafner. “Ab initio molecular-dynamics simulation of the liquid-metal–amorphous-semiconductor transition in germanium”. In: *Phys. Rev. B* 49 (20 1994), pp. 14251–14269. DOI: 10.1103/PhysRevB.49.14251.
- [93] G. Kresse and J. Furthmüller. “Efficiency of ab-initio total energy calculations for metals and semiconductors using a plane-wave basis set”. In: *Comput. Mater. Sci.* 6.1 (1996), pp. 15–50. ISSN: 0927-0256. DOI: 10.1016/0927-0256(96)00008-0.
- [94] G. Kresse and J. Furthmüller. “Efficient iterative schemes for ab initio total-energy calculations using a plane-wave basis set”. In: *Phys. Rev. B* 54 (16 1996), pp. 11169–11186. DOI: 10.1103/PhysRevB.54.11169.
- [95] P. E. Blöchl. “Projector augmented-wave method”. In: *Phys. Rev. B* 50 (24 1994), pp. 17953–17979. DOI: 10.1103/PhysRevB.50.17953.
- [96] N. Ashcroft and N. Mermin. *Solid State Physics (Orlando, Florida)*. 1976.
- [97] W. Setyawan and S. Curtarolo. “High-throughput electronic band structure calculations: Challenges and tools”. In: *Comput. Mater. Sci.* 49.2 (2010), pp. 299–312. ISSN: 0927-0256. DOI: 10.1016/j.commatsci.2010.05.010.
- [98] M. S. Daw and M. I. Baskes. “Semiempirical, Quantum Mechanical Calculation of Hydrogen Embrittlement in Metals”. In: *Phys. Rev. Letters* 50.17 (1983), pp. 1285–1288. DOI: 10.1103/physrevlett.50.1285.
- [99] M. S. Daw and M. I. Baskes. “Embedded-atom method: Derivation and application to impurities, surfaces, and other defects in metals”. In: *Phys. Rev. B* 29.12 (1984), pp. 6443–6453. DOI: 10.1103/physrevb.29.6443.
- [100] F. Ercolessi, E. Tosatti, and M. Parrinello. “Au (100) Surface Reconstruction”. In: *Phys. Rev. Letters* 57.6 (1986), pp. 719–722. DOI: 10.1103/physrevlett.57.719.
- [101] M. S. Daw, S. M. Foiles, and M. I. Baskes. “The embedded-atom method: a review of theory and applications”. In: *Mater. Sci. Rep.* 9.7-8 (1993), pp. 251–310. DOI: 10.1016/0920-2307(93)90001-u.

## BIBLIOGRAPHY

- [102] N. P. Bailey et al. “RUMD: A general purpose molecular dynamics package optimized to utilize GPU hardware down to a few thousand particles”. In: *SciPost Phys.* 3 (6 2017), p. 038. DOI: 10.21468/SciPostPhys.3.6.038.
- [103] M. J. Puska, R. M. Nieminen, and M. Manninen. “Atoms embedded in an electron gas: Immersion energies”. In: *Phys. Rev. B* 24.6 (1981), pp. 3037–3047. DOI: 10.1103/physrevb.24.3037.
- [104] J. K. Nørskov. “Covalent effects in the effective-medium theory of chemical binding: Hydrogen heats of solution in the 3d-metals”. In: *Phys. Rev. B* 26.6 (1982), pp. 2875–2885. DOI: 10.1103/physrevb.26.2875.
- [105] K. W. Jacobsen, J. K. Nørskov, and M. J. Puska. “Interatomic interactions in the effective-medium theory”. In: *Phys. Rev. B* 35.14 (1987), pp. 7423–7442. DOI: 10.1103/physrevb.35.7423.
- [106] J. K. Nørskov and N. D. Lang. “Effective-medium theory of chemical binding: Application to chemisorption”. In: *Phys. Rev. B* 21.6 (1980), pp. 2131–2136. DOI: 10.1103/physrevb.21.2131.
- [107] N. Chetty et al. “Ab initio potential for solids”. In: *Phys. Rev. B* 46.7 (1992), pp. 3798–3809. DOI: 10.1103/physrevb.46.3798.
- [108] W. Haynes. *CRC Handbook of Chemistry and Physics, 95th Edition*. CRC Press, 2014. ISBN: 9781482208689.
- [109] U. R. Pedersen. “Direct calculation of the solid-liquid Gibbs free energy difference in a single equilibrium simulation”. In: *J. Chem. Phys.* 139.10 (2013), pp. 104102–104102. DOI: 10.1063/1.4818747.
- [110] R. O. Simmons and R. W. Balluffi. “Measurement of Equilibrium Concentrations of Lattice Vacancies in Gold”. In: *Phys. Rev.* 125 (3 1962), pp. 862–872. DOI: 10.1103/PhysRev.125.862.
- [111] D. E. Albrechtsen and A. E. Olsen. “Undersøgelser af isomorfer i krystaller”. (In Danish). MA thesis. Roskilde University, 2013.
- [112] H.-M. Hsiao et al. “Thermodynamic assessment of the Ag-Zr and Cu-Zr binary systems”. In: *Calphad* 55 (2016), pp. 77–87. DOI: 10.1016/j.calphad.2016.08.001.
- [113] A. Păduraru et al. “An Interatomic Potential for Studying CuZr Bulk Metallic Glasses”. In: *Adv. Eng. Mater.* 9.6 (2007), pp. 505–508. DOI: 10.1002/adem.200700047.
- [114] L. Bøhling et al. “Estimating the density-scaling exponent of a monatomic liquid from its pair potential”. In: *J. Chem. Phys.* 140.12 (2014), p. 124510. DOI: 10.1063/1.4869114.
- [115] I. Bell, J. Dyre, and T. Ingebrigtsen. “Excess-entropy scaling in supercooled binary mixtures”. In: *Nat. Commun.* 11.4300 (2020). DOI: 10.1038/s41467-020-17948-1.
- [116] D. K. Chokappa and P. Clancy. “A computer simulation study of the melting and freezing properties of a system of Lennard-Jones particles”. In: *Mol. Phys.* 61.3 (1987), pp. 597–615. DOI: 10.1080/00268978700101341.

- [117] A. B. Belonoshko et al. “Melting and critical superheating”. In: *Phys. Rev. B* 73.1 (2006). DOI: 10.1103/physrevb.73.012201.
- [118] J.-Y. Raty, E. Schwegler, and S. A. Bonev. “Electronic and structural transitions in dense liquid sodium”. In: *Nature* 449.7161 (2007), pp. 448–451. DOI: 10.1038/nature06123.
- [119] A. B. Belonoshko et al. “Melting of a polycrystalline material”. In: *Eur. Phys. J. Spec. Top.* 216.1 (2013), pp. 199–204. DOI: 10.1140/epjst/e2013-01743-1.
- [120] Q. Hong and A. van de Walle. “Solid-liquid coexistence in small systems: A statistical method to calculate melting temperatures”. In: *J. Chem. Phys.* 139 (2013), p. 094114. DOI: 10.1063/1.4819792.
- [121] L. Dubrovinsky et al. “The most incompressible metal osmium at static pressures above 750 gigapascals”. In: *Nature* 525.7568 (2015), pp. 226–229. DOI: 10.1038/nature14681.
- [122] N. N. Patel, M. Sunder, and S. M. Sharma. “Laser heated diamond anvil cell facility for high temperature high pressure research: application to material synthesis and melting studies”. In: *Indian J. Phys.* 92.10 (2018), pp. 1259–1269. DOI: 10.1007/s12648-018-1237-x.
- [123] A. Hänström and P. Lazor. “High pressure melting and equation of state of aluminium”. In: *J. Alloys Compd.* 305.1 (2000), pp. 209–215. ISSN: 0925-8388. DOI: 10.1016/S0925-8388(00)00736-2.
- [124] R. Boehler and M. Ross. “Melting curve of aluminum in a diamond cell to 0.8 Mbar: implications for iron”. In: *Earth Planet. Sci. Lett.* 153.3-4 (1997), pp. 223–227. DOI: 10.1016/S0012-821X(97)00188-X.
- [125] J. Bouchet et al. “Melting curve of aluminum up to 300 GPa obtained through ab initio molecular dynamics simulations”. In: *Phys. Rev. B* 80 (9 2009), p. 094102. DOI: 10.1103/PhysRevB.80.094102.
- [126] D. Errandonea et al. “Systematics of transition-metal melting”. In: *Phys. Rev. B* 63 (13 2001), p. 132104. DOI: 10.1103/PhysRevB.63.132104.
- [127] U. R. Pedersen et al. “The EXP pair-potential system. III. Thermodynamic phase diagram”. In: *J. Chem. Phys.* 150.17 (2019), p. 174501. DOI: 10.1063/1.5094395.
- [128] E. Gregoryanz et al. “Melting of Dense Sodium”. In: *Phys. Rev. Letters* 94.18 (2005). DOI: 10.1103/physrevlett.94.185502.
- [129] M. P. Desjarlais. “First-principles calculation of entropy for liquid metals”. In: *Phys. Rev. E* 88.6 (2013). DOI: 10.1103/physreve.88.062145.
- [130] F. A. Lindemann. “Über die Berechnung molekularer Eigenfrequenzen (The calculation of molecular Eigen-frequencies)”. In: *Z. Phys* 11 (14 1910), pp. 609–612.
- [131] L. Burakovsky and D. L. Preston. “Analytic model of the Grüneisen parameter all densities”. In: *J. Phys. Chem. Solids* 65.8-9 (2004), pp. 1581–1587. DOI: 10.1016/j.jpcs.2003.10.076.

## BIBLIOGRAPHY

- [132] R. A. Buckingham. “The classical equation of state of gaseous helium, neon and argon”. In: *Proc. Math. Phys. Eng. Sci.* 168.933 (1938), pp. 264–283. DOI: 10.1098/rspa.1938.0173.
- [133] P. M. Morse. “Diatomic Molecules According to the Wave Mechanics. II. Vibrational Levels”. In: *Phys. Rev.* 34.1 (1929), pp. 57–64. DOI: 10.1103/physrev.34.57.
- [134] A. K. Bacher, T. B. Schrøder, and J. C. Dyre. “The EXP pair-potential system. I. Fluid phase isotherms, isochores, and quasiuniversality”. In: *J. Chem. Phys.* 149.11 (2018), p. 114501. DOI: 10.1063/1.5043546.
- [135] A. K. Bacher, T. B. Schrøder, and J. C. Dyre. “The EXP pair-potential system. II. Fluid phase isomorphs”. In: *J. Chem. Phys.* 149.11 (2018), p. 114502. DOI: 10.1063/1.5043548.
- [136] P. J. Steinhardt, D. R. Nelson, and M. Ronchetti. “Bond-orientational order in liquids and glasses”. In: *Phys. Rev. B* 28 (1983), pp. 784–805. DOI: 10.1103/PhysRevB.28.784.
- [137] VASP support. *Energy vs volume Volume relaxations and Pulay stress, Vaspwiki*. [Online; accessed 08-December-2020]. URL: [www.vasp.at/wiki/index.php/Energy%5C\\_vs%5C\\_volume%5C\\_Volume%5C\\_relaxations%5C\\_and%5C\\_Pulay%5C\\_stress](http://www.vasp.at/wiki/index.php/Energy%5C_vs%5C_volume%5C_Volume%5C_relaxations%5C_and%5C_Pulay%5C_stress).